Learning Control and Inertial Realtime Gait Analysis in Biomedical Applications

Improving Diagnosis and Treatment by Automatic Adaption and Feedback Control

vorgelegt von
Dipl.-Ing. Thomas Seel
geboren in Magdeburg

von der Fakultät IV – Elektrotechnik und Informatik
der Technischen Universität Berlin
zur Erlangung des akademischen Grades

Doktor der Ingenieurwissenschaften
– Dr.-Ing. –

genehmigte Dissertation

Promotionsausschuss:

Vorsitzender: Prof. Dr.-Ing. Clemens Gühmann
Gutachter: Prof. Dr.-Ing. Jörg Raisch
Gutachter: Prof. Dr.-Ing. Dirk Abel
Gutachter: Dr. Juan C. Moreno Sastoque

Tag der wissenschaftlichen Aussprache: 15. Dezember 2015

Berlin 2016

In memory of my dad.

Abstract

Improved medical diagnosis and treatment can be achieved by combining modern technologies with well-developed methods. This dissertation aims for deriving new methods that facilitate the use of inertial measurement units and learning control techniques in biomedical systems and at demonstrating how advanced diagnosis and treatment systems can be designed by incorporating these technologies.

To this end, a modular set of novel methods for inertial realtime gait analysis is proposed. This includes methods for the detection of characteristic gait events as well as for realtime assessment of the foot orientation. Moreover, methods for joint axis and position estimation are derived that exploit the kinematic constraints induced by the joint, and methods for flexion/extension joint angle measurement are proposed. All of these methods avoid the use of magnetometers and can therefore be used indoors as well as in the proximity of ferromagnetic material and magnetic disturbances. Furthermore, they supersede precise sensor mounting requirements as well as restrictive calibration protocols and automatically adjust themselves to the user. For each of the new methods, a practical proof of concept is provided by means of gait experiments with healthy subjects, stroke patients, or transfemoral amputees.

Just as inertial sensing, Iterative Learning Control (ILC) is considered a promising tool for biomedical application systems by a growing number of researchers. This dissertation addresses the fact that classic ILC theory is technically too restrictive for some of these applications and extends the classic ILC design in the lifted-systems framework to the class of repetitive trajectory tracking tasks with variable pass length. Two standard learning laws are considered. The maximum-pass-length error is introduced as a useful concept for convergence analysis of variable-pass-length systems, and necessary and sufficient conditions for monotonic convergence of this error are derived. All results are summarized in a set of practical control design guidelines.

The potential of ILC for biomedical systems is then demonstrated using the example of a continuous blood pressure measurement technique that requires precise control of the blood flow through a superficial artery. This dissertation demonstrates that the controller performance, and thus the measurement accuracy, can be improved by exploiting the repetitive nature of the control problem. A learning cascaded controller is designed and evaluated experimentally.

In a second application example, methods from inertial gait analysis and ILC are combined to propose an adaptive system for improved treatment of the drop foot syndrome via functional electrical stimulation (FES) of the peroneal nerve. A novel three-electrodes setup and a piecewise linear controller output mapping are proposed to provide two independent FES parameters, which are manipulated by a decentralized ILC scheme to control the pitch and roll angle of the paretic foot during swing phase. Experiments with stroke patients demonstrate that this closed-loop approach allows the system to quickly adjust the FES to the patient's needs and to compensate changes in muscular tone and fatigue automatically.

Zusammenfassung

Viele medizinische Diagnose- und Behandlungssysteme können verbessert werden, indem moderne Technologien mit Methoden kombiniert werden, die diese Technologien optimal einsetzen. Diese Arbeit stellt neue Methoden vor, welche die Verwendbarkeit von Inertialsensorik und lernenden Regelungen in medizinischen Systemen verbessern. Darüber hinaus wird anhand zweier Anwendungen aufgezeigt, welche Fortschritte sich durch den Einsatz dieser Technologien erzielen lassen.

Zunächst wird eine Reihe neuer Methoden für die inertialsensorbasierte Echtzeit-Ganganalyse entwickelt. Dies umfasst Verfahren für die Gangphasenerkennung und die Echtzeitmessung von Fußorientierungswinkeln und Kniegelenkwinkeln sowie für die automatische Bestimmung lokaler Gelenkachsen- und Gelenkpositionskoordinaten durch Ausnutzung kinematischer Zwangsbedingungen. All diese Verfahren verzichten auf die Nutzung von Magnetometermessdaten und können daher in Gebäuden sowie in der Nähe ferromagnetischer Materialien und magnetischer Störfelder eingesetzt werden. Des Weiteren ermöglichen sie dem Sensornetzwerk, sich automatisch an den Nutzer anzupassen, wodurch bislang übliche Restriktionen bezüglich exakter Sensoranbringung oder präzise auszuführender Kalibrierungsbewegungen entfallen. Für jede der neuen Methoden wird in experimentellen Untersuchungen der Fortschritt gegenüber dem Stand der Technik aufgezeigt.

Neben der Inertialsensorik gelten auch die iterativ lernenden Regelungen (ILR) einer zunehmenden Zahl von Forschern als vielversprechendes Mittel zur Verbesserung medizinischer Diagnose- und Behandlungssysteme. Da die klassische ILR-Theorie für viele biomedizinische Anwendungen zu restriktiv ist, erfolgt in dieser Dissertation eine Erweiterung dieser Theorie auf sich wiederholende Folgeregelungsaufgaben mit variabler Zyklusdauer. Es werden entsprechende Modifikationen zweier klassischer Lerngesetze vorgeschlagen und Kriterien für die monotone Konvergenz mehrerer geeigneter Regelabweichungsmaße hergeleitet. Alle Erkenntnisse werden schließlich in einem Satz von praktischen Reglerentwurfsempfehlungen zusammengefasst.

Die Verbesserungsmöglichkeiten, die sich durch den Einsatz iterativ lernender Regelungen ergeben, werden am Beispiel eines neuartigen kontinuierlichen Blutdruckmessverfahrens aufgezeigt, welches die präzise Regelung des Blutflusses durch eine oberflächlich verlaufende Arterie erfordert. Die vorliegende Dissertation zeigt, dass die Wiederholbarkeit der Regelungsaufgabe ausgenutzt werden kann, um die Regelgüte – und somit die Genauigkeit des Messverfahrens – zu verbessern. Dazu wird eine lernende Kaskadenregelung entworfen und experimentell evaluiert.

Abschließend wird eine zweite Anwendung betrachtet, in der die Kombination von ILR und inertialsensorbasierter Echtzeit-Bewegungsanalyse zu einer verbesserten Behandlung von Fußheberschwäche führt. Durch eine neuartige Elektrodenanordnung für die funktionelle Elektrostimulation des Peronaeusnervs und mittels geeigneter Stellgrößenentkopplung gelingt die Implementierung dezentraler iterativ lernender Regelungen, welche die Fußorientierungswinkel während der Schwungphase des paretischen Fußes regeln. In Experimenten mit Fallfußpatienten wird gezeigt, dass die lernende Neuroprothese sich innerhalb weniger Schritte den Bedürfnissen des Patienten anpasst und muskuläre Veränderungen automatisch kompensiert.

In favor of We

Dear reader, the following pages contain research results, derivations and discussions, which I hope you find both comprehensible and enlightening. I would like to invite you to go through the pages with me and read every section as if it was you and me who did this research in the moment you read it. When you read a mathematical argument, I do not want it to sound like something I derived long time before you read that line. (You and me know very well that is true, so there is no reason to emphasize this fact.) When you read the description of an experiment, I do not want it to sound like a retrospective report of something that happened in the past. Instead, I want to invite you on a journey on which *we* derive these equations and perform these experiments together and experience every step as if it would happen at the time you read the lines.

Why would I like to do so? Because it is more inviting and more including than a sheer report of the research I did during the last years. If I had tried to do the latter, I had followed some of the rather antiquated style guides that recommend you to string together sequences of facts and to use passive voice to avoid first person pronouns at all cost. I would exanimate every sentence by making sure that everything is done while nobody does anything; I would assure that the chapters are concerned with certain issues, while nobody addresses these issues in the chapters; and I would make every equation follow from another one, while nobody ever derives or combines equations. If I shall ever write paragraphs for an encyclopedia, I may do so. But this dissertation was written to describe a process of gaining knowledge and developing solutions, rather than just presenting the results of both. Therefore, I will use the pronoun *we* in the following, and it will not mean the royal we. It will mean you, my dear reader, and me. Furthermore, I will use present tense, and it will mean that *we* carry out all steps and acquire all knowledge together, as you read. This is the way some of the best publications I read are written, and this is the way I would like to have a thesis written when I read one.

You might disagree. You might argue that this is bad style according to some guide you read or some person who taught you to avoid the use of *we*. In that case, I truly hope you forgive me. I enjoy reading style guides, and I have read quite a few that tell you to ban this pronoun from your scientific writing. However, I never found a compelling argument for this dogma. Most of them refer to multi-author publications and talk about the ambiguity of whom the pronoun might refer to. A few of them claim that using this particular form of *we* sounds condescending to the reader. I have never felt that way when reading publications written in this style. In contrast, I have often felt like becoming part of the research I was reading about. Since you are most likely a scientist, my choice of style will not influence the facts and knowledge you extract from the lines. It will, however, change the way you experience them.

If you have agreed with me from the start, you may wonder why I wrote this preface. Many modern style guides agree with *us* as well and even encourage authors to overcome the antiquated dogma. However, I have met a surprising number of people who judge the style of a sentence by memorized rules rather than by its comprehensibility and appeal. Some of them are among my best friends. I might have failed to convince them this time, maybe also to convince you. *We* may never completely agree on this aspect of style. *We* may, however, understand each others arguments and respect them. This is one main reason for me to write these lines – the other is to cordially welcome you to my dissertation, which I truly hope you enjoy reading.

Sincerely,
Thomas

P.S. Did you notice it? The other dogma of some strict style guides that I dared to infringe? If so, please let me assure you that "But may be used to begin a sentence at all levels of style" (The American Heritage Dictionary). Try to replace the *But* above by *However* – it will no longer mean the same. "*However* indicates a philosophical sigh; *but* presents an insuperable obstacle." (St. Clair McKelway, The New Yorker)

Contents

1 Introduction

1.1 Motivation and Overview

Biomedical engineering strives to enhance health care by the development of advanced technical solutions for improved diagnosis and treatment of diseases and disorders. There are two fundamental ways in which diagnosis and treatment systems can be improved: one is by new technologies, the other is by new methods and algorithms that make the most of these technologies. Systems and control theory can make vital contributions to the latter aspect, since it allows us to understand and improve biomedical systems with high complexity and challenging dynamics.

One of the latest technological revolutions is the dramatic reduction of cost and dimensions of micro-electro-mechanical systems. Due to this development, inertial measurement units (IMUs) have become small and lightweight enough to be used for human motion analysis. This opens up numerous possibilities for the enhancement of existing systems and the development of new solutions for orthopedics, rehabilitation engineering and sports medicine. However, as most new technologies, inertial motion analysis is still subject to several limitations and currently available methods hardly meet the particular practical demands of these application fields. The sensor units must be placed on the body segments in predefined, restrictive positions and orientations, or a series of precise calibration motions must be performed by the user. Moreover, most estimation algorithms require an environment with a homogeneous magnetic field, which is hard to achieve indoors and in the presence of ferromagnetic materials. Finally, only few methods are currently available that estimate motion parameters in realtime, i.e. while the subject moves.

This, however, is a fundamental requirement for the design of modern diagnosis and treatment systems. In almost every domain of health care, there is an increased demand for individualized solutions and treatment. But currently available biomedical systems often require large calibration efforts and individual readjustments by experts. These challenges can be overcome by means of systems and control theory. Using automatic feedback control, one can design systems that adjust their parameters automatically to the individual needs of a user and thereby optimize the treatment. In this context, Iterative Learning Control (ILC) methods are particularly promising. However, the classic ILC theory is technically too restrictive for many biomedical applications, in which the human interacts with the controller and introduces additional variability.

The present dissertation aims at contributing to the continuous improvement of biomedical systems and devices in multiple ways. Chapter 3 provides new methods for inertial realtime gait analysis that overcome a number of current limitations of this technology. In Chapter 4, the theory of iterative learning control is extended to improve its applicability to systems in which the human is an essential part of the control loop. Both inertial measurements and iterative learning control are techniques that have mainly been used for mechanical systems and robotics in the past. It is a main objective of this dissertation to reduce the restrictiveness of these methods and to enhance them in such a way that they can become more useful for biomedical application systems.

Besides these methodological contributions, an equally important goal of the present dissertation is to demonstrate how advanced solutions for diagnosis and treatment can be developed by employing learning control methods and inertial motion analysis techniques. To this end, two specific applications are considered. In Chapter 5, the measurement accuracy of a novel noninvasive blood pressure measurement system is improved by design of a learning cascaded controller. Subsequently, in Chapter 6, an adaptive neuroprosthesis is developed for improved treatment of the drop foot syndrome by functional electrical stimulation (FES). Both systems are evaluated in experiments that demonstrate the advancements one can achieve with respect to the current state of the art by combining modern technologies with methods of systems and control theory.

1.2 Contributions to the State of the Art

As it is common practice in doctoral dissertations, I summarize the contributions of this dissertation in an enumerated list for the reader who is familiar with both the fundamental concepts and the state of the art. With respect to methods of inertial motion analysis and iterative learning control, the contributions of the present dissertation are the following:

1. a method for realtime gait phase detection using an IMU on the foot/shoe
   - the IMU is mounted in unknown arbitrary orientation and position
   - the algorithm uses only measured accelerations and angular rates
   - it adjusts its parameters automatically to the subject's gait characteristics
2. a method for IMU-based realtime foot pitch and roll angle measurement
   - the IMU is mounted in unknown arbitrary orientation and position
   - the algorithm uses only measured accelerations and angular rates
3. a method for identification of the sensor-to-segment orientation and position

   - the algorithm identifies the joint axis of approximate hinge joints and the joint position of approximate hinge joints, saddle joints and spheroidal joints
   - it requires one IMU on each end (segment) of the joint
   - the IMUs are mounted in unknown arbitrary orientation and position
   - the algorithm uses only measured accelerations and angular rates
   - it uses measurement data of arbitrary motions of both ends of the joint
   - it exploits the kinematic constraints that become manifest in the data
4. a method for realtime flexion/extension joint angle measurement
   - the algorithm applies to joints that move approximately like hinge joints
   - it requires one IMU on each end (segment) of the joint
   - the IMUs are mounted in unknown arbitrary orientation and position
   - the algorithm uses only measured accelerations and angular rates
5. a quantification of soft tissue motion artifacts in IMU-based gait analysis
6. a framework for the analysis of ILC systems with variable pass length
   - extension of two standard learning laws to this class of systems
   - derivation of closed-loop dynamics for both learning laws
   - useful learning progress measures for this class of systems
7. necessary and sufficient conditions for monotonic convergence of the vector norm of the maximum-pass-length error for a learning law without Q-filter
8. sufficient conditions for monotonic decrease of the maximum-pass-length error norm above a potentially small threshold for a learning law with Q-filter
9. reduction of the conservativeness in matrix-norm-based convergence criteria by a frequency-weighted indicator for the non-zero Q-filter-related residual error
10. a set of practical guidelines for the design of iterative learning controllers in the presence of variable pass length

In addition to the above, the present dissertation also contributes to the state of the art of noninvasive blood pressure measurement and FES-based drop foot treatment by the following achievements:

1. a learning cascade control scheme for improved accuracy of a noninvasive, continuous blood pressure measurement system
   - the algorithm automatically identifies the current pulse rate
   - it synchronizes the measurement cycles with the heart beat
   - it learns to improve the measurement from cycle to cycle
   - precise blood pressure values are obtained within three measurement cycles
2. an adaptive neuroprosthesis for improved treatment of the drop foot syndrome

- IMU on the foot/shoe for assessment of the treatment outcome (foot motion)
- two FES channels via three electrodes to influence dorsiflexion and eversion
- two suitable parameterizations of the domain of admissible FES intensities
- decentralized ILC scheme for the pitch and roll angle of the paretic foot
- control of the entire pitch and roll angle trajectories during swing phase
- the controller achieves a desired foot motion within at most two strides
- it automatically adjusts the FES intensities to the current needs of the patient
- it supersedes manual adjustments of electrode positions and FES intensities
- it automatically compensates changes in, e.g., muscular tone and fatigue

1.3 Related Publications of the Author

The present doctoral dissertation is based in part on the publications listed below. They are grouped by the field of research to which they contribute. The publications marked IMU-x, $x \in \mathbb{N}$, are contributions to the field of inertial realtime gait analysis. Some results from these publications are presented and used in Chapter 3. The same holds, respectively, for Chapter 4 and for the publications marked ILC-x, $x \in \mathbb{N}$, on iterative learning control. Below these two groups, you will find two more groups of publications, one on blood pressure measurement (marked BPM-x, $x \in \mathbb{N}$) and one on adaptive peroneal stimulation (marked APS-x, $x \in \mathbb{N}$), which are related to Chapters 5 and 6, respectively.

[IMU-1] T. Seel, T. Schauer, J. Raisch, "Joint axis and position estimation from inertial measurement data by exploiting kinematic constraints", *Proc. of the IEEE International Conference on Control Applications (CCA)*, pp. 45–49, 2012.

[IMU-2] T. Seel, T. Schauer, "IMU-based Joint Angle Measurement Made Practical", *Proc. of the 4th European Conference on Technically Assisted Rehabilitation*, 2013.

[IMU-3] T. Seel, L. Landgraf, T. Schauer, "Online Gait Phase Detection with Automatic Adaption to Gait Velocity Changes Using Accelerometers and Gyroscopes", *Biomedical Engineering / Biomedizinische Techik*, 59(S1):795–798, 2014.

[IMU-4] T. Seel, J. Raisch, T. Schauer, "IMU-based joint angle measurement for gait analysis", *Sensors*, 14(4):6891–909, 2014.

[IMU-5] T. Seel, D. Graurock, T. Schauer, "Realtime Assessment of Foot Orientation by Accelerometers and Gyroscopes", *Current Directions in Biomedical Engineering*, 1(1):466–469, 2015.

[ILC-1] T. Seel, T. Schauer, J. Raisch, "Iterative Learning Control for Variable Pass Length Systems", *Proceedings of the 18th IFAC World Congress*, pp. 4880–85, 2011.

[ILC-2] T. Seel and T. Schauer and J. Raisch, "Variable Pass Length ILC in FES-based Drop Foot Rehabilitation", *Workshop AUTOMED*, 2012.

[ILC-3] T. Seel, T. Schauer, J. Raisch, "Iterative Learning Control with Variable Pass Length applied to FES-based Drop Foot Treatment" (in German), *at – Automatisierungstechnik*, 61(9):630–37, 2013.

[ILC-4] T. Seel, T. Schauer, J. Raisch, "Iterative Learning Control for Variable-Pass-Length Systems", *International Journal of Control* (under review), 2016.

[BPM-1] T. Seel, S. Weber, K. Affeld, T. Schauer, "Iterative Learning Cascade Control of Continuous Noninvasive Blood Pressure Measurement", *Proceedings of the IEEE International Conference on Systems, Man, and Cybernetics*, pp. 2207–2212, 2013.

[BPM-2] T. Seel, S. Weber, K. Affeld, T. Schauer, "Iterativ lernende kaskadierte Regelung eines nichtinvasiven Blutdruck-Messsystems nach Penaz", *Workshop AUTOMED*, 2013.

[BPM-3] T. Seel, S. Schneider, K. Affeld, T. Schauer, "Design of a Learning Cascade Controller for a Continuous Noninvasive Blood Pressure Measurement System (in German)", *at – Automatisierungstechnik*, 63(1):5–13, 2015.

[APS-1] T. Seel, M. Valtin, T. Schauer, "Neue Technologien für die Peroneusstimulation: Bessere Versorgung bei Fußheberschwäche", *Deutsche Zeitschrift für klinische Forschung*, 17(4):43–47, 2013.

[APS-2] T. Seel, S. Schäperkötter, M. Valtin, C. Werner, T. Schauer, "Design and control of an Adaptive Peroneal Stimulator with inertial sensor-based gait phase detection", *Proceedings of the 18th Annual International FES Society Conference*, pp. 177–180, 2013.

[APS-3] T. Seel, D. Laidig, M. Valtin, C. Werner, J. Raisch, T. Schauer, "Feedback Control of Foot Eversion in the Adaptive Peroneal Stimulator", In *Proc. of the 22nd IEEE Mediterranean Conference on Control and Automation*, pp. 1482–1487, 2014.

[APS-4] T. Seel, C. Werner, J. Raisch, T. Schauer, "Iterative Learning Control of a Drop Foot Neuroprosthesis – Generating Physiological Foot Motion in Paretic Gait by Automatic Feedback Control", *Control Engineering Practice*, 48:87–97 2016.

[APS-5] T. Seel, M. Ruppel, M. Valtin, T. Schauer, "Multichannel FES Parameterization for Controlling Foot Motion in Paretic Gait", *Current Directions in Biomedical Engineering*, 1(1):480–483, 2015.

[APS-6] T. Seel, M. Valtin, C. Werner, T. Schauer, "Multivariable Control of Foot Motion During Gait by Peroneal Nerve Stimulation via two Skin Electrodes", *IFAC-PapersOnLine*, 48(20):315–320, 2015.

1.4 Related Theses Supervised by the Author

Many of the experimental results that are described and discussed within this dissertation have been obtained with the valuable support of students whose Bachelor thesis or Master thesis I supervised. Several side aspect that are only touched briefly or described very concisely by the present dissertation can be found in further detail, and often in great clarity, within those theses. Therefore, and to acknowledge the vital contribution of many of these young scientists to the research projects behind this dissertation, I provide reference to their works here in chronological order.

[Th-1] Mickaël Guth, "Iterative Learning Control for Variable Pass Length Systems – Application to Trajectory Tracking with Output Constraints on a Laboratory-Scale Gantry Crane", Master Thesis, 2012.

[Th-2] Charlotte Lamotte, "Controller design for the continuous non-invasive blood pressure measurement", Third year internship report, 2012.

[Th-3] Octavian Lupu, "Motion-Intention-Driven Adaptive Stimulation for Stroke Rehabilitation", Master Thesis, 2013.

[Th-4] Florian Heptner, “Entwicklung einer PC-Schnittstelle und Mikrocontroller-basierten Aktuatorregelung für eine nichtinvasive Blutdruckmessung”, Bachelor Thesis, 2013.

[Th-5] Diana Steinecke, “Iterativ lernende Regelung eines nichtinvasiven Blutdruck-Messsystems”, Bachelor Thesis, 2013.

[Th-6] Víctor Cermeño Escobar, “Development and Implementation of an Inertial Sensor-based Online Gait Phase Detection”, Master Thesis, 2013.

[Th-7] Steffen Schäperkötter, “Regelung und experimentelle Evaluierung eines Peroneus-Stimulators mit Inertialsensor-basierter Gangphasenerkennung”, Master Thesis, 2013.

[Th-8] Sebastian Scheel, “Implementation and optimization of an inertial sensor based real-time gait analysis”, Master Thesis, 2014.

[Th-9] Daniel Laidig, “Entwicklung einer adaptiven inertialsensorbasierten Supinationskorrektur für einen Peroneus-Stimulator”, Bachelor Thesis, 2014.

[Th-10] Lucian Landgraf, “Robustheit gegenüber magnetischen Störungen bei der Inertialsensor-basierten Schätzung von Körpersegmentorientierungen”, Master Thesis, 2015.

[Th-11] Florian Röder, “Entwicklung eines Echtzeit-Softwaremoduls für die Inertialsensor-Ganganalyse und die geregelte Elektrostimulation”, Bachelor Thesis, 2015.

[Th-12] Daniela Friedrich, “Terrainabhängige Vorsteuerung einer geregelten Fallfuß-Neuroprothese”, Master Thesis, 2015.

[Th-13] Boris Henckell, “Experimentelle Evaluierung und Weiterentwicklung eines geregelten Peroneusstimulators in der klinischen Praxis”, Master Thesis, 2015.

[Th-14] Mirjana Ruppel, “Implementation and Evaluation of Decoupling Strategies for a Two-Channel Gait Neuroprosthesis”, Bachelor Thesis, 2015.

2 Fundamentals

Before we start to introduce novel concepts and develop new methods, let us briefly review some more fundamental knowledge, which will improve our reception and comprehension of the following chapters. In Section 2.1, we will make ourselves familiar with a few fundamental concepts of inertial measurement hardware and algorithms. We will then review the classic theory of Iterative Learning Control (ILC) design in the lifted-system framework. Finally, the concept of artificial muscle activation by functional electrical stimulation (FES) will be introduced and discussed in the context of motor rehabilitation.

2.1 Inertial Measurement Units

Inertial measurement units (IMUs), also known as inertial sensors, measure acceleration, angular rate and the magnetic field vector in their own three-dimensional local coordinate system. With proper calibration, the axes of this local coordinate system represent an orthonormal base that is typically well aligned with the outer casing of the sensor. When an IMU is rigidly attached to an object, the measured signals can be used to estimate the orientation and velocity (and position) of that object with respect to a fixed (inertial) coordinate system.

Currently, there is a remarkable growth in the use of inertial sensors for human motion analysis across various application domains ranging from rehabilitation engineering and sports research to filmmaking and video game development. Woodman [128] describes these developments as follows: "Until recently the weight and size of inertial sensors has prohibited their use in domains such as human motion capture. Recent improvements in the performance of small and lightweight micro-machined electromechanical systems (MEMS) inertial sensors have made the application of inertial techniques to such problems possible."

In the following, we will briefly review Woodman's excellent technical report on inertial motion analysis [128]. Thereby, we will introduce the fundamental measurement principles of MEMS gyroscopes and accelerometers, and we will discuss a few basic concepts of strapdown inertial measurement systems, which we will need to derive and develop new methods for IMU-based gait analysis in Chapter 3.

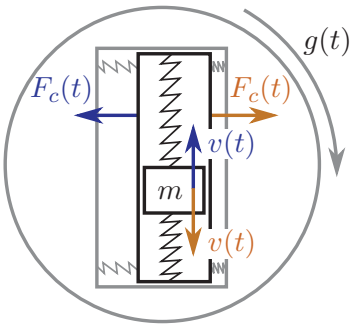

Figure 2.1: Exploiting the Coriolis effect to measure angular velocity: A forced oscillation (indicated by $v(t)$ up and down) of the mass m causes another oscillation (indicated by $F_c(t)$ left and right, respectively) perpendicular to it. After proper calibration, the absolute value of the angular velocity can be determined from the oscillation amplitude, while the phase difference between both oscillations yields the direction of rotation.

2.1.1 MEMS Gyroscopes

Gyroscopes measure the angular velocity at which they rotate with respect to an inertial frame of reference. In contrast to mechanical and optical gyroscopes, MEMS gyroscopes are built using silicon micro-machining techniques, which results in low part counts (a MEMS gyroscope can consist of as few as three parts) and low manufacturing costs [128]. The sensing mechanism exploits the Coriolis effect, which states that a mass $m \in \mathbb{R}_{>0}$ moving with velocity $\mathbf{v}(t) \in \mathbb{R}^{3\times1}$ with respect to a coordinate system that rotates at angular velocity $\mathbf{g}(t) \in \mathbb{R}^{3\times1}$ experiences a force $\mathbf{F}_c(t) \in \mathbb{R}^{3\times1}$, with

$$\mathbf{F}_c(t) = 2m(\mathbf{v}(t) \times \mathbf{g}(t)), \tag{2.1}$$

where the operator $\times$ denotes the vector (cross) product. The measurement principle is illustrated for one coordinate axis (with scalar velocity $v(t)$, angular rate $g(t)$ and force $F_c(t)$) in Figure 2.1. In a three-axis gyroscope, three of those single-axis units are mounted such that their input axes are almost pairwise perpendicular to each other. To compensate for mounting inaccuracies, an orthogonalization matrix is typically identified during calibration and then applied to the three-dimensional measurement output vector.

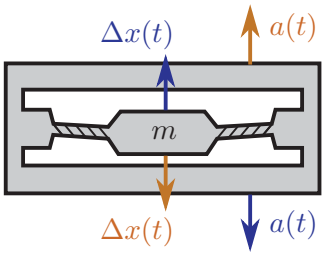

Figure 2.2: Measurement principle of an accelerometer. The mass m is suspended in such a way that it can move slightly up and down (i.e. along the input axis). When the device is accelerated (indicated by $a(t)$ up and down), inertia effects cause a displacement (indicated by $\Delta x(t)$ down and up, respectively) of the mass with respect to the surrounding case.

2.1.2 MEMS Accelerometers

MEMS accelerometers contain a mass that is suspended, for example by a spring or a cantilever, such that it is displaced when the device is accelerated. In mechanical accelerometers, the displacement is measured directly. Surface acoustic wave accelerometers, on the other hand, measure the change in frequency of a vibrating element that is attached, for example, to a beam that bends when the device undergoes acceleration [128]. The former is illustrated for one coordinate axis in Figure 2.2.

When the accelerometer is at rest or when it is moving at constant velocity, the mass is only affected by gravity, i.e. it is drawn toward the center of earth. In that case, the device measures the gravitational acceleration of approximately $9.8\,\mathrm{ms}^{-2}$ in vertical upwards direction. Therefore, an accelerometer can yield information on the inclination of the IMU with respect to the horizontal plane. When the device moves, however, it measures the sum of this gravitational acceleration and the acceleration that is related to change of velocity.

2.1.3 Error Characteristics of Accelerometers and Gyroscopes

When an accelerometer or gyroscope is not undergoing any acceleration or rotation, the measurement output should be the zero vector or $9.8\,\mathrm{ms}^{-2}$ in vertical upwards direction, respectively. In practice, however, an offset from these true values will be measured. The average of this offset is called the bias of an accelerometer or gyroscope [128]. When integrating a measurement signal affected by a (constant) non-zero bias over time, the

result is affected by an error that grows (linearly) with time. This phenomenon is called drift. Obviously, a constant bias error can be estimated by taking a long term average of the measurement output whilst the device is at rest [128]. The bias can then be compensated by subtracting it from the output. This is a standard procedure carried out during calibration. However, as we will see shortly, the mentioned procedure only *approximates* the bias error. Therefore, achieving complete bias compensation is very difficult.

The bias is known to vary when the temperature changes due to changes in the environment or due to sensor self-heating. According to Woodman [128], the relationship between bias and temperature is often highly nonlinear for MEMS sensors. Many commercially available inertial measurement units are equipped with on-board temperature sensing, which some of them use to compensate (some portion of) the temperature dependency automatically.

Furthermore, the bias of a MEMS gyroscope or accelerometer changes with time, even at constant temperature, due to flicker noise in the electronics and in other components susceptible to random flickering [128]. These bias fluctuations can be modeled as a zero-mean, first-order random walk, which results in a second-order random walk error of the integral. However, as Woodman [128] explains, the bias is in practice constrained to be within some range, and therefore the random walk model is only an approximation of the true process for short periods of time.

In addition to the bias error, the measurement output is typically perturbed by thermo-mechanical noise that fluctuates at a rate much greater than the sampling rate of the sensor [128]. As explained in detail by Woodman [128], this noise introduces a zero-mean random walk error into the integrated signal, the standard deviation of which grows proportionally to the square root of time.

Errors in the scale factors, alignments and linearities of the gyroscopes and accelerometers lead to measurement errors that are collectively referred to as calibration errors [128]. Such errors lead to the accumulation of additional drift in the integrated signal, the magnitude of which is proportional to the rate and duration of the motions [29]. Obviously, such errors can be minimized by very precise calibration of the IMU.

For more details on the error characteristics of gyroscopes and accelerometers, please refer to the excellent work by Woodman [128]. With respect to future deliberations on inertial motion analysis in Chapter 3, we shall only keep in mind that the measurements of MEMS gyroscopes and accelerometers are subject to biases that vary, for several reasons, both on short and on long time scales.

2.1.4 Strapdown Integration for Orientation Estimation

The orientation of (the local coordinate system of) an IMU relative to a fixed (reference) coordinate system is determined by integrating the angular velocity signal $\mathbf{g}(t)$ over time. This relative orientation can be described, for example, by a rotation matrix $\mathbf{R}_{\text{ref}}(t)$. This matrix shall be defined such that any vector $\mathbf{x}(t)$ in the coordinates of the moving IMU frame becomes $\mathbf{x}_{\text{ref}}(t) = \mathbf{R}_{\text{ref}}(t)\mathbf{x}(t)$ when expressed in the fixed coordinate system. Obviously, this implies that $\mathbf{x}(t) = \mathbf{R}_{\text{ref}}^T(t)\mathbf{x}_{\text{ref}}(t)$ yields the inverse transformation[1], and congruence of both coordinate systems is given if $\mathbf{R}_{\text{ref}}(t)$ is the identity matrix $\mathbf{I}_{3\times 3}$.

In all future developments and analyses, the motion that the IMU undergoes is assumed to be (at least well approximated by) a motion of piecewise constant angular rate and acceleration. More precisely, denote an initial sample instant by t_0 and assume that the IMU rotates with the constant angular rate

$$\mathbf{g}(t) = \mathbf{g}(t_0 + t_\text{s}) = [g_x(t_0 + t_\text{s}), g_y(t_0 + t_\text{s}), g_z(t_0 + t_\text{s})]^T \; \forall t \in (t_0, t_0 + t_\text{s}], \tag{2.2}$$

where t_s is the sampling time and t_0 denotes an initial sampling instant. Likewise, $\mathbf{g}(t_0 + kt_\text{s}), k \in \mathbb{N}$, shall be the angular rate at which the IMU is rotating during the time interval $t \in (t_0 + (k-1)t_\text{s}, t_0 + kt_\text{s}]$.

For the applications we will address in Chapter 3, it is convenient to choose the fixed reference frame such that the local frame of the IMU and the reference frame coincide for $t = t_0$, which implies $\mathbf{R}_{\text{ref}}(t_0) = \mathbf{I}_{3\times 3}$. Then the orientation $\mathbf{R}_{\text{ref}}(t_0 + t_\text{s})$ of the IMU at the end of the subsequent sampling period is simply the rotation associated with $\mathbf{g}(t_0 + t_\text{s})$ from (2.2). This change in orientation shall be denoted by the rotation matrix $\mathbf{\Delta R}(t_0 + t_\text{s})$. It is a well known fact[2] of Euclidean geometry that this rotation matrix can be calculated from the angular rate by the following equation (for a general time

[1] The inverse of any rotation matrix is equal to its transpose.

[2] See for example Woodman [128], Titterton and Weston [115] and references therein for derivations of the given equation and of slightly different, but mathematically equivalent, expressions.

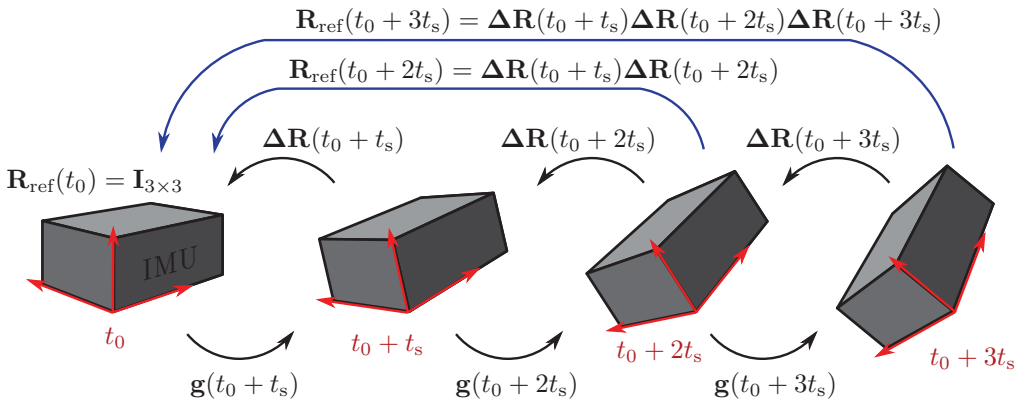

Figure 2.3: Orientation strapdown integration requires concatenation of a series of small rotations associated with consecutive sampling intervals. Each rotation matrix transforms a vector from the local coordinate system of the IMU at one moment in time to the local coordinate system of the IMU at a previous moment in time, as indicated by the arrows.

instant $t = t_0 + kt_s, k \in \mathbb{N}$, and angular rate $\mathbf{g}(t)$):

$$\begin{aligned}\mathbf{\Delta R}(t) := &\cos(||\mathbf{g}(t)t_s||_2)\mathbf{I}_{3\times3} \\ &+ \frac{\sin(||\mathbf{g}(t)t_s||_2)}{||\mathbf{g}(t)||_2}\begin{bmatrix} 0 & -g_z(t) & +g_y(t) \\ +g_z(t) & 0 & -g_x(t) \\ -g_y(t) & +g_x(t) & 0 \end{bmatrix} \\ &+ \frac{1-\cos(||\mathbf{g}(t)t_s||_2)}{||\mathbf{g}(t)||_2^2}\begin{bmatrix} g_x(t) \\ g_y(t) \\ g_z(t) \end{bmatrix}\begin{bmatrix} g_x(t) & g_y(t) & g_z(t) \end{bmatrix},\end{aligned} \tag{2.3}$$

where $||\cdot||_2$ denotes the Euclidean vector norm. It is important to note that this formula yields the rotation matrix that transforms any vector from the local IMU coordinates of a time instant $(t_0 + kt_s), k \in \mathbb{N}$, back into the local coordinate system of the previous sample instant, not vice versa.

Using (2.3), we can likewise calculate the rotation matrices that correspond to the changes of orientation associated with the angular rates measured during all following sampling periods. The orientation matrix $\mathbf{R}_{\text{ref}}(t)$ of any instant $t = t_0 + kt_s, k \in \mathbb{N}$, is then simply the product of all these rotation matrices between t_0 and t, as illustrated in Figure 2.3. Therefore, the calculation of $\mathbf{R}_{\text{ref}}(t)$ can be implemented by the following

recursion:

$$\mathbf{R}_{\mathrm{ref}}(t) = \mathbf{R}_{\mathrm{ref}}(t - t_{\mathrm{s}})\boldsymbol{\Delta}\mathbf{R}(t), \quad t = t_0 + t_{\mathrm{s}}, t_0 + 2t_{\mathrm{s}}, \ldots. \tag{2.4}$$

Please note that the order in which the rotation matrices are multiplied is important, because rotations in three dimensions do *not* commute in general.

Since the calculation of $\mathbf{R}_{\mathrm{ref}}(t)$ requires integration of the angular rates, drift effects deteriorate the accuracy of the obtained orientation estimate typically within few seconds. To compensate this effect, accelerometer and magnetometer readings are often combined with the measured angular rates in a sensor fusion. A number of algorithms have been proposed for sensor orientation estimation, see for example Sabatini [99] and references therein. In most of these algorithms, the recursion (2.4) only serves as a prediction that is repeatedly corrected based on the measured acceleration and magnetic field vector. The drift in the inclination part of the orientation is eliminated using the assumption that the measured acceleration is dominated by gravitational acceleration [56]. Similarly, the estimation of the azimuth (or heading) requires the use of magnetometer measurements. Therefore, time periods of strong accelerations and the presence of magnetic disturbances (as induced, e.g., by ferromagnetic material) may limit the accuracy of the orientation estimates, as demonstrated by Bachmann et al. [7] and by De Vries et al. [19].

Recall that the rotation matrix $\mathbf{R}_{\mathrm{ref}}(t)$ can be used to transform vectors that are given in local IMU coordinates into a fixed reference frame. In Chapter 3, we will exploit this fact to determine, for example, knee joint angles and horizontal foot velocities. However, in IMU-based gait analysis, the aforementioned limitations are of major importance. Restricting the motion analysis to outdoor environments with a homogeneous magnetic field would severely reduce its usefulness. Therefore, in Chapter 3, we will aim at developing methods that avoid the use of magnetometer readings. Furthermore, note that, during walking, the foot undergoes accelerations with a magnitude of several times the gravitational acceleration. Hence, we will develop methods for foot orientation estimation that only employ the accelerations measured during foot rest. While the foot moves, we will use the gyroscope-based method described above and bear the fact that the orientation estimates are only accurate on small time scales.

2.2 Standard Iterative Learning Control

Several control problems in various application domains require the controller to repeat the same trajectory tracking task multiple times. In such control systems, the tracking performance can be improved by learning from previous executions by means of Iterative Learning Control (ILC). However, for ILC theory to be applicable, certain assumptions must hold:

- the control task repeats in trials of equal duration, which is called the pass length,
- the dynamics do not change from trial to trial, i.e. the same input causes the same output when applied again in any of the following trials,[3]
- no input or output saturation shall occur.

If this can be assured, then a well-developed theoretical framework can be applied that is briefly described (for the linear case) in the following. Prior to this, we introduce the *lifted-systems* framework of linear time-invariant systems, which is known as *supervector* framework in some literature and will be used for convergence analysis in the sequel of this chapter.

Example of a Lifted-Systems Representation Consider the special case of a time-invariant, single-input single-output, state-space system with output disturbance $d \in \mathbb{R}$ and with sampling time t_s:

$$\begin{aligned} \mathbf{x}(t+t_\mathrm{s}) &= \mathbf{A}\mathbf{x}(t) + \mathbf{B}u(t), \quad & \mathbf{x}(t_0) &= \mathbf{x}_0 \in \mathbb{R}^{r\times 1}, \\ y(t) &= \mathbf{C}\mathbf{x}(t) + d(t), & t &= t_0, t_0+t_\mathrm{s}, \ldots. \end{aligned} \tag{2.5}$$

Without loss of generality, the relative degree from the input $u(t) \in \mathbb{R}$ to the output $y(t) \in \mathbb{R}$ shall be one, i.e. $\mathbf{CB} \neq 0$. Assume that we want to control the output y in a time interval $t \in [t_0 + t_\mathrm{s}, t_0 + nt_\mathrm{s}]$. Then we define the following input and output vectors

$$\mathbf{u} = [u(t_0), u(t_0+t_\mathrm{s}), \ldots, u(t_0+(n-1)t_\mathrm{s})]^T, \tag{2.6}$$

$$\mathbf{y} = [y(t_0+t_\mathrm{s}), y(t_0+2t_\mathrm{s}), \ldots, y(t_0+nt_\mathrm{s})]^T, \tag{2.7}$$

which capture the entire discrete-time input and output trajectories on a finite time interval and are called *lifted* signals or *lifted* vectors. Using the Markov parameters[4] $p_k =$

[3] This typically implies that the initial conditions are the same in each trial.
[4] i.e. the sample values of the impulse response, see for example Kailath [37]

$\mathbf{CA}^{k-1}\mathbf{B}$ of the above state-space system, we find the lifted-system representation

$$\mathbf{y} = \underbrace{\begin{bmatrix} p_1 & 0 & 0 & \cdots & 0 & 0 \\ p_2 & p_1 & 0 & \cdots & 0 & 0 \\ p_3 & p_2 & p_1 & \cdots & 0 & 0 \\ \vdots & \vdots & \vdots & \ddots & \vdots & \vdots \\ p_{n-1} & p_{n-2} & p_{n-3} & \cdots & p_1 & 0 \\ p_n & p_{n-1} & p_{n-2} & \cdots & p_2 & p_1 \end{bmatrix}}_{=:\mathbf{P}\in\mathbb{R}^{n\times n}} \mathbf{u} + \underbrace{\begin{bmatrix} \mathbf{CA}\mathbf{x}_0 + d(t_0 + t_\mathrm{s}) \\ \mathbf{CA}^2\mathbf{x}_0 + d(t_0 + 2t_\mathrm{s}) \\ \mathbf{CA}^3\mathbf{x}_0 + d(t_0 + 3t_\mathrm{s}) \\ \vdots \\ \mathbf{CA}^{n-1}\mathbf{x}_0 + d(t_0 + (n-1)t_\mathrm{s}) \\ \mathbf{CA}^n\mathbf{x}_0 + d(t_0 + nt_\mathrm{s}) \end{bmatrix}}_{=:\mathbf{v}\in\mathbb{R}^{n\times 1}} . \quad (2.8)$$

The vector $\mathbf{v}$ on the right-hand side of (2.8) is the lifted signal of the zero-input response $v(t)$ that is measured when the input is constantly zero, i.e. $v(t) := y(t)$ if $u(t) = 0\,\forall t$. Although $\mathbf{v}$ is often called *disturbance signal*, it captures both the disturbance $d(t)$ and the initial condition dynamics. Note that it is assumed to be exactly the same signal in each pass. Furthermore, note that the lifted-system matrix $\mathbf{P}$ is Toeplitz since the state-space system (2.5) is time-invariant.

In the following, we consider the more general case of a system with relative degree m, and we assume that the control task repeats in trials (or iterations or passes) of constant finite time duration.

2.2.1 Linear ILC with Constant Pass Length

Due to the need of data storage, discrete-time is considered the natural domain for ILC analysis [11]. For a single-input single-output system with relative degree m, let

$$\mathbf{u}_j = [u(t_{0,j}), u(t_{0,j} + t_\mathrm{s}), \ldots, u(t_{0,j} + (n-1)t_\mathrm{s})]^T \in \mathbb{R}^{n\times 1}, \quad (2.9)$$

$$\mathbf{y}_j = [y(t_{0,j} + mt_\mathrm{s}), y(t_{0,j} + (1+m)t_\mathrm{s}), \ldots, y(t_{0,j} + (n-1+m)t_\mathrm{s})]^T \in \mathbb{R}^{n\times 1}, \quad (2.10)$$

$$\mathbf{v} = [v(t_{0,j} + mt_\mathrm{s}), v(t_{0,j} + (1+m)t_\mathrm{s}), \ldots, v(t_{0,j} + (n-1+m)t_\mathrm{s})]^T \in \mathbb{R}^{n\times 1}, \quad (2.11)$$

be the lifted signal vectors (i.e. the vectors of a finite number of sequent sample values) of the input signal, of the output signal and of an unknown (but iteration-invariant) disturbance signal, respectively. Furthermore, $n \in \mathbb{N}$ is the pass length and $j \in \mathbb{N}_0$ is the trial index (or iteration index or pass index). The system dynamics shall be given by

$$\mathbf{y}_j \;=\; \mathbf{P}\,\mathbf{u}_j \;+\; \mathbf{v}\,, \quad (2.12)$$

where $\mathbf{P} \in \mathbb{R}^{n \times n}$ is the aforementioned lifted-system matrix of the process. Furthermore, the tracking error

$$\mathbf{e}_j = (\mathbf{r} - \mathbf{y}_j) \in \mathbb{R}^{n \times 1} \tag{2.13}$$

is defined with respect to a desired output trajectory $\mathbf{r} \in \mathbb{R}^{n \times 1}$, and the control task is to successively, i.e. from pass to pass, reduce the error (in some norm) to a small number. This shall be achieved by choosing an initial input trajectory $\mathbf{u}_0$ and by applying the following input-update law after each trial:

$$\mathbf{u}_{j+1} \;=\; \mathbf{Q}\,(\,\mathbf{u}_j \;+\; \mathbf{L}\,\mathbf{e}_j\,)\,, \quad j = 0, 1, \ldots, \tag{2.14}$$

where the lifted-system matrices $\mathbf{Q}, \mathbf{L} \in \mathbb{R}^{n \times n}$ are controller parameters that need to be designed accordingly. The learning gain $\mathbf{L}$ is often chosen to have diagonal structure, while the Q-filter matrix $\mathbf{Q}$ is typically the lifted-system representation of a lowpass filter, or it is chosen to be the identity matrix $\mathbf{Q} = \mathbf{I}_{n \times n}$, i.e. the Q-filter is not used.

The goal of the standard learning approach (2.14) is as follows: When a certain section of an output trajectory is lower or higher than it should be, the update law (2.14) modifies a corresponding section of the input trajectory in such a way that the output is increased or decreased, respectively. If an adjustment was not sufficient, the deviation remains and the input will be adjusted again, i.e. the employed learning law has integral action. If, however, certain sections of the output trajectory perfectly track the corresponding section of the reference trajectory, then a well-designed learning controller will try to modify the input trajectory in such a way that these sections of the output trajectory are influenced as little as possible.

To find out whether the learning law (2.14) yields a small tracking error, we analyze how the tracking error changes from one iteration to the next. Combining (2.12), (2.13) and (2.14) results in

$$\mathbf{e}_{j+1} = \mathbf{r} - \mathbf{P}\mathbf{u}_{j+1} - \mathbf{v} = \mathbf{r} - \mathbf{P}\mathbf{Q}(\mathbf{u}_j + \mathbf{L}\mathbf{e}_j) - \mathbf{v} \tag{2.15}$$

with $\mathbf{u}_j = \mathbf{P}^{-1}(\mathbf{r} - \mathbf{e}_j - \mathbf{v})$, which yields the following closed-loop error dynamics:

$$\mathbf{e}_{j+1} \;=\; \mathbf{P}\mathbf{Q}\mathbf{P}^{-1}(\mathbf{I}_{n \times n} - \mathbf{P}\mathbf{L})\,\mathbf{e}_j \;+\; (\mathbf{I}_{n \times n} - \mathbf{P}\mathbf{Q}\mathbf{P}^{-1})\,(\mathbf{r} - \mathbf{v}). \tag{2.16}$$

From this, we conclude that the error converges to the finite value

$$\mathbf{e}_\infty := \lim_{j \to \infty} \mathbf{e}_j = (\mathbf{I}_{n \times n} - \mathbf{P}\mathbf{Q}\mathbf{P}^{-1}(\mathbf{I}_{n \times n} - \mathbf{P}\mathbf{L}))^{-1}(\mathbf{I}_{n \times n} - \mathbf{P}\mathbf{Q}\mathbf{P}^{-1})\,(\mathbf{r} - \mathbf{v}) \tag{2.17}$$

for all $\mathbf{r}, \mathbf{v}, \mathbf{u}_0$ if and only if the spectral radius

$$\rho(\mathbf{PQP}^{-1}(\mathbf{I}_{n\times n} - \mathbf{PL})) = \rho(\mathbf{PQ}(\mathbf{I}_{n\times n} - \mathbf{LP})\mathbf{P}^{-1}) = \rho(\mathbf{Q}(\mathbf{I}_{n\times n} - \mathbf{LP})) \tag{2.18}$$

is smaller than one [75]. Obviously, this finite value $\mathbf{e}_\infty$ is zero for all references $\mathbf{r}$ if and only if the Q-filter is $\mathbf{Q} = \mathbf{I}_{n\times n}$, i.e. if the Q-filter is not used.

Convergence of the tracking error to a small finite value is a valuable property. However, it does not exclude the occurrence of large transient growth. Thus, it is instead often demanded that the largest singular value $\bar{\sigma}(\mathbf{PQP}^{-1}(\mathbf{I}_{n\times n} - \mathbf{PL}))$ is smaller than one, which guarantees strict monotonic convergence in the sense that

$$||\mathbf{e}_{j+1} - \mathbf{e}_\infty||_2 < ||\mathbf{e}_j - \mathbf{e}_\infty||_2 \tag{2.19}$$

holds for every trial $j \in \mathbb{N}_0$ (cf. for example [11]). For unknown $\mathbf{v}$, this condition is also necessary, which can be seen, for example, by choosing $\mathbf{v}$ such that $\mathbf{e}_0 = (\mathbf{r} - \mathbf{Pu}_0 - \mathbf{v})$ points into the direction of maximum gain of $(\mathbf{PQP}^{-1}(\mathbf{I}_{n\times n} - \mathbf{PL}))$. Also, please note that the monotonic convergence condition might be rewritten in any other vector norm and its induced matrix norm.

At the end of this brief introduction to convergence analysis of iterative learning control systems, we shall note that the results discussed above represent only a very small portion of the state of the art in ILC theory. Thanks to numerous contributions of many researchers, a rich body of methods exists for various implementations and frameworks of iterative learning control. For further reading, please refer, for example, to the monographs by Rogers et al. [94] and Moore et al. [63] as well as to the excellent research articles by Freeman [30], Galkowski et al. [32], Norrlöf and Gunnarsson [75], Owens and Hätönen [78] and Paszke et al. [82].

Despite the large body of work on ILC theory, there is currently no method that assures monotonic convergence for ILC systems in which the pass length n varies from trial to trial. In Chapter 4, we will discuss that this is an important phenomenon in many biomedical application systems. We will thus extend the methods described above to variable-pass-length systems in Chapter 4, and we will use these new methods to develop an adaptive gait neuroprosthesis based on functional electrical stimulation in Chapter 6.

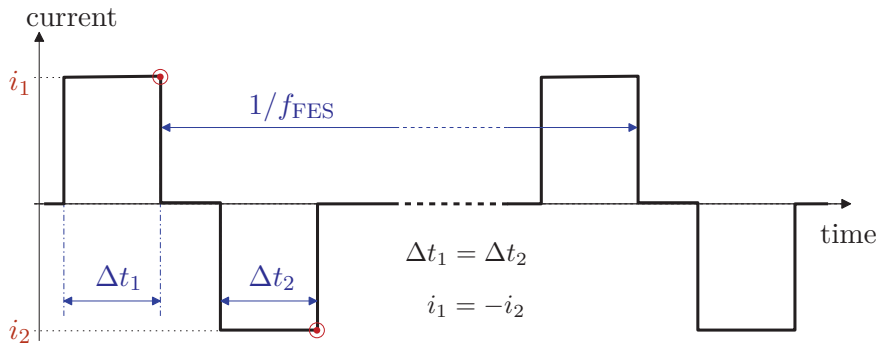

Figure 2.4: Sequence of conventional bi-phasic pulse waves applied at a stimulation frequency f_{FES}. Each pulse wave consists of two pulses with equal shape but opposite sign (current amplitudes i_1, i_2 and pulse widths $\Delta t_1, \Delta t_2$), which assures a zero net current.

2.3 Functional Electrical Stimulation

Functional electrical stimulation (FES) is a technology that enables the artificial activation of muscle contraction by applying tiny electrical pulses via skin electrodes with an adhesive, conductive gel layer. Alternatively, these pulses can be applied via implanted electrodes. However, due to the risk of complications associated with surgery and implants, the noninvasive method is often preferred. Thus, we restrict our discussion to FES via skin electrodes, although many of the following statements and arguments hold equally for FES applied via implanted electrodes.

When using skin electrodes, 20–50 rectangular current pulses per second are typically applied between a pair of electrodes, with each pulse having an amplitude of less than a tenth of an Ampere and a pulse width of less than half a millisecond. If the current amplitude of the pulses is above a threshold of about 5 mA (at a typical pulse width of about 100 μs), each pulse triggers a bunch of action potentials in subcutaneous efferent nerves located near the electrode that is acting as cathode. By increasing the frequency or the current amplitude or the pulse width, one can trigger more action potentials and, thereby, a stronger contraction of the muscle. By modulating these quantities properly, it is possible to induce functional movements such as grasping, cycling, breathing, or swallowing.

Since a non-zero net current through the body is known to cause electrolysis and tissue damage in the long term [91], bi-phasic pulses are typically[5] employed, as explained in

[5] see for example Valtin et al. [118] for an alternative approach

Figure 2.4. This pulse wave triggers action potentials in subcutaneous efferent nerves located near any of the electrodes.

FES is widely applied in motor rehabilitation and in the treatment of motor disabilities. Subjects with upper motor neuron lesions, for example, suffer from a limited ability to move the affected limbs. If the associated peripheral motor nerves are still intact, then FES can be used to recruit the muscles that these nerves innervate, to counteract atrophy and to regain motor functions to some extent. Common examples of successful FES usage include drop foot stimulation [54] and FES cycling for paraplegics [101]. Beyond that, abundant research demonstrates the large potential of FES in neuroprosthesis design, see for example Peckham et al. [84] and references therein, as well in a number of applications beyond the restoration of skeleto-motor functions [97].

2.3.1 Limitations of Functional Electrical Stimulation

The aforementioned potential of FES is limited in several ways. For example, it is important to note that FES typically also triggers action potentials in the afferent nerve fibers of sensory nerves, which causes discomfort at medium and pain at high stimulation intensities. This effect strongly limits the amount of joint torque and force that can be generated by FES. In most subjects, however, the sensation is weak enough to allow the generation of functional movements without discomfort. In subjects with a very low FES tolerance, desensitization can be achieved, to some extent, by repeatedly applying FES with intensities at the subject's maximum comfortable intensity.

Another severe limitation lies in the accelerated fatigue of FES-activated muscles. To understand this phenomenon, it is crucial to know that skeletal muscles contain a mixed population of slow fatigue-resistant (type 1), fast fatigue-resistant (type 2A) and fast fatiguable (type 2B) motor units, where the terms fast and slow refer to the contractile speed of the muscle fibers. The fast fatiguing fibers of type 2B are associated with large-diameter nerve fibers (axons). These axons are more susceptible to FES than the small-diameter axons, which are associated with type 1 and type 2A motor units. Therefore, when current pulses of low intensity are applied, these pulses activate mainly the rapidly fatiguing motor units. As the intensity of the pulses is increased, also the more fatigue-resistant muscle fibers are recruited. In other words, muscle fiber recruitment by FES follows the opposite of Henneman's size principle [36] of natural muscle activation.

In this context, we shall furthermore note that, at constant stimulation intensity, each FES pulse activates almost the same motor units synchronously, which further promotes muscular fatigue. This fact is illustrated in Figure 2.5. In contrast, the central nervous

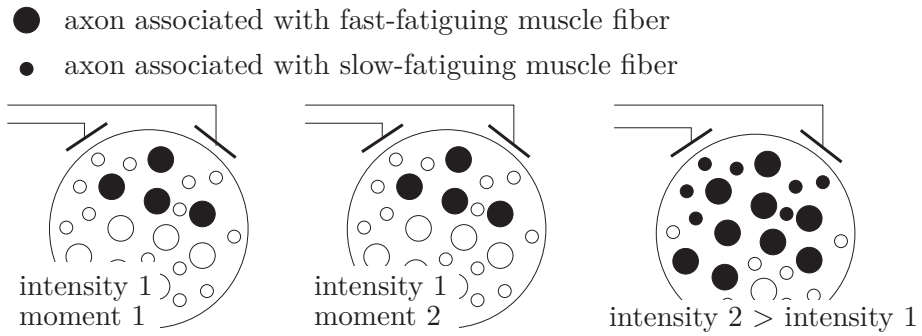

Figure 2.5: Triggering of action potentials in nerve fibers by FES. Identical FES pulses excite almost identical sets of mainly large-diameter axons, which are associated with fast-fatiguing muscle fibers. At higher intensities, action potentials are also triggered in some small-diameter axons, which activate slow-fatiguing muscle fibers. Adapted from Schauer [101].

system activates all motor units asynchronously and in an alternating fashion. Unfortunately, at the current state of the art, such physiological muscle recruitment has not yet been achieved by means of electrical stimulation.

Finally, a major challenge in the use of FES is the variability of its effect both from one subject to another subject and in dependence of the electrode position. Abundant research and numerous experiments have demonstrated that modifying a good electrode position by as little as two or three centimeters can easily result in a reduction of the joint moments and forces by more than 50%. Therefore, and due to the previously described effects, the dynamics of FES-induced motions are typically associated with large uncertainties and time-variance. This represents a major challenge in the development of neuroprostheses for motor rehabilitation and for the compensation of chronic motor dysfunctions.

When facing these challenges, one very promising approach is to design feedback controllers that automatically adjust the FES to the current needs of the user. Currently available systems for FES-based gait support, however, employ only open-loop control strategies and do not adapt to the user. In Chapter 6, we will discuss the limited capabilities of these systems, and we will develop an adaptive gait neuroprosthesis that uses feedback control methods to overcome the discussed limitations.

3 Realtime Gait Analysis with Inertial Sensors

Foot and leg motion analysis plays a central role in diagnosis and treatment of walking disabilities. Functional electrical stimulation (FES) and powered orthoses represent effective tools for active gait support (see for example Melo et al. [61] and Moreno et al. [68]). Both technologies rely on realtime motion assessment. The conventional method for motion assessment is optical motion capture (OMC) by means of reflective markers and an optoelectronic multi-camera system. However, this method has the decisive disadvantages that it is not suitable for realtime applications and that all markers must always be in line of sight with at least two cameras. Furthermore, it is an expensive technology and strictly limiting in space and time, since it restricts the analysis to a laboratory environment.

Ambulatory realtime motion capture can be performed by the use of inertial measurement units (IMU). They represent an inexpensive and easy-to-handle technology without any of the mentioned limitations of OMC. When an IMU is attached to a body segment, it provides measurements of the acceleration, rate of turn and magnetic field vector in its local sensor coordinate system (cf. Chapter 2).

The present chapter provides a modular set of novel methods for IMU-based realtime gait analysis, i.e. methods that derive useful information on the current state of motion from the present or past local measurements of one or more inertial sensors. Several drawbacks and limitations of the current state of the art are overcome by these new methods, especially with respect to the application of realtime control in active gait support systems. Precisely, the chapter is organized as follows:

In Section 3.1, we will develop methods for the detection of characteristic gait events that separate the motion of a foot during each stride into different phases. This gait phase detection will be accomplished by realtime analysis of the measurement signals of a foot-mounted inertial sensor. In contrast to previous approaches, we will avoid the use of magnetometers, and we will not restrict the mounting of the sensor to certain locations or orientations. The algorithm will automatically adapt to the subject's walking velocity and gait characteristics. We will demonstrate the effectiveness of this approach in experimental trials with healthy subjects and stroke patients.

Section 3.2 is dedicated to realtime assessment of the foot orientation by means of a foot-mounted inertial sensor. We will consider a method that uses only accelerometer and gyroscope readings to calculate the foot pitch and roll angle, i.e. the foot orientation

angle in the sagittal[1] and frontal[2] plane, respectively. Since magnetometers are avoided completely, the method can be used indoors as well as in the proximity of ferromagnetic material and magnetic disturbances. Furthermore, we will allow arbitrary mounting orientation of the IMU with respect to the foot or shoe. The method will be validated with respect to an optical motion capture system in trials with transfemoral amputees walking with shoes and healthy subjects walking barefoot, both at different velocities.

In Section 3.3, we will consider inertial measurement units that are attached to rigid bodies, e.g. human limb segments or links of a robotic manipulator, that are connected by hinge joints and spheroidal joints. Novel methods for joint axis estimation and joint position estimation will be proposed that exploit the kinematic constraints induced by these two types of joints. As before, the presented algorithms will use only gyroscope and accelerometer readings, and they will *not* require any knowledge about the positions or orientations of the sensor units with respect to the body segments. Moreover, the proposed methods will *not* include integration, which implies that they will be insensitive to measurement bias. By means of a three-links simulation model, we will validate the methods and analyze convergence of the estimates. Finally, the algorithms will be tested using experimental data from IMU-based human gait analysis.

Section 3.4 is concerned with joint angle calculation based on inertial measurement data in the context of human motion analysis. As before, we will focus on methods that avoid assuming certain orientations in which the sensors are mounted with respect to the body segments. After a review of available approaches that may cope with this challenge, we will derive new methods for flexion/extension joint angle measurement. Once again, these methods will use only gyroscopes and accelerometers and will not rely on a homogeneous magnetic field. For validation purposes, we will analyze results from gait trials of a transfemoral amputee, in which the IMU-based methods is compared to an optical 3D motion capture system.

Since each of the Sections 3.1–3.4 address a separate measurement task, the state of the art will be described for each of them separately, and a short conclusion will be provided at the end of each section. Nevertheless, all of the methods that will be derived are closely related in the sense that they enable the precise realtime assessment of the human gait by means of inertial sensors.

[1] The sagittal plane is the vertical plane which passes from rear (posterior) to front (anterior), dividing the body segment into right and left halves.

[2] The frontal (or coronal) plane is the vertical plane which passes from left to right, dividing the body segment into front (anterior) and rear (posterior) halves.

3.1 Gait Phase Detection

In this section, we will use the acceleration and angular rates measured by a foot-mounted IMU to detect four different gait phases and various transitions between those. First, we identify useful signals with robust characteristics and discuss criteria for the detection of the gait phase transitions. Based on these criteria, we design a threshold-based algorithm, which is then extended to adjust its parameters automatically to the user's gait. Finally, we will evaluate the reliability and robustness of this algorithm in experiments with healthy subjects and stroke patients.

3.1.1 State of the Art in Gait Phase Detection

In the literature, the definitions of gait phases and gait events vary as well as the employed sensor technologies and methods. A good review of ambulatory gait phase detection can be found in Rueterbories et al. [95]. Therein, a large number of methods is reviewed, most of which employ force-based measurements, gyroscopes, accelerometers, tilt sensors, or inertial measurement units comprising only gyroscopes and accelerometers (6D) or additionally magnetometers (9D).

When force sensors are positioned between the ground and the sole of the foot, the ground reaction force can be determined. Force-based gait event detection is still considered a gold standard and used as a reference when determining the accuracy of other methods. However, positioning the sensors on subjects with abnormal gait is difficult [5] and distinguishing the load changes generated during walking from those caused by weight shifting is hardly possible [79]. Furthermore, the practical applicability of force-based systems is reduced by the cosmetic acceptance and durability of the hardware [111].

Since they have become small and lightweight, inertial sensors represent a promising alternative and have been used successfully by many researchers to detect gait events. Various options for sensor placement have been investigated. For example, Sabatini et al. [98] and Veltink et al. [119] placed one IMU on the foot, while several other authors used two IMUs, one on the shank and one on the thigh [20, 43, 60, 126]. For a rather exhaustive list of placements and sensor setups, please refer to the review by Rueterbories et al. [95].

Therein, several further publications are found in which full 9D IMUs are used. Magnetic field measurements, however, are well known to be unreliable inside buildings and in the presence of magnetic disturbances (see for example De Vries et al. [19]). Besides,

our primary goal is to provide a gait phase detection for synchronization of functional electrical stimulation to the human gait in neuroprosthesis, for example in the Adaptive Peroneal Stimulator [105]. Therefore, in the remainder of this review, we focus on methods that both avoid the usage of magnetometers and work in realtime. Mansfield et al. [58] proposed to place an accelerometer on the trunk to detect heel contact events in FES-assisted walking, while Shimada et al. [111] positioned the sensor on the thigh to detect the swing phase of stroke patients. Beyond these achievements, Williamson and Andrews [127] and Kotiadis et al. [41] detected up to three different gait phases by placing an IMU on the shank. This suggests that a larger number of gait phases can be detected if the sensor unit is placed closer to the foot.

In a feedback controlled peroneal stimulator, a foot/shoe-mounted IMU yields the additional advantage that the stimulation outcome, e.g. the foot orientation angles, can be assessed directly. This setup has been proposed, for example, by Veltink et al. [119] for automatic tuning of a two-channel implantable drop-foot stimulator. Similarly, Rueterbories et al. [96] suggest the use of a foot-mounted accelerometer to detect four gait phases from inflection points and curve extrema of the acceleration vector norm. Experimental evaluation was carried out in healthy and in hemiparetic subjects. However, the subjects only walked at a predefined cadence and at self-selected speed, respectively. A shoe-mounted inertial sensor is also used by Negård [74] and Negård et al. [73] in FES-assisted gait training for hemiplegic stroke patients. Four distinct gait phases are detected. The proposed detection algorithm was validated, with respect to an insole pressure measurement system, in five stroke patients walking with weight support on a treadmill at constant speed.

In the following section, a threshold-based method is proposed that uses the same principles but exceeds the state of the art mainly in two ways: It automatically adapts its parameters to the sensor hardware and to the characteristics of the subject's gait. Moreover, the method neither assumes a certain sensor-to-foot/shoe mounting orientation, nor does it assume that this arbitrary mounting orientation is known. In contrast to most previous contributions, the developed algorithm is evaluated in experimental trials with patients walking on stairs, on a treadmill and on level ground at different velocities and with different walking aids.

3.1.2 Novel Methods for Gait Phase Detection

We use a 6D IMU comprised of a three-axial accelerometer and a three-axial gyroscope with a common local coordinate system. The IMU is attached to the midfoot (or respective part of the shoe) in arbitrary position and orientation. That means it might be,

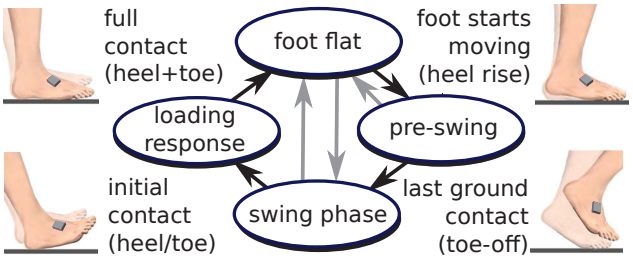

Figure 3.1: Finite state automaton model (phases and transitions) of the gait cycle of one side. During foot-flat phase, the foot rests on the ground, while it has no ground contact during swing phase. By means of a foot-mounted inertial sensor (indicated by gray box), all transitions are detected in realtime.

e.g., tied on the instep or hidden in the sole of a shoe. The IMU provides realtime measurements of the foot acceleration $\mathbf{a}(t) \in \mathbb{R}^3$ and angular rate $\mathbf{g}(t) \in \mathbb{R}^3$ via a wireless link at a sample rate of $f_{\mathrm{IMU}} = 100\,\mathrm{Hz}$, i.e. with a sample period of $t_{\mathrm{s}} = 0.01\,\mathrm{s}$.

The cyclic motion that each foot of the subject exhibits during gait is modeled by the finite state automaton depicted in Figure 3.1. The four states of this automaton correspond to the four gait phases, while the transitions of the automaton correspond to the gait events that mark the beginning and end of these phases [109]. Precisely, *toe-off* and *initial contact* mark the beginning and end of the *swing phase*, while *full-contact* and *heel-rise* mark the beginning and end of the *foot-flat phase*, respectively. This is in accordance with standard literature on gait analysis, see for example Perry et al. [86]. In the remainder of this dissertation, we will call every time period between a heel-rise and the next full-contact a stride. We further denote the stride number by j, and $t_{\mathrm{hr},j}$, $t_{\mathrm{to},j}$, $t_{\mathrm{ic},j}$, $t_{\mathrm{fc},j}$ denote the time instants of the four gait phase transitions of stride j, respectively.

In the following, the accelerations $\mathbf{a}(t)$ and angular rates $\mathbf{g}(t)$ measured by the foot-mounted IMU are used to detect the gait events defined above. This shall be accomplished by a threshold-based algorithm that exploits characteristic features of the inertial signals depicted in Figure 3.2. The plot is based on a large set of data from different gait experiments, for which the true gait phase transitions were identified either manually or by means of a reference measurement system. It is our goal for the remainder of this section to detect these gait events based on the depicted characteristic signals. These signals were chosen carefully after considering a multitude of similar inertial signals. For the sake of brevity, only the result of this process, i.e. the most useful selection of signals, is presented here. Below we discuss how they can be calculated and used to detect the aforementioned gait phase transitions.

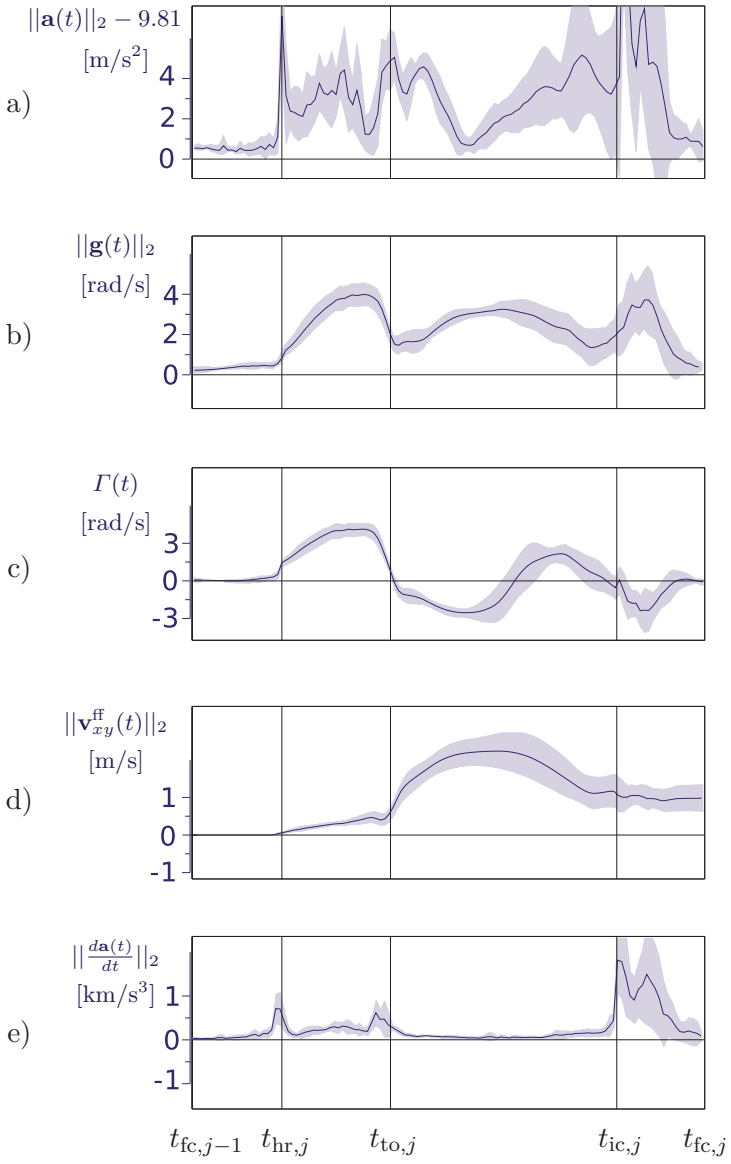

Figure 3.2: Mean (solid) and standard deviation (bands) of characteristic inertial measurement signal trajectories over the human gait cycle: *(a)* acceleration norm $||\mathbf{a}(t)||_2$; *(b)* angular rate norm $||\mathbf{g}(t)||_2$; *(c)* foot tilt rate $\Gamma(t)$; *(d)* vertical velocity $||\mathbf{v}_{xy}^{\mathrm{ff}}(t)||_2$; *(e)* jerk norm $||\frac{d\mathbf{a}(t)}{dt}||_2$. Vertical lines indicate the four gait phase transitions of a typical stride: heel-rise (hr), toe-off (to), initial contact (ic) and full-contact (fc).

3.1.2.1 Detection of Full-Contact and Heel-Rise

For detection of foot-flat phases, we use the standard approach of defining rest bands for the Euclidean vector norms of the measured three-dimensional acceleration and angular rate, i.e.

$$||\mathbf{a}(t)||_2 \in [9.81 - a_{\text{rest}}, 9.81 + a_{\text{rest}}], \tag{3.1}$$
$$||\mathbf{g}(t)||_2 \in [0, g_{\text{rest}}], \tag{3.2}$$

where $||\cdot||_2$ denotes the Euclidean vector norm and the upper bounds $a_{\text{rest}}, g_{\text{rest}} \in \mathbb{R}_{>0}$ represent adjustable threshold parameters.

It is important to note that the IMU yields the same measurement signals when the foot is moving at constant velocity and orientation with respect to the ground[3] and when it is at rest with respect to the ground. However, when both signal norms remain in their rest bands for a sufficiently large number $n_{\text{ff}} \in \mathbb{N}_{>0}$ of consecutive sample instants, then the entire foot (including heel and forefoot) is most likely resting on the ground. Whenever that is the case, the automaton should switch to foot-flat phase regardless of the current state. Formally, this means

$$\begin{aligned} & ||\mathbf{a}(t - kt_{\text{s}})||_2 \in [9.81 - a_{\text{rest}}, 9.81 + a_{\text{rest}}] \; \forall k \in [0, n_{\text{ff}} - 1] \\ \wedge \; & ||\mathbf{g}(t - kt_{\text{s}})||_2 \in [0, g_{\text{rest}}] \qquad\qquad\qquad\quad \forall k \in [0, n_{\text{ff}} - 1] \\ \Rightarrow \quad & \text{foot-flat.} \end{aligned} \tag{3.3}$$

On the contrary, the automaton should transition from foot-flat to pre-swing phase, as soon as the foot starts to move again, i.e. when the following condition holds for a single sample instant:

$$\begin{aligned} \text{foot-flat} \; \wedge \; & \left(\; |\,||\mathbf{a}(t)||_2 - 9.81| > \alpha_{\text{hr}}\, a_{\text{rest}} \quad \vee \quad ||\mathbf{g}(t)||_2 > \alpha_{\text{hr}}\, g_{\text{rest}} \; \right) \\ \Rightarrow \quad & \text{pre-swing,} \end{aligned} \tag{3.4}$$

where $\alpha_{\text{hr}} \in \mathbb{R}, \alpha_{\text{hr}} > 1$, is a hysteresis factor that prevents chattering between foot-flat and pre-swing. The sensitivity of heel-rise detection can be increased or decreased by choosing α_{hr} smaller or larger, respectively. Choosing larger numbers for n_{ff} and small numbers for $a_{\text{rest}}, g_{\text{rest}}$ leads to delayed detection of full-contact. However, doing the opposite increases the chances of false foot-flat detection during swing phase periods with low acceleration and rotation. That the latter is indeed a justified concern is

[3] In fact, the IMU can be said to be at rest in another inertial frame of reference, which is in constant rectilinear motion with respect to the ground.

illustrated by the upper two subplots (a) and (b) of Figure 3.2. Both signal norms exhibit large standard deviations during swing phase. Further analysis of experimental data reveals that strides in which the signal norms remain close to their rest values for a period of up to 0.1 s occur frequently in most subjects. From this we conclude that n_{ff} should be chosen clearly larger than ten (at $f_{\mathrm{IMU}} = 100\,\mathrm{Hz}$) if slightly delayed detection of full-contact is more acceptable than false detection of this event.

3.1.2.2 Detection of Toe-Off

Subplot (c) and (d) of Figure 3.2 show typical courses of two signals that can be used to detect the toe-off: the tilt rate $\Gamma(t) \in \mathbb{R}$, which describes the rate of change of the tilt (inclination) of the foot, and the horizontal foot velocity norm $||\mathbf{v}_{xy}^{\mathrm{ff}}(t)||_2 \in \mathbb{R}_{\geq 0}$. When proper heel-rise detection is established, the tilt rate can be approximated as follows:

$$\Gamma(t) := \frac{\mathbf{g}(t) \cdot \boldsymbol{\phi}(t)}{||\boldsymbol{\phi}(t)||_2}, \quad \boldsymbol{\phi}(t) := \int_{t_{\mathrm{hr},j}}^{t} \mathbf{g}(\tau)\, d\tau, \tag{3.5}$$

where the central dot operator denotes the scalar product and the integral may be replaced by its discrete-time approximation. In this definition of $\Gamma(t)$, we exploit the fact that the integral $\boldsymbol{\phi}(t)$ accumulates the angular rate on the time interval $[t_{\mathrm{hr},j}, t]$ and, thus, is approximately aligned with the average pre-swing tilt axis of the foot, regardless of the local coordinate system. Therefore, no prior knowledge about the sensor-to-foot mounting orientation is required. As Figure 3.2 c illustrates, the tilt rate $\Gamma(t)$ increases during early pre-swing, when the midfoot is tilted (the heel is lifted while the toes remain on the ground). At toe-off (and during swing phase), the tilt rate decreases to zero (and negative values), due to the shank swinging forward around the knee. Please note that the accumulating approach (3.5) also works if the foot is tilted around a combined pitch and roll axis during swing phase, as it is often the case in the paretic gait of stroke patients, for example.

The approach fails, however, if heel and forefoot are raised at the same time, i.e. with the sole remaining parallel to the ground. Such a motion would not precisely be a toe-off, but rather a combined heel-and-toe-rise. Hence, an additional criterion is required, which exploits features of the second aforementioned signal, i.e. the horizontal foot velocity norm $||\mathbf{v}_{xy}^{\mathrm{ff}}(t)||_2$. Estimating this velocity, however, requires integration of the measured acceleration in a fixed coordinate frame. Thus, a few more calculation steps are required: During each foot-flat (ff) phase, the accelerometer readings $\mathbf{a}(t)$ are integrated over time

and the resulting vector is normalized to unit length:

$$\mathbf{z}_{\mathrm{ff},j} := \frac{\hat{\mathbf{z}}_{\mathrm{ff},j}}{||\hat{\mathbf{z}}_{\mathrm{ff},j}||_2}, \quad \hat{\mathbf{z}}_{\mathrm{ff},j} := \int_{t_{\mathrm{fc},j-1}}^{t_{\mathrm{hr},j}} \mathbf{a}(\tau)\, d\tau. \tag{3.6}$$

Since gravitational acceleration dominates when the foot is (almost) at rest, $\mathbf{z}_{\mathrm{ff},j}$ is (almost) vertical. At each heel-rise $t_{\mathrm{hr},j}$, a strapdown integration of the angular rates is restarted that yields the rotation matrix $\mathbf{R}_{\mathrm{ff}}(t)$. As explained in Chapter 2, this matrix transforms the local measurement vectors $\mathbf{a}(t)$ and $\mathbf{g}(t)$ of any time instant $t \in [t_{\mathrm{hr},j}, t_{\mathrm{hr},j+1})$ between two heel-rises into the local coordinate system of the IMU at the preceding foot-flat phase. We shall therefore denote the transformed measurement vectors by

$$\mathbf{a}^{\mathrm{ff}}(t) := \mathbf{R}_{\mathrm{ff}}(t)\mathbf{a}(t), \tag{3.7}$$

$$\mathbf{g}^{\mathrm{ff}}(t) := \mathbf{R}_{\mathrm{ff}}(t)\mathbf{g}(t). \tag{3.8}$$

Please recall that, in the local coordinate system of each foot-flat phase, the gravitational acceleration is known. We can exploit this fact to compensate the gravitational portion of the transformed acceleration $\mathbf{a}^{\mathrm{ff}}(t)$. Obviously, the term $(\mathbf{a}^{\mathrm{ff}}(t) - 9.81\,\mathbf{z}_{\mathrm{ff},j})$ then only captures the acceleration component that is due to velocity changes. Moreover, by projection of the transformed acceleration into the horizontal plane, the horizontal acceleration of the IMU in local coordinates of the preceding foot-flat phase is found:

$$\mathbf{a}^{\mathrm{ff}}_{xy}(t) := \mathbf{a}^{\mathrm{ff}}(t) - (\mathbf{a}^{\mathrm{ff}}(t) \cdot \mathbf{z}_{\mathrm{ff},j})\mathbf{z}_{\mathrm{ff},j}. \tag{3.9}$$

Periodic integration of both quantities over time finally yields the velocity and horizontal velocity, respectively, of the foot for each stride j:

$$\mathbf{v}^{\mathrm{ff}}(t) := \int_{t_{\mathrm{hr},j}}^{t} \mathbf{a}^{\mathrm{ff}}(\tau) - 9.81\,\mathbf{z}_{\mathrm{ff},j}\, d\tau\,, \quad t_{\mathrm{hr},j} \le t < t_{\mathrm{hr},j+1}, \tag{3.10}$$

$$\mathbf{v}^{\mathrm{ff}}_{xy}(t) := \int_{t_{\mathrm{hr},j}}^{t} \mathbf{a}^{\mathrm{ff}}_{xy}(\tau)\, d\tau\,, \qquad t_{\mathrm{hr},j} \le t < t_{\mathrm{hr},j+1}. \tag{3.11}$$

Recall from Chapter 2 that accelerometers may not always yield signal norms of precisely $9.81\,\frac{\mathrm{m}}{\mathrm{s}^2}$ when they are at rest. Such measurement errors cause a strong drift in the velocity estimate $\mathbf{v}^{\mathrm{ff}}(t)$, even while the foot is still resting. The projected quantity $\mathbf{v}^{\mathrm{ff}}_{xy}(t)$ is less affected by such measurement errors. Therefore, we will prefer to use the latter for toe-off detection. On the other hand, and with respect to the previous discussion of combined heel-and-toe-rise, we shall also note that $\mathbf{v}^{\mathrm{ff}}_{xy}(t)$ is less suitable for toe-off detection in the (very rare) case in which the foot is only raised and not moved forward.

With both the tilt rate $\Gamma(t)$ and the horizontal velocity $\mathbf{v}_{xy}^{\mathrm{ff}}(t)$ at hand, we can now formulate the gait phase transition criterion: Toe-off is detected when the current state is pre-swing and one of the following conditions is fulfilled: $\Gamma(t)$ falls below a threshold Γ_{to} after having exceeded $2\,\Gamma_{\mathrm{to}}$, or $||\mathbf{v}_{xy}^{\mathrm{ff}}(t)||_2$ exceeds a threshold v_{to}. Formally, this is expressed as follows:

$$\begin{aligned} \text{pre-swing} \wedge \Big(\; (\; \Gamma(t) < \Gamma_{\mathrm{to}} \;) \; \wedge \; (\; \exists \tau \in [t_{\mathrm{hr},j}, t], \Gamma(\tau) > 2\Gamma_{\mathrm{to}}) \\ \vee \quad ||\mathbf{v}_{xy}^{\mathrm{ff}}(t)||_2 > v_{\mathrm{to}} \; \Big) \\ \Rightarrow \quad \text{swing phase.} \end{aligned} \tag{3.12}$$

The sensitivity of toe-off detection can be increased by decreasing the threshold values Γ_{to} and v_{to}. This might eventually lead to false (early) toe-off detection, while too large threshold values might cause the automaton to remain in pre-swing until full-contact is detected. Since the instep and the attached IMU already move forward during pre-swing, i.e. before the toe-off, it can be difficult to find a suitable value for the velocity threshold v_{to}. This issue is addressed in the following by means of a slightly more elaborate approach.

3.1.2.3 Using Forefoot Velocity Estimates for Toe-Off Detection

The described method for toe-off detection allows for arbitrary mounting orientation, which means it can be used regardless of how the IMU is attached to the foot or shoe. Nevertheless, some measurement systems, for which the proposed methods might be employed, restrict the sensor mounting already by hardware design. To give an example, a miniature IMU might be embedded into the sole or the heel of the shoe. In such systems, the approximate position $\mathbf{o}_{\mathrm{forefoot}} \in \mathbb{R}^3$ of the forefoot in the local sensor coordinates[4] is typically known. This allows us to propose the following optional extension of the described method for toe-off detection.

Using $\mathbf{o}_{\mathrm{forefoot}}$, we can estimate the acceleration $\hat{\mathbf{a}}(t)$ of the forefoot by subtracting the tangential and radial accelerations caused by rotations of the IMU around the forefoot according to the kinematic equations of rotating rigid bodies (see e.g. [38, Section

[4] For example, the forefoot might be approximately 8 cm in positive x-direction from the IMU. Note that these local coordinates of the forefoot do not change with time since the IMU is attached rigidly to the foot.

2.7]):

$$\hat{\mathbf{a}}(t) := \mathbf{a}^{\mathrm{ff}}(t) - \Big(\mathbf{g}(t) \times \mathbf{o}_{\mathrm{forefoot}} \times \mathbf{g}(t) + \mathbf{o}_{\mathrm{forefoot}} \times \frac{d\mathbf{g}(t)}{dt}\Big), \tag{3.13}$$

where the operator $\times$ denotes the vector (cross) product. To perform this calculation, the time-derivative of the angular rate is required. It can be determined, for example, via the symmetric third-order approximation

$$\frac{d\mathbf{g}(t)}{dt} \approx \frac{\mathbf{g}(t-2t_{\mathrm{s}}) - 8\mathbf{g}(t-t_{\mathrm{s}}) + 8\mathbf{g}(t+t_{\mathrm{s}}) - \mathbf{g}(t+2t_{\mathrm{s}})}{12t_{\mathrm{s}}}\,. \tag{3.14}$$

The obtained forefoot acceleration $\hat{\mathbf{a}}(t)$ is then transformed to foot-flat coordinates and projected into the horizontal plane:

$$\hat{\mathbf{a}}^{\mathrm{ff}}(t) := \mathbf{R}_{\mathrm{ff}}(t)\hat{\mathbf{a}}(t), \tag{3.15}$$

$$\hat{\mathbf{a}}^{\mathrm{ff}}_{xy}(t) := \hat{\mathbf{a}}^{\mathrm{ff}}(t) - (\hat{\mathbf{a}}^{\mathrm{ff}}(t) \cdot \mathbf{z}_{\mathrm{ff},j})\,\mathbf{z}_{\mathrm{ff},j}\,. \tag{3.16}$$

As before, periodic integration over time yields the velocity and horizontal velocity of the forefoot for each stride j:

$$\hat{\mathbf{v}}^{\mathrm{ff}}(t) := \int_{t_{\mathrm{hr},j}}^{t} \hat{\mathbf{a}}^{\mathrm{ff}}(\tau) - 9.81\,\mathbf{z}_{\mathrm{ff},j}\; d\tau\,, \qquad t_{\mathrm{hr},j} \le t < t_{\mathrm{hr},j+1}, \tag{3.17}$$

$$\hat{\mathbf{v}}^{\mathrm{ff}}_{xy}(t) := \int_{t_{\mathrm{hr},j}}^{t} \hat{\mathbf{a}}^{\mathrm{ff}}_{xy}(\tau)\; d\tau\,, \qquad t_{\mathrm{hr},j} \le t < t_{\mathrm{hr},j+1}\,. \tag{3.18}$$

Figure 3.3 illustrates the benefits of using this approach. While the IMU already moves during pre-swing, the forefoot starts to move just at toe-off.

Please note that using the zero vector $\mathbf{o}_{\mathrm{forefoot}} = (0,0,0)^T$ results in $\hat{\mathbf{v}}^{\mathrm{ff}}(t) = \mathbf{v}^{\mathrm{ff}}(t)\ \forall t$ and in $\hat{\mathbf{v}}^{\mathrm{ff}}_{xy}(t) = \mathbf{v}^{\mathrm{ff}}_{xy}(t)\ \forall t$. This shall be our default parameter setting for the experimental validation in Section 3.1.3, since it represents the more general case of unknown forefoot position vector.

3.1.2.4 Detection of Initial Contact

Even for considerably low walking speed, the initial contact is characterized by a large peak in the jerk norm $||d\mathbf{a}(t)/dt||_2 \in \mathbb{R}_{\geq 0}$, as illustrated in the bottom subplot (e) of Figure 3.2. We define a threshold $r_{\mathrm{ic}} \in \mathbb{R}$ and detect initial contact by the jerk norm exceeding that threshold. However, jerk norm peaks may also occur at (or near) toe-off, especially in paretic gait. Hence, we propose two additional conditions. A certain time

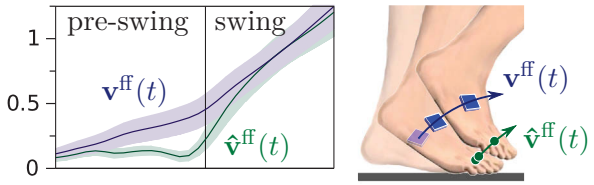

Figure 3.3: Sensor and toe velocity during pre-swing and swing – mean (solid) and standard deviations (bands) calculated over several strides. The toe velocity $\hat{\mathbf{v}}^{\mathrm{ff}}(t)$, which can be calculated if the approximate local coordinates of the forefoot are known, enables a more precise detection of toe-off.

$T_{\mathrm{sw,min}} \geq 0$ since toe-off needs to have passed before initial contact detection is enabled. Moreover, the velocity $||\mathbf{v}^{\mathrm{ff}}(t)||_2$ must have fallen below a certain ratio $0 < \alpha_{\mathrm{ic}} \leq 1$ of its maximum-since-heel-rise value. Formally, this is expressed as follows:

$$\begin{aligned} \text{swing} \;&\wedge\; t - t_{\mathrm{hr},j} > T_{\mathrm{sw,min}} \\ &\wedge\; \exists \tau \in [t_{\mathrm{hr},j}, t], ||\mathbf{v}^{\mathrm{ff}}(\tau)||_2 > v_{\mathrm{to}} \\ &\wedge\; ||\mathbf{v}^{\mathrm{ff}}(t)||_2 < \alpha_{\mathrm{ic}} \max_{\tau \in [t_{\mathrm{hr},j}, t]} ||\mathbf{v}^{\mathrm{ff}}(\tau)||_2 \\ &\wedge\; ||d\mathbf{a}(t)/dt||_2 > r_{\mathrm{ic}} \\ &\Rightarrow \quad \text{loading response.} \end{aligned} \tag{3.19}$$

The underlying assumption is that the velocity norm increases at toe-off, while it decreases (before or) at initial contact. Please recall that a toe-off does not necessarily imply a large horizontal velocity norm. The velocity criterion might (unintentionally) be fulfilled by (small) signal fluctuations appearing right after a toe-off with small $||\mathbf{v}^{\mathrm{ff}}(t)||_2$. Therefore, in (3.19), the velocity norm is furthermore required to have exceeded its toe-off threshold v_{to}.

If the velocity criterion and the time criterion are fulfilled when the jerk exceeds its threshold r_{ic}, then the automaton switches to loading reponse. Obviously, the second velocity criterion can be deactivated by choosing $\alpha_{\mathrm{ic}} = 1$. Likewise, the time criterion can be deactivated by choosing $T_{\mathrm{sw,min}} = 0$. The smaller we choose α_{ic} and the larger we choose $T_{\mathrm{sw,min}}$ and r_{ic}, the more we lower the sensitivity of the initial-contact detection, which implies that the probability of false detection decreases, while the probability of missing an initial contact rises. If the latter occurs, full-contact will nevertheless be detected by the criterion described in Section 3.1.2.1.

Finally, we shall briefly discuss a special case that is particularly relevant for paretic gait: When the subject stumbles, the foot might briefly touch ground and thus decelerate but move on forward before it comes to rest. In such gait, we may choose a rather large α_{ic} and a rather small $T_{\mathrm{sw,min}}$. This will assure that the automaton detects already the first (initial) ground contact, whereafter it remains in the loading-response state until full-contact is detected.

This approach holds a decisive advantage for adaptive FES-based gait support systems that use foot motion measurements from previous swing phases to adjust stimulation intensity parameters. Such adjustments are typically based on the assumption that the observed foot motion is a direct outcome of the applied stimulation and that it is not influenced by large stride-specific forces as they appear at the described intermediate ground contacts. With the proposed method, this assumption holds exactly for the period of time during which the automaton is in swing phase. Hence, the stimulation system can be designed to only consider measurement samples from the swing phase for adjustments.

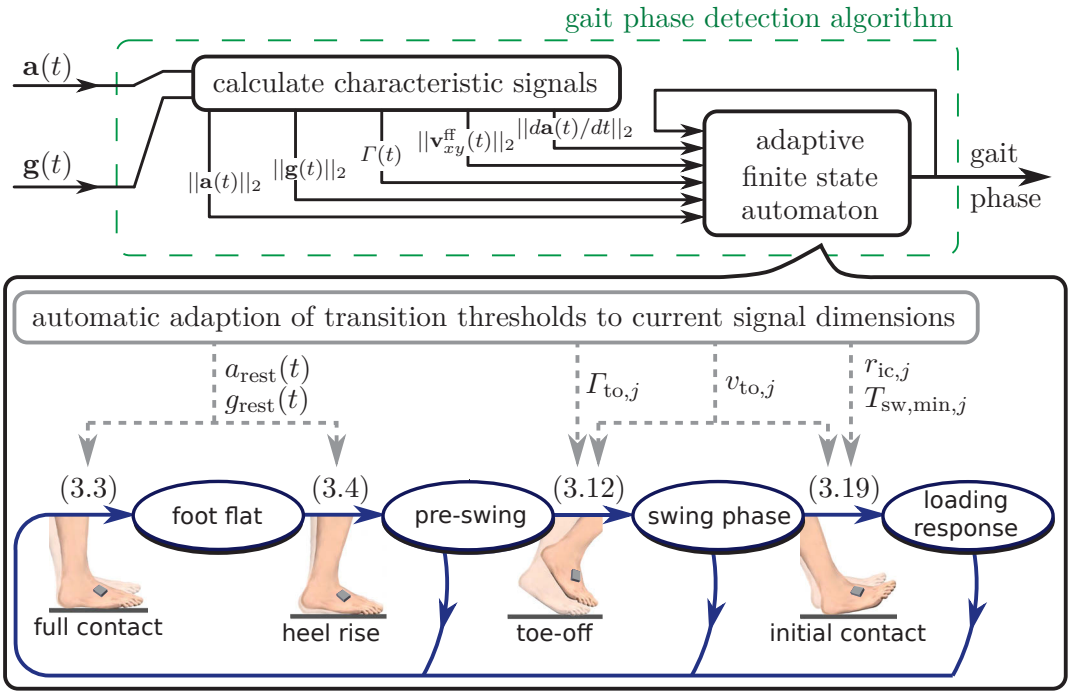

Figure 3.4: Overview diagram of the adaptive gait phase detection algorithm. The accelerations and angular rates measured on the foot or shoe are used to calculate characteristic signals, which exhibit prominent features (peaks, sign changes etc.) at gait phase transitions. These signals drive a threshold-based state automaton, the output of which is the detected gait phase. All thresholds are automatically adapted to the current gait velocity and signal dimensions, which change with gait velocity and from subject to subject.

3.1.2.5 Automatic Threshold Adaption

Comparing the norm signal trajectories $||\mathbf{g}(t)||_2$, $||\mathbf{a}(t)||_2$ for different subjects and different IMUs at different walking speeds yields the following findings. The amplitudes of signal fluctuations during foot-flat as well as the signal amplitudes during motion vary largely across subjects, walking speed and sensor hardware. This implies that it is difficult (if at all possible) to find generic rest band limits a_{rest}, g_{rest} that yield proper full-contact and heel-rise detection under all conditions. Likewise, this argument is also true for the signals and thresholds used to detect toe-off and initial contact. Therefore, we extend the previously described algorithms in such a way that they automatically adapt their thresholds to the current signal characteristics. Figure 3.4 summarizes the information processing structure of the algorithms and criteria described above and illustrates how these methods are extended.

Regarding full-contact and heel-rise detection, we continuously calculate the mean values $\mu_a(t)$, $\mu_g(t)$ and standard deviations $\sigma_a(t)$, $\sigma_g(t)$ of the last $n_\sigma \in \mathbb{N}_{>0}$ samples values of $||\mathbf{a}(t)||_2, ||\mathbf{g}(t)||_2$, respectively:

$$\mu_a(t) := \frac{\sum_{k=0}^{n_\sigma - 1} ||\mathbf{a}(t - kt_\text{s})||_2}{n_\sigma}, \tag{3.20}$$

$$\sigma_a(t) := \sqrt{\frac{\sum_{k=0}^{n_\sigma - 1} (||\mathbf{a}(t - kt_\text{s})||_2 - \mu_a(t))^2}{n_\sigma - 1}}, \tag{3.21}$$

$$\mu_g(t) := \frac{\sum_{k=0}^{n_\sigma - 1} ||\mathbf{g}(t - kt_\text{s})||_2}{n_\sigma}, \tag{3.22}$$

$$\sigma_g(t) := \sqrt{\frac{\sum_{k=0}^{n_\sigma - 1} (||\mathbf{g}(t - kt_\text{s})||_2 - \mu_g(t))^2}{n_\sigma - 1}}. \tag{3.23}$$

We further determine the smallest values $\sigma_{a,\min}(t)$, $\sigma_{g,\min}(t)$ of the last n_obs samples of the standard deviation signals $\sigma_a(t)$, $\sigma_g(t)$, respectively:

$$\begin{aligned} \sigma_{a,\min}(t) &:= \min_{k \in [0, n_\text{obs} - 1]} \sigma_a(t - kt_\text{s}), \\ \sigma_{g,\min}(t) &:= \min_{k \in [0, n_\text{obs} - 1]} \sigma_g(t - kt_\text{s}). \end{aligned} \tag{3.24}$$

We now set n_σ smaller than the shortest possible duration (in samples) of a foot-flat phase, and we set the observation window size n_obs larger than the longest duration of (at least) one stride. Then the standard deviations $\sigma_{a,\min}$ and $\sigma_{g,\min}$ characterize the amplitudes of the foot-flat signal fluctuations under the current circumstances (e.g. sensor, subject, gait velocity). Hence, we set the rest band limits a_{rest}, g_{rest} continuously

to a multiple of these quantities:

$$a_{\text{rest}}(t) = \alpha_\sigma \, \sigma_{a,\min}(t), \quad g_{\text{rest}}(t) = \alpha_\sigma \, \sigma_{g,\min}(t), \quad \alpha_\sigma \in \mathbb{R}_{>1} \, . \tag{3.25}$$

Let us assume that the described adaption strategy leads to proper heel-rise and full-contact detection under all relevant circumstances. Then we would also like to compensate the influence of these varying circumstances on toe-off and initial contact detection. To this end, we determine the maximum values of $\Gamma(t)$, $||\mathbf{v}_{xy}^{\text{ff}}(t)||_2$ and $||d\mathbf{a}(t)/dt||_2$ between each two foot-flat phases:

$$\Gamma_{\max,j} := \max_{\tau \in [t_{\text{hr},j}, t_{\text{fc},j}]} \Gamma(\tau) \, , \tag{3.26}$$

$$v_{\max,j} := \max_{\tau \in [t_{\text{hr},j}, t_{\text{fc},j}]} ||\mathbf{v}_{xy}^{\text{ff}}(\tau)||_2 \, , \tag{3.27}$$

$$r_{\max,j} := \max_{\tau \in [t_{\text{hr},j}, t_{\text{fc},j}]} ||d\mathbf{a}(\tau)/dt||_2 \, . \tag{3.28}$$

In each foot-flat phase, we set the threshold values Γ_{to}, v_{to} and r_{ic} for the next stride to 25% of the average of the last $m_{\text{adapt}} \in \mathbb{N}$ stridewise maximum values, respectively:

$$\Gamma_{\text{to},j+1} = 0.25 \, \frac{\sum_{k=0}^{m_{\text{adapt}}-1} \Gamma_{\max,j-k}}{m_{\text{adapt}}}, \tag{3.29}$$

$$v_{\text{to},j+1} = 0.25 \, \frac{\sum_{k=0}^{m_{\text{adapt}}-1} v_{\max,j-k}}{m_{\text{adapt}}}, \tag{3.30}$$

$$r_{\text{ic},j+1} = 0.25 \, \frac{\sum_{k=0}^{m_{\text{adapt}}-1} r_{\max,j-k}}{m_{\text{adapt}}}, \tag{3.31}$$

where the lower index j indicates that the thresholds now vary from stride to stride.

Finally, we also determine the time duration

$$T_{\neg\text{ff},j} := t_{\text{fc},j} - t_{\text{hr},j} \tag{3.32}$$

between each two consecutive foot-flat phases and set $T_{\text{sw,min}}$ to 20% of the average of this quantity over the last m strides:

$$T_{\text{sw,min},j} = 0.20 \, \frac{\sum_{k=1}^{m_{\text{adapt}}} T_{\neg\text{ff},j-k}}{m_{\text{adapt}}}, \quad T_{\neg\text{ff},j} := t_{\text{fc},j} - t_{\text{hr},j}. \tag{3.33}$$

This is based on the observation that 20% of $T_{\neg\text{ff},j}$ usually corresponds to about 30–50% of the swing phase duration, i.e. a time window during which initial contact is very unlikely, even in paretic gait.

The proposed periodic adaptions assure that the gait phase detection algorithm is always tuned to suit the current subject, sensor hardware and gait velocity. The speed of adaption can be increased or decreased by choosing smaller or larger values for m_{adapt}, respectively. Suitable initial values for all adaptive algorithm parameters (i.e. $a_{\text{rest}}(t)$, $g_{\text{rest}}(t)$, $\Gamma_{\text{to},j}$, $v_{\text{to},j}$, $r_{\text{ic},j}$ and $T_{\text{sw,min}}$) are obtained by applying the adaption to several strides of representative recorded data.

With respect to (3.33), note that adapting $T_{\text{sw,min,j}}$ based on the average swing phase duration itself would be more direct, but it would imply that the parameter adaption depends on the detection for which the parameter is used. To avoid such dependency loops, we employ the described indirect approach instead.

Note furthermore that, beyond this example, the entire gait phase detection algorithm is designed such that circular interdependencies are avoided. The detection of toe-off and initial contact only depends on proper detection of full-contact and heel-rise, which in turn only depends on the raw signal norms $||\mathbf{a}(t)||_2, ||\mathbf{g}(t)||_2$. Therefore, even if the subject's gait characteristics could change dramatically from one stride to the next, the algorithm described above would automatically adjust its parameters via the following steps:

1. The new amplitude of the foot-flat signal fluctuations are determined according to (3.24), and the new rest band threshold are set according to (3.25).

2. Full-contact and heel-rise are properly detected, i.e. the automaton at least switches back and forth between foot-flat and pre-swing phase.

3. The new values of $\Gamma_{\text{max},j}$, $v_{\text{max},j}$, $r_{\text{max},j}$ and $T_{\neg\text{ff},j}$ are determined and the respective thresholds are adjusted according to (3.29), (3.30), (3.31) and (3.33).

4. Toe-off and (subsequently) initial contact are properly detected.

Since each of these steps only depends (if at all) on previous steps, deadlocks are avoided and the algorithm successively adapts to the new gait characteristics.

3.1.3 Stroke Patient Experiments on Gait Phase Detection

For many application systems, including active realtime gait support systems, it is crucial that the developed gait phase detection method achieves proper gait phase detection not only in healthy gait, but also in paretic gait. Therefore, the proposed algorithm is

evaluated in realtime simulations[5] using measurement data from gait experiments with both healthy subjects and stroke patients. Participants gave informed consent and the study was approved by the ethics committee at Charité Universitätsmedizin Berlin.

The total number of 32 experimental trials can be split into three groups: ambulatory stroke patients in subacute[6] phase (7 experiments), chronic[7] drop foot patients (15 experiments) and healthy subjects (10 experiments). In every experiment, an IMU (RehaWatch, Hasomed GmbH, Magdeburg, Germany) was attached to the foot of the paretic side (or an arbitrary side in case of healthy subjects). The accelerometer and gyroscope signals were recorded at 100 Hz while the subjects walked between ten and fifty strides, depending on their strength and abilities. The experiments have been carried out either on level ground (21 experiments), on a treadmill (7 experiments), or on stairs (4 experiments).

The subacute stroke patients performed each experimental trial at self-selected walking speed, as well as at 25% faster and at 25% slower speed (or at maximum velocity if 25% faster was not achievable). The chronic drop foot patients, on the other hand, were asked to walk at comfortable speed on level ground with one of the following different levels of support: with a conventional drop foot stimulator (6 experiments), with walking sticks (2 experiments), with ankle-foot orthosis (2 experiments). Healthy subjects were asked to walk at comfortable speed, either on level ground or on a treadmill or on stairs.

The resulting collection of data sets covers a wide range of different subjects, walking conditions, terrains and velocities. The number of subjects is certainly too small for a proper comparison of the gait phase detection quality between all these conditions. However, this data collection allows us to evaluate whether the proposed method is capable of detecting all four gait phase transitions properly under all considered conditions. If that was not the case, the algorithm would fail for at least one of the included data sets.

Since the goal of this evaluation is only to provide the described proof of concept, the parameters of the gait phase detection algorithm are chosen by the following arguments of common sense rather than by optimizing them for the given data. The sample frequency of the IMUs is $f_{\mathrm{IMU}} = 100\,\mathrm{Hz}$. Even in slow walking, the time passed between two full-contacts does not exceed 1.5 s. In fast walking, on the other hand, the duration of a

[5] This means that the data is processed in an online manner, i.e. only current and previous data samples are used by the algorithm.
[6] i.e. these patients were in a very early stage of stroke rehabilitation
[7] i.e. these patients suffered from a chronic disability to lift the foot, cf. Chapter 6

foot-flat phase is above 0.3 s. Therefore, choosing

$$n_{\text{obs}} = 200, \quad n_\sigma = 20 \tag{3.34}$$

assures that the foot-flat signal fluctuation amplitudes are properly determined. The rest thresholds are then set to $\alpha_\sigma = 4$ times the determined standard deviation, and the full-contact detection parameter is chosen $n_{\text{ff}} = 20$. The latter implies that detection of the foot-flat phase is delayed by up to 0.2 s. However, for many applications in the domain of active gait support systems, a reliable detection of this event is more important than a prompt detection (see for example Chapter 6). For similar reasons, we choose a hysteresis parameter of $\alpha_{\text{hr}} = 2$, i.e. the raw signal norms must exceed eight times the determined standard deviation before heel-rise is detected. This certainly leads to some detection delays, but it substantially lowers the risk of false heel-rise detection. The initial-contact criterion is used with $\alpha_{\text{ic}} = 0.75$, and the automatic adaption horizon is set to $m_{\text{adapt}} = 5$.

The results that the gait phase detection algorithm yields for the given data are inspected visually stride-by-stride. Based on careful evaluation of the characteristic signals defined above and based on partially available video recordings, incorrect gait phase transitions are identified. Despite the large variety of subjects, terrains, gait velocities and walking supports, more than 95% of the overall more than 300 strides are completely detected in the sense that all four gait phase transitions are detected properly. Before we discuss the remaining 5%, we inspect the case of completely successful gait phase detection in more detail.

Figure 3.5 presents exemplary results from four strides of a chronic drop foot patient. All three subplots reveal that each signal varies from stride to stride (not only in amplitude) and that repeatability is only given to a very limited extent. In the upper subplot (a) of Figure 3.5, the signal norms exhibit much larger fluctuations during the second and third foot-flat phase than during the first foot-flat phase. Due to the automatic adaption, the rest band limits are raised gradually. The loading response of the first (and third) stride is almost n_{ff} samples short, which indicates that the foot touched ground with heel and toes almost simultaneously – in contrast to the second (and fourth) depicted strides.

At the same time, the amplitudes of tilt rate and velocity in the middle subplot (b) of Figure 3.5 remain almost the same, although the signals themselves do not precisely repeat from one stride to the next. For example, the velocity is subject to a much stronger drift during the first depicted foot-flat phase than during all following ones. Likewise, the course of the tilt rate during swing phase varies largely. This demonstrates how important it is to extract only those features for gait phase detection that are reliably repeatable. In all four strides of the presented data and in a large portion of

the analyzed data, the velocity exceeds its toe-off threshold almost at the same time at which the tilt rate falls below its threshold. This suggests that both criteria are based on rather robust[8] signal features.

As the lower subplot (c) of Figure 3.5 shows, the jerk norm peaks also vary from stride to stride. While there is hardly a peak at the first toe-off, the signal clearly exceeds the jerk threshold during early swing phase of each following stride. Due to the time and velocity criterion, these peaks are disregarded. The actual initial contact is detected reliably, although the foot hits ground much softer in the initial contact of the last depicted stride.

Figure 3.6 further illustrates the previously discussed fact that signal features and gait characteristics may change considerably from stride to stride. The comparison of both subplots reveals that these effects are stronger in level ground walking than in walking on a treadmill while holding on to a handrail.

As mentioned above, all gait phases are correctly detected in 95% of all strides. In the remaining 5% of the strides, either of the following phenomena is observed. In about 3% of the strides, the initial contact is not properly detected due to sudden, large changes in the jerk peak amplitudes. In about 2% of the strides, the foot-flat phase is not correctly detected due to sudden, large changes in the signal norm fluctuation amplitudes. The former phenomenon is found to be slightly more common in subacute stroke patients than in chronic drop foot patients and in healthy subjects, while the latter phenomenon is more common in walking stairs than in level ground or treadmill walking. However, none of the analyzed walking trials contain more than two incorrectly detected transitions, and the majority of the trials contain not a single one. This result allows us to state that the proposed algorithm is capable of detecting the four gait phases in all subjects and under all considered walking conditions.

Beyond this proof of concept, it is an important research question how accurately the gait phase transitions are detected with respect to the time delay between the actual gait event and its detection. This question is addressed by Müller et al. [70], who compare a similar version of the proposed gait phase detection to a method that is based on an optical motion tracking system. Therein, the time delay between optical detection and inertial detection is found to be small for all gait phase transitions except for the full-contact. Since the latter is of minor importance in FES-based gait support, the algorithm is found to be well-suited for this application.

[8] robust in the sense that this feature remains even if other aspects of the signal change significantly

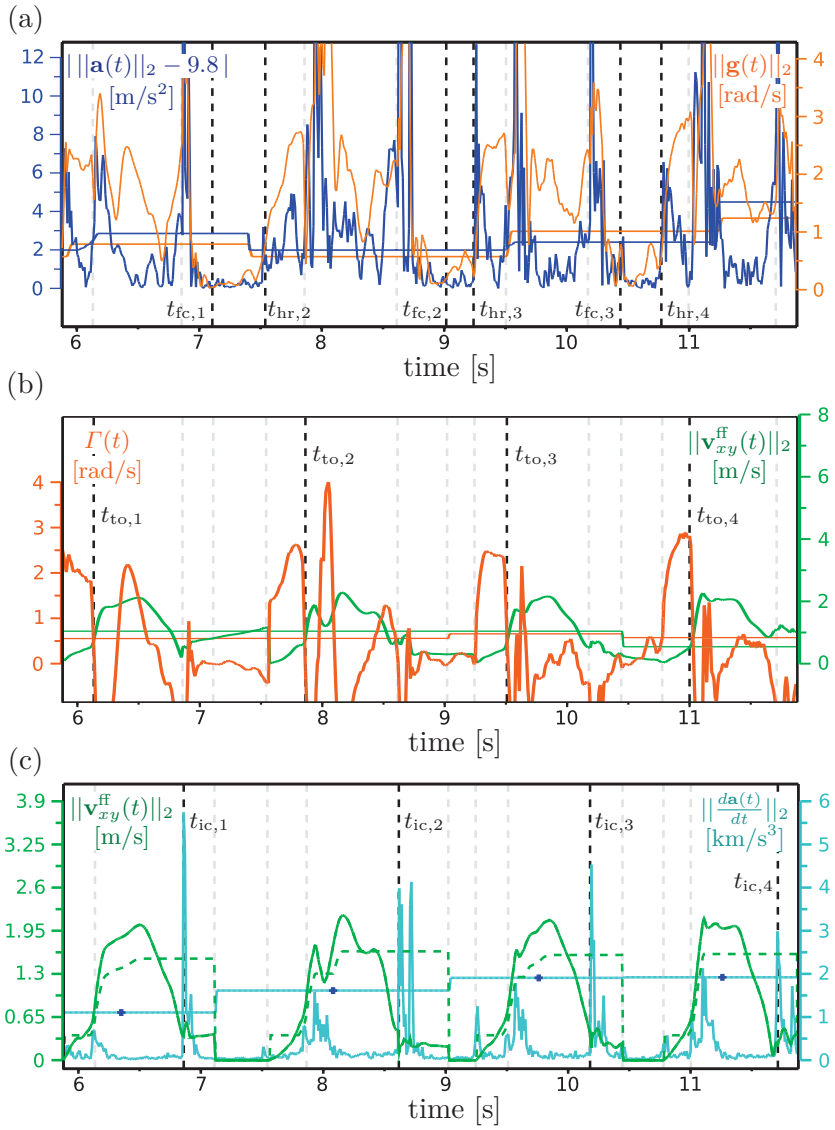

Figure 3.5: Experimental results in a drop foot patient walking on level ground at self-selected speed with FES support. *(a)* Automatically adapted thresholds of acceleration and angular rate are used to detect full-contact and heel-rise. *(b)* Toe-off is detected by sign change in tilt rate and a sudden increase in toe velocity. *(c)* Initial contact is detected by a large jerk after/during $||\mathbf{v}^{\mathrm{ff}}_{xy}(t)||_2$ has fallen below 75% of its maximum-since-heel-rise velocity (dashed line). Markers on the threshold line indicate fulfillment of the time criterion.

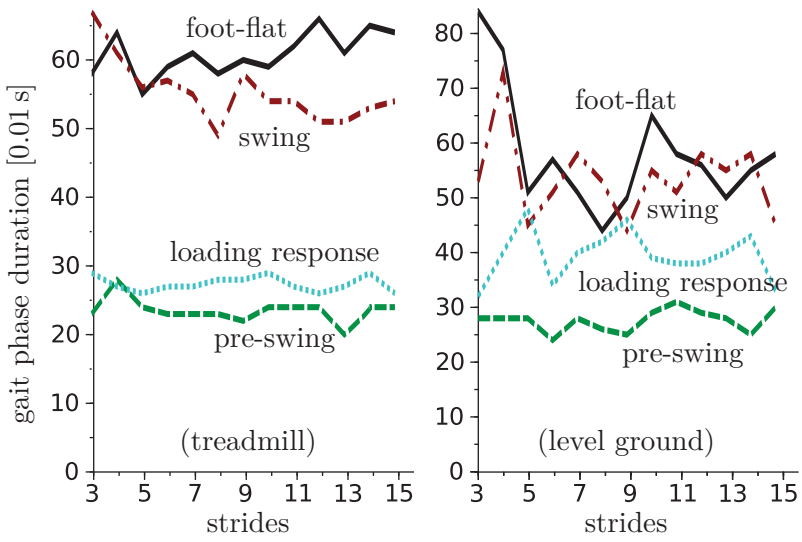

Figure 3.6: Comparison of gait phase durations for a drop foot patient walking on a treadmill and on level ground at self-selected speed. Stride-to-stride variance is significantly smaller when the patient walks on the continuously moving treadmill and holds on to the handrail.

3.1.4 Conclusions and Future Research

We developed a new method for realtime gait phase detection that employs a single inertial sensor on the foot or shoe and adapts its parameters automatically to the current signal dimensions that may vary with sensor hardware, with the subject, and with the walking velocity. We demonstrated that the method can handle the challenge of irregularity in stroke patient's gait and is suitable for a large range of terrains and walking speeds. Since only accelerometer and gyroscope readings are used, the method is robust with respect to magnetic disturbances and the presence of ferromagnetic material.

In future research, the algorithm might be extended to facilitate analysis of running motions. If, beyond the provided proof-of-concept, a detailed performance evaluation for certain walking conditions is of interest, then a clinical evaluation study with a larger and more homogeneous set of participants is advisable. As Müller et al. demonstrate, the proposed method also achieves proper gait phase detection in barefoot walking, which is highly relevant for several applications and will be very useful in the experimental evaluation of the method for foot orientation angle measurement that is derived in the following section.

3.2 Inertial Foot Orientation Angle Estimation

In the previous section, it was demonstrated that a foot-mounted inertial measurement unit can be used to detect gait events in realtime. Now we use the measurement data of the same IMU to assess foot orientation angles in pitch and roll direction. Such measurements are of particular interest in the analysis of paretic gait, since foot orientation with respect to the ground is strongly related to the risk of stumbling and falling. If the foot orientation is assessed in realtime, the measured angles can furthermore be used to adjust stimulation intensity parameters in feedback-controlled gait neuroprostheses. In the following, we derive methods that accomplish such realtime measurements by means of a 6D IMU, i.e. without the use of magnetometer readings.

3.2.1 State of the Art in Inertial Foot Motion Assessment

There are a number of standard methods that estimate the orientation of the foot from the measurement data of an IMU attached to the foot, see for example the review by Sabatini [99] and references therein. Veltink et al. [119] propose to integrate the measured angular velocity and to compensate integration drift by assuming certain initial and final conditions for each stride. Precisely, the foot is required to be flat on the ground and on the same vertical level at the beginning and the end of every stride. However, this approach fails on stairs, and it was not evaluated with respect to a reference method.

Sabatini et al. [98] employ an inertial measurement unit composed of one biaxial accelerometer and one monoaxial rate gyroscope. The IMU is placed on the instep of the foot such that the sensitive axes of the accelerometer are located in the sagittal plane. By sensor construction, the gyroscope sensitive axis is then perpendicular to this plane, so as to measure the angular velocity component that is parallel to the mediolateral[9] axis. As before, integration of the angular rate and periodic drift compensation are used. The obtained sagittal orientation angles are, however, not compared to the results of a reference method.

Liu et al. [48] use similarly restrictive sensor mountings, but they compare their results to the orientation angles determined by a marker-based optoelectronic reference system. Root-mean-square deviations are found to be below 4°. However, the method is based on offline data analysis and requires a calibration trial in which the subject is requested to walk along a straight leading line.

[9] i.e. the horizontal axis of the body that points from the center straight to the left (for the left half of the body) or to the right (for the right half of the foot)

Van den Noort et al. [120] evaluate the accuracy of methods for inertial gait analysis with respect to an optical reference system in children suffering from cerebral palsy. IMUs are placed on each foot, shank, thigh and on the torso. Anatomical calibration of the sensors is according to the Outwalk protocol [17]. The Kinematic Coupling algorithm [57] is employed to estimate the orientations of all IMUs, and joint angles are calculated from those. However, only the joint angles are evaluated with respect to the results of the marker-based optical motion tracking system. Accuracies below 2° are reported, which suggests that the accuracies of the foot orientation is in the same range.

Furthermore, it is important to note that these results are obtained with the optical markers of the reference system being placed directly on top of the IMUs. This is remarkable because the markers are placed on anatomical landmarks in the actual gold standard method, i.e. in standard optical motion analysis. Even with a very rigid mounting, a foot/shoe-mounted IMU will certainly move, to some extent, relative to the foot or shoe. Therefore, the discussed evaluation study is too simplified to fully assess the accuracy of IMU-based foot orientation measurements.

In the remainder of this section, we will develop a method for realtime foot orientation assessment and evaluate it with respect to the actual gold standard method of optical motion analysis with markers placed on anatomical landmarks. Since, in indoor environments, the magnetic field is often heavily disturbed and far from homogeneous [19], we will consider an IMU-based method that calculates pitch and roll angles while completely avoiding the use of magnetometer readings. Furthermore, we will allow arbitrary mounting orientation in the sense that none of the local IMU coordinate axes are required to coincide with any physiological axis of the foot.

3.2.2 Methods for Foot Orientation Angle Estimation

The pitch angle α and roll angle β of the foot are defined via the posterior-anterior[10] axis $\mathbf{x}_{\text{foot}}$ and mediolateral axis $\mathbf{y}_{\text{foot}}$ of the foot, as illustrated in Figure 3.7. Please note that, by definition, these axes are horizontal when the foot rests on level ground. Furthermore, the coordinates of both axes $\mathbf{x}_{\text{foot}}$ and $\mathbf{y}_{\text{foot}}$ in the local coordinate system of the IMU are (almost) constant, since the sensor is (almost) rigidly connected with the foot. Nevertheless, we consider these coordinates to be unknown because it is hard to achieve (and restrictive to demand) a mounting orientation that aligns any of the local coordinate axes with the anatomical axes of the foot. Hence, we must determine these axis coordinates before we can measure the foot orientation angles.

[10] i.e. the horizontal axis of the body that points from rear straight to front

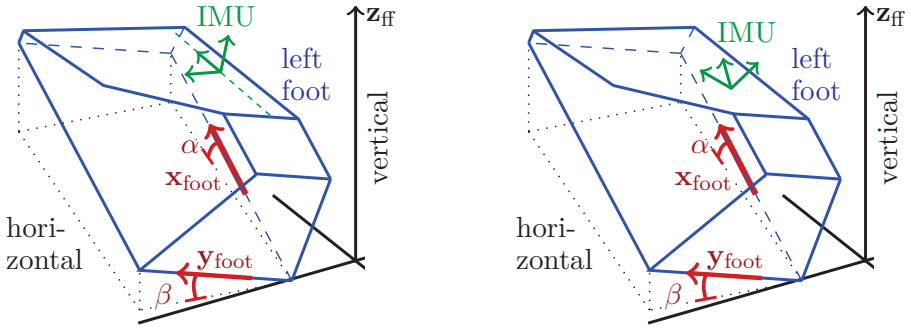

Figure 3.7: The angle α that the posterior-anterior axis $\mathbf{x}_{\text{foot}}$ of the foot and its projection into the horizontal plane (dotted lines) confine is a proper measure of foot pitch, while foot roll can be quantified analogously using the mediolateral axis $\mathbf{y}_{\text{foot}}$ of the foot. *Left:* The local coordinate axes of the IMU are not aligned with any of the anatomical axes, but one of the local axes lies in the sagittal plane. *Right:* The IMU is attached in completely arbitrary orientation.

3.2.2.1 Determining Local Coordinates of Anatomical Foot Axes

As we will see, for example, in Chapter 6, it is often desirable to attach the inertial sensor to the instep of the foot. Since the instep is not a level surface, all we can typically assure in practice is that one of the local coordinate axes lies in the sagittal plane[11], as illustrated in Figure 3.7. In the following, we exploit this fact to determine the coordinates of the posterior-anterior axis $\mathbf{x}_{\text{foot}}$ and the mediolateral axis $\mathbf{y}_{\text{foot}}$ of the foot, before we consider the even more general case of completely arbitrary mounting orientation.

Almost Arbitrary Mounting Orientation: Without loss of generality, let us assume that the local axis $\mathbf{x}_{\text{local}} = (1, 0, 0)^T$ of the IMU is known to lie in the sagittal plane of the foot and to point approximately forward. Furthermore, assume that the gait phase detection algorithm described in Section 3.1 is employed and achieves realtime detection of the heel-rise $t_{\text{hr},j}$ and full-contact $t_{\text{fc},j}$ of the current stride j. During every foot-flat phase, i.e. when the foot rests on the ground, the local accelerometer readings $\mathbf{a}(t)$ are integrated over time, and the resulting vector $\hat{\mathbf{z}}_{\text{ff},j}$ is normalized to unit length

[11] Note that this does *not* imply that this local axis is aligned with $\mathbf{x}_{\text{foot}}$, since the instep is not level.

(cf. Section 3.1.2.2), which yields

$$\mathbf{z}_{\mathrm{ff},j} = \frac{\hat{\mathbf{z}}_{\mathrm{ff},j}}{||\hat{\mathbf{z}}_{\mathrm{ff},j}||_2}, \quad \hat{\mathbf{z}}_{\mathrm{ff},j} = \int_{t_{\mathrm{fc},j-1}}^{t_{\mathrm{hr},j}} \mathbf{a}(\tau)\, d\tau. \tag{3.35}$$

Since gravitational acceleration dominates when the foot is (almost) at rest, $\mathbf{z}_{\mathrm{ff},j}$ is (almost) vertical. Therefore, we calculate the local coordinates of the mediolateral axis $\mathbf{y}_{\mathrm{foot}}$ during the first foot-flat phase as follows:

$$\hat{\mathbf{y}}_{\mathrm{foot}} := \mathbf{z}_{\mathrm{ff},1} \times \mathbf{x}_{\mathrm{local}}, \tag{3.36}$$

$$\mathbf{y}_{\mathrm{foot}} := +\hat{\mathbf{y}}_{\mathrm{foot}}/||\hat{\mathbf{y}}_{\mathrm{foot}}||_2 \text{ for a left foot,}$$

$$\text{and } \mathbf{y}_{\mathrm{foot}} := -\hat{\mathbf{y}}_{\mathrm{foot}}/||\hat{\mathbf{y}}_{\mathrm{foot}}||_2 \text{ for a right foot.} \tag{3.37}$$

Note that the side-dependent sign definition assures that the mediolateral axis $\mathbf{y}_{\mathrm{foot}}$ points indeed from medial to lateral for both feet. Subsequently, we calculate the local coordinates of the posterior-anterior axis $\mathbf{x}_{\mathrm{foot}}$ as follows:

$$\hat{\mathbf{x}}_{\mathrm{foot}} := \mathbf{z}_{\mathrm{ff},1} \times \mathbf{x}_{\mathrm{local}} \times \mathbf{z}_{\mathrm{ff},1}, \tag{3.38}$$

$$\mathbf{x}_{\mathrm{foot}} := \hat{\mathbf{x}}_{\mathrm{foot}}/||\hat{\mathbf{x}}_{\mathrm{foot}}||_2,$$

where the vector product operations correspond to a projection of $\mathbf{x}_{\mathrm{local}}$ into the horizontal plane, to which $\mathbf{z}_{\mathrm{ff},1}$ is perpendicular. By construction, the axis triplet $\mathbf{x}_{\mathrm{foot}}, \mathbf{y}_{\mathrm{foot}}, \mathbf{z}_{\mathrm{ff},1}$ is an orthonormal base.

Completely Arbitrary Mounting Orientation: If inertial sensors are attached by the users, it is a common demand that inaccurate mounting of the sensor shall not entail measurement errors. Thus, let us briefly assume that none of the axes can be assured to lie in any anatomical plane. Then instead, $\mathbf{x}_{\mathrm{foot}}$ and $\mathbf{y}_{\mathrm{foot}}$ can be automatically identified from the measurement data of a stride as follows. We assume that (at least during the first stride) the foot travels mainly forward, or more precisely: into the direction at which the posterior-anterior axis of the foot was pointing right before the stride. This is typically assured even in paretic gait. We integrate the horizontal foot velocity $\mathbf{v}_{xy}^{\mathrm{ff}}(t)$ defined in Section 3.1 between heel-rise and full-contact. Exploiting the fact that the foot is resting at full-contact, we remove integration drift and calculate the local coordinates of the posterior-anterior axis $\mathbf{x}_{\mathrm{foot}}$ of the foot:

$$\mathbf{x}_{\mathrm{foot}} = \frac{\hat{\mathbf{x}}_{\mathrm{foot}}}{||\hat{\mathbf{x}}_{\mathrm{foot}}||_2}, \quad \hat{\mathbf{x}}_{\mathrm{foot}} := \int_{t_{\mathrm{hr},1}}^{t_{\mathrm{fc},1}} (\mathbf{v}_{xy}^{\mathrm{ff}}(\tau) - \frac{\tau - t_{\mathrm{hr},1}}{t_{\mathrm{fc},1} - t_{\mathrm{hr},1}} \mathbf{v}_{xy}^{\mathrm{ff}}(t_{\mathrm{fc},j}))\, d\tau. \tag{3.39}$$

Subsequently, we calculate the local coordinates of the mediolateral axis $\mathbf{y}_{\text{foot}}$, once again with side-dependent sign, as follows:

$$\begin{aligned} \mathbf{y}_{\text{foot}} &:= \mathbf{z}_{\text{ff},1} \times \mathbf{x}_{\text{foot}} \text{ for a left foot,} \\ \text{and } \mathbf{y}_{\text{foot}} &:= \mathbf{x}_{\text{foot}} \times \mathbf{z}_{\text{ff},1} \text{ for a right foot.} \end{aligned} \tag{3.40}$$

Note that the vector product of two orthogonal unit vectors yields a unit vector and that, therefore, the axis triplet $\mathbf{x}_{\text{foot}}, \mathbf{y}_{\text{foot}}, \mathbf{z}_{\text{ff},1}$ is an orthonormal base.

3.2.2.2 Calculating Foot Pitch and Roll Angles

Recall from Section 3.1 that, at each heel-rise $t_{\text{hr},j}$ of each stride j, a strapdown integration [100] of the angular rates is restarted that yields the rotation matrix $\mathbf{R}_{\text{ff}}(t)$. This matrix transforms any vector given in the local coordinates of any time instant $t \in [t_{\text{hr},j}, t_{\text{hr},j+1})$ between two heel-rises into the local coordinate system of the preceding foot-flat phase.

Figure 3.8: In the pathological gait of drop foot patients, foot lift is weak during swing phase, i.e. the toes hang below the heel (negative pitch). Additionally, increased muscle tone often promotes the inversion of the foot, i.e. the outer edge of the foot is lower than the inner edge (negative roll). Both angles are defined with respect to level ground.

If we transform $\mathbf{x}_{\text{foot}}$ into this coordinate system, in which the vertical axis $\mathbf{z}_{\text{ff},j}$ is known, we can calculate the time-dependent foot orientation angle in pitch direction as follows:

$$\tilde{\alpha}(t) := \frac{\pi}{2} - \sphericalangle(\mathbf{z}_{\text{ff},j}, \mathbf{R}_{\text{ff}}(t)\mathbf{x}_{\text{foot}}) = \arcsin(\mathbf{z}_{\text{ff},j}^T \mathbf{R}_{\text{ff}}(t)\mathbf{x}_{\text{foot}}) \quad \in [-\frac{\pi}{2}, +\frac{\pi}{2}], \tag{3.41}$$

where $\sphericalangle(\cdot)$ denotes the angle that two three-dimensional vectors confine. Please note that the pitch angle is defined to be positive when the toes are above the heel and negative when the heel is above the toes, as illustrated in Figure 3.8. Likewise, we

calculate the time-dependent foot orientation angle in roll direction:

$$\tilde{\beta}(t) := \frac{\pi}{2} - \sphericalangle(\mathbf{z}_{\mathrm{ff},j}, \mathbf{R}_{\mathrm{ff}}(t)\mathbf{y}_{\mathrm{foot}}) = \arcsin(\mathbf{z}_{\mathrm{ff},j}^T \mathbf{R}_{\mathrm{ff}}(t)\mathbf{y}_{\mathrm{foot}}) \quad \in [-\frac{\pi}{2}, +\frac{\pi}{2}]. \tag{3.42}$$

Due to the side-dependent axis definition, the roll angle is always positive when the outer edge of the foot is above the inner edge, both for a right and a left foot, cf. Figure 3.8.

As we discussed in Chapter 2, strapdown integration of angular rates is always subject to drift, since (even after proper calibration) the gyroscopes have non-zero bias. Therefore, the accuracy of $\tilde{\alpha}(t)$ and $\tilde{\beta}(t)$ decreases with time[12] between each two foot-flat phases. At every full-contact $t_{\mathrm{fc},j}$, however, we can remove the drift from $\tilde{\alpha}(t), \tilde{\beta}(t)$ on the time interval $t \in [t_{\mathrm{hr},j}, t_{\mathrm{fc},j}]$ by assuming that neither the gyroscope bias nor the slope of the ground changed significantly between the two foot-flat phases. The resulting angles are denoted $\alpha(t), \beta(t)$ and calculated as follows:

$$\alpha(t) := \tilde{\alpha}(t) - \frac{t - t_{\mathrm{hr},j}}{t_{\mathrm{fc},j} - t_{\mathrm{hr},j}}(\tilde{\alpha}(t_{\mathrm{fc},j}) - \tilde{\alpha}(t_{\mathrm{hr},j})), \tag{3.43}$$

$$\beta(t) := \tilde{\beta}(t) - \frac{t - t_{\mathrm{hr},j}}{t_{\mathrm{fc},j} - t_{\mathrm{hr},j}}(\tilde{\beta}(t_{\mathrm{fc},j}) - \tilde{\beta}(t_{\mathrm{hr},j})). \tag{3.44}$$

3.2.3 Experimental Evaluation of Foot Pitch Angles

We now focus on the question how accurate the obtained orientation angles are with respect to the results of a conventional optical motion capture (OMC) method under different walking conditions. As before, our goal is not to carry out a detailed clinical study, but rather to provide a proof of concept that demonstrates the capability of the proposed method to provide reliable realtime foot orientation angles under different walking conditions.

In contrast to almost all IMU validation studies, we place the optical markers on anatomical landmarks instead of attaching them to the IMUs. Obviously, this means that additional deviations between the measurements of both systems might be caused by relative motions of the optical markers with respect to IMUs. We nevertheless choose this approach, since we want to answer the question how accurate the proposed method for foot orientation angle measurement is with respect to the conventional method and its standard protocol. This approach confers the decisive advantage that the entire gait analysis methods are compared instead of comparing only the measurement systems.

[12] For example, on level ground and with standard sensor hardware, we found that the angle $\tilde{\alpha}(t_{\mathrm{fc},j})$ at the end of each integration interval is typically in the range of 2°, whereas its true value is zero.

Figure 3.9: Experimental setup with IMUs and optical markers attached to shoes and bare feet. Note that the data of the IMUs that are attached to the shanks is not used in this study.

As a reference method, we choose the optical gait analysis protocol by Davis et al. [18], since it is widely accepted and used [8]. As the marker sets of all standard protocols, the optical marker set of the Davis protocol includes only two markers on the foot, i.e. one marker attached to the skin on the lateral malleolus and one marker attached to the skin on the head of the fifth metatarsal (see Figure 3.9). This implies that we can only determine the pitch angle of the foot, but not the roll angle, from the measured optical marker positions. Therefore, the current evaluation is limited to comparing foot pitch angles obtained by both measurement methods. However, please note that the IMU-based methods for foot pitch and foot roll angles are identical up to the coordinate axis around which the integration is carried out.

For evaluation of the proposed methods, we process the recorded data from trials of two different experiments, denoted the *shoe* and the *barefoot* experiment, in a simulated-online manner. In the barefoot experiment, two healthy subjects (one male, one female, both aged 30–40 and body-mass index 20–25) walked barefoot at slow and fast pace, whereas in the shoe experiment, two transfemoral amputees (both male, aged 40–50 and body-mass index 20–25) walked with a leg prosthesis at self-selected speed while wearing shoes on both the prosthetic and the contralateral foot.

In both trial series, optical markers of a visual motion capture system were attached to the foot as described above, and a wireless inertial sensor (MTw by Xsens, Enschede,

Netherlands) was attached dorsally on the instep of each foot. In the shoe experiment, the V612 system (Vicon Motion Systems Ltd., UK) was used to track the optical markers, while the Smart-DX system (BTS Bioengineering, New York, USA) was used in the barefoot experiment.

In both experiments, the subject walked through the observation volume of the optical system at least six times. For each of these trials, the foot pitch angle is computed according to (3.41) and (3.43). Likewise, we also calculate the foot pitch angle from the three-dimensional optical marker positions of each of these trials.

The root mean square error (RMSE) with and without drift correction is determined for each trial of each subject. We then calculate the average and standard deviations over all trials for each foot. Table 3.1 shows the results, as well as the corresponding walking velocities. In Figure 3.10a, the pitch angles of Subject 2 (cf. Table 3.1) are plotted over one stride for both the prosthetic and the contralateral side. Furthermore, pitch angles for different walking velocities of the barefoot walking Subject 3 are presented in Figure 3.10b.

	walking velocity $[\frac{m}{s}]$	RMSE $\tilde{\alpha}$ [°] (pure strapdown integr.)	RMSE α [°] (periodic drift compens.)
Subj.1-shoe	0.81	2.66 ± 0.73	2.24 ± 0.41
Subj.1-prosth.	0.81	1.40 ± 0.21	1.20 ± 0.26
Subj.2-shoe	1.42	5.78 ± 1.49	3.97 ± 0.51
Subj.2-prosth.	1.42	3.97 ± 1.31	2.93 ± 0.75
Subj.3-barefoot	1.62	3.61 ± 0.87	3.63 ± 0.83
Subj.3-barefoot	0.85	3.14 ± 0.39	3.09 ± 0.36
Subj.4-barefoot	1.52	3.90 ± 0.91	3.79 ± 0.73
Subj.4-barefoot	0.78	3.37 ± 0.37	3.41 ± 0.31

Table 3.1: Deviations between inertial and optical measurements. Columns show the walking velocity (vel.) as well as the root mean square error (RMSE), the average values (and standard deviations) of which are calculated over several strides. The rows refer to different subjects and their different footwear: barefoot, shoe and shoe on the prosthetic side (prosth.).

3.2.3.1 Discussion of the Results

We first analyze the influence of the footwear for slow walking, i.e. Subject 1 (with shoes) versus the slow walking trials (second lines in Table 3.1) of Subjects 3 and 4

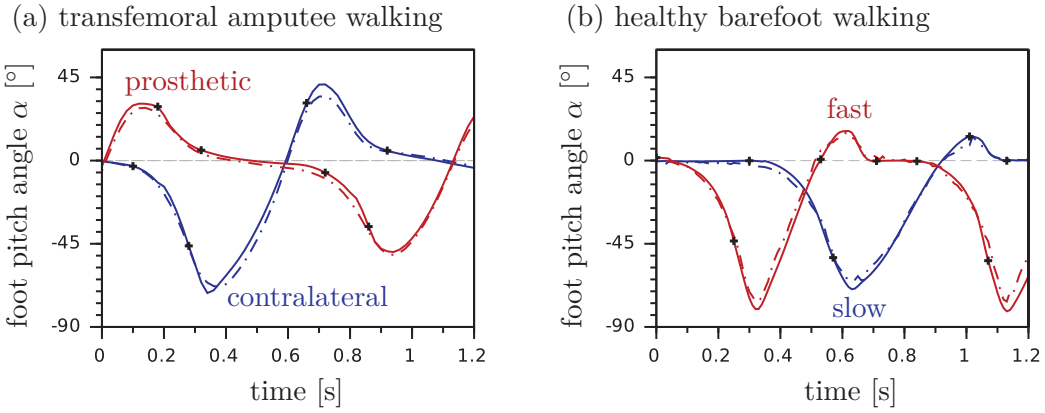

Figure 3.10: IMU-based foot pitch angles (solid) and reference angles (dashed) from an optical motion capture system, *(a)* for one walking trial of Subject 2 (both sides shown) and *(b)* for one slow and one fast walking trial of Subject 4 (only one side shown for each trial). For additional illustration, plus markers indicate the gait phase transitions detected by means of the algorithm developed in Section 3.1.

(barefoot). The deviations between the results of both measurement systems are larger in the barefoot trials than in the trials with shoes. This is probably due to the fact that the foot is not a rigid body. Deformations of the foot during stance-phase and push-off lead to relative motion of the IMU and the optical markers with respect to each other. Since the IMU was attached directly to the skin in the barefoot trials, the effect is stronger therein than in the shoe-trials, in which the shoe dampens this effect. However, the discussed difference is no longer present in the fast walking trials (i.e. in Subject 2 versus first lines of Subjects 3 and 4).

Figure 3.10a reveals the characteristics of the pitch angle for the prosthetic and the contralateral foot of Subject 2. The agreement between optical and inertial measurements is equally well on both sides. However, the data in Table 3.1 demonstrates that the deviations are slightly smaller on the prosthetic side, which might be due to the physical differences between the human foot and a prosthetic foot. Since the prosthetic foot is more rigid, it allows for less deformation and less relative motion of the markers and IMU with respect to each other.

Figure 3.10b presents the pitch angles of Subject 3 for two different walking velocities. If we compare RMSEs between the slow and fast trials of Subject 3 and 4, it is noticeable that the deviations are smaller in slower walking. The same observation is also made when comparing Subject 1 and Subject 2, the latter of which walked at a much faster

pace. It is a well-known fact that the accuracy of both measurement systems decreases for very fast motions. When the subject walks at about $1.5\,\mathrm{ms}^{-1}$, the foot travel almost twice as fast during swing phase and undergoes accelerations of multiple times the gravitational acceleration. Hence, inertia effects easily cause relative motion of the markers and the IMU with respect to each other and to the foot bones.

By applying the periodic online drift compensation proposed in (3.43), the RMSE is reduced by approximately 15–30% in the shoe-walkers. In the barefoot walkers, however, the RMSE remains in the range of 3–4° even when the compensation is applied. In order to find out how severe these deviations are in practice, we determine the stride-to-stride variance in foot orientation angle trajectories of healthy subjects. This natural variance is found to be typically in the range of 3–5° (standard deviation) for foot pitch angle trajectories, which is as large as the disagreement between both measurement systems in barefoot walkers and larger than the RMSE values achieved with periodic drift compensation in shoe walkers.

3.2.4 Conclusions

A method for realtime foot pitch and roll angle estimation was proposed that avoids magnetometers and copes with arbitrary sensor-to-segment mounting orientation. It is therefore well suited for feedback control of mobile gait support systems, in particular if the IMU is attached to the foot/shoe by the patients themselves.

The method was validated with respect to a conventional optical motion capture method in subjects walking at different velocities with different footwear. Results indicate that deformations of the foot and shoe lead to relative motion of the optical markers and the IMUs with respect to each other, which are strongest in barefoot walking and weakest in prosthetic feet. A more detailed study with a larger number of subjects is advisable if the latter aspect is found to be of great interest.

The deviations between inertial and optical measurements are in the range of 2–4° under all tested conditions, which is smaller than or in the range of the natural variance observed in human gait. With respect to the intended application in FES-based gait support systems and active orthoses, we conclude that these deviations are small enough to allow automatic correction of pathological foot motion via feedback control. In Chapter 6, we will validate this claim by developing an adaptive drop foot neuroprosthesis that controls the entire foot pitch and roll angle trajectories of the swing phase by automatic adjustments of FES parameters.

3.3 Joint Axis and Position Estimation

In the previous section, we have used inertial measurement units to measure the orientation of the midfoot, i.e. a single (almost) rigid body, with respect to a fixed coordinate frame. Beyond this, IMUs can also be used to analyze the motion of kinematic chains consisting of multiple (almost) rigid bodies connected by joints with certain degrees of freedom. To this end, each joint segment is typically equipped with one IMU, and the goal is to measure position and orientation of the links as well as one, two or three joint angles, in case of a hinge, saddle joint, or spheroidal joint, respectively. These motion parameters can be calculated from the measured accelerations and angular velocities by strapdown integration and some coordinate transformation from the sensor coordinate system to a joint-related coordinate system. For the latter, however, information is required about the (constant) mounting orientation and position of the sensors with respect to the segments they are mounted on, as illustrated in Figure 3.11.

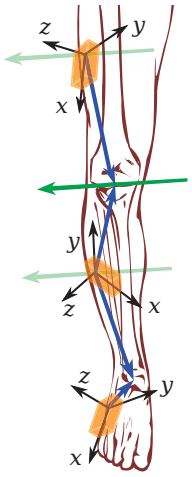

Figure 3.11: Arbitrary placement of inertial sensors on the human body. The coordinates of the joint axis direction (green arrows) and the joint position (blue arrows) in the local coordinate systems of the sensors (each labeled x-y-z) characterize the sensor-to-segment mounting.

In Section 3.3.1, we will review previously suggested approaches, which will lead us to the conclusion that there is high demand for methods that enable accurate estimation of sensor-to-segment mounting orientations and positions. We will then demonstrate how this information can be extracted from the measurement data of almost arbitrary movements by exploiting the kinematic constraints of the respective joints. In Sections 3.3.2 and 3.3.3, we will investigate how the rotational and translational restrictions of the joints become manifest in the angular velocities and accelerations of the sensor units.

A geometric model is introduced in order to provide a proof of concept via simulations of a kinematic chain in Section 3.3.5. Finally, in Section 3.3.6, we analyze experimental results based on inertial measurement data from a human gait analysis.

3.3.1 State of the Art in Joint Axis and Position Estimation

A fundamental problem in IMU-based human motion analysis is that the local coordinate axes of the IMUs are not aligned with any physiologically meaningful axes; see Figure 3.11 for an illustration. First, we shall note that in some publications this problem is ignored completely by assuming that the IMUs can be mounted precisely in a predefined orientation toward the joint; see for example Favre et al. [24], Liu et al. [49, 50]. As can also be seen in the figures therein, this is a rather rough approximation. In the more realistic and less restrictive case of arbitrary mounting orientation, it is required to identify the sensor-to-segment mounting orientation and position of the sensors attached to both ends of the joint. As illustrated in Figure 3.11, these mounting orientations and positions are characterized by the local coordinates of the joint axis and the joint position, respectively. Both quantities might be measured manually, but in three-dimensional space, this is a cumbersome task that yields low accuracy results, as demonstrated for example by Liu et al. [50].

Fortunately, at least for the axis direction vectors, alternatives exist. A common approach to estimate these vectors is via calibration postures and/or calibration movements. Some authors, e.g. Favre et al. [25] and Takeda et al. [114], make the subject stand with vertical, straight legs for a few seconds and use the acceleration measured during that time interval to determine the local coordinates of the longitudinal axis of the segment. Additional sitting calibration postures are used by Takeda et al. [114]. Besides static postures, predefined calibration motions can be used to identify the coordinates of physically meaningful axes in the upper and lower sensor coordinate system. Examples can be found in Figure 3.12 and in Favre et al. [25, 26], O'Donovan et al. [77]. Moreover, a combination of postures and motions might be used to identify the sensor-to-segment orientations, as for example in the Outwalk protocol [17, 27]. It employs pure flexion/extension motions and static poses to find the local coordinates of joint-related axes. Finally, the protocol used by Roetenberg et al. [93] solves a closed kinematic chain to refine joint axis and position coordinates that have been obtained from a combination of calibration postures, predefined motion and manual measurements of body dimensions. However, it is important to note that, both in calibration postures and calibration motions, the accuracy is limited by the precision with which the subject can perform the postures or motions. Therefore, we will propose a novel method for joint axis estimation from arbitrary motions in Section 3.3.2.

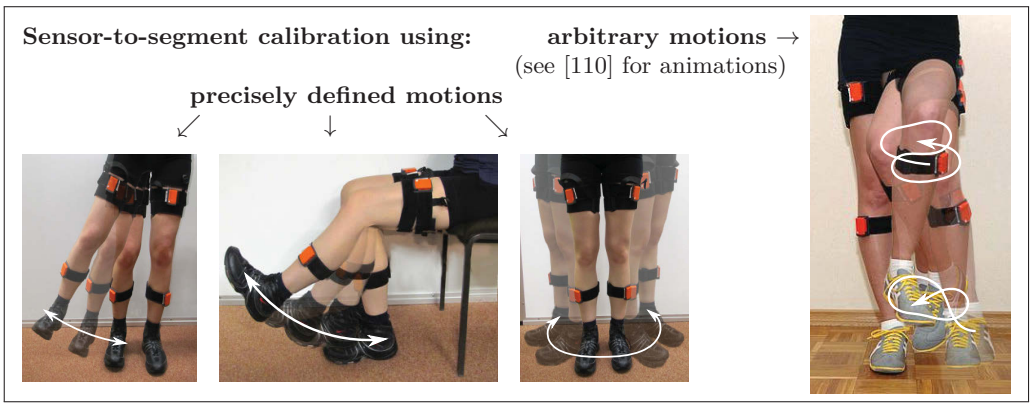

Figure 3.12: Examples for calibration motions that are used in the literature [17, 25, 27, 77, 93] to determine the coordinates of physiologically meaningful axes, e.g. the knee joint axis, in the local coordinate systems of the sensors. In such methods, the precision depends on how accurately the subject performs the motion. In contrast, we propose a method that uses arbitrary motions and identifies the sensor-to-segment mounting from the measurement data by exploiting kinematic constraints.

Besides the need of knowing the joint axis, some joint angle algorithms require additional knowledge of the joint position in local sensor coordinates; see for example Liu et al. [50], Luinge et al. [57], Roetenberg et al. [92]. Those methods can therefore only be used if reliable estimates of the local joint position coordinates are available. Besides, it has been demonstrated by Young [131] that joint position vectors can be used to improve the accuracy of body segment orientation estimates if the kinematic constraints of the joints are exploited. Vice versa, kinematic constraints have been used by Roetenberg *et al.* to estimate the joint positions based on accelerations and angular rates measured during motion, as briefly described in Roetenberg et al. [92]. The method is also mentioned as an optional part of the body segment orientation Kalman filter described in Luinge et al. [57]. In Section 3.3.3, we will propose an alternative method that exploits the same constraints but uses a nonlinear least-squares technique.

3.3.2 Constraints Induced by Hinge Joints

Consider two rigid segments that are free to rotate and move in space but are connected by a hinge joint, as depicted in Figure 3.13. The segments shall be called the first and the second segment, and each of them shall be equipped with a three-axial gyroscope that is attached to the segment in some unknown arbitrary orientation. The unit joint

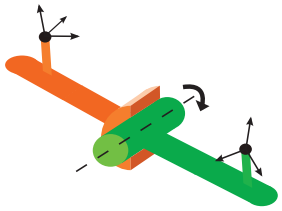

Figure 3.13: Two rigid segments that are connected by a hinge joint, each of them equipped with a three-axial gyroscope (represented by its local coordinate system). The orientations of the gyroscopes toward their segments are assumed to be, and in many application actually are, unknown.

axis vector with respect to the local coordinate system of the gyroscope attached to the first segment shall be referred to as $\mathbf{j}_1$; and $\mathbf{j}_2$ shall be the very same unit joint axis vector but in the coordinates of the local coordinate system of the gyroscope attached to the second segment. Moreover, let the angular velocities measured by the gyroscopes in the coordinates of their local frames be $\mathbf{g}_1(t)$ and $\mathbf{g}_2(t)$ for the first and the second segment, respectively. Then it is a geometrical fact that $\mathbf{g}_1(t)$ and $\mathbf{g}_2(t)$ differ only by the joint angle velocity and a (time-variant) rotation matrix. Hence, their projections into the joint plane[13] have the same lengths for each instant in time, which is mathematically equivalent to

$$||\mathbf{g}_1(t) \times \mathbf{j}_1||_2 - ||\mathbf{g}_2(t) \times \mathbf{j}_2||_2 = 0 \; \forall t, \tag{3.45}$$

where $||\cdot||_2$ denotes the Euclidean norm. This constraint holds for every moment in time regardless of where and in which orientation the sensors are mounted on the segments [103].

This fact turns out to be very useful when faced with the task of identifying the hinge joint axis in case the orientation of the sensors toward the segments is unknown. We can simply choose a large set of measured gyroscopic data from both sensors and search for the joint axis coordinates that fulfill (3.45) for all time instants in a least-squares sense. More precisely, we consider the joint axis candidates $\hat{\mathbf{j}}_1$ and $\hat{\mathbf{j}}_2$ in the spherical coordinates $\phi_1, \phi_2 \in [-\frac{\pi}{2}, \frac{\pi}{2}]$, $\theta_1, \theta_2 \in [0, 2\pi)$ with

$$\hat{\mathbf{j}}_1 = (\cos(\phi_1)\cos(\theta_1), \cos(\phi_1)\sin(\theta_1), \sin(\phi_1))^T, \tag{3.46}$$

$$\hat{\mathbf{j}}_2 = (\cos(\phi_2)\cos(\theta_2), \cos(\phi_2)\sin(\theta_2), \sin(\phi_2))^T, \tag{3.47}$$

[13] i.e. the plane to which the joint axis is the normal vector

where ϕ_i and θ_i are the inclination and azimuth, respectively, of $\hat{\mathbf{j}}_i$ in the i^{th} sensor coordinate system, $i = 1, 2$. In these reduced coordinates, we then define the sum of squared errors

$$\Psi(\phi_1, \phi_2, \theta_1, \theta_2) := \sum_{k=1}^{N} e_{\text{axis},k}^2 \tag{3.48}$$

$$\text{with} \quad e_{\text{axis},k} = ||\mathbf{g}_1(t_0 + kt_\text{s}) \times \hat{\mathbf{j}}_1||_2 - ||\mathbf{g}_2(t_0 + kt_\text{s}) \times \hat{\mathbf{j}}_2||_2. \tag{3.49}$$

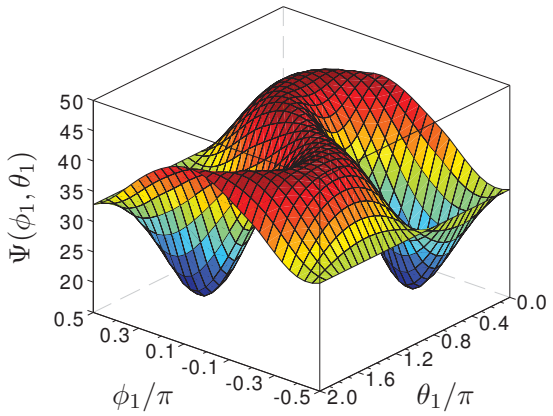

Figure 3.14: Sum of squares $\Psi(\phi_1, \phi_2, \theta_1, \theta_2)$ of the error in the kinematic constraint (3.45) plotted over the spherical coordinates of $\hat{\mathbf{j}}_1$ while keeping the spherical coordinates of $\hat{\mathbf{j}}_2$ at their true values. The two minima represent the true coordinates ($\mathbf{j}_1$ and $-\mathbf{j}_1$) of the joint axis in local coordinates of the first sensor.

Figure 3.14 depicts the typical form of this cost function. Since (3.45) is invariant with respect to the signs of $\mathbf{j}_1$ and $\mathbf{j}_2$, this cost function has four minima, which correspond to the four possible combinations of signs, $(\mathbf{j}_1, \mathbf{j}_2)$, $(-\mathbf{j}_1, \mathbf{j}_2)$, $(\mathbf{j}_1, -\mathbf{j}_2)$ and $(-\mathbf{j}_1, -\mathbf{j}_2)$. By minimizing $\Psi(\phi_1, \phi_2, \theta_1, \theta_2)$ over its arguments, we can identify these true joint axis coordinates.

Whether the proposed least-squares approach yields the true joint axis coordinates depends on the motion that is performed while the gyroscopic data is recorded. If the joint angle remained constant, i.e. if the links were rigidly connected, then $\mathbf{g}_1(t) = \mathbf{R}\,\mathbf{g}_2(t)$ would hold at all times, where $\mathbf{R}$ is the (unknown) constant rotation matrix from the second to the first sensor frame. Therefore, (3.45) would hold for any combination $(\mathbf{j}_1, \mathbf{j}_2)$, $\mathbf{j}_1 = \mathbf{R}\,\mathbf{j}_2$, no matter what movement the two rigidly connected links perform.

This leads to the conclusion that motions during which the joint angle remains constant are not suitable for joint axis identification.

Instead, the motion of the segment should be such that the kinematic constraint of the joint axis becomes manifest in the measured angular rates. Further investigations reveal that it takes as little as moving the first segment while the second is fixed, and then vice versa, to assure that the cost function (3.48) exhibits the depicted clear minima that correspond to the true local axis coordinates $\pm\mathbf{j}_1$ and $\pm\mathbf{j}_2$.

3.3.2.1 Matching Signs of the Joint Axis Coordinates

Solving the least-squares problem defined above yields two estimates $\hat{\mathbf{j}}_1$ and $\hat{\mathbf{j}}_2$ of the local joint axis coordinates that are approximately equal to the true coordinates $\pm\mathbf{j}_1$ and $\pm\mathbf{j}_2$ with one of the four combinations of signs. Whether the signs of the obtained estimates match is important for many further calculations. For example, only if $\hat{\mathbf{j}}_1$ and $\hat{\mathbf{j}}_2$ point to the same direction, then calculating the integral of $(\hat{\mathbf{j}}_1 \cdot \mathbf{g}_1(t) - \hat{\mathbf{j}}_2 \cdot \mathbf{g}_2(t))$ over time yields an estimate of the hinge joint angle that is very precise up to slow drift[14]. Therefore, it is important to determine two estimates $\hat{\mathbf{j}}_1$ and $\hat{\mathbf{j}}_2$ the signs of which match, i.e. which point to the same direction.

In practice, this can easily be achieved by a quick look at the *approximate* mounting orientations of the sensors. An example is given in Figure 3.11, where the z-axes of both sensors point roughly laterally[15], which implies that the z-coordinates of $\mathbf{j}_1$ and $\mathbf{j}_2$ have the same sign. If instead, to give another example, the local y-axis of the first sensor points roughly medially, while the local z-axis of the second sensor points roughly laterally, then the y-coordinate of $\mathbf{j}_1$ and the z-coordinate of $\mathbf{j}_2$ have opposite signs.

In case the mounting of the sensors cannot be observed at all, the correct pairing of the signs can also be determined from the inertial data itself. As a first step, we choose a period of time from the identification data during which the angular velocities around the joint axis are negligible, i.e. $\mathbf{g}_1(t) \cdot \hat{\mathbf{j}}_1 \approx 0, \mathbf{g}_2(t) \cdot \hat{\mathbf{j}}_2 \approx 0$. Next, we define an arbitrary pair of joint plane axes $\mathbf{x}_i, \mathbf{y}_i \in \mathbb{R}^3, i = 1, 2$, for each local frame

$$\mathbf{x}_1 = \hat{\mathbf{j}}_1 \times \mathbf{c}, \quad \mathbf{y}_1 = \hat{\mathbf{j}}_1 \times \mathbf{x}_1, \quad \mathbf{x}_2 = \hat{\mathbf{j}}_2 \times \mathbf{c}, \quad \mathbf{y}_2 = \hat{\mathbf{j}}_2 \times \mathbf{x}_2, \tag{3.50}$$

[14] We will consider the task of joint angle estimation in further detail in Section 3.4.

[15] More precisely, the coordinate axes point into the lateral half space, which is an easy observation; we do *not restrict* the mounting orientation in any way.

where $\mathbf{c} \in \mathbb{R}^3$ is any arbitrary vector that fulfills $\mathbf{c} \nparallel \mathbf{j}_1, \mathbf{c} \nparallel \mathbf{j}_2$. We then use these coordinate axes to project, for each sample, the angular velocities into the joint plane:

$$\mathbf{g}_{i,\mathrm{proj}}(t) = \begin{bmatrix} \mathbf{g}_i(t) \cdot \mathbf{x}_i \\ \mathbf{g}_i(t) \cdot \mathbf{y}_i \end{bmatrix} \in \mathbb{R}^2, \; i = 1, 2. \tag{3.51}$$

If we plot these projections versus the joint plane coordinates for both sensors, as in Figure 3.15, then we find that they have the same length for each sample, which is in fact the fundamental idea behind the kinematic constraint (3.45). Moreover, the traces of the projected angular rates reveal the correct sign pairing for the joint axis estimates $\hat{\mathbf{j}}_1$ and $\hat{\mathbf{j}}_2$ that were used to calculate them. The traces are congruent (up to some rotation around the origin) if the signs of $\hat{\mathbf{j}}_1$ and $\hat{\mathbf{j}}_2$ match, and they are (rotated) mirror images of each other if the signs do not match.

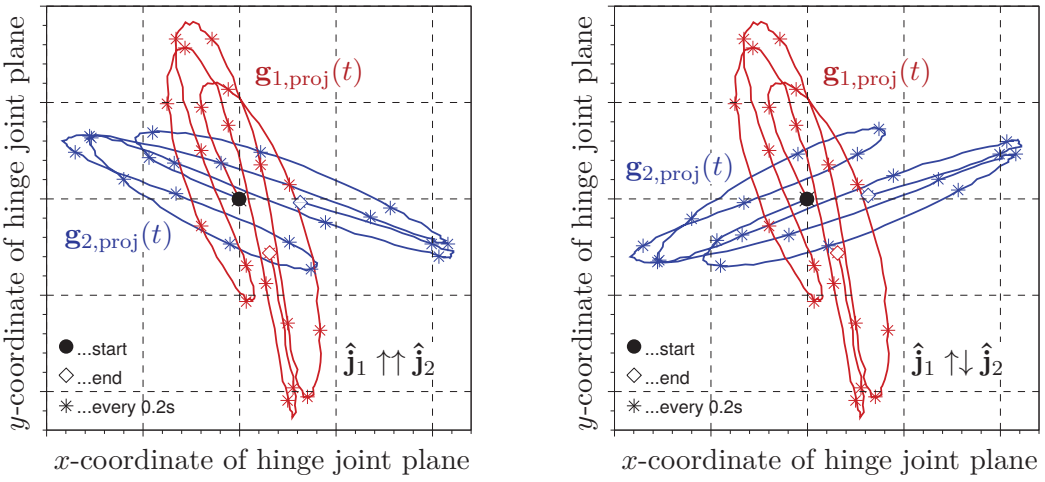

Figure 3.15: Projection of the measured angular rates of both sensors into the joint plane (defined by the coordinates in (3.50)) for a motion with little flexion/extension. In both plots, the projections have the same length at each moment in time, cf. (3.45). However, when the joint axis signs match, the two curves are congruent up to some rotation around the origin (*left*), while they are mirror images of each other in the case of opposite signs (*right*).

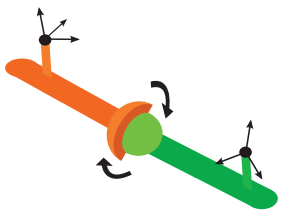

Figure 3.16: Two rigid segments that are connected by a spheroidal joint, each of them equipped with an inertial measurement unit consisting of a three-axial gyroscope and a three-axial accelerometer (represented by their common local coordinate system). Both the exact locations of the IMUs and their orientations toward their segments are assumed to be, and in many applications actually are, unknown.

3.3.3 Constraints Induced by Spheroidal Joints

Now we consider two links connected by a spheroidal joint, as depicted in Figure 3.16. Since this joint has three degrees of freedom, there is no general relation between the measured angular velocities of the first and the second sensor. In order to exploit the kinematic constraints, we need to incorporate the accelerometer readings. Let the accelerations of the sensors be $\mathbf{a}_1(t)$ and $\mathbf{a}_2(t)$ for the first and the second segment, respectively. Define $\mathbf{o}_1$ and $\mathbf{o}_2$ as the joint position vectors pointing from the origin of the first and the second sensor frame, respectively, to the joint center[16]. Then the kinematic equations of rotating rigid bodies (see e.g. [38, Section 2.7]) lead to the constraint:

$$||\mathbf{a}_1(t) - \boldsymbol{\Gamma}(\mathbf{g}_1(t)\,,\,\mathbf{o}_1)||_2 - ||\mathbf{a}_2(t) - \boldsymbol{\Gamma}(\mathbf{g}_2(t)\,,\,\mathbf{o}_2)||_2 = 0\ \forall t, \tag{3.52}$$

$$\boldsymbol{\Gamma}(\mathbf{g}_i(t)\,,\,\mathbf{o}_i) := \mathbf{g}_i(t) \times \mathbf{o}_i \times \mathbf{g}_i(t) + \mathbf{o}_i \times \frac{d\mathbf{g}_i(t)}{dt},\ i = 1, 2,$$

where the time derivative $\frac{d\mathbf{g}_i(t)}{dt}$ of the angular rates can be calculated, for example, using (3.14). The term $\boldsymbol{\Gamma}(\mathbf{g}_i(t)\,,\,\mathbf{o}_i)$ defined above represents the (radial and tangential) acceleration component that is due to rotation around the joint center. Consequently, $(\mathbf{a}_1(t) - \boldsymbol{\Gamma}(\mathbf{g}_1(t)\,,\,\mathbf{o}_1))$ yields the acceleration of the joint center in the coordinates of the first local frame, which must be equal to $(\mathbf{a}_2(t) - \boldsymbol{\Gamma}(\mathbf{g}_2(t)\,,\,\mathbf{o}_2))$ up to multiplication by some (time-variant) rotation matrix. Hence, the constraint (3.52) holds for each instant in time and can be used to estimate $\mathbf{o}_1$ and $\mathbf{o}_2$ from a large number of measured data sets containing accelerometer and gyroscope readings.

[16] Note that, just as before, the subscripts 1 and 2 indicate that the vectors are defined in the coordinates of the first and second local frame, respectively.

As discussed before, it is required that the motion performed during data recording is rich enough to make the kinematic constraint become manifest in the measurement data. Note, for example, that if we restrict the relative motion of both segments to only one plane, then we basically have a hinge joint instead of a spheroidal joint, and (3.52) is true for all points along the (virtual) hinge joint axis. This, as well as the feasibility of the estimation itself, will be validated by simulation in Section 3.3.5. Prior to this, we briefly discuss one specific implementation of the proposed methods for joint axis and position estimation.

3.3.4 Algorithm Implementation

Assume that N data sets, precisely $\{\mathbf{g}_1(t_k), \mathbf{g}_2(t_k)\}_{k=1}^{N}, N \gg 4$, were measured. By restricting the joint axis estimates to unit length, the estimation problem becomes four-dimensional. Hence, we denote the estimates of the joint axis vectors by $\hat{\mathbf{j}}_1$ and $\hat{\mathbf{j}}_2$ and use the parameterization by spherical coordinates from Section 3.3.2:

$$\boldsymbol{\xi}_{\text{axis}} := [\phi_1, \theta_1, \phi_2, \theta_2]^T, \tag{3.53}$$

$$\begin{aligned} \hat{\mathbf{j}}_1 &= [\cos(\phi_1)\cos(\theta_1), \cos(\phi_1)\sin(\theta_1), \sin(\phi_1)]^T, \\ \hat{\mathbf{j}}_2 &= [\cos(\phi_2)\cos(\theta_2), \cos(\phi_2)\sin(\theta_2), \sin(\phi_2)]^T. \end{aligned} \tag{3.54}$$

In order to find the coordinates $\boldsymbol{\xi}_{\text{axis}}$ that minimize the sum of squares $\Psi(\boldsymbol{\xi}_{\text{axis}})$ defined in (3.48), we will consider one specific implementation that solves this nonlinear least-squares problem by means of a Gauss-Newton algorithm [28]. To this end, the following gradients of the left-hand side terms of (3.45) with respect to $\mathbf{j}_1$ and $\mathbf{j}_2$ are derived:

$$\frac{d(||\mathbf{g}_i(t) \times \mathbf{j}_i||_2)}{d\mathbf{j}_i} = \frac{(\mathbf{g}_i(t) \times \mathbf{j}_i \times \mathbf{g}_i(t))^T}{||\mathbf{g}_i(t) \times \mathbf{j}_i||_2} \in \mathbb{R}^{1\times 3}, \quad i = 1, 2. \tag{3.55}$$

Note furthermore that the derivatives $(d\mathbf{j}_i / d\boldsymbol{\xi}_{\text{axis}}), i = 1, 2$, are easily derived from (3.54). This allows us to calculate the Jacobian matrix

$$\mathbf{J}_{\text{axis}} := \frac{d\mathbf{e}_{\text{axis}}}{d\boldsymbol{\xi}_{\text{axis}}} \in \mathbb{R}^{N\times 4} \tag{3.56}$$

of the error vector $\mathbf{e}_{\text{axis}} \in \mathbb{R}^{N\times 1}$, the k^{th} entry of which is denoted $e_{\text{axis},k}$ and defined in (3.49). The k^{th} row of the Jacobian $\mathbf{J}_{\text{axis}}$ is

$$\frac{de_{\text{axis},k}}{d\boldsymbol{\xi}_{\text{axis}}} = \frac{(\mathbf{g}_1(t) \times \mathbf{j}_1 \times \mathbf{g}_1(t))^T}{||\mathbf{g}_1(t) \times \mathbf{j}_1||_2} \frac{d\mathbf{j}_1}{d\boldsymbol{\xi}_{\text{axis}}} - \frac{(\mathbf{g}_2(t) \times \mathbf{j}_2 \times \mathbf{g}_2(t))^T}{||\mathbf{g}_2(t) \times \mathbf{j}_2||_2} \frac{d\mathbf{j}_2}{d\boldsymbol{\xi}_{\text{axis}}} \in \mathbb{R}^{1\times 4}. \tag{3.57}$$

The Gauss-Newton algorithm is then implemented as follows. At first, random initial values for $\boldsymbol{\xi}_{\text{axis}}$ are generated. Then the following update loop is executed repeatedly:

1. Use (3.54) to calculate $\hat{\mathbf{j}}_1$ and $\hat{\mathbf{j}}_2$ from $\boldsymbol{\xi}_{\text{axis}}$.
2. Calculate the error vector $\mathbf{e}_{\text{axis}} \in \mathbb{R}^{N\times 1}$ and the Jacobian $\mathbf{J}_{\text{axis}}$.
3. Update $\boldsymbol{\xi}_{\text{axis}}$ by $\boldsymbol{\xi}_{\text{axis}} - (\mathbf{J}_{\text{axis}}^T\mathbf{J}_{\text{axis}})^{-1}\mathbf{J}_{\text{axis}}^T\,\mathbf{e}_{\text{axis}}$ and repeat from 1.

A similar update scheme is applied for the estimation of the local joint position coordinates, but there we need data sets $\{\mathbf{g}_1(t_k), \mathbf{g}_2(t_k), \mathbf{a}_1(t_k), \mathbf{a}_2(t_k)\}_{k=1}^N, N \gg 6$, that contain also accelerometer readings. Furthermore, the optimization variable is the concatenation of the estimated joint position vectors

$$\boldsymbol{\xi}_{\text{pos}} = \begin{bmatrix}\hat{\mathbf{o}}_1\\ \hat{\mathbf{o}}_2\end{bmatrix} \in \mathbb{R}^6. \tag{3.58}$$

The entries of the error vector $\mathbf{e}_{\text{pos}} \in \mathbb{R}^{N\times 1}$ are then defined by

$$e_{\text{pos,k}} := ||\mathbf{a}_1(t_k) - \boldsymbol{\Gamma}(\mathbf{g}_1(t_k)\,,\,\hat{\mathbf{o}}_1)||_2 - ||\mathbf{a}_2(t_k) - \boldsymbol{\Gamma}(\mathbf{g}_2(t_k)\,,\,\hat{\mathbf{o}}_2)||_2. \tag{3.59}$$

In order to determine the Jacobian matrix

$$\mathbf{J}_{\text{pos}} := \frac{d\mathbf{e}_{\text{pos}}}{d\boldsymbol{\xi}_{\text{pos}}} \in \mathbb{R}^{N\times 6}, \tag{3.60}$$

we consider the following gradients of the left-hand side terms of (3.52), for $i = 1, 2$,

$$\frac{d\Big(||\mathbf{a}_i(t) - \boldsymbol{\Gamma}(\mathbf{g}_i(t)\,,\,\mathbf{o}_i)||_2\Big)}{d\mathbf{o}_i} = \frac{\Big(\mathbf{a}_i(t) - \boldsymbol{\Gamma}(\mathbf{g}_i(t)\,,\,\mathbf{o}_i)\Big)^T}{||\mathbf{a}_i(t) - \boldsymbol{\Gamma}(\mathbf{g}_i(t)\,,\,\mathbf{o}_i)||_2}\,\frac{d\Big(\mathbf{a}_i(t) - \boldsymbol{\Gamma}(\mathbf{g}_i(t)\,,\,\mathbf{o}_i)\Big)}{d\mathbf{o}_i}. \tag{3.61}$$

Note that any vector product can be written as a matrix multiplication, and denote the matrix-multiplication representation of the vector product $(\mathbf{a}\times\cdot)$ of any vector $\mathbf{a} \in \mathbb{R}^{3\times 1}$ by the skew-symmetric matrix $\mathbf{M}_{\mathbf{a}\times} \in \mathbb{R}^{3\times 3}$, i.e.

$$\mathbf{a}\times\mathbf{b} = \mathbf{M}_{\mathbf{a}\times}\mathbf{b} = -\mathbf{M}_{\mathbf{a}\times}^T\mathbf{b}\;\forall\mathbf{b} \in \mathbb{R}^{3\times 1}. \tag{3.62}$$

With this definition, we can rewrite $\mathbf{\Gamma}(\mathbf{g}_i(t)\,,\,\mathbf{o}_i)$ in the following steps[17]

$$\mathbf{g}_i(t) \times \mathbf{o}_i = \mathbf{M}_{\mathbf{g}_i(t)\times}\mathbf{o}_i\,, \tag{3.63}$$
$$\mathbf{g}_i(t) \times \mathbf{o}_i \times \mathbf{g}_i(t) = -\mathbf{M}^2_{\mathbf{g}_i(t)\times}\mathbf{o}_i\,, \tag{3.64}$$
$$\mathbf{o}_i \times \frac{d\mathbf{g}_i(t)}{dt} = -\mathbf{M}_{\dot{\mathbf{g}}_i(t)\times}\mathbf{o}_i\,, \tag{3.65}$$
$$\mathbf{\Gamma}(\mathbf{g}_i(t)\,,\,\mathbf{o}_i) = (-\mathbf{M}^2_{\mathbf{g}_i(t)\times} - \mathbf{M}_{\dot{\mathbf{g}}_i(t)\times})\,\mathbf{o}_i\,. \tag{3.66}$$

This allows us to simplify the gradients (3.61) as follows:

$$\begin{aligned}\frac{d\Big(||\mathbf{a}_i(t) - \mathbf{\Gamma}(\mathbf{g}_i(t)\,,\,\mathbf{o}_i)||_2\Big)}{d\mathbf{o}_i} &= \frac{\Big(\mathbf{a}_i(t) - \mathbf{\Gamma}(\mathbf{g}_i(t)\,,\,\mathbf{o}_i)\Big)^T}{||\mathbf{a}_i(t) - \mathbf{\Gamma}(\mathbf{g}_i(t)\,,\,\mathbf{o}_i)||_2}\,(\mathbf{M}^2_{\mathbf{g}_i(t)\times} + \mathbf{M}_{\dot{\mathbf{g}}_i(t)\times}) \\ &= \left(\Big(\mathbf{M}^2_{\mathbf{g}_i(t)\times} + \mathbf{M}_{\dot{\mathbf{g}}_i(t)\times}\Big)^T \frac{\mathbf{a}_i(t) - \mathbf{\Gamma}(\mathbf{g}_i(t)\,,\,\mathbf{o}_i)}{||\mathbf{a}_i(t) - \mathbf{\Gamma}(\mathbf{g}_i(t)\,,\,\mathbf{o}_i)||_2}\right)^T \\ &= \left(\Big(\mathbf{M}^2_{\mathbf{g}_i(t)\times} - \mathbf{M}_{\dot{\mathbf{g}}_i(t)\times}\Big) \frac{\mathbf{a}_i(t) - \mathbf{\Gamma}(\mathbf{g}_i(t)\,,\,\mathbf{o}_i)}{||\mathbf{a}_i(t) - \mathbf{\Gamma}(\mathbf{g}_i(t)\,,\,\mathbf{o}_i)||_2}\right)^T,\end{aligned} \tag{3.67}$$

where the fact that $\mathbf{M}^2_{\mathbf{g}_i(t)\times}$ is a symmetric matrix is exploited. Using (3.66), we finally rewrite the gradients in the compact form

$$\frac{d\Big(||\mathbf{a}_i(t) - \mathbf{\Gamma}(\mathbf{g}_i(t)\,,\,\mathbf{o}_i)||_2\Big)}{d\mathbf{o}_i} = \left(\frac{-\mathbf{\Gamma}\Big(-\mathbf{g}_i(t)\,,\,\mathbf{a}_i(t) - \mathbf{\Gamma}(\mathbf{g}_i(t)\,,\,\mathbf{o}_i)\Big)}{||\mathbf{a}_i(t) - \mathbf{\Gamma}(\mathbf{g}_i(t)\,,\,\mathbf{o}_i)||_2}\right)^T, \tag{3.68}$$

which allows us to write the k^{th} row of the Jacobian $\mathbf{J}_{\text{pos}}$ as follows:

$$\frac{de_{\text{pos},k}}{d\boldsymbol{\xi}_{\text{pos}}} = \left[\begin{array}{c} -\dfrac{\mathbf{\Gamma}\Big(-\mathbf{g}_1(t)\,,\,\mathbf{a}_1(t) - \mathbf{\Gamma}(\mathbf{g}_1(t)\,,\,\mathbf{o}_1)\Big)}{||\mathbf{a}_1(t) - \mathbf{\Gamma}(\mathbf{g}_1(t)\,,\,\mathbf{o}_1)||_2} \\ \dfrac{\mathbf{\Gamma}\Big(-\mathbf{g}_2(t)\,,\,\mathbf{a}_2(t) - \mathbf{\Gamma}(\mathbf{g}_2(t)\,,\,\mathbf{o}_2)\Big)}{||\mathbf{a}_2(t) - \mathbf{\Gamma}(\mathbf{g}_2(t)\,,\,\mathbf{o}_2)||_2} \end{array}\right]^T. \tag{3.69}$$

With this analytic expression for the Jacobian, it is straight forward to employ a Gauss-Newton algorithm as the one described above for the joint axis identification.

The proposed implementations are rather simple in comparison to many more elaborate methods one might want to employ instead. This simple approach, however, will prove to yield good results in Section 3.3.6. One of the advantages of the proposed method

[17] Note that, for any $\mathbf{a}, \mathbf{b} \in \mathbb{R}^{3\times 1}$, we have $\mathbf{a} \times \mathbf{b} = -\mathbf{b} \times \mathbf{a}$ and $(\mathbf{a} \times \mathbf{b}) \times \mathbf{a} = \mathbf{a} \times (\mathbf{b} \times \mathbf{a})$.

lies in its simple numerics. The matrix that needs to be inverted in the calculation of the pseudoinverse is of dimension 4×4 in the joint axis identification and of dimension 6×6 in the joint position identification.

Besides using other optimization techniques, one might consider several modifications of the cost function. To give an example, in the kinematic constraint equations (3.45), (3.52) of both estimation algorithms, one might as well divide the difference of the two norms by the sum of both norms, and thereby use a relative error instead. However, in the presence of measurement errors we prefer to give more weight to the data sets that yield large norms. Hence we use the absolute errors, as defined above.

Furthermore, please note that the derived methods do *not* require high sample rates. For normal-speed motions, recording data at a sample rate as low as 10 Hz will yield equally good results (at less computational load) as recording at 100 Hz, since data sets with almost the same angular velocities and accelerations hardly contribute to the estimation. This holds the advantage that the proposed algorithms are suitable for large IMU networks with considerably low sample rates.

Finally, we shall briefly discuss a straight-forward extension of the above (batch-like) optimization toward an online implementation: One might start applying the given update procedure as soon as a reasonable number of measured data sets, typically about ten, is available and then repeat the loop (steps 1–3) whenever a new data set is added, for example every 0.1 s. Then the order of the least-squares problem N increases gradually, and every updated estimate serves as a (very good) initial condition to the next larger least-squares problem. Depending on the computational power, one might choose individually for each data processing hardware, how many data sets are added before the loop is repeated, and how many times it is repeated before the next data sets are added. If the implementation is such that the oldest data set is removed from the memory whenever a new data set is added, then the sensor-to-segment orientation and position of the IMUs can be tracked even if the sensor mountings (body straps) are not rigid (firm) enough to prevent slow slipping and shifting of the IMUs with respect to the segments.

3.3.5 Simulation Results Using a Three-Segments Model

A kinematic simulation model of a leg is developed, which consists of three segments (representing thigh, shank and foot) connected by a hinge joint and a spheroidal joint (representing knee and ankle), see Figure 3.17. Each simulated inertial measurement unit is rigidly connected to the respective segment. Prior to each simulation run, the

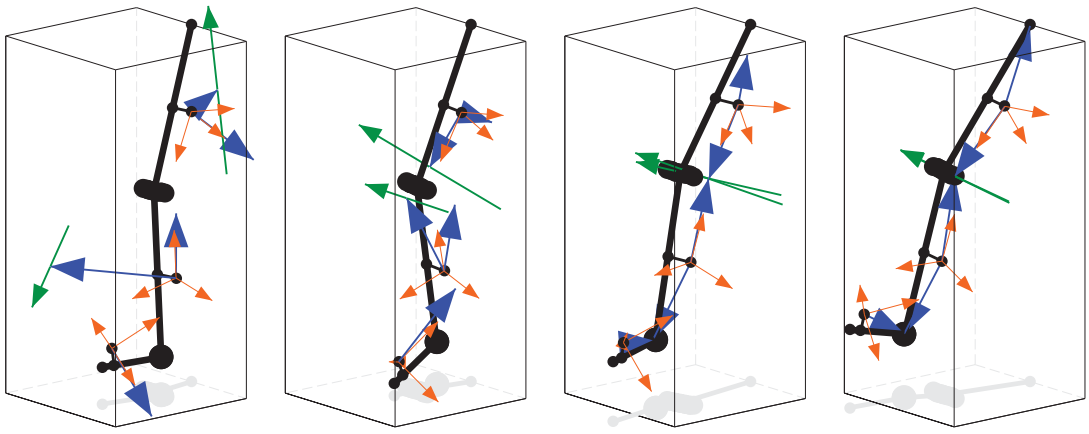

Figure 3.17: Simulation of a kinematic chain comprised of three segments connected by a hinge joint (indicated by cylinder) and a spheroidal joint (indicated by sphere). Each simulated IMU (orange axis triplets) is rigidly connected to its segment (black beams) with randomly chosen mounting orientation and position. The local joint axis coordinates (green axis pair) and the local coordinates of both joints (blue vector pairs) are estimated starting from random initial values. In a few seconds of leg and foot circling (and about ten Gauss-Newton steps), the estimates converge to the true values. See [110] for a video animation.

positions and orientations of the sensor coordinate systems are chosen randomly from reasonable intervals. The true joint axis and joint position vectors, in the coordinates of the respective sensor frames, is calculated and stored for comparison with the estimates. Subsequently, the segments perform a user-defined motion including arbitrary translation and rotation within the bounds of the kinematic constraints. Based on an adjustable sample rate, the accelerations and angular velocities of the sensors are computed in the coordinates of their local frames. A user-defined amount of measurement noise is added, and the data is then provided to the estimation algorithms.

Both the joint axis estimation algorithm and the joint position estimation algorithm are implemented as described in Section 3.3.4. The former is employed to determine the knee joint axis from the simulated measurement data of the thigh and the shank sensor, while the latter is employed to determine the ankle joint position from the simulated measurement data of the shank and the foot sensor. Both algorithms are tested for various motions, sample rates and noise amplitudes, both online and offline. It is found that two to three periods of (simultaneous) small-amplitude oscillations in the direction

of each degree of freedom already yield enough data for an accurate estimation. Moreover, even for a few hundred randomly chosen initial conditions, the estimates always converge to the close proximity of the true values within five to ten iterations, see for example Figure 3.17. At a signal-to-noise ratio of 100, the estimated joint axes and the true axis confine angles of less than 1°, while the joint position estimates differ from the true values by less than 3%.

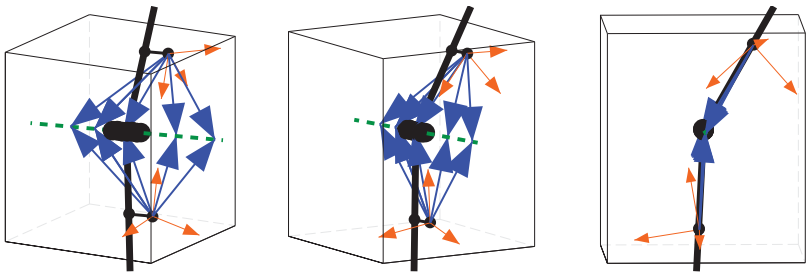

Figure 3.18: Different viewing angles of several joint position estimation results on a simulated hinge joint. Each execution of the joint position estimation yields a pair of local coordinates that describe a point on the joint axis.

As a final step, we apply the joint position estimation to the measurement data of the thigh and shank sensor. We find that almost every run converges to a different pair of joint position vectors, but each pair describes a point that happens to lie on the hinge joint axis, as illustrated in Figure 3.18. Therefore, we use the estimated joint axis coordinates $\hat{\mathbf{j}}_1, \hat{\mathbf{j}}_2$ to shift the obtained joint position coordinates $\hat{\mathbf{o}}_1, \hat{\mathbf{o}}_2$ along the joint axis as close as possible to the sensors:

$$\hat{\mathbf{o}}_{1,\text{proj}} = \hat{\mathbf{o}}_1 - \hat{\mathbf{j}}_1 \frac{\hat{\mathbf{o}}_1 \cdot \hat{\mathbf{j}}_1 + \hat{\mathbf{o}}_2 \cdot \hat{\mathbf{j}}_2}{2}, \tag{3.70}$$

$$\hat{\mathbf{o}}_{2,\text{proj}} = \hat{\mathbf{o}}_2 - \hat{\mathbf{j}}_2 \frac{\hat{\mathbf{o}}_1 \cdot \hat{\mathbf{j}}_1 + \hat{\mathbf{o}}_2 \cdot \hat{\mathbf{j}}_2}{2}. \tag{3.71}$$

In other words, the point that is described by $\hat{\mathbf{o}}_1, \hat{\mathbf{o}}_2$ is projected into the plane that is perpendicular to the joint axis and has equal distance to the origins of both sensor coordinate systems. In Figure 3.17, these projected local joint position coordinates are illustrated by the two blue vectors pointing from the thigh and shank sensor coordinate systems to the middle of the green knee joint axis vectors.

3.3.6 Experimental Results

For the sake of experimental validation of the proposed estimation algorithms, we apply them to measurement data from an IMU-based gait analysis trial. Wireless inertial sensors (MTw by Xsens, Enschede, Netherlands) are attached to the right thigh, shank and foot using elastic straps. The true position and orientation of the local sensor frames with respect to the ankle and knee are roughly[18] determined using a combination of manual measurements and calibration movements, as in Liu et al. [50] and O'Donovan et al. [77], respectively. Subsequently, the subject performs leg and foot circling for about five seconds and then walks about thirty meters at average speed. The accelerometer and gyroscope readings are recorded and provided to the algorithms developed above at a sample rate of 40 Hz.

One hundred algorithm runs are performed using random initial values and different subsets[19] of the available data to analyze both convergence and variance of the estimates. Results are presented in Figure 3.19. In all runs, both the knee joint axis and the ankle joint position are identified correctly within less than twenty Gauss-Newton steps. However, the error vector norms do not entirely converge to zero and the final estimates vary by about ± 0.01 (in the units of the plots, respectively). This is not surprising, since the sensor-to-leg connections are not very rigid, and since the knee and ankle are not exactly a hinge and a spheroidal joint. But, as demonstrated, the least-squares approach copes with these inaccuracies and still yields precise estimates. Obviously, yet higher accuracy and less variance is expected in more rigid setups such as robotic manipulators.

3.3.7 Conclusions and Future Research

We developed least-squares methods for the estimation of local joint axis and position coordinates from 6D inertial measurement data. Explicit analytic expressions of the required Jacobians have been provided as well as an example for algorithm implementation and a number of optional modifications. The drawback of potential misalignment of the axis estimates has been addressed, and two simple practical solutions have been suggested.

Unlike other methods for sensor-to-segment calibration, the developed method does *not* require precise calibration poses or motions. The sensor units can be attached in ar-

[18] i.e. up to the limitations in accuracy that are inherent to these methods, cf. semicircles in Figure 3.19
[19] Note, however, that all subsets include data from both the circling and the walking phase.

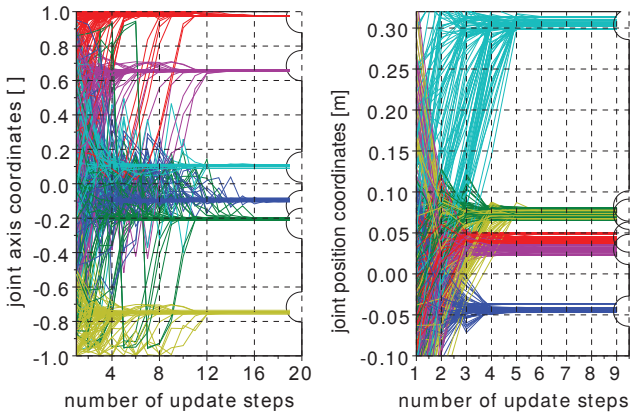

Figure 3.19: Joint axis and position estimation from IMU-based gait analysis data. For one hundred random initial values and with different subsets of the available data stream under consideration, the estimates always converge to the true values (marked by semicircles) within less than twenty iterations. The final values show little variance despite the flexibilities in the mechanical setup.

bitrary position and orientation, and the calibration can be carried out automatically as the subject starts to move the respective limbs arbitrarily. The algorithm neither requires high sample rates nor integration of measurement data. We demonstrated that, regardless of the choice of initial estimates, convergence to the true joint axis and position coordinates is obtained both in simulation and experiment. In less rigid setups, e.g. when skin motion artifacts occur in human motion analysis, it identifies the major axis of motion (and the average joint position) thanks to the least-squares approach.

The obtained joint axis and position coordinates can be used in human motion analysis to transform the sensor readings into joint-related coordinate systems, to calculate joint angles, or to apply bias-eliminating techniques as in Young [131]. Further fields of application include robotic manipulators, linked vehicles, or any other mechanical setup in which rigid bodies are connected by joints.

3.4 Flexion/Extension Joint Angle Measurement

Despite many recent advances, current IMU-based joint angle measurement methods still require restrictive setup procedures as well as an environment with a homogeneous magnetic field. In this section, we derive a set of new, practical methods for realtime measurement of flexion/extension joint angles of the human knee and ankle during walking. We start by discussing a few challenges of human motion analysis and the state of the art in knee joint angle estimation in Sections 3.4.2 and 3.4.1, respectively. Subsequently, in Section 3.4.3, we develop methods that use only gyroscopes and accelerometers and, therefore, do not rely on a homogeneous magnetic field. The algorithms are derived and discussed for the human knee joint, since it is an approximate hinge joint. Beyond this, it is demonstrated in Section 3.4.4 how the proposed methods can be employed for flexion/extension angle measurement on the ankle joint, which exhibits two degrees of freedom but performs mainly flexion/extension during walking. Finally, in Section 3.4.5, we analyze results from gait trials of a transfemoral amputee in which the novel IMU-based methods are compared to a conventional optical 3D motion capture system.

3.4.1 Robotic Hinge Joint *vs.* Human Knee

To motivate the need for more practical methods, we briefly highlight some of the major challenges of IMU-based human joint angle measurement. Although many of the following statements are true in more general cases, we will focus our arguments on hinge joints, i.e. joints with one rotational degree of freedom. It has been demonstrated in many publications, e.g. Cheng et al. [15] and the references therein, that inertial measurement data can be used to calculate hinge joint angles when at least one IMU is attached to each side of the joint. In most robotic and mechanical applications, the sensors can be mounted in such a way that one of the local coordinate axes coincides with the hinge joint axis; see for example Cheng et al. [15], Moreno et al. [67]. In that case, the hinge joint angle can be calculated by integrating the difference of both angular rates around the corresponding coordinate axis. Since even the most precise calibration will yield a non-zero bias, this calculated angle will be subject to drift. However, multiple techniques have been suggested to eliminate this effect using additional information from the accelerometers or the magnetometers, see e.g. Cheng et al. [15].

Similarly, inertial measurement units can be used to calculate hinge joint angles on the human body, for example on the knee joint[20]. However, there is a very important difference between the human leg and most robotic setups: It is very difficult to attach

[20] we will discuss the fact that the human knee is not a perfect hinge joint in Sections 3.4.2 and 3.4.4

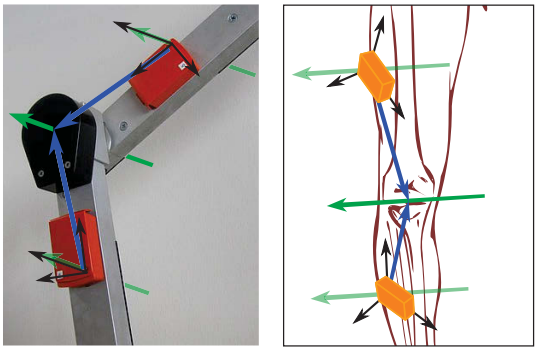

Figure 3.20: While most robotic actuators (*left*) consist of rigid joints and segments with even, orthogonal surfaces, the human leg (*right*) exhibits none of these properties. Black axis triplets indicate the local coordinate systems of the attached inertial measurement units. Green and blue arrows indicate the (local) joint axis and position coordinates, respectively.

IMUs to the leg in such a way that one of the local coordinate axes coincides exactly with the knee joint axis, as illustrated in Figure 3.20. There have been some attempts (see e.g. Favre et al. [24], Liu et al. [50]), but since the human body lacks even surfaces and right angles, the accuracy of such approaches is limited. In contrast, the body straps that are commonly used to attach IMUs to the leg yield an almost arbitrary orientation of the IMU toward its segment. Nevertheless, the hinge joint angle can be calculated from the inertial measurement data. However, the data from both sensor units must first be transformed into joint-related coordinate systems, i.e. coordinate systems in which one or two axes coincide with the joint axis and/or the longitudinal axis of the segment [129]. This is a major challenge in IMU-based joint angle measurement, not only on hinge-type joints. How these challenges have been faced in previous contributions, is discussed in the following section.

3.4.2 State of the Art in IMU-Based Knee Joint Angle Estimation

Many algorithms and techniques have been suggested for IMU-based knee joint angle estimation. Despite the variety of approaches, the vast majority of authors agree that the flexion/extension angle of the knee joint is the angle between the upper and lower leg along the main axis of relative motion, i.e. the knee joint axis [16, 25, 50, 114]. In other words, the projections of the upper and lower leg into the joint plane, to which the joint axis is normal, confine this angle; see Figure 3.21. However, we shall note that consid-

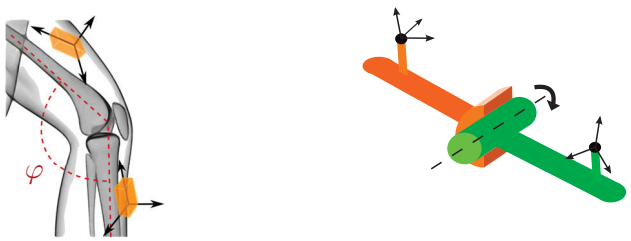

Figure 3.21: Placement of inertial sensors on the human body and definition of the joint angle (*left*). Kinematic model of a hinge joint with local sensor coordinate systems attached to both ends (*right*). The local sensor coordinate axes are not aligned with the physiological axes and planes by which the joint angle φ is defined.

ering the knee as a hinge joint is an approximation. Although flexion/extension is the major degree of freedom, a biological joint, such as the knee, is not perfectly constrained to rotation around one axis. This is often addressed by additionally considering abduction/adduction and internal/external rotation, which leads to a three-dimensional knee joint angle, as in Brennan et al. [10] and Favre et al. [24, 25]. However, abduction/adduction and internal/external rotation angles hardly ever exceed a range of $\pm 10°$ [25, 86] and are strongly affected by soft-tissue artifacts [89, 113]. Therefore, these additional degrees of freedom are often neglected and only flexion/extension is considered, see for example Cooper et al. [16], Cutti et al. [17], Ferrari et al. [27], Liu et al. [50], Takeda et al. [114].

As mentioned before, the simplest approaches in the literature assume that the IMUs are attached such that one of the local coordinate axes is aligned with the joint axis. Integrating the difference of the angular rates of the upper and lower sensor around that axis will yield a drifting flexion/extension angle. Favre et al. [24] removed this drift using a high-pass filter. In another publication with the same mounting assumption, it was demonstrated that the joint angle can also be estimated from the measured accelerations if the position of the joint in both local coordinate systems is known [50]. Thereby, a root mean square error (RMSE) of less than 4° with respect to an optical reference system was achieved. Although both techniques may seem restricted to a special sensor mounting, they are just as helpful in the case of arbitrary mounting orientation, as long as the local joint axis coordinates are known.

A fundamentally different approach is employed by Takeda et al. [114]. After identifying the local coordinates of the longitudinal axes of the shank and thigh, the authors calculate the inclination of both segments and approximate the flexion/extension angle by the difference of these inclinations. Thereby, they achieve an RMSE of approximately

7° with respect to an optical reference system. However, their method is bound to the assumption that the knee axis remains horizontal during the entire motion. While that might be an acceptable approximation for most walking and running situations, this assumption does not hold during quick direction changes and for a number of other motions, like skating, hurdles or martial arts. Cooper et al. [16] have enhanced the aforementioned method. Instead of assuming a horizontal knee axis, the authors model the knee as a pure hinge joint and exploit its kinematic constraints using an extended Kalman filter. Thereby, they are able to calculate flexion/extension angles in good accordance with an optical reference system, both at the speed of running (8 km/h, RMSE $< 4°$) and walking (3 km/h, RMSE $< 1°$). Approximately the same precision for walking is achieved by Favre et al. [25]. Here, however, the complete orientation of each IMU with respect to a global reference coordinate system is calculated using a fusion algorithm that combines gyroscope and accelerometer readings. Similarly, the algorithm used by Roetenberg et al. [92] and Luinge et al. [57] estimates sensor orientations from accelerations and angular rates. Van den Noort et al. [120] achieved an RMSE below 4° by combining that algorithm with the Outwalk protocol mentioned in Section 3.3.1. Finally, a mean error (RMSE not available) below 2° was reported for the proprietary algorithm used by Zhang et al. [132]. While it employs calibration poses and optional calibration motions to identify sensor-to-segment orientations (and, thus, the joint axis coordinates), the algorithm uses a biomechanical model and kinematic constraints to overcome integration drift [93].

It is important to note that almost all of the mentioned RMS errors were obtained with the reference system markers being rigidly attached (usually in clusters on rectangular or L-shaped cardboard or plastic tiles) to the inertial sensors in order to eliminate the effect of soft tissue and skin motion artifacts on the measured joint angle difference [92, 132]. The only exception from this statement is the work by Takeda et al. [114]. They placed optical markers on anatomical landmarks, as it is common practice in optical gait analysis. Consequently, they obtain a clearly larger RMS error than those authors who connected the reference markers to the IMUs (about 7° as opposed to about 2–3°). This means that most previous contributions only compare the measurement accuracy of the optical and the inertial system, instead of comparing the results of an optical gait analysis to those of an inertial gait analysis. The latter aspect has received too little attention in previous publications. Therefore, we will place optical reference markers on anatomical landmarks during the experiments in Section 3.4.5, although this might increase the observed error.

Which of the reviewed methods is most suitable for a specific application depends also on the available sensor information. In many of the mentioned publications, the orientations of the thigh and shank are used to calculate the flexion/extension angle [16, 25, 27, 114]. This is straight forward if reliable sensor orientation estimates are available and if the

local joint axis coordinates are known. However, knowing the joint axis allows one to reduce the problem to one dimension immediately. Therefore, especially if reliable orientation estimates are not immediately available, it might be advantageous to use one of the methods by Liu et al. [50] or Favre et al. [24] instead, or to combine them in a new way. We will examine both approaches in Sections 3.4.3 and 3.4.5.

3.4.3 New Methods for IMU-Based Joint Angle Measurement

As explained in Section 3.3, handling arbitrary sensor-to-segment mounting is a major challenge in gait analysis with inertial sensors. Manual measurements, as well as calibration poses and movements, are commonly suggested solutions. Furthermore, we discussed that the use of magnetometers is typically limited by the assumption of a homogeneous magnetic field. In this section, we describe a set of methods for IMU-based joint angle estimation that allow us to face these two challenges in a new way. We will combine elements of the methods reviewed above, but unlike most previous attempts, we will:

- avoid sensor-to-segment mounting assumptions,
- require no manual measurements of any distances, joint coordinates or similar,
- not rely on the accuracy with which the subject performs predefined postures or movements,
- and avoid the use of magnetometers.

Instead of employing any of these commonly used assumptions and restrictions, we make use of the fact that the knee joint behaves approximately like a mechanical hinge joint. In Section 3.3, the kinematic constraints that result from this fact were exploited to obtain the position vector and the direction vector of the knee flexion/extension axis in the local coordinates of both sensors. As mentioned before, this information is crucial to precise joint angle calculation. We will use it to fill the gap between the sensor coordinate systems and the joint-related coordinate systems in which the angles are defined. This will allow us to calculate flexion/extension joint angles on joints with a major axis of motion, for example the knee and the ankle during walking. First, we will propose a combination of the methods from Section 3.3 and a standard literature approach for 9D IMUs. Then, we will introduce a method that uses only angular rates and accelerations, while the use of magnetometer readings is completely avoided.

Before we describe the respective algorithms, let us define the available measurement signals. Assume that two inertial sensors, one attached to the upper leg and the other

attached to the lower leg, measure the accelerations $\mathbf{a}_1(t), \mathbf{a}_2(t) \in \mathbb{R}^3$ and angular rates $\mathbf{g}_1(t), \mathbf{g}_2(t) \in \mathbb{R}^3$ at some sample period t_s. Additionally, we assume that the time derivatives $\frac{d\mathbf{g}_1}{dt}(t), \frac{d\mathbf{g}_2}{dt}(t) \in \mathbb{R}^3$ of the angular rates are determined, for example via the third order approximation (3.14).

We assume that the local joint axis coordinates $\mathbf{j}_1, \mathbf{j}_2$ and the local joint position coordinates $\mathbf{o}_1, \mathbf{o}_2$ have been successfully identified using the methods described in Section 3.3. As explained before, this is crucial for IMU-based joint angle measurement. The identified values of $\mathbf{j}_1, \mathbf{j}_2$ and $\mathbf{o}_1, \mathbf{o}_2$ are now used to calculate the flexion/extension angle of an anatomical joint with one major degree of freedom. While we consider a knee joint to explain the methods, we extend them to the more general case of saddle and spheroidal joints in Section 3.4.4.

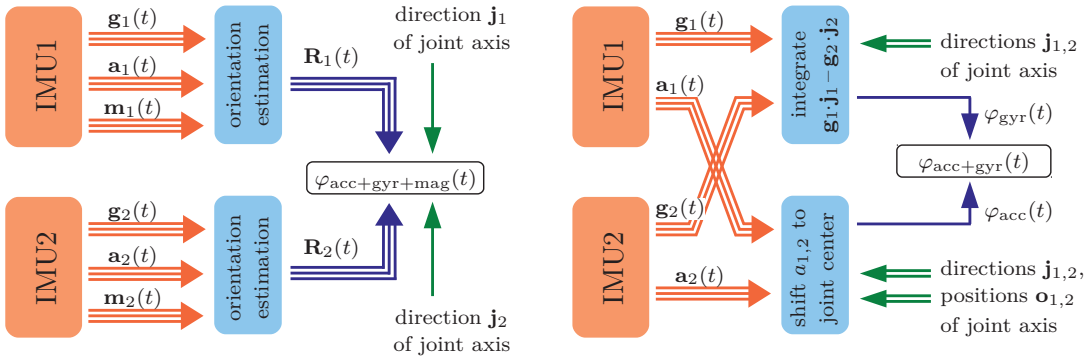

Figure 3.22: Two algorithms for IMU-based knee joint angle calculation are considered. *Left:* Sensor orientation estimates are used to calculate the orientational difference (i.e. the joint angle) around a given axis. *Right:* The problem is reduced to one dimension immediately by integrating the difference of the angular rates around the joint axis. An acceleration-based joint angle estimate is used to remove drift via sensor fusion.

Figure 3.22 shows the main ideas of the two methods for joint angle measurement that we will describe. The first method assumes that each IMU provides highly accurate estimates of its orientation with respect to a common fixed reference coordinate system. Together with the local joint axis coordinates, these orientations directly yield an accurate flexion/extension angle. This approach is well known from the literature, see for example Favre et al. [25], Takeda et al. [114], Van den Noort et al. [120]. The second and novel method reduces the problem to the joint plane from the very start by integrating both angular rates only around the joint axis, which yields a slowly drifting, but otherwise highly accurate joint angle [108]. This angle is combined in a sensor fusion with a noisy, but driftless, joint angle estimate that is calculated from the measured acceler-

ations. At this point, the second method also uses the joint position vectors. Finally, and most importantly, the second method does not rely on magnetometer readings. It calculates the joint angle only from the measured accelerations and angular rates.

3.4.3.1 Joint Angle from Sensor Orientation Estimates

Some inertial sensors are equipped with on-board orientation estimation, which is usually based on a sensor fusion of the acceleration, angular rate and magnetic field vector measurements. The resulting estimates describe the orientation of the sensors with respect to a fixed reference coordinate system, in terms of either quaternions, rotation matrices, or Euler angles. Recall from Section 3.4.2 that it is an established method to use sensor orientation estimates for the calculation of joint angles; see for example Favre et al. [25], Takeda et al. [114], Van den Noort et al. [120]. In the following, we assume that the orientation of both sensors with respect to a common fixed reference frame (i.e. the reference frame must be identical for each sensor) are given by rotation matrices, which we denote by $\mathbf{R}_1(t)$ and $\mathbf{R}_2(t)$. They shall be defined, such that they transform a locally measured vector into the reference frame, i.e. the following holds:

$$\mathbf{R}_1(t)\mathbf{j}_1 = \mathbf{R}_2(t)\mathbf{j}_2 \; \forall t. \tag{3.72}$$

Under these circumstances, the flexion/extension angle $\varphi_{\text{acc+gyr+mag}}(t)$ can simply be computed as:

$$\varphi_{\text{acc+gyr+mag}}(t) = \sphericalangle_{3D}\left(\mathbf{R}_1(t)(\mathbf{j}_1 \times \mathbf{c}), \mathbf{R}_2(t)(\mathbf{j}_2 \times \mathbf{c})\right), \quad \mathbf{c} \nparallel \mathbf{j}_1, \mathbf{c} \nparallel \mathbf{j}_2\,, \tag{3.73}$$

where $\sphericalangle_{3D}(\,)$ denotes the (signed) angle between two vectors in $\mathbb{R}^3$ and $\mathbf{c} \in \mathbb{R}^3$ can be any vector that makes none of the vector products zero (for example, $\mathbf{c} = [1, 0, 0]^T$ can be used, unless $\mathbf{j}_1$ or $\mathbf{j}_2$ happens to be exactly $[\pm 1, 0, 0]^T$). It is important to note that, by construction, this joint angle can only be as precise as the employed sensor orientation estimates, and it might be drifting if the orientation estimates are drifting.

3.4.3.2 Joint Angle from Accelerometer and Gyroscope Readings

In the following, we will compute the flexion/extension angle only from accelerations and angular rates. A gyroscope-based flexion/extension angle can be calculated by

integrating the difference of the angular rates around the joint axis, i.e.

$$\varphi_{\mathrm{gyr}}(t) = \int_0^t (\mathbf{g}_1(\tau) \cdot \mathbf{j}_1 - \mathbf{g}_2(\tau) \cdot \mathbf{j}_2)\, d\tau\,. \tag{3.74}$$

Furthermore, with the knowledge of the joint axis coordinates, it is straight forward to develop more practical versions of many of the restrictive methods from the literature reviewed above, which require the sensor axes to coincide with joint axes or segment axes. In particular, we can extend the approach used by Liu et al. [50] to three-dimensional space. We shift the measured accelerations onto the joint axis by applying:

$$\tilde{\mathbf{a}}_1(t) = \mathbf{a}_1(t) - \boldsymbol{\Gamma}(\mathbf{g}_1(t)\,,\, \mathbf{o}_1), \quad \tilde{\mathbf{a}}_2(t) = \mathbf{a}_2(t) - \boldsymbol{\Gamma}(\mathbf{g}_2(t)\,,\, \mathbf{o}_2)\,, \tag{3.75}$$

with $\boldsymbol{\Gamma}(\mathbf{g}_i(t)\,,\, \mathbf{o}_i), i = 1, 2$, being defined in (3.52). As explained in Section 3.3.3, $\tilde{\mathbf{a}}_1(t)$ and $\tilde{\mathbf{a}}_2(t)$ are the same quantity measured in two different local coordinate systems, which rotate with respect to each other around one axis. Therefore, the flexion/extension angle can be approximated[21] by the angle between the projections of $\tilde{\mathbf{a}}_1(t)$ and $\tilde{\mathbf{a}}_2(t)$ into the joint plane. Consequently, we use the pairs of joint plane axes $\mathbf{x}_1, \mathbf{y}_1, \mathbf{x}_2, \mathbf{y}_2 \in \mathbb{R}^3$ defined in Section 3.3.2.1 to calculate the accelerometer-based joint angle by:

$$\varphi_{acc}(t) = \sphericalangle_{2d} \left(\begin{bmatrix} \tilde{\mathbf{a}}_1(t) \cdot \mathbf{x}_1 \\ \tilde{\mathbf{a}}_1(t) \cdot \mathbf{y}_1 \end{bmatrix}, \begin{bmatrix} \tilde{\mathbf{a}}_2(t) \cdot \mathbf{x}_2 \\ \tilde{\mathbf{a}}_2(t) \cdot \mathbf{y}_2 \end{bmatrix} \right), \tag{3.76}$$

where $\sphericalangle_{2d}(\,)$ denotes the (signed) angle between two vectors in $\mathbb{R}^2$. The resulting angle $\varphi_{acc}(t)$ is not affected by drift, since we did not employ any integration to calculate it.

We shall note that the above equations are sensitive to measurement errors if the shifted accelerations $\tilde{a}_{1/2}(t)$ are almost collinear with the joint axes $\mathbf{j}_{1/2}$. However, in almost every practical situation, the gravitational acceleration dominates the acceleration signals $\mathbf{a}_1(t), \mathbf{a}_2(t)$ and $\tilde{\mathbf{a}}_1(t), \tilde{\mathbf{a}}_2(t)$. Therefore, the effect should only be significant when the knee axis is close to vertical or during the periods in which the knee is strongly accelerated in the medial or lateral direction. Both situations are rare in walking and most other motions of sports or daily activities. Please also note that $\boldsymbol{\Gamma}(\mathbf{g}_{1/2}(t)\,,\, \mathbf{o}_{1/2})$ in (3.75) is typically small compared to gravitational acceleration and therefore sensitivity to inaccuracies in $\mathbf{o}_1, \mathbf{o}_2$ is low. Especially in slow and normal-speed walking, the proposed method is expected to yield almost the same accuracy when using $\mathbf{o}_1 = \mathbf{o}_2 = [0, 0, 0]^T$.

Figure 3.23 shows the typical course of the two angle estimates $\varphi_{\mathrm{gyr}}(t)$ and $\varphi_{\mathrm{acc}}(t)$ that we derived in this subsection. The gyroscope-based angle is very precise on short time

[21] With ideal measurements, the two angles would be identical, but due to measurement inaccuracies, it is rather an approximation.

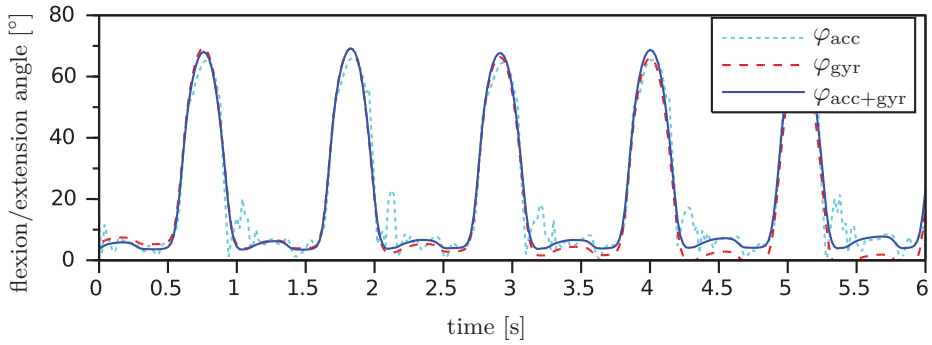

Figure 3.23: Sensor fusion of the gyroscope-based and the accelerometer-based knee joint angle of a leg prosthesis. The noisy but driftless angle $\varphi_{\mathrm{acc}}(t)$ is combined with the drifting but (apart from that) very precise angle $\varphi_{\mathrm{gyr}}(t)$ using the complementary filter (3.77). The resulting angle $\varphi_{\mathrm{acc+gyr}}(t)$ is accurate on small and on large time scales.

scales, but exhibits some slow drift[22] of about 1.5°/s. The accelerometer-based angle does not drift, but it is affected by the accelerometer noise and seems to be less reliable in moments of large acceleration changes. Therefore, it is advantageous to combine both angles using a standard tool of sensor fusion, for example a complementary filter [130] or a Kalman filter. The result shall be denoted by $\varphi_{\mathrm{acc+gyr}}(t)$. A simple implementation example of a complementary filter is given by

$$\varphi_{\mathrm{acc+gyr}}(t) = \lambda\,\varphi_{\mathrm{acc}}(t) + (1-\lambda)\,(\varphi_{\mathrm{acc+gyr}}(t-t_{\mathrm{s}}) + \varphi_{\mathrm{gyr}}(t) - \varphi_{\mathrm{gyr}}(t-t_{\mathrm{s}}))\ , \qquad (3.77)$$

where $\lambda \in [0,1]$ is an adjustable filter weight. Figure 3.23 presents the result of the sensor fusion for $\lambda = 0.01$ and a sample period $t_{\mathrm{s}} = 0.02\,\mathrm{s}$. As demonstrated, the combined angle $\varphi_{\mathrm{acc+gyr}}(t)$ does not follow the spikes of the acceleration-based angle and also does not exhibit the drift of the gyroscope-based angle. In Section 3.4.5, we will examine how accurate this IMU-based flexion/extension angle measurement is with respect to an optical reference measurement system. Prior to this, we briefly discuss the applicability of the developed methods to joints with more than one rotational degree of freedom.

3.4.4 Applicability of the Methods to Saddle and Spheroidal Joints

The methods that were introduced in the preceding subsection assume that two segments are connected by a joint with one rotational degree of freedom. As mentioned before, the

[22] Please note that the drift depends on the bias of the gyroscopes.

human knee is not exactly such a hinge joint, since it admits some rotation in the frontal and the transversal plane of up to about 8° [86]. These motions are even stronger when saddle or spheroidal joints, for example the ankle or the hip, are considered. Therefore, we briefly discuss the influence of these additional motions on the methods proposed above. The joint axis estimation, which exploits the kinematic constraint (3.45) of a hinge joint, can as well be employed on saddle and spheroidal joints. In such cases, the method will always identify the main axis of motion, i.e. the axis that minimizes the error norm defined in Section 3.3.4. This means that motion in other directions (i.e. degrees of freedoms of the joint) may occur, but the motion should be primarily around one (dominant) axis of the joint. In Section 3.4.5, we will demonstrate that, in the case of the ankle joint, data from normal walking is sufficient to identify the approximate plantarflexion/dorsiflexion[23] axis.

Beyond this, note that small additional rotations in the other dimensions do not affect any of the geometrical arguments used in the algorithms above. Therefore, these algorithms can be employed for flexion/extension angle measurement on real saddle or spheroidal joints, for example the hip or the ankle. In Section 3.4.5, we will examine how accurately these methods work on the plantar/dorsiflexion of ankle joints.

3.4.5 Experimental Evaluation of Joint Angle Estimation

The two methods that were introduced in Section 3.4.3 are now evaluated in repeated gait experiments with a transfemoral amputee (age 40–45, height 180–185 cm, weight 80–85 kg, K-level 4, i.e. the highest level of the Amputee Mobility Predictor). The subject is wearing a leg prosthesis and has given informed consent to the investigations. Reflective markers are placed on the subject's body segments at corresponding physiological landmarks; see Figure 3.24. The 3D positions of these markers are recorded at 120 Hz by an optical motion tracking system with ten cameras (V612 by Vicon Motion Systems Ltd., UK). Furthermore, we use elastic body straps to equip the upper leg, the lower leg and the foot of both the prosthesis and the contralateral leg with one inertial measurement unit (MTw by Xsens, Enschede, Netherlands) each, as depicted in Figure 3.24. At a measurement rate of 60 Hz, these six inertial sensors provide 3D accelerations and angular rates in their local coordinates, as well as estimates of sensor orientations with respect to a common global reference frame. We neither restrict the mounting of the IMUs to certain locations or orientations, nor do we measure these quantities. Instead, the subject is instructed to perform a combined circling motion of the upper and lower leg with a few arbitrary changes in direction and amplitude (see

[23] i.e. the mediolateral axis of the ankle joint that admits pitch motions of the foot with respect to the shank

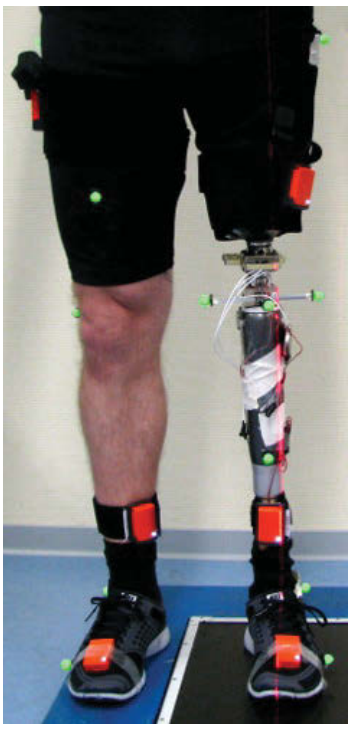

Figure 3.24: Placement of inertial measurement units and optical markers on the legs of a transfemoral amputee. The optical markers are placed at the typical physiological landmarks. The inertial measurement units are attached using body straps, without restricting their position or orientation.

Figure 3.12 and [110] for illustration). This motion is executed for about ten seconds on both sides.

The methods from Section 3.3 are used to estimate the direction and position vectors of the knee joint axis on both sides from the recorded inertial data. Then the subject walks repeatedly about ten meters at self-selected speed on a straight line within the range of an optical gait analysis system and far away from potential magnetic disturbances. The data that is gathered during one of these walking trials is used to identify the direction and position vectors of the ankle plantar/dorsiflexion joint axis on both sides. From the measurement data gathered during the following trials, we calculate the knee flexion/extension angles and the ankle plantar/dorsiflexion angle of both legs using both of the methods from Section 3.4.3.

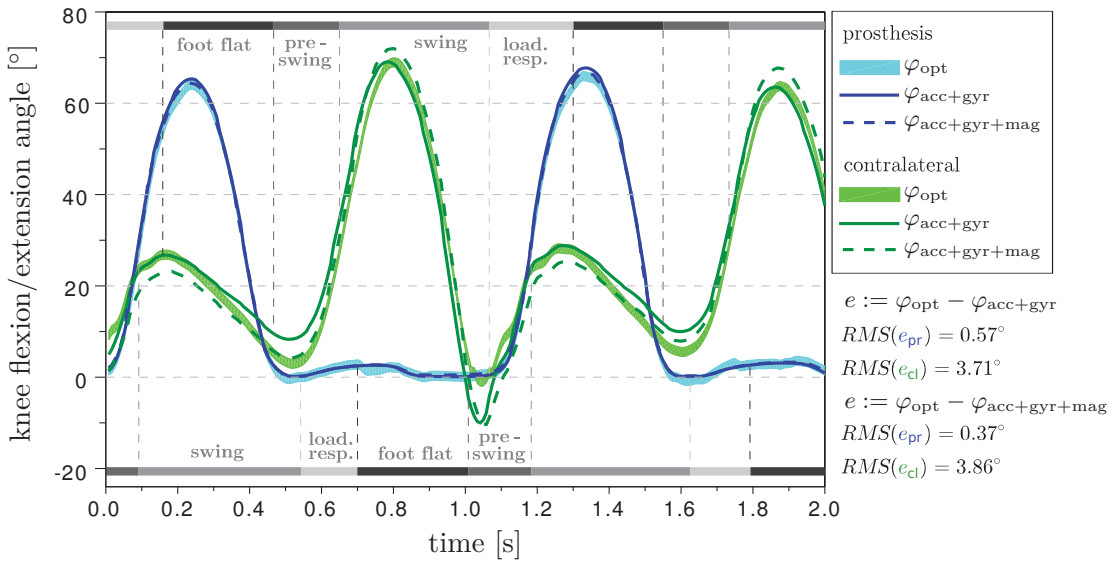

Figure 3.25: Comparison of the two IMU-based knee flexion/extension angle measurements ($\varphi_{acc+gyr+mag}(t)$ and $\varphi_{acc+gyr}(t)$) with the result of an optical gait analysis system ($\varphi_{opt}(t)$). On the prosthesis side, there is no significant deviation (RMS below 0.6°). However, on the contralateral side, skin and muscle motion effects, which are strongest during pre-swing and heel-strike, lead to RMS deviations of almost 4°.

The resulting ankle and knee joint angle traces of two different trials are provided in Figures 3.25 and 3.26. The qualitative difference between the angle trajectories of the prosthesis and the biological leg is considerable, but this aspect is outside the focus of this dissertation and, therefore, shall not be discussed here. For additional orientation, gait phase transitions are indicated, which were detected based on inertial measurement data from the foot sensor using an offline version of the algorithm described in Section 3.1.

With respect to the optical system, both IMU-based methods achieve a root-mean-square deviation of less than 0.6° on the prosthesis side and less than 4° on the contralateral side. The deviations of a larger set of trials are summarized in Table 3.2. In all of them, both IMU-based approaches yield similar values, although they use the inertial data in completely different ways.

Quantifying soft tissue motion artifacts: It is important to note that the errors on the biological leg are about four times larger than on the prosthesis. One might suppose

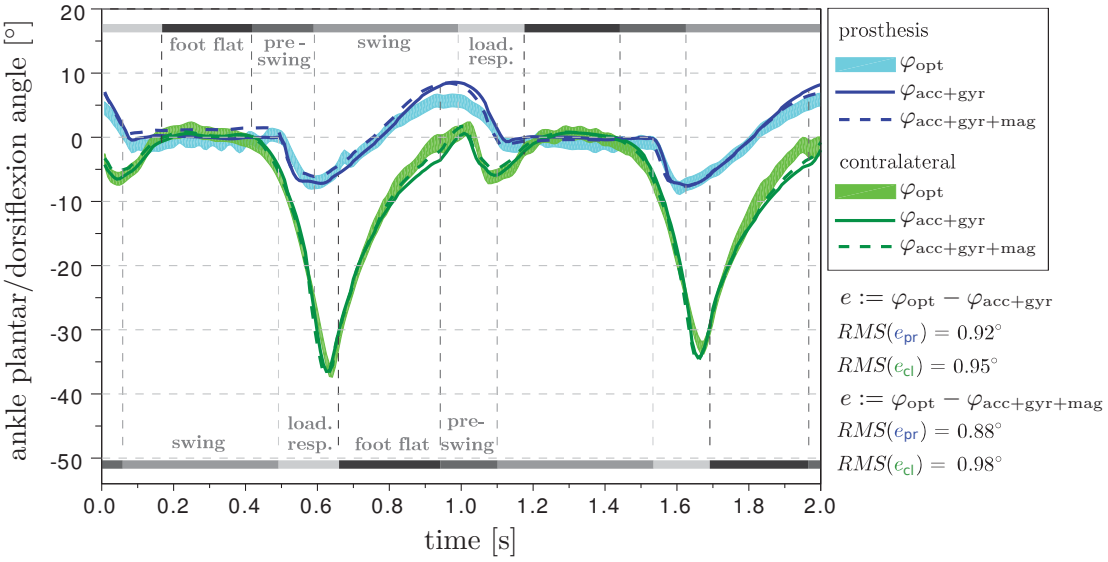

Figure 3.26: Comparison of the two IMU-based ankle plantar/dorsiflexion angle measurements ($\varphi_{acc+gyr+mag}(t)$ and $\varphi_{acc+gyr}(t)$) with the result ($\varphi_{opt}(t)$) of an optical gait analysis system. Both on the prosthesis side and on the contralateral side, the deviation is about 1°.

that this is because of the human knee being less close to a perfect hinge joint. However, we just explained in Section 3.4.4 that the IMU-based algorithms ignore abduction/adduction and internal/external rotations, just as the optical analysis does. Therefore, a more reasonable explanation is found in the following remarkable difference between the two sides. On the prosthesis, the IMUs and the optical markers are rigidly connected by the artificial thigh and shank. In contrast, on the biological leg, the inertial sensors and the markers move relative to each other as a result of muscle and skin motions. It is very likely that such soft tissue motions cause the observed deviations on the contralateral side. This argument is supported by the fact that deviations between optical and IMU-based angles are largest during pre-swing and at initial contact, i.e. when the leg is accelerated and decelerated. Furthermore, there are a number of experimental studies (see Section 3.4.2) in which the optical markers were placed directly on the inertial sensors or onto rigid plastic or wood parts that also held the inertial sensors. Obviously, with such a setup, the IMUs and optical markers of each segment can no longer move relative to each other. In these studies, deviations of less than 2° between both measurement systems were observed, which further supports the argument that the additional deviation of 2–3° on the biological leg result from skin and muscle motions. It is a major

		Trials						RMSE	
		1	2	3	4	5	6	σ	**average**
knee	prosthesis	0.46°	0.89°	0.59°	0.95°	0.57°	0.77°	0.19°	**0.71**°
	contralateral	3.25°	2.76°	3.10°	3.16°	0.40°	3.83°	1.20°	**3.30**°
ankle	prosthesis	0.92°	1.03°	0.91°	0.65°	0.67°	0.69°	0.16°	**0.81**°
	contralateral	0.95°	1.50°	1.25°	1.53°	1.85°	2.61°	0.57°	**1.62**°

Table 3.2: Deviations between the knee flexion/extension and ankle plantar/dorsiflexion angle measurements of the optical and the inertial system for six gait trials of a transfemoral amputee. Results are given for $\varphi_{\text{acc+gyr}}$ only, since both methods yield very similar results. The deviations vary little ($\sigma \approx 1°$). For the knee joint angles, the same difference in the accuracies of the prosthesis and biological leg is observed as in Figure 3.25.

result of this study that these soft tissue motion artifacts can be quantified by direct comparison of both legs of the transfemoral amputee.

3.4.6 Conclusions and Future Research

We discussed methods for IMU-based joint angle measurement on the human body. Special attention was dedicated to the challenge of arbitrary mounting orientation and position and to avoiding precise calibration motions as well as to avoiding the use of magnetometers.

We described two methods for the calculation of precise flexion/extension angles on hinge, saddle and spheroidal joints. The first method is known from the literature and requires precise estimates of the sensor orientations with respect to a common fixed reference frame. The second and novel method employs only accelerometer and gyroscope readings. Both methods were evaluated against an optical gait analysis system on the gait of a transfemoral amputee. For both, we obtained highly precise results with root-mean-square deviations of about 1° on the ankle joints, as well as on the prosthetic knee, and we discussed the effect of skin and muscle motions on the contralateral knee, which led to slightly larger deviations of about 3°. Future research will be dedicated to the question of how these effects can be compensated or minimized.

Furthermore, we shall note that the proposed algorithms use only present and past measurement data, i.e. they are suitable for online use. Therefore, and since they supersede precise sensor mounting requirements as well as restrictive calibration protocols, these new methods pave the way for a plug-and-play gait analysis, in which one simply attaches

the IMUs, moves the legs for a few seconds and then receives joint angle measurements in realtime. This will be the subject of future research, including extensions for 2D and 3D joint angle measurements on ankle and hip joints.

4 Iterative Learning Control for Variable-Pass-Length Systems

Iterative Learning Control (ILC) methods have been used successfully in a multitude of application systems including robotics, process engineering and biological systems (see for example Ahn et al. [1] and references therein). Beyond that, a growing number of researchers consider ILC a promising tool for numerous control problems in biomedical application systems, see for example Duschau-Wicke et al. [22], Freeman et al. [31], Klauer et al. [39], Wang et al. [121]. In the following, we will discuss why the conventional ILC theory is technically too restrictive for some of these applications. We will identify non-classic phenomena that typically arise when the trials in which the control task repeats are cyclic motions or processes of the human body. Subsequently, we will extend the standard ILC design in the lifted-system framework to the class of repetitive trajectory tracking tasks with variable pass length.

Two learning laws will be considered – the standard input update with a single learning gain matrix and the extended version with lowpass filter in the update loop. For both cases, we will derive and analyze the closed loop dynamics, and we will discuss in which sense the tracking error can be reduced by which control design strategies. In particular, the maximum-pass-length (MPL) error will be introduced as a useful concept for convergence analysis of variable-pass-length systems. Necessary and sufficient conditions for monotonic convergence of different vector norms of this error will be derived. We will then summarize all results in a set of practical control design guidelines. Finally, the special dynamics that occur in variable-pass-length learning will be illustrated by a simulation study.

4.1 Introduction and Motivation

Several control problems in various application domains require the controller to repeat the same trajectory tracking task from the same initial condition multiple times. In such control systems, the tracking performance can be improved by learning from previous executions by means of iterative learning control. Please refer to Chapter 2 for a brief introduction to ILC.

Depending on the analysis framework, the input and output trajectories of the system to be controlled can be described in the frequency domain or by lifted vectors. In many standard ILC application domains, especially in robotics, the analysis of the system

dynamics as well as the controller design are carried out in the frequency domain, rather than in the lifted-system framework. This yields some advantages[1], but for frequency domain methods to be applicable, the trial duration is assumed to be magnitudes larger than both the sampling time and the characteristic time constant of the system to be controlled. This requirement does not hold in many ILC applications, especially in those from the field of biomedical engineering. Therefore, it is advisable to use the lifted-system framework when aiming to derive new methods for such applications.

A brief review of recent contributions reveals that the potential application fields for ILC in biomedical engineering are numerous, including diabetes treatment (e.g. Wang et al. [123]), rehabilitation robotics (e.g. del-Ama et al. [3], Duschau-Wicke et al. [22], Liu et al. [51]), robotic surgery (e.g. Cagneau et al. [12]) and blood pressure measurement (e.g. Seel et al. [106]). However, in these applications, often even the basic assumptions of iterative learning control do not hold. One of these assumptions is that the dynamics (including the initial condition) do not change from pass to pass, i.e. the same input causes the same output when applied again in any of the following trials. This very restrictive assumption has been relaxed by several author's contributions, where ILC methods yielding robustness of convergence properties with respect to iteration-variant dynamics and initial conditions were proposed, see for example Donkers et al. [21], Moon et al. [62], Park et al. [81]. However, a more fundamental assumption of ILC is that each trial shall be of the same duration (i.e. the same pass length). In the previously mentioned applications, the trials in which the control task repeats are, for example, human arm motions, strides, or heart beats. In contrast to the rigidly defined motions of robotic actuators, these processes can hardly be assumed or constrained to repeat in trials of constant duration. Hence, the trial duration is not constant.

In the remainder of this section, we will discuss two ways in which a repetitive control task can be defined for such application systems. At first, let us consider the case in which there exists a desired trial duration but the trials terminate before this time has passed. To illustrate this case, two examples from the context of functional electrical stimulation (FES) are briefly discussed in the following:

Functional Electrical Stimulation for Upper Limb Movement: A complex functional arm movement shall be produced via electrical stimulation of the respective muscles through skin electrodes, as considered for example by Freeman et al. [31], Soska et al. [112] and Klauer et al. [39]. If the desired motion is complex, then very precise and well-timed stimulation patterns need to be applied. However, the system dynamics

[1] For example, the frequency-domain representations of the system dynamics and the controller dynamics commute, which is in general not the case for their lifted-system representations.

are very nonlinear and uncertain, since they depend on many details such as the exact electrode position. Therefore, it can be hard to set stimulation parameters that generate (anything close to) the desired motion in the first trial. For successive learning of the corresponding stimulation profile, the use of a robust ILC algorithm based on a linear model seems promising. However, at least for the first passes, it is expected that the actually achieved trajectory leaves the neighborhood of the reference trajectory very early. Even if the ILC algorithm is very robust, the data gathered outside this neighborhood is hardly useful since the dynamics and disturbances vary largely over state space. Therefore, and for reasons of safety, a trial should be terminated whenever output and reference begin to differ too much. Nevertheless, between the beginning and the (early) termination of each trial, some valuable data is gathered that could be used for learning if there was a way to deal with varying pass lengths.

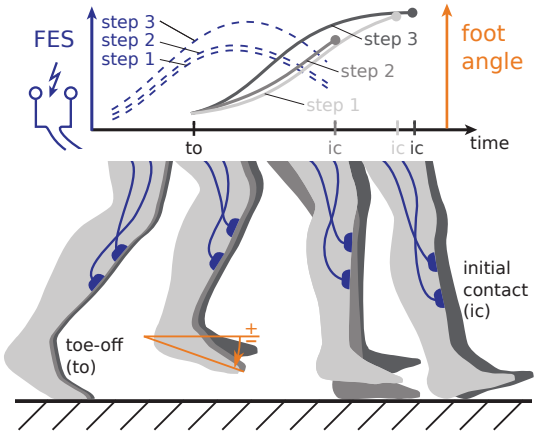

Figure 4.1: Iterative learning control of functional electrical stimulation for supporting the foot motion during gait. The stimulation intensity trajectory is adjusted from stride to stride to influence the foot orientation angle trajectory. Hip and knee joint are moved by the patients themselves. Depending on their strength and abilities, the steps are often cut short by suddenly putting the foot down. Thus, swing phase duration varies from step to step.

Functional Electrical Stimulation for Gait Assistance: Many stroke patients suffer from the drop foot syndrome, a limited ability to dorsiflex the foot, i.e. to lift the foot toward the tibia. Patients walking at constant speed on a treadmill can be supported, for example, by controlling the ankle joint angle via electrical stimulation of the tibialis anterior muscle. This is illustrated in Figure 4.1. Due to the repetitive nature of gait, ILC is a promising method for improving the stimulation profile for the swing phase from step to step and to maintain the desired foot motion despite slow

parameter variance. However, the foot is only in swing phase (i.e. above the ground) as long as the hip joint and the knee joint are sufficiently flexed. Thus, depending on the patient's strength and abilities, the steps are often cut short by suddenly putting the foot down. This means that the swing phase duration varies largely even when patients walk at constant speed. In order to apply ILC methods, we must find a way to learn from trials of varying duration.

Both application examples demonstrate that trials might be terminated early, either by events that depend on the states of the system or on the controller performance, or by randomly occurring events. A number of further examples for this phenomenon are found in the aforementioned literature on other biomedical application systems. Due to a lack of suitable methods, the fact that the trial duration varies is typically ignored completely, or a heuristic approach is used with no guarantee of convergence being maintained (cf. for example Nahrstaedt et al. [71], Longman and Mombaur [55]).

As mentioned above, there is a second way in which a repetitive control task can be defined for application systems with variable trial duration. In particular, there exist applications in which not only the trial duration but also the entire reference duration varies (see for example Moore et al. [66] or Kurniawan et al. [42]). More precisely, the reference trajectory that shall be tracked in one trial is scaled to a different time length in another (shorter or longer) trial. This is illustrated by an example from the previously discussed application context: Assume that FES is used to (successfully) perform the same arm motion (for example drawing a large circle or a point-to-point reaching motion) first within five seconds and then within three seconds. In that case, the time scale of the entire tracking problem changes. Similar phenomena arise in the second example if the gait velocity changes, as well as in FES cycling [122] and in control of respiratory motion [4]. To highlight the fact that not only the trial duration but also the reference duration changes, we will call these systems variable-*reference*-length systems.

In previous contributions, several solutions have been proposed which extend standard ILC theory to the case of variable reference length. Moore et al. [66] suggested to parameterize the input and output trajectory by a different (monotonously increasing) parameter than the time. In walking, this parameter might be the gait cycle percentage, while the crank angle might be used in FES cycling. This method, which is known as spatial-based ILC, certainly represents an effective tool for handling repetitive control problems with variable reference length. It is, however, not applicable to the previously described class of variable-pass-length systems with fixed reference duration. In the remainder of this chapter, we focus on the first class of systems, i.e. on control problems with early trial termination and thus incomplete measurement information.

4.2 Previous Work on Iterative Learning Control Systems with Variable Pass Length

Currently, there are very few results available that consider convergence of ILC systems in which the pass length is not constant. However, a few similar problems have been addressed in the literature.

Moore [65] as well as Moore and Mathews [64] consider the problem of controlling a gas-metal arc welding process, in which the time interval between detachments of mass droplets from the end of a consumable electrode is considered a trial. They propose a discontinuous, switching-based iterative learning control scheme that forces the system to exhibit a uniform trial length. However, they assume that the system can be forced to restart a trial by a known input, and they show convergence only for a very simple input-update law with a diagonal learning gain matrix.

Li et al. [45, 46, 47] address an iterative learning control design problem for discrete-time systems with randomly varying trial lengths. A stochastic matrix and an iteration-average operator are introduced to present a unified expression of the ILC scheme. However, they assume the trial length to be a stochastic variable with a known (uniform) probability distribution, and they only show convergence of the expectation of the tracking error to a small value after a large number of trials.

Ahn et al. [2] consider an ILC scheme that is implemented via a networked control system in which data dropout occurs. They present a Kalman filtering approach and show that it is possible to design a learning gain such that the system eventually converges to a desired trajectory as long as there is no complete data dropout. With some substantial extensions, this method might be used for variable-pass-length systems. Ahn et al. assume, however, that the data dropout probabilities are known, and they do not establish monotonic convergence of the tracking error in any sense.

In the following, we will fill this gap by providing methods that assure monotonic convergence for ILC systems with variable pass lengths. Under the sole assumption of a (potentially very small) lower bound and a (potentially very large) upper bound of the trial duration, we will show that monotonic convergence of the tracking error can be achieved in different senses by applying slightly modified versions of standard input-update laws.

4.3 Iterative Learning Control for Variable-Pass-Length Systems

In this section, a new class of iterative learning systems is introduced and its closed-loop dynamics are derived. It is assumed, that the pass length n can vary from pass to pass and that pass termination is sudden. This means that, for each pass $j \in \mathbb{N}_0$, the pass length n_j is not known before the pass ends. However, a possibly very small lower bound $\underline{n}$ and a possibly very large upper bound $\overline{n}$ shall be given. Consequently, a full-length desired output $\mathbf{r} \in \mathbb{R}^{\overline{n}\times 1}$ must be defined, and (for each pass j) a full-length input $\bar{\mathbf{u}}_j \in \mathbb{R}^{\overline{n}\times 1}$ with

$$\bar{\mathbf{u}}_j := [u(t_{0,j}), u(t_{0,j} + t_\mathrm{s}), \ldots, u(t_{0,j} + (\overline{n} - 1)t_\mathrm{s})]^T, \tag{4.1}$$

must be prepared, although only the first n_j samples of that trajectory will actually be applied to the system. In contrast, the output trajectory that is measured during the same trial is denoted by $\mathbf{y}_j \in \mathbb{R}^{n_j\times 1}$ and contains only $n_j \leq \overline{n}$ sample values.

In order to cope with the varying length of the output vector and for the sake of a more compact notation, we introduce the *remove-last-*$(\overline{n} - n_j)$*-elements* operator $\langle\cdot\rangle_{n_j} : \mathbb{R}^{\overline{n}\times 1} \to \mathbb{R}^{n_j\times 1}$ and the *append-*$(\overline{n} - n_j)$*-zero-elements* operator $\langle\cdot\rangle_{\overline{n}} : \mathbb{R}^{n_j\times 1} \to \mathbb{R}^{\overline{n}\times 1}$. Clearly, $\langle\cdot\rangle_{n_j}$ and $\langle\cdot\rangle_{\overline{n}}$ correspond to premultiplication by the matrices $[\mathbf{I}_{n_j\times n_j}, \mathbf{0}_{n_j\times(\overline{n}-n_j)}]$ and $[\mathbf{I}_{n_j\times n_j}, \mathbf{0}_{n_j\times(\overline{n}-n_j)}]^T$, respectively, where $\mathbf{I}_{n_j\times n_j}$ denotes the n_j-dimensional identity matrix and $\mathbf{0}_{n_j\times(\overline{n}-n_j)}$ denotes a zero matrix with n_j rows and $(\overline{n} - n_j)$ columns. Thus, for example, the desired output signal for pass length n_j becomes $\langle\mathbf{r}\rangle_{n_j}$, and the tracking error $\mathbf{e}_j \in \mathbb{R}^{n_j\times 1}$ measured in pass j can be denoted by

$$\mathbf{e}_j := \langle\mathbf{r}\rangle_{n_j} - \mathbf{y}_j\,. \tag{4.2}$$

For the last $(\overline{n} - n_j)$ samples of the reference trajectory, there exists no measurement information, since the trial actually ends after n_j sample periods. This means that the complete input trajectory $\bar{\mathbf{u}}_j$ must be updated using the incomplete error information $\mathbf{e}_j$. This can be achieved, for example, by using the following modified version of a standard ILC learning law:

$$\bar{\mathbf{u}}_{j+1} = \bar{\mathbf{u}}_j + \mathbf{L}\,\langle\mathbf{e}_j\rangle_{\overline{n}}\,, \quad j = 0, 1, \ldots, \tag{4.3}$$

where $\mathbf{L} \in \mathbb{R}^{\overline{n}\times\overline{n}}$ is an adjustable learning gain matrix. As in classic ILC systems, an initial input $\bar{\mathbf{u}}_0$ must be chosen for the first trial based on the (limited) prior knowledge of the system dynamics. Every following input is then calculated using (4.3). Although many of the following arguments would also hold for a learning gain that depends on

the trial index, we will consider only the standard case of an iteration-invariant matrix $\mathbf{L}$ in the present dissertation.

Rationale of the Variable-Pass-Length Learning Law: Recall from Chapter 2 that, whenever certain sections of the measured output trajectory perfectly track the corresponding sections of the reference trajectory, then a well-designed learning controller will try to modify the input trajectory in such a way that these sections of the output trajectory are influenced as little as possible. By setting the last $\overline{n} - n_j$ samples of the error information vector to zero, we likewise demand a learning step that affects the last $\overline{n} - n_j$ samples of the output as little as possible. This is a very reasonable strategy, since there is no measurement information about the values that these samples would have under the current input trajectory.

In the following, we will introduce a linear system model and analyze the resulting closed loop dynamics in the presence of variable pass length.

4.3.1 Linear System Dynamics

Assume that the input-output dynamics of the system to be controlled can be approximated by a linear, discrete-time process with Markov parameters $p_k, k = 1, 2, \ldots$. The maximum-pass-length output $\bar{\mathbf{y}}_j \in \mathbb{R}^{\overline{n}\times 1}$ of the system, i.e. the output that the system would yield if trial j was of full length, can then be described by

$$\bar{\mathbf{y}}_j := \begin{bmatrix} \mathbf{y}_j \\ \hat{\mathbf{y}}_j \end{bmatrix} := \mathbf{P}\bar{\mathbf{u}}_j + \mathbf{v}\,, \quad \mathbf{P} = \begin{bmatrix} p_1 & 0 & 0 & \cdots & 0 \\ p_2 & p_1 & 0 & \cdots & 0 \\ p_3 & p_2 & p_1 & \cdots & 0 \\ \vdots & \vdots & \ddots & \ddots & \vdots \\ p_{\bar{n}} & p_{\bar{n}-1} & \cdots & p_2 & p_1 \end{bmatrix}, \tag{4.4}$$

where $\mathbf{P} \in \mathbb{R}^{\overline{n}\times\overline{n}}$ is the lifted-system matrix of the process and $\mathbf{v} \in \mathbb{R}^{\overline{n}\times 1}$ is a bounded, unknown, iteration-invariant disturbance.

Assume that the system dynamics $\mathbf{P}, \mathbf{v}$ are only imprecisely known, and recall that the trials end after n_j samples. The last $\overline{n} - n_j$ samples of $\bar{\mathbf{y}}_j$ are denoted by $\hat{\mathbf{y}}_j$ and represent the unknown output that would (hypothetically) be measured if the trial was of maximum length $n_j = \overline{n}$. This portion of the complete output $\bar{\mathbf{y}}_j$ is not known to the controller when computing $\bar{\mathbf{u}}_{j+1}$. In fact, the only certain information the controller obtains in each iteration is the measured output $\mathbf{y}_j$.

4.3.2 Derivation of Closed-Loop Dynamics

Although we assume that the true system dynamics are only imprecisely known, we can nevertheless derive equations that describe how the complete output $\bar{\mathbf{y}}_j$ and the tracking error evolve for a particular lifted-system matrix $\mathbf{P}$ under consideration. Thereby, we will develop a method that enables us to verify, for a given $\mathbf{P}$, whether a certain controller $\mathbf{L}$ yields desirable convergence properties in the presence of variable pass lengths.

In order to derive closed-loop dynamics, we define the maximum-pass-length (MPL) error $\bar{\mathbf{e}}_j \in \mathbb{R}^{\overline{n}\times 1}$ analogously to the previous definition of the maximum-pass-length output:

$$\bar{\mathbf{e}}_j := \begin{bmatrix} \mathbf{e}_j \\ \hat{\mathbf{e}}_j \end{bmatrix} := \mathbf{r} - \bar{\mathbf{y}}_j. \tag{4.5}$$

Therein, $\mathbf{e}_j \in \mathbb{R}^{n_j\times 1}$ is the actually measured control deviation, and $\hat{\mathbf{e}}_j \in \mathbb{R}^{(\overline{n}-n_j)\times 1}$ is the hypothetical error that would occur on the last $\overline{n}-n_j$ sample instants if the trial was of full length.

The previous definitions allow us to rewrite the update law (4.3) in the following, more convenient form:

$$\begin{aligned} \bar{\mathbf{u}}_{j+1} &= \bar{\mathbf{u}}_j + \mathbf{L}\,\langle\,\langle\mathbf{r}\rangle_{n_j} - \mathbf{y}_j\,\rangle_{\overline{n}} \\ &= \bar{\mathbf{u}}_j + \mathbf{L}\,\mathbf{H}_{n_j}\,\bar{\mathbf{e}}_j\ , \end{aligned} \tag{4.6}$$

in which the last $\overline{n}-n_j$ samples of the MPL error are canceled by multiplication with the block-diagonal matrix[2] $\mathbf{H}_{n_j} = \text{blockdiag}\{\mathbf{I}_{n_j\times n_j}, \mathbf{0}_{(\overline{n}-n_j)\times(\overline{n}-n_j)}\}$.

By inserting (4.4) and (4.6) into (4.5), we obtain

$$\bar{\mathbf{e}}_{j+1} = \mathbf{r} - \Big(\mathbf{P}(\bar{\mathbf{u}}_j + \mathbf{L}\mathbf{H}_{n_j}\bar{\mathbf{e}}_j) + \mathbf{v}\Big) = \mathbf{r} - \Big(\mathbf{r} - \bar{\mathbf{e}}_j + \mathbf{P}\mathbf{L}\mathbf{H}_{n_j}\bar{\mathbf{e}}_j\Big)\,, \tag{4.7}$$

which yields the following closed-loop MPL error dynamics:

$$\bar{\mathbf{e}}_{j+1} \;=\; \Big(\mathbf{I}_{\overline{n}\times\overline{n}} - \mathbf{P}\mathbf{L}\mathbf{H}_{n_j}\Big)\,\bar{\mathbf{e}}_j. \tag{4.8}$$

[2] By definition, $\mathbf{H}_{n_j}\mathbf{a} = \langle\langle\mathbf{a}\rangle_{n_j}\rangle_{\overline{n}}\ \forall\mathbf{a}\in\mathbb{R}^{\overline{n}\times 1}$

In order to gain more insight into the interrelation of the measured error $\mathbf{e}_j$ and the hypothetical error $\hat{\mathbf{e}}_j$, we introduce the following trial-dependent partition:

$$\begin{bmatrix} \mathbf{G}_{1,j} & \mathbf{G}_{2,j} \\ \mathbf{G}_{3,j} & \mathbf{G}_{4,j} \end{bmatrix} := \mathbf{I}_{\overline{n}\times\overline{n}} - \mathbf{PL}, \tag{4.9}$$

$$\mathbf{G}_{1,j} \in \mathbb{R}^{n_j\times n_j},\ \mathbf{G}_{2,j} \in \mathbb{R}^{n_j\times(\overline{n}-n_j)},\ \mathbf{G}_{3,j} \in \mathbb{R}^{(\overline{n}-n_j)\times n_j},\ \mathbf{G}_{4,j} \in \mathbb{R}^{(\overline{n}-n_j)\times(\overline{n}-n_j)}. \tag{4.10}$$

We then use (4.5) to rewrite the closed-loop dynamics as follows:

$$\begin{bmatrix} \mathbf{e}_{j+1} \\ \hat{\mathbf{e}}_{j+1} \end{bmatrix} = \begin{bmatrix} \mathbf{G}_{1,j} & \mathbf{0}_{n_j\times(\overline{n}-n_j)} \\ \mathbf{G}_{3,j} & \mathbf{I}_{(\overline{n}-n_j)\times(\overline{n}-n_j)} \end{bmatrix} \begin{bmatrix} \mathbf{e}_j \\ \hat{\mathbf{e}}_j \end{bmatrix} = \begin{bmatrix} \mathbf{G}_{1,j} & \mathbf{G}_{2,j} \\ \mathbf{G}_{3,j} & \mathbf{G}_{4,j} \end{bmatrix} \begin{bmatrix} \mathbf{e}_j \\ \mathbf{0}_{(\overline{n}-n_j)\times 1} \end{bmatrix} + \begin{bmatrix} \mathbf{0}_{n_j\times 1} \\ \hat{\mathbf{e}}_j \end{bmatrix}. \tag{4.11}$$

Since the pass length may change from trial to trial, please note that, in general, $\mathbf{e}_{j+1}$ on the left-hand side and $\mathbf{e}_j$ on the right-hand side do not have the same dimensions.

Equilibria of the Closed-Loop Dynamics: With respect to (4.8), we shall note a remarkable difference between constant-pass-length and variable-pass-length ILC. If the pass length is constant $n_j = \overline{n}\ \forall j$ and $(\mathbf{I}_{\overline{n}\times\overline{n}} - \mathbf{PL})$ is regular, then the only equilibrium of (4.8) is the zero vector, i.e. perfect tracking of the given reference. For $n_j < \overline{n}$, however, every vector $\bar{\mathbf{e}}_j$ whose first n_j entries are zero is mapped onto itself by (4.8). This implies, for example, the following. If the sequence $\{n_j\}$ of pass lengths is such that $n_j \leq n^*\ \forall j$ with some $n^* < \overline{n}$, then the entire nullspace of $\mathbf{H}_{n^*}$ is an equilibrium manifold of the closed-loop dynamics (4.8).

In the following sections, we will discuss in which sense the tracking error may reduce in variable-pass-length systems, we will investigate how the learning gain matrix $\mathbf{L}$ must be chosen to guarantee such a reduction, and we will discuss some fundamental effects that appear in learning from trials with variable length. Prior to this, a low-dimensional example of the error dynamics matrices in (4.8) is provided to improve the comprehensiveness of the subsequent convergence analysis.

Example of the MPL Error Dynamics Matrices: Assume that $\overline{n} = 4$, $\underline{n} = 2$, and (without loss of generality) denote the product of $\mathbf{P}$ and $\mathbf{L}$ by

$$\mathbf{PL} = \begin{bmatrix} a & b & c & d \\ e & f & g & h \\ k & l & m & o \\ p & q & r & s \end{bmatrix}. \tag{4.12}$$

Then the MPL error dynamics matrices are given by

$$(\mathbf{I}_{4\times4} - \mathbf{PLH}_4) = \begin{bmatrix} 1-a & -b & -c & -d \\ -e & 1-f & -g & -h \\ -k & -l & 1-m & -o \\ -p & -q & -r & 1-s \end{bmatrix}, \tag{4.13}$$

$$(\mathbf{I}_{4\times4} - \mathbf{PLH}_3) = \begin{bmatrix} 1-a & -b & -c & 0 \\ -e & 1-f & -g & 0 \\ -k & -l & 1-m & 0 \\ -p & -q & -r & 1 \end{bmatrix}, \tag{4.14}$$

$$(\mathbf{I}_{4\times4} - \mathbf{PLH}_2) = \begin{bmatrix} 1-a & -b & 0 & 0 \\ -e & 1-f & 0 & 0 \\ -k & -l & 1 & 0 \\ -p & -q & 0 & 1 \end{bmatrix}. \tag{4.15}$$

Obviously, the dynamics matrices are column-wise blends of the classic closed-loop dynamics matrix ($\mathbf{I}_{\overline{n}\times\overline{n}} - \mathbf{PL}$) and the identity matrix. Thus, note for example that with perfect plant inversion, i.e. $\mathbf{L} = \mathbf{P}^{-1}$, the matrix ($\mathbf{I}_{4\times4} - \mathbf{PLH}_4$) becomes a zero matrix, while the rightmost one and two columns of ($\mathbf{I}_{4\times4} - \mathbf{PLH}_3$) and ($\mathbf{I}_{4\times4} - \mathbf{PLH}_2$), respectively, would still be those of a four-by-four identity matrix.

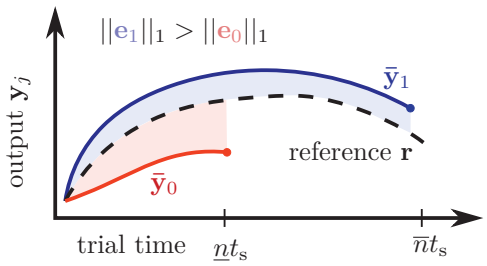

Figure 4.2: In variable-pass-length ILC, the norm of the measured error $\mathbf{e}_j$ is not a useful performance measure, since it depends largely on the trial duration. The longer trial 1 might yield a larger error norm than the shorter trial 0, although the former exhibits better reference tracking than the latter.

4.4 Learning Dynamics for the Standard Input-Update Law

4.4.1 Learning Progress on the Measured Time Interval

In classic ILC systems, controller design and implementation aims at reducing the p-norm[3] $||\mathbf{e}_j||_p$ of the measured error from one trial to the next, for some $p \in \{1, 2, \infty\}$. In variable-pass-length ILC, the p-norm of the measured tracking error $\mathbf{e}_j$ will vary as n_j varies, even if the input trajectory is not updated at all. A long trial might yield a larger error norm than a short trial, despite the former yielding better reference tracking than the latter, as illustrated in Figure 4.2.

Hence, we need a different concept to describe whether the reference tracking is improved by an update step in the presence of variable pass length. Since, in each trial j, the controller receives the measurement values of the first n_j samples, it is reasonable to demand that the reference tracking should be improved by the following update at least on those first n_j samples. In order to describe the degree to which this goal is achieved in each trial, we define the learning progress indicator $\Delta_{p,j}$ as follows:

$$\Delta_{p,j} := \frac{||\mathbf{e}_j||_p - ||\langle \bar{\mathbf{e}}_{j+1} \rangle_{n_j}||_p}{||\mathbf{e}_j||_p} = 1 - \frac{||\langle \bar{\mathbf{e}}_{j+1} \rangle_{n_j}||_p}{||\mathbf{e}_j||_p}, \tag{4.16}$$

where $\Delta_{p,j} > 0$ means that the norm of the tracking error is reduced by the update, and $\Delta_{p,j} = 1$ refers to perfect tracking being achieved by the update.

[3] $||\mathbf{x}||_1 := \sum_1^n |x(n)| \; \forall \mathbf{x} \in \mathbb{R}^{n\times 1}$, $||\mathbf{x}||_2 := \sqrt{\sum_1^n (x(n))^2} \; \forall \mathbf{x} \in \mathbb{R}^{n\times 1}$, $||\mathbf{x}||_\infty =: \max_n |x(n)| \; \forall \mathbf{x} \in \mathbb{R}^{n\times 1}$

Note that the numerator is formulated such that the p-norm is calculated over the first n_j samples of the $(j+1)^{\text{th}}$ output trajectory, regardless of whether n_{j+1} is smaller or larger than, or equal to, n_j. Obviously, such a quantity cannot be assessed experimentally, unless the sequence $\{n_j\}$ is nondecreasing with j. We can, however, answer the question whether a given $\mathbf{P}$ and $\mathbf{L}$ yield a closed-loop system with positive learning progress. By inserting (4.11) into (4.16) we obtain

$$\Delta_{p,j} = 1 - \frac{||\mathbf{G}_{1,j}\mathbf{e}_j||_p}{||\mathbf{e}_j||_p} \geq 1 - ||\mathbf{G}_{1,j}||_p \,, \tag{4.17}$$

where we exploited the fact that every vector p-norm and its induced matrix norm[4] are submultiplicative[5].

Recall the partition (4.9) and note that the induced p-norm of a matrix cannot be smaller than the induced p-norm of any of its sub-matrices. Therefore, the learning progress is positive for any p-norm if the matrix p-norm $||\mathbf{I}_{\overline{n}\times\overline{n}} - \mathbf{PL}||_p$ is smaller than one.

Due to the conservative nature of induced matrix norms, the learning progress may very well be positive even if $||\mathbf{I}_{\overline{n}\times\overline{n}} - \mathbf{PL}||_p$ is larger than one. In practice, however, neither the sequence $\{n_j\}$ of pass lengths nor the disturbance $\mathbf{v}$ are known. A learning gain $\mathbf{L}$ that yields $\Delta_{p,j} > 0$ only for some disturbances or pass length sequences is hardly useful. Likewise, it is desirable to find a learning gain that does not need to be redesigned when the reference trajectory $\mathbf{r}$ or the initial input profile $\bar{\mathbf{u}}_0$ are changed. Therefore, a condition is needed that assures positive learning progress for all possible values of $\{n_j\}$, $\mathbf{v}$, $\mathbf{r}$ and $\bar{\mathbf{u}}_0$. The following theorem states that this is only assured if $||\mathbf{I}_{\overline{n}\times\overline{n}} - \mathbf{PL}||_p$ is smaller than one.

Theorem 1. *For a repetitive process* (4.4) *with input-update law* (4.6)*, the learning progress* $\Delta_{p,j}$ *is positive in every trial, for any sequence of pass lengths* $\{n_j\}$*, for any reference* $\mathbf{r}$*, disturbance* $\mathbf{v}$*, and bounded initial input* $\bar{\mathbf{u}}_0$*, i.e.*

$$\frac{||\langle\bar{\mathbf{e}}_{j+1}\rangle_{n_j}||_p}{||\mathbf{e}_j||_p} < 1 \quad \forall\, j \in \mathbb{N}_0, n_j \in \{\underline{n}, ..., \overline{n}\}, \mathbf{r}, \mathbf{v}, \bar{\mathbf{u}}_0 \in \mathbb{R}^{\overline{n}\times 1}, \tag{4.18}$$

if and only if

$$\gamma_p := ||\mathbf{I}_{\overline{n}\times\overline{n}} - \mathbf{PL}||_p = \left|\left|\begin{bmatrix}\mathbf{G}_{1,j} & \mathbf{G}_{2,j}\\ \mathbf{G}_{3,j} & \mathbf{G}_{4,j}\end{bmatrix}\right|\right|_p < 1. \tag{4.19}$$

[4] i.e. $||\mathbf{A}||_p := \max\{||\mathbf{Ax}||_p, ||\mathbf{x}||_p = 1\}$
[5] i.e. $||\mathbf{ABx}||_p \leq ||\mathbf{A}||_p||\mathbf{B}||_p||\mathbf{x}||_p \;\forall \mathbf{A}, \mathbf{B}, \mathbf{x}$

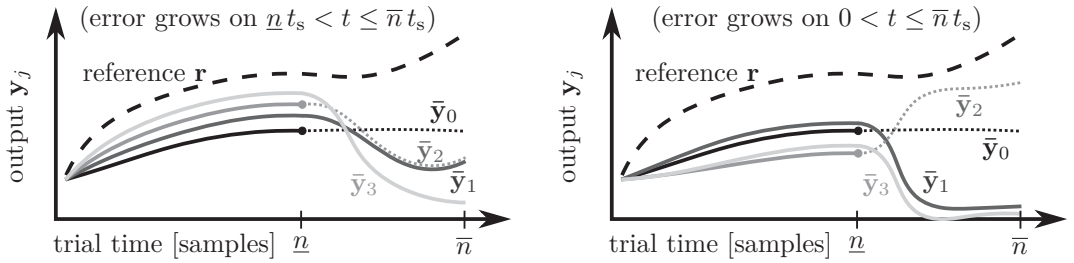

Figure 4.3: Hidden error growth in ILC systems with variable pass length. Every second trial is cut short, dotted lines indicate the hypothetical output $\hat{\mathbf{y}}_j$. In both plots, the tracking error is reduced in the sense of (4.18) in each trial. Nevertheless, the tracking may get worse on the last $\overline{n} - n_j$ samples (*left*) and may theoretically even get worse on the entire time interval (*right*).

Proof. Sufficiency of the stated condition follows from (4.17). To prove necessity by contradiction, consider the special case in which the first pass length n_0 is equal to $\overline{n}$, and assume some reference $\mathbf{r}$ and initial input $\bar{\mathbf{u}}_0$ to be given. If $\gamma_p \geq 1$, then there exists at least one disturbance signal $\mathbf{v}$ that results in $\bar{\mathbf{e}}_0$ lying in the direction of maximum gain of $(\mathbf{I}_{\overline{n}\times\overline{n}} - \mathbf{PL})$, which means

$$||\mathbf{r} - \mathbf{v} - \mathbf{P}\bar{\mathbf{u}}_0||_p = ||\bar{\mathbf{e}}_0||_p = ||\mathbf{e}_0||_p \quad \leq \quad ||(\mathbf{I}_{\overline{n}\times\overline{n}} - \mathbf{PL})\bar{\mathbf{e}}_0||_p = ||\langle\bar{\mathbf{e}}_1\rangle_{n_0}||_p, \tag{4.20}$$

i.e. the learning progress $\Delta_{p,0}$ from trial $j = 0$ to trial $j =$ is not positive. Hence, the condition (4.19) is also necessary. □

Theorem 1 highlights the relevance of the convergence indicator γ_p for learning progress in a given vector p-norm. It provides a both simple and useful result with strong analogy to the classic case of constant pass length (cf. Chapter 2). In constant-pass-length ILC systems, a positive learning progress is equivalent to strict monotonic convergence of the error norm, and (4.19) coincides with the well-known condition for strict monotonic convergence.

However, the property (4.18) is still not sufficient to guarantee that the tracking error remains bounded in the presence of variable pass length. Figure 4.3 illustrates this remarkable fact. While the example dynamics chosen therein may seem unrealistic or extreme, they nevertheless demonstrate that, in each trial, the performance on the first n_j samples might be improved at the cost of (severely) worsening the performance on the last $\overline{n} - n_j$ samples. Hence, a more rigorous convergence concept is needed that also accounts for hidden growth of the hypothetical tracking error $\hat{\mathbf{e}}_j$.

4.4.2 Monotonic Convergence of the Maximum-Pass-Length Error

The convergence properties of $\bar{\mathbf{e}}_j$ well describe whether the controller performance actually improves. Therefore, we aim at designing controllers that ensure reduction of a p-norm $||\bar{\mathbf{e}}_j||_p$ of the MPL error, for example its sum-of-absolute-values norm ($p = 1$), its Euclidean norm ($p = 2$), or its maximum-absolute-value norm ($p = \infty$). Obviously, if $||\bar{\mathbf{e}}_j||_p$ is monotonically decreasing in j, then also $||\mathbf{e}_j||_p$ is bounded by trial-wise decreasing upper bounds, since

$$||\mathbf{e}_j||_p \leq ||\bar{\mathbf{e}}_j||_p \; \forall j \; \forall p \in \{1, 2, \infty\}. \tag{4.21}$$

Therefore, the concept of the MPL error is very useful for convergence analysis. In order to have monotonic convergence for an arbitrary sequence of pass lengths $\{n_j\}$ and an arbitrary disturbance signal $\mathbf{v}$, the following condition must hold:

Lemma 1 (**Monotonic convergence of the MPL error p-norm**). *For a repetitive process* (4.4) *with input-update law* (4.6)*, the monotonic convergence condition of the MPL error is*

$$\begin{aligned} & ||\bar{\mathbf{e}}_{j+1}||_p \;\leq\; ||\bar{\mathbf{e}}_j||_p \quad \forall\, j \in \mathbb{N}_0, n_j \in \{\underline{n}, ..., \overline{n}\}, \mathbf{r}, \mathbf{v}, \bar{\mathbf{u}}_0 \in \mathbb{R}^{\overline{n}\times 1} \\ \Leftrightarrow \qquad & ||\mathbf{I}_{\overline{n}\times\overline{n}} - \mathbf{PLH}_n||_p \;\leq\; 1 \quad \forall\, n \in \{\underline{n}, ..., \overline{n}\}, \end{aligned} \tag{4.22}$$

for some vector norm $||\cdot||_p$ and its induced matrix norm.

Proof. Necessity and sufficiency follow from the definition of an induced matrix norm, i.e. $||\mathbf{A}||_p := \max\{||\mathbf{Ax}||_p, ||\mathbf{x}||_p = 1\}$, from the MPL error closed-loop dynamics (4.8), and from the fact that (in each trial j) the pass length may take any value $n_j \in \{\underline{n}, ..., \overline{n}\}$. □

In practice, checking the condition of Lemma 1 would entail the need to calculate the norm of $(\overline{n} - \underline{n} + 1)$ matrices of dimension $\overline{n} \times \overline{n}$, which is a potentially large number of large-scale matrices when high sampling rates are used. Fortunately, simplified conditions can be found for the 1-norm $||\mathbf{e}_j||_1$ and the ∞-norm by exploiting the special structure of the closed-loop error dynamics matrices $(\mathbf{I}_{\overline{n}\times\overline{n}} - \mathbf{PLH}_n), n \in \{\underline{n}, ..., \overline{n}\}$.

The following theorem exploits this special structure and provides a necessary and sufficient condition for monotonic convergence of the 1-norm (i.e. the sum of the absolute values) of the MPL error [102].

Theorem 2 (**Monotonic convergence of the MPL error 1-norm**). *Given a repetitive process* (4.4) *with input-update law* (4.6)*, the 1-norm of the MPL error $\bar{\mathbf{e}}_j$ is mono-*

tonically decreasing, i.e.

$$||\bar{\mathbf{e}}_{j+1}||_1 \leq ||\bar{\mathbf{e}}_j||_1 \quad \forall\, j \in \mathbb{N}_0, n_j \in \{\underline{n}, ..., \overline{n}\}, \mathbf{r}, \mathbf{v}, \bar{\mathbf{u}}_0 \in \mathbb{R}^{\overline{n}\times 1}, \tag{4.23}$$

if and only if

$$\gamma_1 = ||\mathbf{I}_{\overline{n}\times\overline{n}} - \mathbf{PL}||_1 \leq 1\,. \tag{4.24}$$

Proof. Necessity follows from Lemma 1, since (4.24) repeats a special case ($n = \overline{n}, p = 1$) of the condition therein. Sufficiency is proved by the following argument, which holds for every $n \in [\underline{n}, \overline{n})$:

$$(\mathbf{I}_{\overline{n}\times\overline{n}} - \mathbf{PLH}_n) = (\mathbf{I}_{\overline{n}\times\overline{n}} - \mathbf{PL})\mathbf{H}_n + (\mathbf{I}_{\overline{n}\times\overline{n}} - \mathbf{H}_n)\,. \tag{4.25}$$

Note that the last $\overline{n} - n$ columns of $(\mathbf{I}_{\overline{n}\times\overline{n}} - \mathbf{PL})\mathbf{H}_n$ are zero and that $(\mathbf{I}_{\overline{n}\times\overline{n}} - \mathbf{H}_n) = \text{blockdiag}\{\mathbf{0}_{n\times n}, \mathbf{I}_{(\overline{n}-n)\times(\overline{n}-n)}\}$. Recall that the induced matrix norm $||\cdot||_1$ is the maximum absolute column sum of the matrix. Therefore, we obtain

$$\begin{aligned} ||\mathbf{I}_{\overline{n}\times\overline{n}} - \mathbf{PLH}_n||_1 &= \max(||(\mathbf{I}_{\overline{n}\times\overline{n}} - \mathbf{PL})\mathbf{H}_n||_1, 1) &(4.26)\\ &\leq \max(||\mathbf{I}_{\overline{n}\times\overline{n}} - \mathbf{PL}||_1||\mathbf{H}_n||_1, 1) \leq \max(\gamma_1, 1)\,. &(4.27)\end{aligned}$$

With Lemma 1, monotonic convergence follows. □

Of course, *strict* monotonic convergence is more desirable than just monotonic convergence. But even for $\gamma_1 < 1$, it turns out that $||\mathbf{I}_{\overline{n}\times\overline{n}} - \mathbf{PLH}_n||_1 = 1\ \forall\, n < \overline{n}$, since the last $\overline{n} - n$ columns each have an absolute-value sum of one. To clarify this issue, the following corollary is given:

Corollary 1 (**Almost-strict monotonic convergence of the MPL error 1-norm**)**.** *If the matrix* $\mathbf{L}$ *satisfies* $\gamma_1 = ||\mathbf{I}_{\overline{n}\times\overline{n}} - \mathbf{PL}||_1 < 1$*, then* $||\bar{\mathbf{e}}_{j+1}||_1 < ||\bar{\mathbf{e}}_j||_1$ *for arbitrary pass length* $n_j \in \{\underline{n}, ..., \overline{n}\}$*, unless the first* n_j *entries of* $\bar{\mathbf{e}}_j$ *are zero. This follows from* (4.11) *and from the special property* $||\bar{\mathbf{e}}_j||_1 = ||\mathbf{e}_j||_1 + ||\hat{\mathbf{e}}_j||_1\ \forall j$ *of the 1-norm, which allows the following conclusion:*

$$||\bar{\mathbf{e}}_{j+1}||_1 \leq ||\mathbf{I}_{\overline{n}\times\overline{n}} - \mathbf{PL}||_1||\mathbf{e}_j||_1 + ||\hat{\mathbf{e}}_j||_1 < ||\bar{\mathbf{e}}_j||_1\,. \tag{4.28}$$

In practice, this simply means that the learning algorithm is not guaranteed to improve the last $\overline{n} - n_j$ input samples until long enough passes occur. But it always learns from measured errors on the first n_j samples and (unless they are all zero) improves the overall controller performance by reducing the 1-norm of the MPL error, even for short pass lengths.

In some applications, it is of special importance how the maximum deviation between reference trajectory and measured output evolves from trial to trial. To address this question, the following theorem provides a necessary and sufficient condition for monotonic convergence of the ∞-norm (i.e. the maximum absolute value) of the MPL error [102].

Theorem 3 (**Monotonic convergence of the MPL error ∞-norm**). *For a repetitive process* (4.4) *with input-update law* (4.6)*, the ∞-norm of the MPL error is monotonically decreasing, i.e.*

$$||\bar{\mathbf{e}}_{j+1}||_\infty \leq ||\bar{\mathbf{e}}_j||_\infty \quad \forall\, j \in \mathbb{N}_0, n_j \in \{\underline{n}, ..., \overline{n}\}, \mathbf{r}, \mathbf{v}, \bar{\mathbf{u}}_0 \in \mathbb{R}^{\overline{n}\times 1}, \tag{4.29}$$

if and only if

$$||\mathbf{I}_{\overline{n}\times\overline{n}} - \mathbf{PL}||_\infty \leq 1 \ \wedge\ (\mathbf{PL})_{i,k} = 0 \ \forall k < i \ \forall i > \underline{n}\,, \tag{4.30}$$

where i and k are the row index and column index of $\mathbf{P}$, respectively.

Proof. Sufficiency and necessity is proved by the following argument, which holds for every $n \in [\underline{n}, \overline{n})$:

$$(\mathbf{I}_{\overline{n}\times\overline{n}} - \mathbf{PLH}_n) = \mathbf{H}_n(\mathbf{I}_{\overline{n}\times\overline{n}} - \mathbf{PL})\mathbf{H}_n - (\mathbf{I}_{\overline{n}\times\overline{n}} - \mathbf{H}_n)\mathbf{PLH}_n + (\mathbf{I}_{\overline{n}\times\overline{n}} - \mathbf{H}_n)\,, \tag{4.31}$$

as $\mathbf{H}_n\mathbf{H}_n = \mathbf{H}_n$. Note that the last $(\overline{n} - n)$ rows of $\mathbf{H}_n(\mathbf{I}_{\overline{n}\times\overline{n}} - \mathbf{PL})\mathbf{H}_n$ are zero, and that the first n rows of both other terms on the right-hand side are zero. Recall that the induced matrix norm $||\cdot||_\infty$ is the maximum absolute row sum of the matrix. Therefore, we conclude

$$\begin{aligned}||\mathbf{I}_{\overline{n}\times\overline{n}} - \mathbf{PLH}_n||_\infty = \max\Big(\, &||\mathbf{H}_n(\mathbf{I}_{\overline{n}\times\overline{n}} - \mathbf{PL})\mathbf{H}_n||_\infty\,, \\ &||(\mathbf{I}_{\overline{n}\times\overline{n}} - \mathbf{H}_n)\mathbf{PLH}_n + (\mathbf{I}_{\overline{n}\times\overline{n}} - \mathbf{H}_n)||_\infty\Big).\end{aligned} \tag{4.32}$$

With respect to the second term, note furthermore that the last $(\overline{n} - n)$ columns of $(\mathbf{I}_{\overline{n}\times\overline{n}} - \mathbf{H}_n)\mathbf{PLH}_n$ are zero and that $(\mathbf{I}_{\overline{n}\times\overline{n}} - \mathbf{H}_n) = \text{blockdiag}\{\mathbf{0}_{n\times n}, \mathbf{I}_{(\overline{n}-n)\times(\overline{n}-n)}\}$. With i and k denoting the row index and column index, respectively, it follows that

$$||\mathbf{I}_{\overline{n}\times\overline{n}} - \mathbf{PLH}_n||_\infty = \max\Big(||\mathbf{H}_n(\mathbf{I}_{\overline{n}\times\overline{n}} - \mathbf{PL})\mathbf{H}_n||_\infty\,,\, \max_{i>n} \sum_{k=1}^{n} |(\mathbf{PL})_{i,k}| + 1\Big)\,. \tag{4.33}$$

Note that the right-hand side is at least one, and note that it is equal to one for all $n \in \{\underline{n}, ..., \overline{n}\}$ if and only if (4.30) holds. Combining this with Lemma 1 completes the proof. □

As for the 1-norm, we find that even if (4.30) holds with $||\mathbf{I}_{\overline{n}\times\overline{n}} - \mathbf{PL}||_\infty$ being *strictly* less than unity, we still have $||\mathbf{I}_{\overline{n}\times\overline{n}} - \mathbf{PLH}_n||_\infty = 1$ for all pass lengths $n < \overline{n}$. However, as a corollary of the above proof, we find the following:

Corollary 2 (**Almost-strict monotonic convergence of MPL error ∞-norm**). *From the proof of Theorem 3, we conclude that*

$$||\bar{\mathbf{e}}_{j+1}||_\infty \leq \max(\, ||\mathbf{H}_{n_j}(\mathbf{I}_{\overline{n}\times\overline{n}} - \mathbf{PL})\mathbf{H}_{n_j}||_\infty \, ||\mathbf{e}_j||_\infty \,,\, ||\hat{\mathbf{e}}_j||_\infty \,). \tag{4.34}$$

Since furthermore $||\mathbf{H}_{n_j}(\mathbf{I}_{\overline{n}\times\overline{n}} - \mathbf{PL})\mathbf{H}_{n_j}||_\infty \leq ||\mathbf{I}_{\overline{n}\times\overline{n}} - \mathbf{PL}||_\infty$ *holds, we find that the slightly more demanding condition* $((4.30) \wedge ||\mathbf{I}_{\overline{n}\times\overline{n}} - \mathbf{PL}||_\infty < 1)$ *yields the property*

$$||\mathbf{e}_j||_\infty > ||\hat{\mathbf{e}}_j||_\infty \quad \Rightarrow \quad ||\bar{\mathbf{e}}_{j+1}||_\infty < ||\mathbf{e}_j||_\infty = ||\bar{\mathbf{e}}_j||_\infty \,. \tag{4.35}$$

In practice, this means that the controller performance strictly improves (in the sense of the ∞-norm of the MPL error) in each pass that is long enough to contain the sample(s) of largest error. If, however, $\mathbf{P}, \mathbf{L}, \mathbf{r}, \mathbf{v}, \bar{\mathbf{u}}_j$ are such that the largest deviation between output and reference would occur after the end of the trial, then only monotonic convergence is assured, until the trial length or the input trajectory change in such a way that the largest deviation occurs in the actually measured error $\mathbf{e}_j$.

Please note that both Theorems 2 and 3 are such that only the maximum-pass-length matrix ($\mathbf{I}_{\overline{n}\times\overline{n}} - \mathbf{PL}$) and its norm need to be calculated to check for (almost-strict) monotonic convergence. But in the ∞-norm case, perfect plant inversion[6] is required, at least in the lower left corner of ($\mathbf{PL}$). Therefore this criterion is deemed less practical.

4.4.2.1 Convergence of the 2-norm

For monotonic convergence of the Euclidean norm $||\bar{\mathbf{e}}_j||_2$, no criterion is found that significantly simplifies the condition given by Lemma 1. But based on the above criteria for monotonic convergence of the MPL error in the 1-norm and the ∞-norm, the dynamic behavior of $||\bar{\mathbf{e}}_j||_2$ can be assessed using the well-known facts

$$||\mathbf{A}||_2 \leq ||\mathbf{A}||_1 \cdot ||\mathbf{A}||_\infty \; \forall \, \mathbf{A} \in \mathbb{R}^{n\times n}, \tag{4.36}$$

$$||\mathbf{a}||_\infty \leq ||\mathbf{a}||_2 \leq ||\mathbf{a}||_1 \; \forall \, \mathbf{a} \in \mathbb{R}^{n\times 1}. \tag{4.37}$$

Precisely, the following properties shall be noted:

[6] i.e. choosing $\mathbf{L}$ such that $\mathbf{PL}$ is the identity matrix

P1: If the MPL error converges monotonically both in the 1-norm and in the ∞-norm, then it is also converges monotonically in the 2-norm.

P2: If the MPL error converges to zero in any of the three norms, then so it does in the other two.

P3: If its 1-norm converges to a small value ε, then both its 2-norm and its ∞-norm converge to or even fall below ε, with the 1-norm as an upper bound on both.

Therefore, it is in general sufficient to design a learning gain matrix $\mathbf{L}$ that satisfies the condition (4.24).

4.5 Learning Dynamics for Input-Update Laws with Q-Filter

In the previous section, a modified version of the standard learning law $\mathbf{u}_{j+1} = \mathbf{u}_j + \mathbf{L}\mathbf{e}_j$ has been employed. This is a reasonable choice for many applications. Often, however, one wants to restrict the learning process to a low-frequency range in which model uncertainties are at least limited. In order to avoid that high-frequency components accumulate in the input trajectory via repetitive application of the update law, the aforementioned standard learning law is often extended by a lowpass filter in standard (i.e. constant-pass-length) ILC. Thus, in analogy, we propose the following for the variable-pass-length case:

$$\bar{\mathbf{u}}_{j+1} \;=\; \mathbf{Q}\,(\bar{\mathbf{u}}_j \;+\; \mathbf{L}\,\langle \mathbf{e}_j \rangle_{\overline{n}}) \;=\; \mathbf{Q}\left(\bar{\mathbf{u}}_j \;+\; \mathbf{L}\,\mathbf{H}_{n_j}\,\bar{\mathbf{e}}_j\right)\,, \tag{4.38}$$

where $\mathbf{Q} \in \mathbb{R}^{\overline{n}\times\overline{n}}$ is a symmetric matrix with Toeplitz structure containing the Markov parameters of a lowpass filter with cutoff frequency denoted by $f_{\mathbf{Q}}$. Multiplying a lifted signal by $\mathbf{Q}$ corresponds to applying a zero-phase lowpass filter to the signal, see for example Elci et al. [23] and Gustafsson et al. [33].

Using this modified learning law leads to more complex closed-loop dynamics. By combining (4.4), (4.5) and (4.38), and under the assumption of a regular lifted-system matrix $\mathbf{P}$, we obtain the following maximum-pass-length error dynamics:

$$\bar{\mathbf{e}}_{j+1} \;=\; \mathbf{P}\mathbf{Q}\mathbf{P}^{-1}(\mathbf{I}_{\overline{n}\times\overline{n}} - \mathbf{P}\mathbf{L}\mathbf{H}_{n_j})\,\bar{\mathbf{e}}_j + (\mathbf{I}_{\overline{n}\times\overline{n}} - \mathbf{P}\mathbf{Q}\mathbf{P}^{-1})(\mathbf{r} - \mathbf{v}). \tag{4.39}$$

In order to gain more insight into the interrelation between the measured error $\mathbf{e}_j$ and the hypothetical error $\hat{\mathbf{e}}_j$, (recall and) introduce the following trial-dependent partition:

$$\begin{bmatrix} \mathbf{G}_{1,j} & \mathbf{G}_{2,j} \\ \mathbf{G}_{3,j} & \mathbf{G}_{4,j} \end{bmatrix} := \mathbf{I}_{\overline{n}\times\overline{n}} - \mathbf{P}\mathbf{L}, \qquad \begin{bmatrix} \mathbf{K}_{1,j} & \mathbf{K}_{2,j} \\ \mathbf{K}_{3,j} & \mathbf{K}_{4,j} \end{bmatrix} := \mathbf{P}\mathbf{Q}\mathbf{P}^{-1}, \tag{4.40}$$

$$\mathbf{G}_{1,j} \in \mathbb{R}^{n_j\times n_j},\ \mathbf{G}_{2,j} \in \mathbb{R}^{n_j\times(\overline{n}-n_j)},\ \mathbf{G}_{3,j} \in \mathbb{R}^{(\overline{n}-n_j)\times n_j},\ \mathbf{G}_{4,j} \in \mathbb{R}^{(\overline{n}-n_j)\times(\overline{n}-n_j)},$$

$$\mathbf{K}_{1,j} \in \mathbb{R}^{n_j\times n_j},\ \mathbf{K}_{2,j} \in \mathbb{R}^{n_j\times(\overline{n}-n_j)},\ \mathbf{K}_{3,j} \in \mathbb{R}^{(\overline{n}-n_j)\times n_j},\ \mathbf{K}_{4,j} \in \mathbb{R}^{(\overline{n}-n_j)\times(\overline{n}-n_j)}.$$

This, together with the MPL error definition (4.5), allows us to rewrite (4.39) as follows:

$$\begin{aligned}\begin{bmatrix}\mathbf{e}_{j+1}\\ \hat{\mathbf{e}}_{j+1}\end{bmatrix} &= \begin{bmatrix}\mathbf{K}_{1,j} & \mathbf{K}_{2,j}\\ \mathbf{K}_{3,j} & \mathbf{K}_{4,j}\end{bmatrix}\begin{bmatrix}\mathbf{G}_{1,j} & \mathbf{0}_{n_j\times(\overline{n}-n_j)}\\ \mathbf{G}_{3,j} & \mathbf{I}_{(\overline{n}-n_j)\times(\overline{n}-n_j)}\end{bmatrix}\begin{bmatrix}\mathbf{e}_j\\ \hat{\mathbf{e}}_j\end{bmatrix}\\ &\qquad + \begin{bmatrix}\mathbf{I}_{n_j\times n_j}-\mathbf{K}_{1,j} & -\mathbf{K}_{2,j}\\ -\mathbf{K}_{3,j} & \mathbf{I}_{(\overline{n}-n_j)\times(\overline{n}-n_j)}-\mathbf{K}_{4,j}\end{bmatrix}(\mathbf{r}-\mathbf{v})\\ &= \begin{bmatrix}\mathbf{K}_{1,j} & \mathbf{K}_{2,j}\\ \mathbf{K}_{3,j} & \mathbf{K}_{4,j}\end{bmatrix}\left(\begin{bmatrix}\mathbf{G}_{1,j}\\ \mathbf{G}_{3,j}\end{bmatrix}\mathbf{e}_j + \begin{bmatrix}\mathbf{0}\\ \hat{\mathbf{e}}_j\end{bmatrix}\right)\\ &\qquad + \begin{bmatrix}\mathbf{I}_{n_j\times n_j}-\mathbf{K}_{1,j} & -\mathbf{K}_{2,j}\\ -\mathbf{K}_{3,j} & \mathbf{I}_{(\overline{n}-n_j)\times(\overline{n}-n_j)}-\mathbf{K}_{4,j}\end{bmatrix}(\mathbf{r}-\mathbf{v})\,. \end{aligned} \tag{4.41}$$

As before, please note that, in general, the measured error $\mathbf{e}_{j+1}$ of trial $j+1$ on the left-hand side and the measured error $\mathbf{e}_j$ of trial j on the right-hand side do not have the same dimensions.

These dynamics exhibit a different structure than the previously considered dynamics (4.8). Lemma 1 as well as Theorems 1–3 cannot be applied or trivially extended to the present case. Therefore, a positive learning progress $\Delta_{p,j} > 0\ \forall j$ or even monotonic convergence of the MPL error norm $||\bar{\mathbf{e}}_j||_p$ cannot be guaranteed by any of the criteria from Section 4.4. Even the deceptively intuitive choice of a learning gain and Q-Filter that assure $||\mathbf{PQP}^{-1}(\mathbf{I}_{\overline{n}\times\overline{n}}-\mathbf{PLH}_n)||_p \leq 1\ \forall n \in \{\underline{n},...,\overline{n}\}$ does not provide any of these properties in general.

Equilibria of the Closed-Loop Dynamics: With respect to (4.39) and (4.41), we shall note a remarkable difference between constant-pass-length and variable-pass-length ILC. Consider the following steady-state equation for each $n \in \{\underline{n},...,\overline{n}\}$:

$$(\mathbf{I}_{\overline{n}\times\overline{n}}-\mathbf{PQP}^{-1}(\mathbf{I}_{\overline{n}\times\overline{n}}-\mathbf{PLH}_n))\mathbf{e}_{\infty,n} = (\mathbf{I}_{\overline{n}\times\overline{n}}-\mathbf{PQP}^{-1})(\mathbf{r}-\mathbf{v}). \tag{4.42}$$

If the pass length is constant $n_j = \overline{n}\ \forall j$, then all solutions of (4.42) with $n = \overline{n}$ are equilibria of the closed loop system (4.39). Typically, the inverse of $(\mathbf{I}_{\overline{n}\times\overline{n}}-\mathbf{PQP}^{-1}(\mathbf{I}_{\overline{n}\times\overline{n}}-\mathbf{PL}))$ exists, and the equilibrium is a single steady-state error trajectory, the entries of which are small if $\mathbf{Q} \approx \mathbf{I}_{\overline{n}\times\overline{n}}$ (cf. Chapter 2). For an arbitrary sequence of pass lengths, however, there exists, in general, no equilibrium.

In the following, we will analyze the closed-loop dynamics and investigate how the controller parameters $\mathbf{L}, \mathbf{Q}$ must be chosen to guarantee a positive learning progress and a reduction of the maximum-pass-length error p-norm.

4.5.1 Learning Progress on the Measured Time Interval

Consider the input update at trial j and recall that the tracking error on the first n_j sample instants is $\mathbf{e}_j = \langle \mathbf{r} \rangle_{n_j} - \mathbf{y}_j$. We want to quantify how effectively the update (4.38) uses this information to improve the control signal. To this end, we recall the concept of the learning progress $\Delta_{p,j}$, which was defined in (4.16) as the relative reduction (from trial j to trial $j+1$) of the tracking error p-norm on the first n_j sample instants. With (4.41), we obtain

$$\Delta_{p,j} = 1 - \frac{\left|\left|(\mathbf{K}_{1,j}\mathbf{G}_{1,j} + \mathbf{K}_{2,j}\mathbf{G}_{3,j})\mathbf{e}_j + \mathbf{K}_{2,j}\hat{\mathbf{e}}_j + \begin{bmatrix}\mathbf{I}_{n_j \times n_j} - \mathbf{K}_{1,j} & -\mathbf{K}_{2,j}\end{bmatrix}(\mathbf{r} - \mathbf{v})\right|\right|_p}{||\mathbf{e}_j||_p}, \tag{4.43}$$

where $||\cdot||_p$ denotes any vector p-norm and its induced[7] matrix norm. Recall furthermore that $\Delta_{p,j}$ is between zero and one if the learning step reduces the error p-norm on the first n_j samples, and it is negative if that norm increases.

To simplify the right-hand side of (4.43), it is helpful to introduce the following scalar convergence indicator $\tilde{\gamma}_p$, residual indicator $\tilde{\epsilon}_p$ and crosstalk indicator $\tilde{\kappa}_p$:

$$\tilde{\gamma}_p := ||\mathbf{P}\mathbf{Q}\mathbf{P}^{-1}(\mathbf{I}_{\overline{n}\times\overline{n}} - \mathbf{P}\mathbf{L})||_p\,, \tag{4.44}$$

$$\tilde{\epsilon}_p := ||\mathbf{I}_{\overline{n}\times\overline{n}} - \mathbf{P}\mathbf{Q}\mathbf{P}^{-1}||_p\,, \tag{4.45}$$

$$\tilde{\kappa}_p := ||\mathbf{P}\mathbf{Q}\mathbf{P}^{-1}||_p\,. \tag{4.46}$$

Please note that these indicators do *not* depend on the current pass length, nor on the reference or disturbance. They are constants that can easily be calculated for any given system $\mathbf{P}$ and iterative learning controller $\mathbf{L}, \mathbf{Q}$. Therefore, we will try to formulate convergence criteria and controller design guidelines in terms of these indicators.

Recall that any p-norm is submultiplicative[8] and that the p-norm of a matrix cannot be smaller than the p-norm of any of its sub-matrices. Revisiting (4.40), we find the

[7] recall that $||\mathbf{A}||_p := \max\{||\mathbf{A}\mathbf{x}||_p, ||\mathbf{x}||_p = 1\}$

[8] i.e. recall that $||\mathbf{A}\mathbf{B}\mathbf{x}||_p \leq ||\mathbf{A}||_p||\mathbf{B}||_p||\mathbf{x}||_p \; \forall \mathbf{A}, \mathbf{B}, \mathbf{x}$

following useful properties of $\tilde{\gamma}_p$, $\tilde{\epsilon}_p$ and $\tilde{\kappa}_p$:

$$\tilde{\gamma}_p \geq ||\mathbf{K}_{1,j}\mathbf{G}_{1,j} + \mathbf{K}_{2,j}\mathbf{G}_{3,j}||_p, \tag{4.47}$$

$$\tilde{\epsilon}_p \geq \left|\left|\begin{bmatrix}\mathbf{I}_{n_j\times n_j} - \mathbf{K}_{1,j} & -\mathbf{K}_{2,j}\end{bmatrix}\right|\right|_p \geq ||\mathbf{K}_{2,j}||_p, \tag{4.48}$$

$$\tilde{\kappa}_p \geq \left|\left|\begin{bmatrix}\mathbf{K}_{2,j}\\ \mathbf{K}_{4,j}\end{bmatrix}\right|\right|_p. \tag{4.49}$$

Exploiting the first two of these properties, we obtain the following lower bound (worst case) of the learning progress:

$$\Delta_{p,j} \geq 1 - \frac{\tilde{\gamma}_p||\mathbf{e}_j||_p + \tilde{\epsilon}_p\left(||\hat{\mathbf{e}}_j||_p + ||\mathbf{r}-\mathbf{v}||_p\right)}{||\mathbf{e}_j||_p}. \tag{4.50}$$

This approximation is certainly very conservative. However, it allows us to derive a few compact statements on the learning dynamics:

If perfect model knowledge was available, then the choice $\mathbf{L} = \mathbf{P}^{-1}$ and $\mathbf{Q} = \mathbf{I}_{\overline{n}\times\overline{n}}$ would assure $\tilde{\gamma}_p = \tilde{\epsilon}_p = 0$ and thus a learning progress of 1, i.e. reduction of the first n_j sample values of the tracking error to zero in each trial j. In the more realistic case that a convergence indicator $0 < \tilde{\gamma}_p < 1$ can be assured, the following monotonous error reduction property is given:

$$||\mathbf{e}_j||_p > \frac{\tilde{\epsilon}_p}{1-\tilde{\gamma}_p}(||\hat{\mathbf{e}}_j||_p + ||\mathbf{r}-\mathbf{v}||_p) \quad \Rightarrow \quad \Delta_{p,j} > 0\,. \tag{4.51}$$

This means that there is positive learning progress (at least) until the norm $||\mathbf{e}_j||_p$ of the tracking error falls below a certain threshold, which is small if the convergence indicator $\tilde{\gamma}_p$, the residual indicator $\tilde{\epsilon}_p$ and the hypothetical error norm $||\hat{\mathbf{e}}_j||_p$ are small. This result is in accordance with the well-known result from classic ILC theory that a non-zero steady state error is obtained if a Q-filter $\mathbf{Q} \neq \mathbf{I}_{\overline{n}\times\overline{n}}$ is used.

Within this statement lies the major difference between the results of Section 4.4 and all of the results that we will obtain for the update law (4.38) with Q-filter. Only when the tracking error on the first n_j samples is large enough, then $\tilde{\gamma}_p < 1$ assures that there is positive learning progress.

The usefulness of such statements largely depends on the conservativeness of the threshold that defines what *large enough* means. Therefore, we will aim at reducing the conservativeness of (4.51) in the following.

4.5.2 Frequency-Weighted Residual Indicator

Assume that a nontrivial Q-filter is used, which is neither $\mathbf{Q} \approx \mathbf{0}_{\overline{n}\times\overline{n}}$ nor $\mathbf{Q} \approx \mathbf{I}_{\overline{n}\times\overline{n}}$, i.e. the cutoff frequency $f_{\mathbf{Q}}$ is neither close to zero nor close to the Nyquist frequency[9]. Then, for all regular lifted-system matrices $\mathbf{P}$, we find that the scalar crosstalk indicator $\tilde{\kappa}_p = ||\mathbf{PQP}^{-1}||_p$ defined above can hardly be less than one. This is not surprising, since multiplication by a lowpass Q-filter leaves low-frequency lifted signals almost unchanged. At the same time, premultiplying a high-frequency lifted signal by $\mathbf{Q}$ yields a lifted signal with very small norm. Therefore, the residual indicator $\tilde{\epsilon}_p = ||(\mathbf{I}_{\overline{n}\times\overline{n}} - \mathbf{PQP}^{-1})||_p$ can hardly be smaller than one.

Since this seems to be a very restrictive result, we briefly interpret it in more detail by inspecting the system dynamics (4.4) and the learning law (4.38), which leads to the following conclusion. If there are high-frequency portions in the reference $\mathbf{r}$ or disturbance $\mathbf{v}$, then these lead to high-frequency portions in the tracking error that will not be removed by the learning controller unless $f_{\mathbf{Q}}$ is larger than those frequencies. This is in accordance with our previous statement that the Q-filter restricts the learning process to a low-frequency range.

In that sense, however, using $\tilde{\epsilon}_p$ in the left-hand side of the error reduction condition (4.51) is highly conservative. In the very realistic case that both $\mathbf{r}$ and $\mathbf{v}$ contain only frequencies (far) below the chosen $f_{\mathbf{Q}}$, we may expect the error norm being reduced to a much smaller value than (4.51) suggests.

In order to obtain a less conservative result, we define the frequency-weighted matrix norm $||\cdot||_{\leq f_0,p} : \mathbb{R}^{\overline{n}\times\overline{n}} \to \mathbb{R}$ as follows:

$$||\mathbf{A}||_{\leq f_0,p} := ||\mathbf{AQ}_{f_0}||_p \; \forall \mathbf{A} \in \mathbb{R}^{\overline{n}\times\overline{n}}, \tag{4.52}$$

where $\mathbf{Q}_{f_0} \in \mathbb{R}^{\overline{n}\times\overline{n}}$ is the regular lifted-system matrix of a lowpass filter with some cutoff frequency f_0 (between 0 and the Nyquist frequency) and unity p-norm $||\mathbf{Q}_{f_0}||_p = 1$. Note that $\mathbf{Q}_{f_0}$ has the same dimensions and structure as $\mathbf{Q}$, but their cutoff frequencies f_0 and $f_{\mathbf{Q}}$ are (in general) not the same. While the latter is a controller design parameter, the former is a parameter of the matrix norm definition (4.52).

Recall that the induced p-matrix norm is the largest gain by which the p-norm of a vector increases when multiplied with the matrix. Following this definition, the frequency-weighted matrix norm $||\cdot||_{\leq f_0,p}$ yields the largest gain by which the p-norm of a low-

[9] i.e. half of the sampling frequency of a discrete-time system

frequency vector increases when multiplied with the matrix[10]. Furthermore, please note that, by definition, the proposed matrix norm $||\cdot||_{\leq f_0,p}$ exhibits the fundamental properties of a matrix norm, i.e. it is definite, homogeneous and subadditive.

Using this frequency-weighted matrix norm, we now define the frequency-weighted residual indicator

$$\tilde{\epsilon}_{\leq f_0,p} := ||\mathbf{I}_{\overline{n}\times\overline{n}} - \mathbf{P}\mathbf{Q}\mathbf{P}^{-1}||_{\leq f_0,p}\,, \tag{4.53}$$

which is found to be clearly below one for Q-filters with $f_{\mathbf{Q}} > f_0$. This allows us to reduce the conservativeness of (4.51) and state the following useful result.

Theorem 4 (**Positive learning progress**)**.** *Consider a repetitive process* (4.4) *with regular* $\mathbf{P}$ *and input-update law* (4.38)*, and assume that the reference and disturbance signals contain only frequencies below a known frequency* f_0*, i.e.*

$$\mathbf{Q}_{f_0}(\mathbf{r} - \mathbf{v}) = (\mathbf{r} - \mathbf{v}), \tag{4.54}$$

where $\mathbf{Q}_{f_0}$*, with* $||\mathbf{Q}_{f_0}||_p = 1$*, is a regular lifted matrix of a lowpass filter with cutoff frequency* f_0*. Assume furthermore that the learning gain matrix* $\mathbf{L}$ *is chosen such that* $\tilde{\gamma}_p < 1$*. Then the learning progress* $\Delta_{p,j}$ *defined in* (4.43) *is positive, i.e. the tracking error is reduced on the first* n_j *samples from trial* j *to trial* $j+1$*, if the norm of the measured tracking error is sufficiently large, namely*

$$||\mathbf{e}_j||_p > \frac{\tilde{\epsilon}_{\leq f_0,p}||\mathbf{r} - \mathbf{v}||_p + ||\mathbf{K}_{2,j}\hat{\mathbf{e}}_j||_p}{1 - \tilde{\gamma}_p}. \tag{4.55}$$

Proof. We start the proof by repeating (4.43) and deduce a lower bound by exploiting sub-additivity as well as the properties (4.47) and (4.48) of the indicators defined above:

$$\Delta_{p,j} \geq 1 - \frac{\tilde{\gamma}_p||\mathbf{e}_j||_p + ||\mathbf{K}_{2,j}\hat{\mathbf{e}}_j||_p + \left|\left|\begin{bmatrix}\mathbf{I}_{n_j\times n_j} - \mathbf{K}_{1,j} & -\mathbf{K}_{2,j}\end{bmatrix}(\mathbf{r} - \mathbf{v})\right|\right|_p}{||\mathbf{e}_j||_p}. \tag{4.56}$$

Since adding additional elements to a vector does not decrease its p-norm, we obtain

$$\Delta_{p,j} \geq 1 - \frac{\tilde{\gamma}_p||\mathbf{e}_j||_p + ||\mathbf{K}_{2,j}\hat{\mathbf{e}}_j||_p + ||(\mathbf{I}_{\overline{n}\times\overline{n}} - \mathbf{P}\mathbf{Q}\mathbf{P}^{-1})(\mathbf{r} - \mathbf{v})||_p}{||\mathbf{e}_j||_p}\,. \tag{4.57}$$

[10] more precisely: $||\mathbf{A}||_{\leq f_0,p} = \max\{||\mathbf{A}\mathbf{x}||_p, \mathbf{x} = \mathbf{Q}_{f_0}\,\hat{\mathbf{x}}, ||\hat{\mathbf{x}}||_p = 1\}$.

We now write the difference on the right-hand side as a fraction and use (4.53), (4.54) to complete the proof:

$$\Delta_{p,j} \geq \frac{||\mathbf{e}_j||_p - \left(\tilde{\gamma}_p||\mathbf{e}_j||_p + ||\mathbf{K}_{2,j}\hat{\mathbf{e}}_j||_p + ||(\mathbf{I}_{\overline{n}\times\overline{n}} - \mathbf{P}\mathbf{Q}\mathbf{P}^{-1})\mathbf{Q}_{f_0}(\mathbf{r}-\mathbf{v})||_p\right)}{||\mathbf{e}_j||_p} \tag{4.58}$$

$$\geq \frac{(1-\tilde{\gamma}_p)||\mathbf{e}_j||_p - (||\mathbf{K}_{2,j}\hat{\mathbf{e}}_j||_p + \tilde{\epsilon}_{\leq f_0,p}||\mathbf{r}-\mathbf{v}||_p)}{||\mathbf{e}_j||_p}\,. \tag{4.59}$$

Clearly, the numerator of the right-hand side is positive if (4.55) holds and $\tilde{\gamma}_p < 1$. Therefore, the learning progress $\Delta_{p,j}$ is positive. □

4.5.3 Monotonic Decrease of the Maximum-Pass-Length Error

As already discussed in Section 4.3, it is technically not sufficient to consider only the measured tracking error $\mathbf{e}_j$. In fact, it is easy to construct an example in which the error is reduced on the first n_j samples in each trial j, while the (complete) maximum-pass-length error grows to infinity. This is also illustrated in Figure 4.3 on page 99. Technically, Theorem 4 is formulated too weakly to exclude such hidden error growth.

Therefore, the following corollary is given that establishes sufficient conditions for monotonic decrease of the MPL error in the presence of variable pass length.

Corollary 3 (**Monotonic decrease of the MPL error norm above a threshold**)**.** *If the conditions of Theorem 4 hold with the slight modification*

$$||\mathbf{e}_j||_p > \frac{\tilde{\epsilon}_{\leq f_0,p}||\mathbf{r}-\mathbf{v}||_p + \tilde{\kappa}_p||\hat{\mathbf{e}}_j||_p}{1-\tilde{\gamma}_p}, \tag{4.60}$$

then also the norm $||\bar{\mathbf{e}}_j||_p$ of the maximum-pass-length error is reduced from trial j to the next, i.e. $||\bar{\mathbf{e}}_{j+1}||_p < ||\bar{\mathbf{e}}_j||_p$. To prove this, apply the triangle inequality to the closed-loop error dynamics (4.41)*, which leads to*

$$\frac{||\bar{\mathbf{e}}_{j+1}||_p}{||\bar{\mathbf{e}}_j||_p} \leq \frac{||\bar{\mathbf{e}}_{j+1}||_p}{||\mathbf{e}_j||_p} \leq \frac{\tilde{\gamma}_p||\mathbf{e}_j||_p + \left|\left|\begin{bmatrix}\mathbf{K}_{2,j}\\ \mathbf{K}_{4,j}\end{bmatrix}\hat{\mathbf{e}}_j\right|\right|_p + \tilde{\epsilon}_{\leq f_0,p}||\mathbf{r}-\mathbf{v}||_p}{||\mathbf{e}_j||_p}\,. \tag{4.61}$$

Using the inequalities (4.47), (4.49) *and $||\mathbf{e}_j||_p > \tilde{\epsilon}_{\leq f_0,p}||\mathbf{r}-\mathbf{v}||_p + \tilde{\kappa}_p||\hat{\mathbf{e}}_j||_p + \tilde{\gamma}_p||\mathbf{e}_j||_p$ from* (4.60)*, we immediately see that the right-hand side of* (4.61) *is less than one.*

This result still seems to exhibit some weakness in the sense that $\tilde{\kappa}_p$ is typically close to one, as discussed above. Furthermore, replacing $||\bar{\mathbf{e}}_j||_p$ by $||\mathbf{e}_j||_p$ in the first step of (4.61) is still quite conservative. Both issues can be resolved if we decide to use the 1-norm for convergence analysis. We then find the following condition for monotonic convergence, which is clearly less conservative.

Theorem 5 (**Monotonic decrease of MPL error 1-norm above a threshold**)**.** *Consider a repetitive process* (4.4) *with regular* $\mathbf{P}$ *and input-update law* (4.38)*, and assume that the reference and disturbance signals contain only frequencies below a known frequency* f_0*, i.e.*

$$\mathbf{Q}_{f_0}(\mathbf{r}-\mathbf{v}) = (\mathbf{r}-\mathbf{v}), \tag{4.62}$$

where $\mathbf{Q}_{f_0}$*, with* $||\mathbf{Q}_{f_0}||_1 = 1$*, is a regular lifted matrix of a lowpass filter with cutoff frequency* f_0*. Assume furthermore that the learning gain matrix* $\mathbf{L}$ *is chosen such that* $\tilde{\gamma}_1 < 1$*. Then the 1-norm of the maximum-pass-length error is reduced from trial* j *to trial* $j+1$*, i.e.* $||\bar{\mathbf{e}}_{j+1}||_1 < ||\bar{\mathbf{e}}_j||_1$*, if its measured portion is large enough to fulfill the following condition:*

$$||\mathbf{e}_j||_1 > \frac{\tilde{\epsilon}_{\leq f_0,1}||\mathbf{r}-\mathbf{v}||_1 + (\tilde{\kappa}_1 - 1)||\hat{\mathbf{e}}_j||_1}{1-\tilde{\gamma}_1}\,. \tag{4.63}$$

Proof. The proof follows the lines of the proof of Corollary 3, but it exploits the fact that the 1-norm of a vector is the sum of the absolute values of its entries. Therefore, we find

$$\frac{||\bar{\mathbf{e}}_{j+1}||_1}{||\bar{\mathbf{e}}_j||_1} = \frac{||\bar{\mathbf{e}}_{j+1}||_1}{||\mathbf{e}_j||_1 + ||\hat{\mathbf{e}}_j||_1} \leq \frac{\tilde{\gamma}_1||\mathbf{e}_j||_1 + \tilde{\kappa}_1||\hat{\mathbf{e}}_j||_1 + \tilde{\epsilon}_{\leq f_0,1}||\mathbf{r}-\mathbf{v}||_1}{||\mathbf{e}_j||_1 + ||\hat{\mathbf{e}}_j||_1}\,, \tag{4.64}$$

which is less than one, since (4.63) yields

$$||\mathbf{e}_j||_1 > \tilde{\gamma}_1||\mathbf{e}_j||_1 + \tilde{\epsilon}_{\leq f_0,1}||\mathbf{r}-\mathbf{v}||_1 + (\tilde{\kappa}_1 - 1)||\hat{\mathbf{e}}_j||_1\,.$$

□

Theorem 4, Corollary 3 and Theorem 5 provide practically useful conditions for convergence analysis. In particular, the conditions (4.55) and (4.63) yield upper bounds of the residual errors that may occur when a Q-filter is used. It is known from standard ILC theory that these residual errors depend on $\mathbf{r}-\mathbf{v}$. In variable-pass-length systems, however, they also depend on the hypothetical tracking error $\hat{\mathbf{e}}_j$ that occurs on the last $\overline{n} - n_j$ samples.

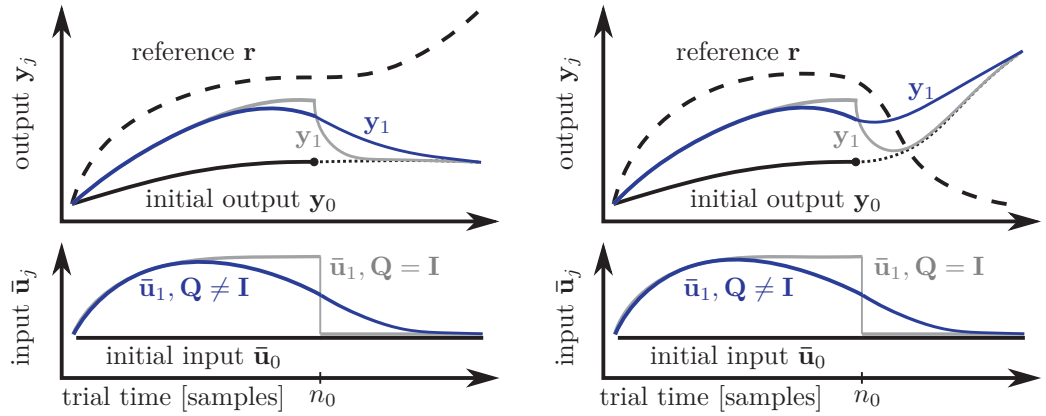

Figure 4.4: Blending effect of a zero-phase Q-filter in variable-pass-length learning (first trial short, second complete). The tracking error $\mathbf{e}_0$ measured on the first n_0 samples influences the last $\overline{n}-n_0$ samples of the next input $\bar{\mathbf{u}}_1$ and output $\mathbf{y}_1$. Vice versa, the last $\overline{n}-n_0$ samples of $\langle \mathbf{e}_0 \rangle_{\overline{n}}$ used in (4.38) slightly deteriorate the output $\mathbf{y}_1$ at sample instants just before n_0. The extrapolating effect of the Q-filter is usually advantageous (*left*), but if $(\mathbf{r}-\mathbf{v})$ contains high frequencies, it might become slightly disadvantageous (*right*).

An explanation for this phenomenon is found by inspecting the learning law (4.38). Due to the Q-filter, the last $\overline{n}-n_j$ samples of the previous input trajectory $\mathbf{u}_j$ have an influence on the first n_j samples of the updated input trajectory $\mathbf{u}_{j+1}$, and vice versa. This results in a crosstalk of the first n_j and the last $\overline{n}-n_j$ samples of the tracking error in the closed-loop dynamics (4.41). If the Q-filter was $\mathbf{Q}=\mathbf{I}_{\overline{n}\times\overline{n}}$ and $\mathbf{L}$ was almost the inverse of $\mathbf{P}$, then the first segment (samples 1 to n_j) of the error would be reduced, while the second segment (samples $\overline{n}-n_j$ to $\overline{n}$) would remain almost unchanged, see also Section 4.4 above. A Q-filter with $f_{\mathbf{Q}}$ below the Nyquist frequency, however, causes a blending of the first segment (the one with error reduction) and the second segment (the one with unchanged error).

This blending effect is illustrated in Figure 4.4. As suggested therein, the potential deterioration of the learning progress is small if $f_{\mathbf{Q}}$ is sufficiently large. This interrelation also becomes manifest in the condition (4.55) for positive learning progress, wherein $\hat{\mathbf{e}}_j$ is multiplied by $\mathbf{K}_{2,j}$. Since $\mathbf{K}_{2,j}$ is (for all n_j) an off-diagonal block element of $\mathbf{PQP}^{-1}$, its entries are small for large Q-filter frequencies $f_{\mathbf{Q}}$.

Figure 4.4 further suggests that the aforementioned deterioration of the learning progress on the first n_j samples is partially compensated or even outweighed by a reduction of the tracking error on the last $\overline{n}-n_j$ samples that is due to the extrapolating effect

of the blending. This partial compensation of both effects is also evident in the factor $(\tilde{\kappa}_1 - 1)$ appearing before the norm $||\hat{\mathbf{e}}_j||_1$ of the hypothetical tracking error in the condition (4.63) for monotonic decrease of the MPL error 1-norm.

In Section 4.8, we will investigate the discussed effects further by simulations. Prior to this, we extend the above findings to the case of multiple-input multiple-output systems and summarize them in guidelines for controller design.

4.6 Multiple-Input Multiple-Output Systems

To simplify the preceding derivations and arguments, we have assumed that the input and the output of the system to be controlled are both scalar. At this point, we shall briefly comment on the value of the above results for multiple-input multiple-output systems with $u(t), y(t), r(t), v(t) \in \mathbb{R}^{m\times 1}$.

Obviously, for such systems $\bar{\mathbf{u}}_j, \bar{\mathbf{y}}_j, \bar{\mathbf{e}}_j, \mathbf{r}, \mathbf{v} \in \mathbb{R}^{m\overline{n}\times 1}$ and $\mathbf{y}_j, \mathbf{e}_j \in \mathbb{R}^{mn_j\times 1}$ with

$$
\begin{aligned}
&\bar{\mathbf{u}}_j := \Big[u(t_{0,j})^T, u(t_{0,j}+t_\mathrm{s})^T, \ldots, u(t_{0,j}+(\overline{n}-1)t_\mathrm{s})^T\Big]^T,\\
&\mathbf{P}, \mathbf{L}, \mathbf{Q} \in \mathbb{R}^{m\overline{n}\times m\overline{n}},\\
&\langle\cdot\rangle_{n_j} : \mathbb{R}^{m\overline{n}\times 1} \to \mathbb{R}^{mn_j\times 1},\\
&\langle\cdot\rangle_{\overline{n}} : \mathbb{R}^{mn_j\times 1} \to \mathbb{R}^{m\overline{n}\times 1},\\
&\mathbf{H}_{n_j} := \mathrm{blockdiag}\{\mathbf{I}_{mn_j\times mn_j}, \mathbf{0}_{m(\overline{n}-n_j)\times m(\overline{n}-n_j)}\}.
\end{aligned}
$$

With these slight modifications and with $\mathbf{I}_{mn_j\times mn_j}$ instead of $\mathbf{I}_{n_j\times n_j}$, we find that the learning law, the definition of the maximum-pass-length error and the closed-loop dynamics are equivalent to (4.3), (4.5), (4.8), respectively.

Likewise, we proceed by redefining the dimensions of the partitions

$$
\begin{aligned}
&\mathbf{G}_{1,j} \in \mathbb{R}^{mn_j\times mn_j}, && \mathbf{G}_{2,j} \in \mathbb{R}^{mn_j\times m(\overline{n}-n_j)},\\
&\mathbf{G}_{3,j} \in \mathbb{R}^{m(\overline{n}-n_j)\times mn_j}, && \mathbf{G}_{4,j} \in \mathbb{R}^{m(\overline{n}-n_j)\times m(\overline{n}-n_j)},\\
&\mathbf{K}_{1,j} \in \mathbb{R}^{mn_j\times mn_j}, && \mathbf{K}_{2,j} \in \mathbb{R}^{mn_j\times m(\overline{n}-n_j)},\\
&\mathbf{K}_{3,j} \in \mathbb{R}^{m(\overline{n}-n_j)\times mn_j}, && \mathbf{K}_{4,j} \in \mathbb{R}^{m(\overline{n}-n_j)\times m(\overline{n}-n_j)}.
\end{aligned}
$$

This finally reveals that all of the results of Sections 4.4 and 4.5 also hold analogously for the considered case of multiple-input multiple-output systems.

4.7 Controller Design Guidelines

As Theorem 4 suggests, it is advantageous to choose a learning gain matrix that leads to a small convergence indicator $\tilde{\gamma}_p$. As also discussed above, the choice $\mathbf{L} = \mathbf{P}^{-1}$ leads to the fastest convergence. This, however, assumes that the input-output dynamics of the system to be controlled are precisely known. If model uncertainties are significant, then a more careful choice is advisable. As discussed in many contributions to classic ILC (see for example Bristow et al. [11] and references therein), a small diagonal learning gain will yield $||\mathbf{I}_{\overline{n}\times\overline{n}} - \mathbf{PL}||_p$ just below one for a large class of system dynamics, which results in slow convergence with a potentially large residual error but good robustness with respect to model uncertainties.

When faced with the question of how to choose the cutoff frequency $f_{\mathbf{Q}}$ of the Q-filter, one should note the following relationships. For a given f_0, the indicator $\tilde{\epsilon}_{\leq f_0,p}$ becomes small if $f_{\mathbf{Q}}$ is raised above f_0. However, as discussed before, a small $f_{\mathbf{Q}}$ improves robustness with respect to model uncertainties by preventing high-frequency portions of the measured output from influencing the learning process. As in standard control theory, one must balance between controller performance (bandwidth) on the one hand and robustness and measurement noise rejection on the other hand.

From the preceding discussion we conclude the following controller design guidelines for ILC systems of the form (4.4), (4.38):

G1. An upper bound f_0 for the largest frequency that occurs in the reference signal $\mathbf{r}$ or in the disturbance signal $\mathbf{v}$ should be known.

G2. The model $\mathbf{P}$ should approximate the input-output dynamics of the system (at least with small or moderate uncertainties) for frequencies between 0 and f_0.

G3. The cutoff frequency $f_{\mathbf{Q}}$ of the Q-filter $\mathbf{Q}$ should be smaller than the smallest frequency at which large model uncertainties occur.

G4. At the same time, $f_{\mathbf{Q}}$ should be chosen such that a small residual indicator $\tilde{\epsilon}_{\leq f_0,p}$ is achieved for the given system dynamics $\mathbf{P}$. This typically implies $f_{\mathbf{Q}} > f_0$.

G5. The learning gain matrix $\mathbf{L}$ should be chosen such that a small convergence indicator $\tilde{\gamma}_p$ is achieved for some induced matrix norm $||\cdot||_p$.

Following these guidelines will prevent hidden error growth and will assure that the tracking error is quickly reduced (at least) until its norm falls below a small threshold.

4.8 Simulation Study of an Example System

The goal of this section is to illustrate some variable-pass-length learning phenomena and to demonstrate the usefulness of the criteria derived above. For this purpose, controller design and simulations are carried out for a simple example application system that is motivated by Nahrstaedt et al. [71]. There, functional electrical stimulation of the tibialis anterior muscle is used to induce a predefined foot movement during the swing phase of gait (i.e. between toe-off and initial contact, when the foot moves forward without ground contact).

4.8.1 FES System Model

The stimulation pulse width of the FES current pulses (in tenths of milliseconds) and the ankle joint angle[11] (in degrees) are the input variable $u(t)$ and the output variable $y(t)$, respectively. Then the following linear difference equation model approximates the input-output dynamics of the system at a sampling interval of $t_\mathrm{s} = 0.02\,\mathrm{s}$ (cf. Nahrstaedt et al. [72]):

$$\begin{aligned} &y(t) + a_1 y(t - t_\mathrm{s}) + a_2 y(t - 2t_\mathrm{s}) = bu(t - 2t_\mathrm{s}), \\ &a_1 = -0.8097002,\ a_2 = -0.0777289,\ b = 0.6634. \end{aligned} \tag{4.65}$$

The ankle joint angle $y(t)$ shall be controlled to follow a predefined reference trajectory in each trial, i.e. in the swing phase of each stride.

Based on experimental data (Seel et al. [105]), the duration of swing phase in the gait of stroke patients is estimated to vary between 0.6 s and 1.0 s, which corresponds to $\underline{n} = 30$ and $\overline{n} = 50$. Therefore, the following full-length lifted signal vectors are defined:

$$\bar{\mathbf{u}}_j = [u_j(t_0 - t_\mathrm{s}),\, u_j(t_0), \ldots,\, u_j(t_0 + 48t_\mathrm{s})]^T \in \mathbb{R}^{\overline{n}\times 1}, \tag{4.66}$$

$$\bar{\mathbf{y}}_j = [y_j(t_0 + t_\mathrm{s}),\, y_j(t_0 + 2t_\mathrm{s}), \ldots,\, y_j(t_0 + 50t_\mathrm{s})]^T \in \mathbb{R}^{\overline{n}\times 1}, \tag{4.67}$$

$$\mathbf{r} = [r(t_0 + t_\mathrm{s}),\, r(t_0 + 2t_\mathrm{s}), \ldots,\, r(t_0 + 50t_\mathrm{s})]^T \in \mathbb{R}^{\overline{n}\times 1}, \tag{4.68}$$

$$\mathbf{v} = [v(t_0 + t_\mathrm{s}),\, v(t_0 + 2t_\mathrm{s}), \ldots,\, v(t_0 + 50t_\mathrm{s})]^T \in \mathbb{R}^{\overline{n}\times 1}, \tag{4.69}$$

where the input-output time shift of two samples is chosen to compensate the relative degree of the system dynamics (4.65). The Markov parameters of (4.65) are determined

[11] for the sake of simplicity, only the dorsiflexion joint angle is considered in this chapter, i.e. the angle between the instep and the tibia; see Chapter 6 for a more detailed consideration of this application

and, from those, the (regular, lower triangular Toeplitz) lifted-system matrix $\mathbf{P}$ is calculated.

Based on experimental data, reasonable values for the sequence of pass lengths $\{n_j\}$, for the disturbance signal $\mathbf{v}$ and for the desired output $\mathbf{r}$ are found. The initial input $\bar{\mathbf{u}}_0$ is chosen to be a constant pulse width of 0.2 ms.

4.8.2 Iterative Learning Controller Design

A two-parameter learning gain matrix $\mathbf{L}_{\text{opt}}$ is employed with $(\mathbf{L}_{\text{opt}})_{i,i} = l_1 \; \forall i \in [1, \overline{n}]$ on the main diagonal and $(\mathbf{L}_{\text{opt}})_{i,i-1} = l_2 \; \forall i \in [2, \overline{n}]$ just below the main diagonal. If no Q-filter was used, this would correspond to the following first-order controller dynamics:

$$\begin{aligned} u_{j+1}(t) = u_j(t) &+ l_1 \left(r(t + 2t_\text{s}) - y_j(t + 2t_\text{s}) \right) \\ &+ l_2 \left(r(t + 1t_\text{s}) - y_j(t + 1t_\text{s}) \right), \quad t = t_0, t_0 + t_\text{s}, \ldots, t_0 + (n_j - 1)t_\text{s} \,. \end{aligned} \tag{4.70}$$

The parameters of $\mathbf{L}_{\text{opt}}$ are chosen by numerically minimizing the norm $||\mathbf{I}_{\overline{n}\times\overline{n}} - \mathbf{P}\mathbf{L}_{\text{opt}}||_1$, as suggested by Theorem 2, over wide ranges of both l_1 and l_2. For $l_1 = 1.5$, $l_2 = -1.35$, an approximate plant inversion with a small convergence indicator of $\gamma_1 < 0.13$ is achieved. Therefore, when employing the learning law (4.6), almost-strict[12] monotonic convergence of $||\bar{\mathbf{e}}_j||_1$ (for all $j, n_j, \mathbf{v}, \mathbf{u}_0$) follows from Corollary 1 without further computational effort. By calculation of $\max_{n\in\{\underline{n},\ldots,\overline{n}\}} ||\mathbf{I}_{\overline{n}\times\overline{n}} - \mathbf{P}\mathbf{L}_{\text{opt}}\mathbf{H}_n||_2 \approx 1.004$, it is furthermore found that the Euclidean norm $||\bar{\mathbf{e}}_j||_2$ of the maximum-pass-length error is not only bounded by $||\bar{\mathbf{e}}_j||_1$ from above, but also bounded to rise (if at all) in no pass by more than 0.4%.

A zero-phase lowpass filter (2^{nd}-order Butterworth) is used as a Q-filter. Since $\mathbf{r}$ and $\mathbf{v}$ are known to contain only frequencies below $f_0 = 2\,\text{Hz}$, the Q-filter cutoff frequency is chosen to be $f_\mathbf{Q} = 5\text{Hz}$, such that $\tilde{\epsilon}_{\leq f_0,2} = 0.214$. Calculation of the convergence indicator defined in Section 4.5 yields $\tilde{\gamma}_2 = 0.092$. According to Corollary 3, this implies that the Euclidean norm of the MPL error decreases, (at least) as long as the measured error norm is larger than a small threshold.

In practice, much less reliable model knowledge might be available. Therefore, and for the sake of comparison, a second learning gain $\mathbf{L}_{\text{diag}}$ is designed by simply choosing a small diagonal learning gain $\mathbf{L}_{\text{diag}} = 0.12\,\mathbf{I}_{\overline{n}\times\overline{n}}$, which yields a convergence indicator of $\tilde{\gamma}_2 = 0.954$. Obviously, this also guarantees monotonic decrease of $||\bar{\mathbf{e}}_j||_2$ for large

[12] in the sense of Corollary 1, i.e. $||\bar{\mathbf{e}}_{j+1}||_1 < ||\bar{\mathbf{e}}_j||_1$ for all $n_j \in \{\underline{n}, ..., \overline{n}\}$ unless $\mathbf{e}_j$ is the zero vector

measured error norms, but a much slower decrease and a potentially larger residual error norm should be expected.

4.8.3 Simulation Results

The lifted-system model $\mathbf{P}, \mathbf{v}$ from Section 4.8.1 is simulated with both learning controllers $\{\mathbf{L}_{\text{opt}}, \mathbf{Q}\}$ and $\{\mathbf{L}_{\text{diag}}, \mathbf{Q}\}$ designed in Section 4.8.2. The scenario consists of seven passes (trials) with pass lengths of $\{n_j\}_{j=0}^{6} = \{34, 40, 30, 46, 50, 50, 37\}$. Simulation results are presented in Figures 4.5 and 4.6.

The output trajectories depicted in Figure 4.5 illustrate a core phenomenon of variable-pass-length learning: Whenever a pass is long enough to encounter samples that have not been reached before, the controller starts to learn this piece of trajectory almost from scratch, i.e. starting with the according piece of $\bar{\mathbf{y}}_0$ that (hypothetically) would have been measured in the first pass if it had been long enough. Due to very fast and accurate learning dynamics, the very next output already resembles the reference (up to the longest pass length seen so far). The similarity of $\mathbf{y}_2$ and $\mathbf{y}_3$ shows that, when shorter passes occur, controller performance is not improved significantly any more.

In contrast, the diagonal controller $\mathbf{L}_{\text{diag}}$ learns more slowly and in a qualitatively different fashion. The measured errors result in input updates that clearly affect the output less precisely. After the first three learning steps (with pass lengths $n_0 = 34$, $n_1 = 40$ and $n_2 = 30$), the error on the first 30 samples is still significant. However, the samples $40 - 46$ of $\mathbf{y}_3$ are closer to the reference than the same samples of $\mathbf{y}_3$ in Figure 4.5. This extrapolating behavior of the less precise input-update law seems advantageous. However, if either $\mathbf{v}$ or $\mathbf{r}$ would exhibit steeper slopes on the time interval $t \in [\underline{n}\, t_{\text{s}}, ..., \overline{n}\, t_{\text{s}}]$, this behavior would obviously lead to inferior performance (similar to the effect in Figure 4.4).

In several further simulations, similarly quick reduction of the tracking error is observed for both learning gain matrices, which demonstrates that the criteria derived in the previous sections are rather conservative – just as the convergence criteria of classic ILC theory. Nevertheless, simulations with modified controller parameters l_0, l_1, l_2 reveal that the proposed convergence indicators γ_p and $\tilde{\gamma}_p$ are useful predictors of the learning speed in the presence of variable pass length. Controllers with smaller indicators achieve, in general, faster convergence. Therefore, it is advisable to minimize them during controller design.

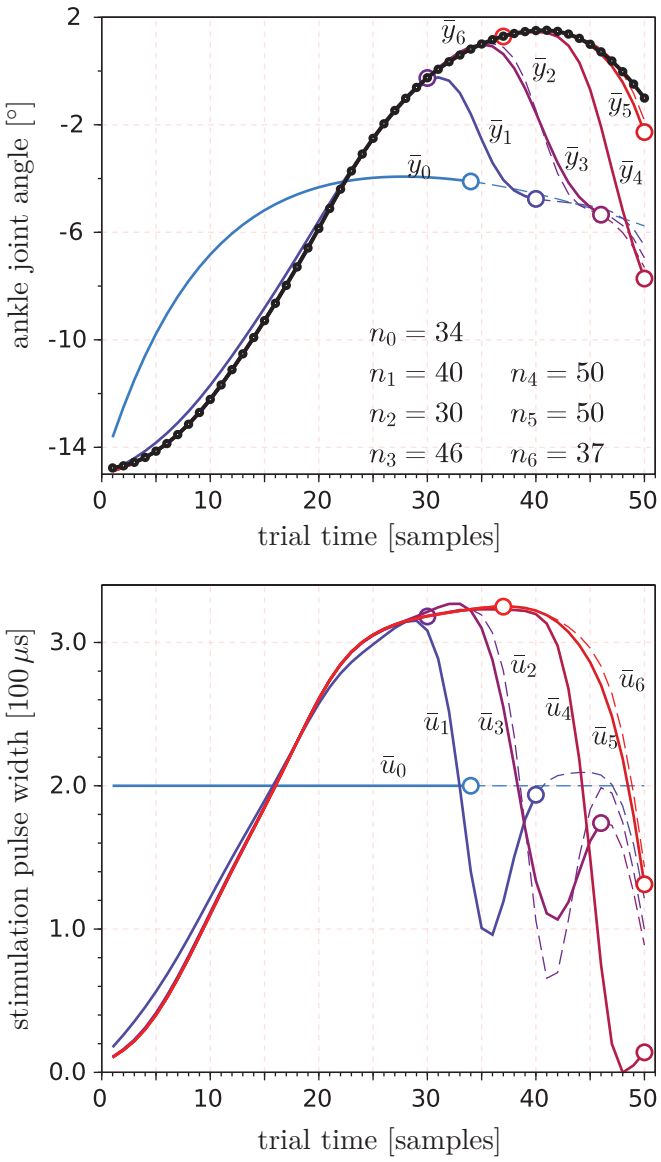

Figure 4.5: Variable-pass-length ILC with optimized learning gain $\mathbf{L}_{\text{opt}}$: The controller learns to produce the reference $\mathbf{r}$ (black solid with dots) quickly. However, at the largest previously seen pass length, the output drops to its initial trace at the end of each pass that is longer than all previous passes, for example at sample 34 of $\mathbf{y}_1$ and at sample 40 of $\mathbf{y}_3$. The end of each pass is marked with a dot. Lines are continued in dashed style to illustrate the (hypothetical) maximum-pass-length errors $\bar{\mathbf{e}}_j = \mathbf{r} - \bar{\mathbf{y}}_j$.

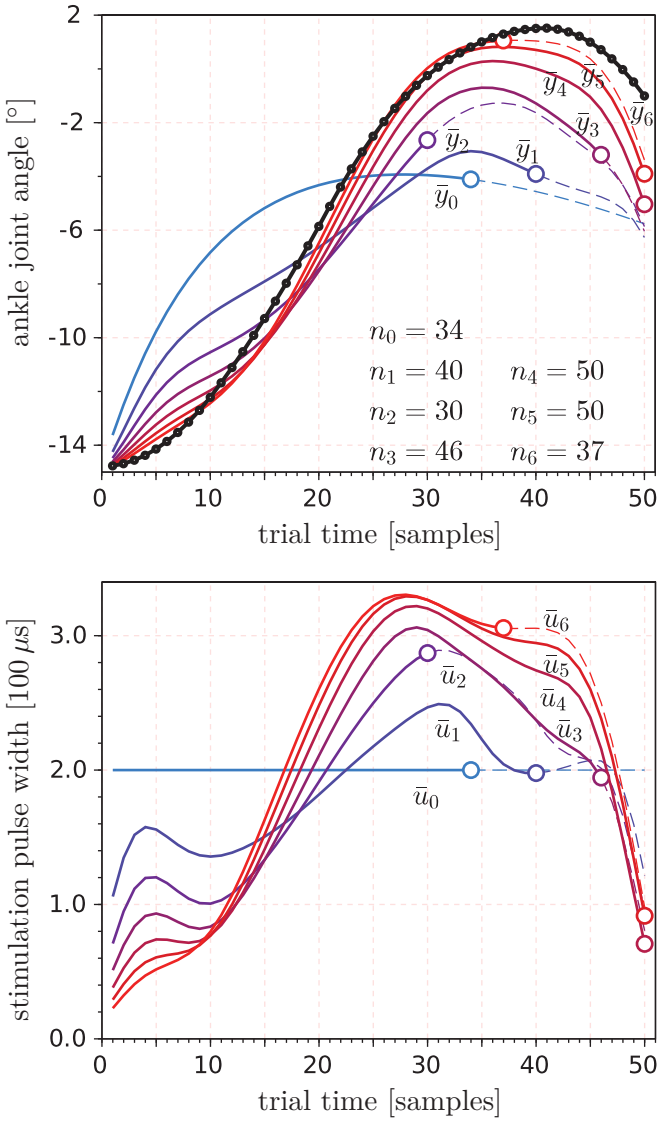

Figure 4.6: Variable-pass-length ILC with diagonal learning gain $\mathbf{L}_{\text{diag}}$: Starting from a constant input $\bar{\mathbf{u}}_0$, the controller learns to produce the reference $\mathbf{r}$ (black solid with dots) more slowly and in a qualitatively different fashion than the controller with two-parameter learning gain.

4.8.4 Numerical Values for Simulation

Finally, for the sake of completeness, the numerical values of the system model and the controller components are provided.

The lifted-system matrix $\mathbf{P} \in \mathbb{R}^{50\times 50}$ is Toeplitz and thus completely defined by the values of its first column. These can be gained from the impulse response of (4.65) by omitting the leading zero-values. Precisely, the first column of $\mathbf{P}$ is

$$\mathbf{P}(:,1) = [0.6634000, 0.5371551, 0.4865000, 0.4356716, \ldots]\,. \tag{4.71}$$

Furthermore, every fifth entry of the reference and the disturbance, respectively, is provided here (to be connected by splines):

$$\begin{aligned}
\mathbf{r}(1:5:50) =& [-14.767, -13.86, -11.679, -8.6404, && (4.72)\\
& -5.114825, -1.962725, 0.0655, 1.1659, 1.51685, 0.71465], && (4.73)\\
\mathbf{v}(1:5:50) =& [-14.952, -14.772, -14.692, -14.712, && (4.74)\\
& -14.832, -15.052, -15.372, -15.792, -16.312, -16.932]. && (4.75)
\end{aligned}$$

The learning gain matrix $\mathbf{L}_{\text{diag}}$ is a Toeplitz diagonal matrix with $\mathbf{L}_{\text{diag}}(i,i) = 0.12\,\mathbf{I}_{\overline{n}\times\overline{n}}$. The learning gain matrix $\mathbf{L}_{\text{opt}}$ is a Toeplitz matrix with $\mathbf{L}_{\text{opt}}(i,i) = 1.5\ \forall i \in [1,50]$ and $\mathbf{L}_{\text{opt}}(i+1,i) = -1.35\ \forall i \in [1,49]$. All other entries of $\mathbf{L}_{\text{opt}}$ are zero. The Q-filter is calculated in two steps. First a Butterworth filter with cutoff frequency of 5Hz is designed:

$$Q(z) = \frac{0.067 + 0.135z + 0.067z^2}{0.413 - 1.143z + z^2}\,. \tag{4.76}$$

Then its response to its own time-inverted impulse response yields the first row of its lifted representation

$$\mathbf{Q}(1,:) = [0.214255, 0.1898998, 0.1331573, 0.0738052, \ldots]\,. \tag{4.77}$$

The symmetric Toeplitz matrix $\mathbf{Q}$ is fully defined by this vector. Multiplying a lifted signal vector by $\mathbf{q}$ corresponds to a forward-and-then-backward filtering of the signal with the above filter $Q(z)$ and thus attenuates high frequencies without introducing lag, see for example Elci et al. [23].

4.9 Conclusions

A framework for the analysis of repetitive systems with variable pass length was developed. Iterative learning control schemes with and without lowpass filtering were proposed. The resulting closed-loop learning dynamics were derived and analyzed with respect to monotonous reduction of the tracking error. To cope with the variable dimension of the measured tracking error, we introduced a learning progress measure and the hypothetical maximum-pass-length error. Both concepts proved to be useful for convergence analysis in the presence of variable pass lengths.

For the standard input-update law without Q-filter, we obtained necessary and sufficient conditions that guarantee monotonic convergence of the MPL error norm. For the extended learning law with Q-filter, we derived conditions that assure a reduction of the tracking error at least until it falls below a potentially very small threshold. In this context, the issue of conservativeness in matrix-norm-based convergence criteria was addressed by proposing a frequency-weighted residual indicator to assess the non-zero residual error that is associated with Q-filter usage.

Based on all findings, we derived practical guidelines for the design of iterative learning controllers in the presence of variable pass length. Since we did not restrict $\mathbf{P}$ to be Toeplitz, all convergence criteria can be employed for a very large class of systems including time-variant (but iteration-invariant) systems. Furthermore, all findings and guidelines hold as well if the pass length is (almost) constant and can therefore also be employed for convergence analysis and controller design in classic ILC systems. Although motivated by biomedical applications, the new methods are equally useful for control problems from other application domains in which the same challenges occur, see for example Guth et al. [34].

The simulation example analyzed in Section 4.8 illustrated some of the complexity that the closed-loop dynamics of ILC systems can exhibit when the pass length is not constant. Furthermore, we utilized the example to demonstrate how the proposed convergence criteria can be used to design controllers and predict convergence rates. With respect to the latter, the derived criteria were found to be similarly conservative as classic convergence conditions. Nevertheless, the controller design guidelines for $\mathbf{L}$ and $\mathbf{Q}$ will proof to be very useful in Chapters 5 and 6. There, we will apply the guidelines to iterative learning control tasks in noninvasive blood pressure measurement and in FES-based foot motion control during walking, respectively.

Future efforts may aim at simplified criteria for monotonic convergence of the Euclidean MPL error norm as well as at convergence analysis in nonlinear variable-pass-length

systems. One may as well focus on the special cases in which additional (prior or learned) knowledge on the input-output dynamics or the disturbance is available that allows a reliable prediction of the hypothetical error that would have occurred in a trial after its early termination.

Beyond all that, it should be noted that in the motivational examples in Section 4.1, as in most other biomedical applications, the variability of the pass length is only one of the difficulties that complicate the employment of classic ILC theory. Issues like input saturation or iteration-variance (in the process dynamics, the initial conditions, the disturbance, or the reference signal) should be addressed individually as well as in the context of variable-pass-length systems.

5 Continuous Noninvasive Blood Pressure Measurement

To overcome the limitations of standard blood pressure measurement techniques, a non-invasive continuous method has recently been developed by Weber et al. [124, 125]. This method requires precise control of the blood flow through a superficial artery. The flow is measured using ultrasound and influenced by manipulating the pressure inside an inflatable air balloon which is placed over the artery. Previous attempts to solve the inherent control problem using standard feedback control have resulted in limited controller performance [125].

This chapter is concerned with the question whether the controller performance can be improved by exploiting the repetitive nature of the control problem. To this end, we will design a learning cascade controller, which consists of two standard feedback control loops and an iterative learning controller. The proposed controller will be evaluated experimentally using the artificial cardiovascular system model developed by Weber et al. [125].

5.1 Introduction to the Application

Blood pressure measurement is of vital importance in the diagnosis and treatment of many diseases. In particular, it is a cornerstone for the diagnosis and treatment of, as well as for the research on, arterial hypertension [88]. For more than one hundred years [44], the sphygmomanometry developed by Riva-Rocci and Korotkoff has been the most commonly used method. Its limitations, however, are becoming increasingly evident and, therefore, alternative solutions are under investigation [80]. Especially when continuous blood pressure monitoring is desirable, this conventional method is of disadvantage, since it only allows repeated measurements at intervals of a few minutes. Furthermore, only the maximum and the minimum of the blood pressure curve, i.e. the systolic and the diastolic blood pressure, respectively, are identified. Finally, according to O'Brien [76], most devices that use this measurement principle do not meet the standards set by the British Hypertension Society (BHS) protocol and by the US Association for the Advancement of Medical Instrumentation (AAMI).

These problems, and especially the problem of continuous measurement, are overcome by another non-invasive technique that was proposed by Penaz [85] about twenty years ago. The method uses continuous plethysmographic detection of the arterial volume

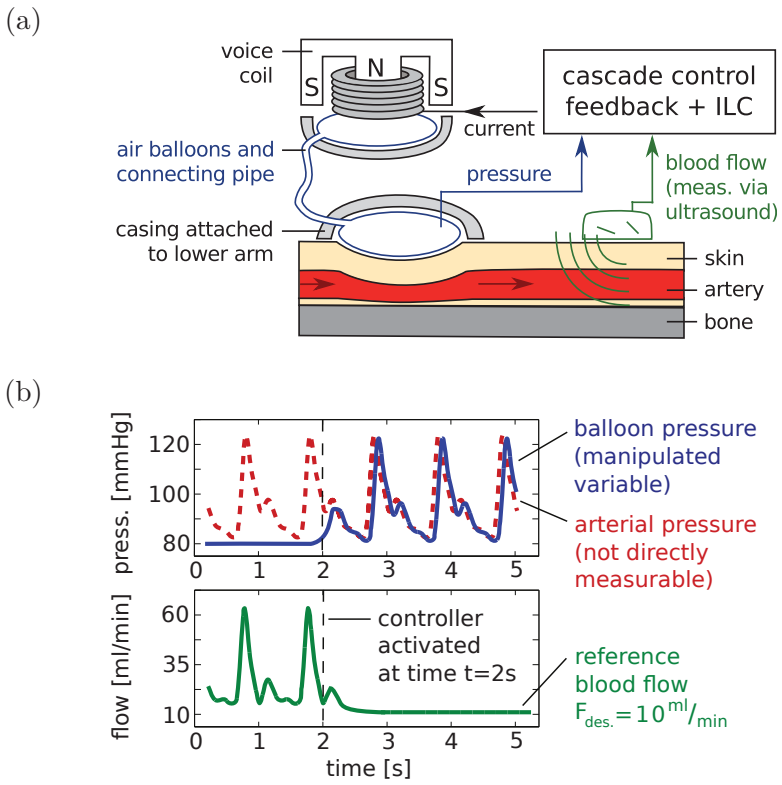

Figure 5.1: *(a)* Non-invasive blood pressure measurement system. A voice coil and two interconnected inflatable air balloons are used to press upon a superficial artery and thus reduce the blood flow, which is measured via a Doppler ultrasound sensor. *(b)* By controlling this flow to a constant small value, one obtains equality – up to a small constant offset – between the controller-induced balloon pressure and the arterial blood pressure.

in a given measurement volume and closed-loop control for continuously changing the pressure in the measurement volume such that the arterial volume is maintained at a constant value, at which the tension of the arterial wall equals zero. Thereby, the desired arterial pressure is obtained as the pressure in the measurement volume.

Weber et al. [125] enhanced the original approach by using ultrasound to measure the arterial blood flow and maintain it at a small constant value. In that control system, the manipulated variable is the pressure of an inflatable air balloon which is attached to the lower arm such that it pushes upon the radial artery. As in the original setup, the periodic pressure curve that is required to accomplish the control task equals the course of the blood pressure to be determined. Figure 5.1 depicts the main components of the measurement system and illustrates the measurement principle. Weber et al. [125] employed a simple feedback controller to regulate the arterial blood flow to a small constant value. At a coarse scale, this goal was achieved. However, the ultrasound-based flow measurement is characterized by a particularly bad signal-to-noise ratio. Therefore, setpoint deviations of up to a third of the peak amplitude were obtained.

Regardless of the particular controller and its parameterization, traditional feedback control can only achieve limited bandwidth in the presence of measurement noise. In this specific application, limited bandwidth implies limited blood pressure measurement accuracy. In order to improve the controller performance, we will exploit the fact that the blood pressure curve is periodic and exhibits only small changes from one pulse to the next. More precisely, by looking at the pressure and flow curves of consecutive pulses batch-wise, we can adapt the balloon pressure curve of the next pulse based on the flow curve of the previous trials and thereby introduce a feedback from pulse to pulse. This approach is known as Iterative Learning Control (ILC) and has been introduced in Chapter 2. Applying ILC yields the additional advantage that lowpass filters with zero phase shift [23] can be applied to the noisy flow measurement signal. Therefore, it is expected that the controller performance, and thus the accuracy of the novel measurement system, can be improved significantly by the use of ILC.

In the remainder of this chapter, we examine the challenges and benefits of ILC methods to the flow control task in the introduced non-invasive continuous blood pressure measurement system. A cascaded control structure consisting of two discrete-time feedback controllers, surrounded by an iterative learning control loop, is designed. The system identification and model-based controller design is carried out in Section 5.2. Subsequently, the controller performance is evaluated in Section 5.3 via a series of experiments with a laboratory model of the cardiovascular system.

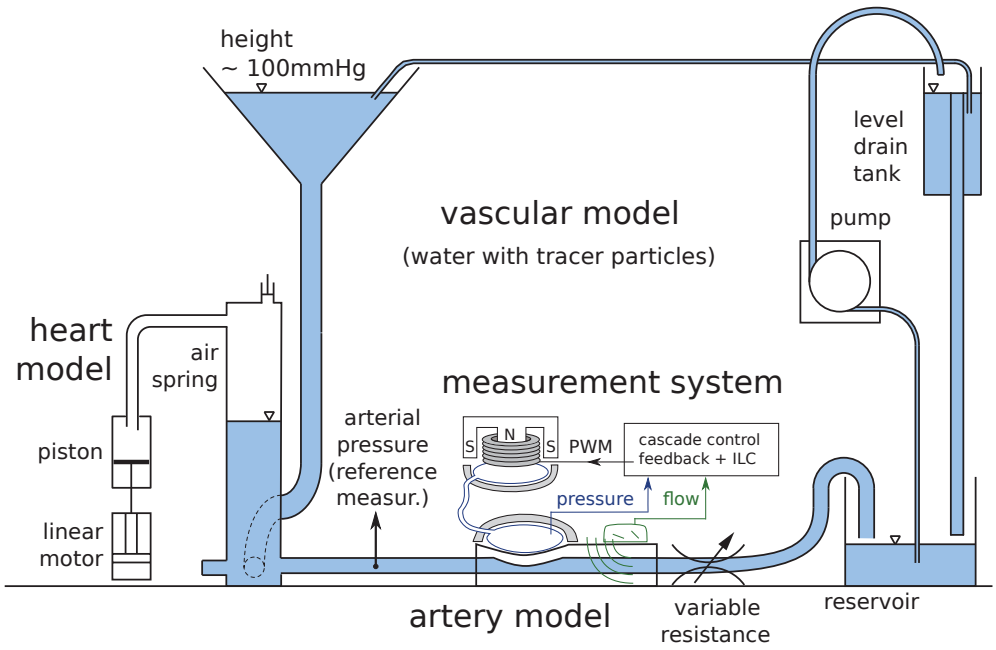

Figure 5.2: Experimental setup including a laboratory model of the cardiovascular system and the novel measurement system. The cardiovascular system model has been developed and was provided by Weber et al. [125]. It provides an artificial artery with either constant or physiologically pulsating blood pressure. The latter is achieved by means of an oscillating piston, which is driven by a linear motor. Adapted from Weber et al. [125].

5.2 Controller Design

For controller design, the experimental setup described by Weber et al. [125] and in Figure 5.2 is used. It provides an artificial artery with either constant or physiologically pulsating blood pressure. The measurable signals are the air balloon pressure and the ultrasound signal of the arterial blood flow. Both signals are obtained at a sample rate of 400 Hz, but the ultrasound signal is lowpass filtered and downsampled to 20 Hz in order to remove a large portion of the severe measurement noise. Even after this treatment, the signal exhibits a signal-to-noise ratio below 3. Since the precise relation of the ultrasound signal to physical flow units is unknown (and not essential for the solution of the given control task), we denote the maximum amplitude of the ultrasound signal observed during normal operation by $y_{\max}$ and present the signal in percent of this value in the remainder of this chapter.

The current of the voice coil actuator is set via pulse width modulation (PWM) at a sample rate of 400 Hz. The larger the duty cycle is chosen, the more the actuator pushes on an inflatable polyurethane balloon. Via the connecting tube of about 50 cm length, this increase in pressure is forwarded to the second pressure balloon, which is constrained by a housing to push, through a gelatin layer, on the artificial artery. Through this artery flows a fluid, which carries tracer particles to mimic the ultrasound Doppler effect observed in blood. When the balloon pushes on the gelatin layer, the flow of this fluid is reduced and the amplitude of the ultrasound signal decreases.

In the following, a control structure is designed to maintain the blood flow at a constantly small value by manipulating the voice coil current. The innermost loop of the cascaded structure is a fast feedback control of the balloon pressure. The reference of this control loop is set by a feedback control of the blood flow. The reference of this loop is updated periodically by an ILC algorithm. Figure 5.3 illustrates this controller structure by a block diagram. In the following subsections, the design of the feedback controllers and the ILC are carried out in detail.

5.2.1 Pressure and Flow Controller

The design of the pressure controller is carried out via model-based, discrete-time pole placement. In a first step, the dynamics from voice coil duty cycle (in %) to balloon pressure (in mmHg) are identified by applying a pseudo-random binary signal to the current and estimating the parameters of a discrete-time transfer function from the pressure response recorded at 400 Hz. The pressure of the artificial artery is chosen

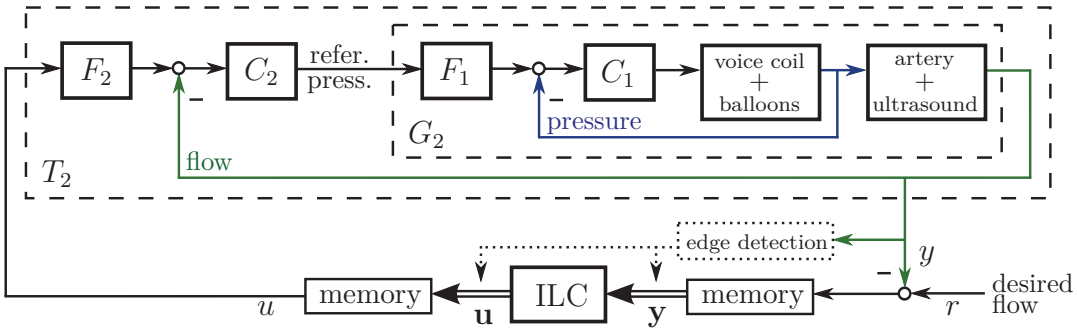

Figure 5.3: Block diagram of the controller structure. Measurement signals are the pressure, which is controlled by the inner feedback loop, and the flow, which is controlled by the outer feedback loop. Both controllers are two-degree-of-freedom structures consisting of prefilters F_i and feedbacks C_i, $i = 1, 2$. The outermost loop is closed by an iterative learning controller, which learns in trials triggered by an edge detection of the flow signal. The ILC records the output trajectory of each trial and batch-wise updates the input trajectory that is applied as a reference to the outer feedback control loop.

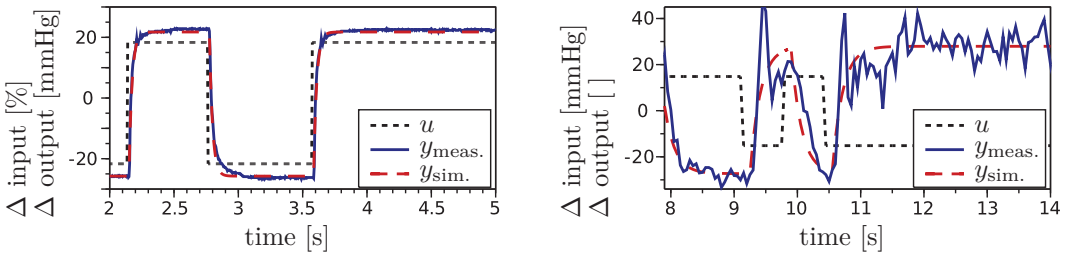

Figure 5.4: System identification of the open-loop pressure dynamics and the flow dynamics with closed pressure loop. *Left:* The deviations of the voice coil current and the balloon pressure from their operating point values are plotted as input and output, respectively. *Right:* The deviations of the reference pressure and the blood flow from their operating point values are plotted as input and output, respectively. In both cases, a first order transfer function (see (5.1) and (5.4)) yields good accordance of simulated and measured data.

constant during this identification experiment. Estimation is carried out using standard least-squares techniques (see for example Ljung [52]). Figure 5.4 shows that a first-order transfer function with a dead time of three sampling instants is a good approximation of the actual pressure dynamics. Precisely, we obtain:

$$G_1(z) = \frac{22.59z}{z - 0.8098} \frac{1}{z^3} . \tag{5.1}$$

This result is used to calculate transfer functions of a prefilter $F_1(z)$ and a feedback controller $C_1(z)$ via pole placement (see for example Åström and Wittenmark [6]). Integral action is used in the feedback controller, while unity DC gain of the closed-loop system is assured by the prefilter. The dominating closed-loop dynamics are chosen to exhibit a rise time of 0.05 s, i.e. twenty samples, and a damping coefficient of 0.9. The resulting controller transfer functions are

$$F_1(z) = \frac{0.0023z}{0.011z - 0.0085} , \tag{5.2}$$

$$C_1(z) = \frac{0.011z^3 - 0.0085z^2}{z^3 - 0.7721z^2 + 0.0081z - 0.236} . \tag{5.3}$$

In a similar manner, the flow controller is designed. A pseudo-random binary signal is applied to the reference of the pressure control loop (in mmHg) and the response of the ultrasound blood flow signal (in % of $y_{\max}$) is recorded at 20 Hz. Least-squares parameter estimation yields the following first-order transfer function with a dead time of three sampling instants:

$$G_2(z) = \frac{-0.0488z}{z - 0.7353} \frac{1}{z^3} . \tag{5.4}$$

Figure 5.4 shows that this well approximates the deterministic portion of the actual flow dynamics (i.e. the dynamics without the measurement noise). The prefilter $F_2(z)$ and a feedback controller $C_2(z)$ are designed to yield a rise time of 0.6 s, i.e. twelve samples, and a damping of 1 via pole placement. As before, integral action is included, and the closed loop is assured to have a DC-gain of one. This results in the following transfer functions:

$$F_2(z) = \frac{0.7913z}{2.9506z - 2.1161} , \tag{5.5}$$

$$C_2(z) = \frac{-2.9506z^3 + 2.1161z^2}{z^3 - 0.8645z^2 + 0.0048z - 0.1403} . \tag{5.6}$$

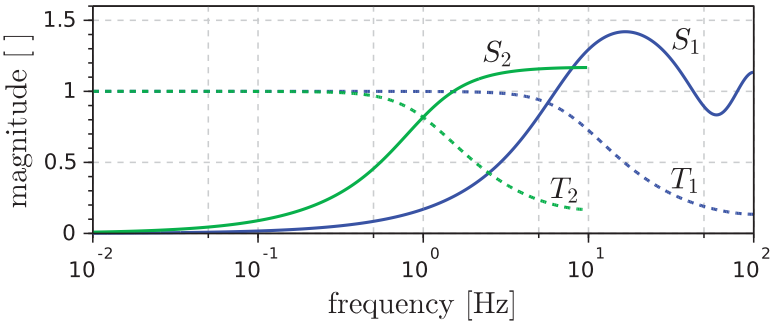

Figure 5.5: Sensitivity plots of the inner and outer feedback control loop. Dashed lines indicate the gain of the (noise-attenuation- and reference-tracking-related) complementary sensitivity functions $T_1(z), T_2(z)$, while the continuous lines represent the gain of the (disturbance-rejection-related) sensitivity functions $S_1(z), S_2(z)$. Both controllers are designed to yield similar damping, but the inner loop exhibits a significantly larger bandwidth.

Figure 5.5 provides sensitivity plots of both control loops. The inner loop is significantly faster than the outer loop. The ultrasound signal contains a high level of noise in the frequency range from 5 Hz to 10 Hz (cf. Figure 5.4). Therefore, the rise time of the flow control can hardly be decreased without amplifying this noise.

To investigate how severe this bandwidth limitation is, we activate the linear motor (cf. Figure 5.2) such that it induces a physiologically pulsating pressure in the artificial artery. As the experimental results in Figure 5.6 illustrate, the standard feedback control is not fast enough to maintain the flow at a constant value. The oscillating arterial pressure represents a disturbance that is hardly rejected by the controller. Only the largest peaks in the flow signal are attenuated. This has been observed before by Weber et al. [125]. In the following, we extend the controller by an ILC algorithm, which allows us to overcome the classic bandwidth limitations by exploiting the periodicity of the control task.

5.2.2 Iterative Learning Controller

As explained before, the measurement principle requires that the balloon pushes on the artery in such a way that the flow is reduced to a constant small value. From a medical point of view, however, continuous reduction of the blood flow through the artery is not desirable. Hence, the controller is deactivated periodically, and the balloon pressure is reduced to a minimum value that allows for sufficient blood circulation. Precisely,

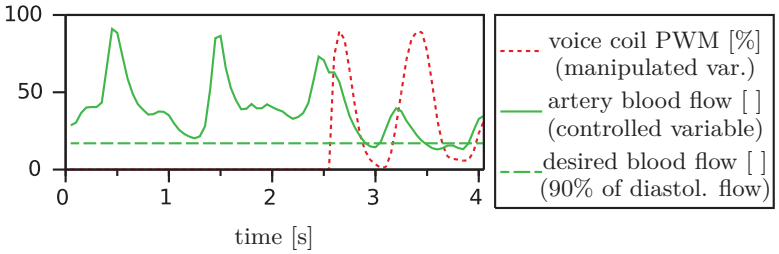

Figure 5.6: Classic cascade feedback control (without ILC, active from 2.5 s) of the blood flow at physiologically pulsating blood pressure. The bandwidth of the control loop is limited. The periodic peaks can only be attenuated partially. Note that an additional symmetric moving-average lowpass filter has been applied to the blood flow signal in order to improve perception of the plot.

we alternate between letting three pulses pass and activating the controller for two pulses. How the controller activation can be synchronized with the pulse of a human will be discussed in Section 5.2.3. Prior to this, we focus on improving the controller performance that is achieved during the periods in which the controllers are active.

As a result of the previous section, we obtain a damped, but still oscillating flow signal in each of these activation periods. In order to eliminate the repeating deviations from the reference value, we design an iterative learning controller. The double pulses in which the controllers are active are defined as the trials (or passes) of the ILC. In each of these trials, a feedforward control input trajectory will be applied as reference to the flow feedback controller. This input trajectory is updated between the trials based on measurement information from previous trials.

The ILC is designed in the lifted framework of repetitive discrete-time systems (cf. Section 2.2). At a pulse rate f_p and a sample rate of $f_s = 20\,\mathrm{Hz}$, the trial duration (or pass length) is $n = \lceil 2f_s/f_p \rceil$ samples, i.e. the smallest integer that is larger than or equal to $2f_s/f_p$. In every trial $j \in \mathbb{N}_0$ with starting time $t_{0,j}$, the n sample values of the measured blood flow $y(t)$ are recorded and stacked in the following lifted signal vector

$$\mathbf{y}_j = [y_j(t_{0,j} + 1/f_s), y_j(t_{0,j} + 2/f_s), \ldots, y_j(t_{0,j} + n/f_s)]^T \in \mathbb{R}^{n\times 1}. \tag{5.7}$$

The manipulated variable of the ILC shall be denoted $u(t)$ and is given as a reference to the flow feedback controller (see Figure 5.3). The n samples of that output, which are modified by the ILC algorithm, are stacked in the lifted signal vector

$$\mathbf{u}_j = [u_j(t_{0,j} + (1-d)/f_s), u_j(t_{0,j} + (2-d)/f_s), \ldots, u_j(t_{0,j} + (n-d)/f_s)]^T \in \mathbb{R}^{n\times 1}, \tag{5.8}$$

where $d \in \mathbb{N}_0$ is a controller parameter that is chosen to eliminate dead time in the system dynamics. Furthermore, an iteration-invariant lifted signal vector $\mathbf{r} \in \mathbb{R}^{n\times 1}$ is defined, the entries of which are all equal to the desired flow value. During the first trial, the input is chosen constant at $\mathbf{u}_0 = \mathbf{r}$. At the end of each trial, the recorded deviation $\mathbf{e}_j$ between the flow $\mathbf{y}_j$ and its reference value $\mathbf{r}$ is used to calculate the input $\mathbf{u}_{j+1}$ of the next trial via the following learning law:

$$\mathbf{u}_{j+1} = \mathbf{Q}(\mathbf{u}_j + \lambda \mathbf{e}_j), \quad \mathbf{e}_j = \mathbf{r} - \mathbf{y}_j, \quad j = 0, 1, \dots , \tag{5.9}$$

where $\lambda \in \mathbb{R}$ is the learning gain, and $\mathbf{Q} \in \mathbb{R}^{n\times n}$ is the lifted-system matrix of a non-causal lowpass filter. More precisely, $\mathbf{Q}$ is a symmetric Toeplitz matrix containing the Markov parameters of a second-order Butterworth filter, whose cutoff frequency $f_{\mathbf{Q}}$ serves as an adjustable controller parameter. The learning gain λ is a positive scalar that can be increased to obtain faster convergence while getting closer to overshooting, and thus to instability.

In order to assess stability in the iteration domain formally, a model of the plant is required. From (5.4), (5.5) and (5.6), we calculate the following closed-loop transfer function of the feedback controlled system (cf. Figure 5.3):

$$T_2(z) = \frac{F_2(z)\, C_2(z)\, G_2(z)}{1 + C_2(z)\, G_2(z)} = \frac{0.0407}{0.6405z - 1.5998z^2 + z^3}\,. \tag{5.10}$$

By calculating the first n Markov parameters p_i of $T_2(z)$, we obtain the following lifted-system matrix:

$$\mathbf{P} = \begin{pmatrix} p_1 & 0 & \cdots & 0 \\ p_2 & p_1 & \cdots & 0 \\ \vdots & \vdots & \ddots & \vdots \\ p_n & p_{n-1} & \cdots & p_1 \end{pmatrix}, \qquad \begin{aligned} p_1 &= 0.0407, \\ p_2 &= 0.0651, \\ p_3 &= 0.0781, \\ &\vdots \end{aligned} \tag{5.11}$$

Recall from Chapter 2 that asymptotic stability in the iteration domain is assured for all $\mathbf{r}, \mathbf{v}, \mathbf{u}_0$ if and only if

$$\rho(\mathbf{Q}(\mathbf{I}_{n\times n} - \lambda \mathbf{P})) < 1, \tag{5.12}$$

where ρ denotes the spectral radius and $I_{n\times n}$ is the identity matrix of dimension $n \times n$. Similarly, monotonic convergence of the tracking error can be assessed via the criterion

$$\bar{\sigma}(\mathbf{P}\mathbf{Q}\mathbf{P}^{-1}(\mathbf{I}_{n\times n} - \lambda \mathbf{P})) < 1 \quad \Rightarrow \quad ||\mathbf{e}_{j+1} - \mathbf{e}_\infty||_2 < ||\mathbf{e}_j - \mathbf{e}_\infty||_2 \; \forall j\,, \tag{5.13}$$

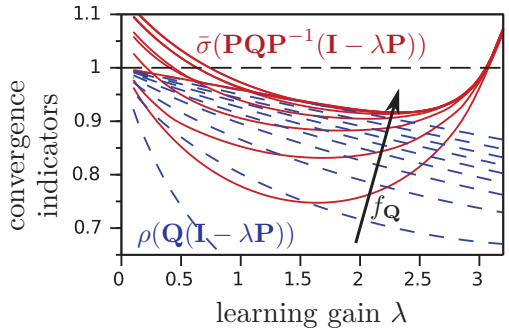

Figure 5.7: Spectral radius (blue dashed) and maximum singular value (red solid) of the closed-loop dynamics lifted matrix over the learning gain. Both lines are plotted for a set of Q-filter cutoff frequencies ranging from the Nyquist frequency of 10 Hz (uppermost curves) down to $f_\mathbf{Q} = 1$ Hz (lowest curves). As indicated by the horizontal dashed line, asymptotic stability and monotonic convergence can be achieved for $\lambda < 3$, while decreasing $f_\mathbf{Q}$ seems to improve the rate of convergence.

where $\bar{\sigma}$ denotes the maximum singular value of a matrix, i.e. the induced matrix norm of the Euclidean vector norm $||\cdot||_2$, and $\mathbf{e}_\infty := \lim_{j\to\infty} \mathbf{e}_j$ is the limit value of the tracking error (cf. Chapter 2). Note furthermore that $\bar{\sigma}(\mathbf{PQP^{-1}}(\mathbf{I}_{n\times n} - \lambda\mathbf{P}))$ is equivalent to the convergence indicator $\tilde{\gamma}_2$, which should be small according to the controller design guidelines[1] we derived in Chapter 4.

In order to determine suitable values for the ILC parameters, we calculate the spectral radius $\rho(\mathbf{Q}(\mathbf{I}_{n\times n} - \lambda\mathbf{P}))$ and the largest singular value $\bar{\sigma}(\mathbf{PQP^{-1}}(\mathbf{I}_{n\times n} - \lambda\mathbf{P}))$ for a large number of learning gains λ and Q-filter cutoff frequencies, see Figure 5.7. It is found that the fastest convergence should be expected for small cutoff frequencies $f_\mathbf{Q}$ of about 1 Hz and a learning gain of $\lambda \approx 1.5$. For these values, the maximum singular value indicates that large tracking error norms will be reduced by at least 20% in each trial. In contrast, learning gains below $\lambda \approx 0.75$ and above $\lambda \approx 3$ may lead to transient growth.

However, small Q-filter cutoff frequencies are known to cause large residual tracking errors. Therefore, the controller design guidelines we derived in Chapter 4 recommend to choose $f_\mathbf{Q}$ larger than the largest frequency of the reference and disturbance signal in order to assure that the error norm falls below a small threshold. In the present application, the disturbances caused by the pulsating arterial pressure are found to

[1] Recall that these guidelines also apply to the classic case of constant pass length.

exhibit frequencies of up to 5 Hz, which indicates that $f_{\mathbf{Q}}$ should be chosen close to 10 Hz, i.e. $\mathbf{Q}$ should be (almost) the identity matrix.

Since all of the theoretical criteria and guidelines above are conservative in some sense, we also analyze the convergence of the tracking error experimentally. To this end, the artery model is set to provide a physiologically pulsating blood pressure, and the three control loops are activated and deactivated in the periodic fashion described above. While keeping parameters of the classic feedback controllers $F_1(z), C_1(z), F_2(z), C_2(z)$ constant, we evaluate the learning behavior for various Q-filter cutoff frequencies $f_{\mathbf{Q}}$ and learning gains λ in a sequence of experiments. Figure 5.8 shows the development of input and output trajectories for well-chosen controller parameters, and Figure 5.9 shows the development of the tracking error norm in the iteration domain for two other parameter settings.

In accordance with the theoretic predictions above, Figure 5.9 shows that smaller learning gains yield slower convergence and that smaller cutoff frequencies yield larger steady-state errors. Increasing λ and $f_{\mathbf{Q}}$ leads to increased convergence rates and smaller residual errors. However, for learning gains above $\lambda \approx 2$, divergence and overshooting is observed in some experiments. Therefore, we choose the controller parameters close to $\lambda = 1$ and $f_{\mathbf{Q}} = 10$ Hz. As seen in Figure 5.8, these settings lead to a reduction of the tracking error to less than 30% in the first learning step, which is clearly better than the maximum singular values of $\bar{\sigma} \geq 0.75$ in Figure 5.7 indicated.

In Section 5.3, we will investigate, whether the designed learning controller yields a precise blood pressure measurement. Prior to this, however, we shall shortly discuss the issue of limited repeatability in this non-standard ILC application.

5.2.3 Iteration-Variance and Pulse Rate Detection

In the past discussion, we constantly assumed that neither the system dynamics nor the disturbances vary significantly. Short time had passed between system identification and controller design and evaluation. However, by repeating the experimental evaluation multiple times, we find that results vary considerably due to slight variations in the placement of the ultrasound sensor, in the thickness and consistency of the gelatin layer and in the concentration of the fluid tracer particles. Depending on the magnitude of these variations, we observe either a deterioration of the controller performance or even divergence and input saturation. Further investigation of this behavior reveal that the strongly model-based design of the feedback controllers in Section 5.2.1 yields a flow feedback controller with poor robustness. Since the aforementioned variations can

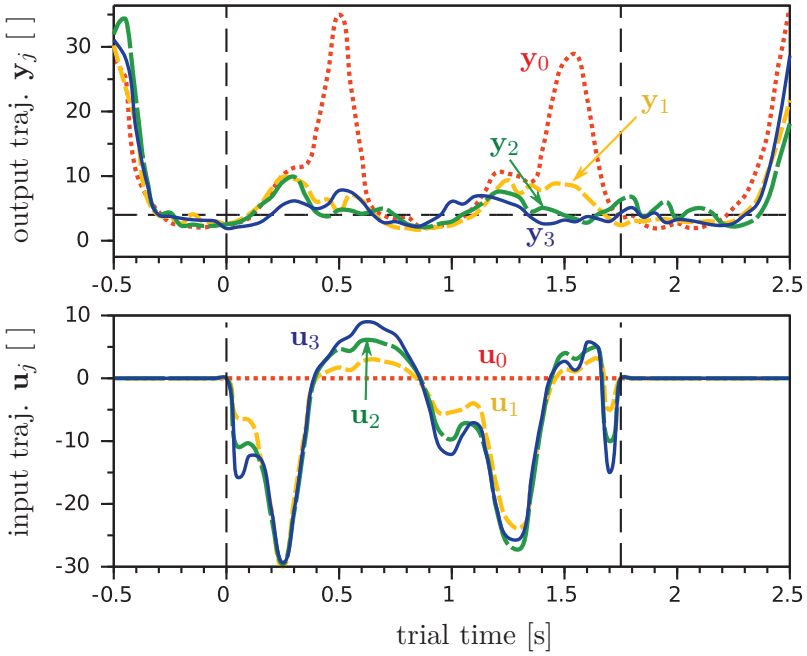

Figure 5.8: Iterative learning control ($f_{\mathbf{Q}} = 10\,\mathrm{Hz}$, $\lambda = 1$) of the blood flow through an artificial artery. *Top:* Within one step of learning, the flow is reduced to the constant small reference value indicated by the horizontal dashed line. Vertical dashed lines indicate the beginning and end of the ILC trials. *Bottom:* The input of the ILC, which is fed as a reference to the flow feedback loop, is adjusted from trial to trial based on the measured error and the ILC update law (5.9). Compared to the first update, changes in the second and third update are only minor. (All signals are given in percent of the maximum ultrasound signal value $y_{\max}$.)

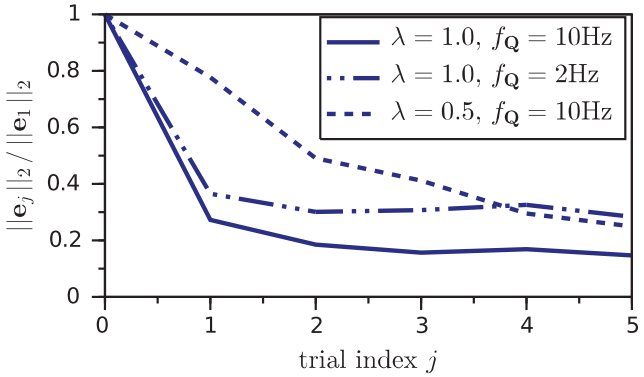

Figure 5.9: Convergence of the error norm for different ILC parameters. For $\lambda = 0.5$, convergence is slow. When using a Q-filter with $f_\mathbf{Q} = 2\,\text{Hz}$, the steady-state error is unacceptably large. However, for $\lambda = 1.0$ and $\mathbf{Q} = \mathbf{I}_{n\times n}$, the Euclidean norm of the error is quickly reduced to about 20% of its initial value and remains at this level in the following trials.

hardly be avoided in practice, the flow controller (5.5), (5.6) is replaced by a slower and more robust feedback controller with a rise time of 0.9 s. The ILC, in contrast, is found to cope well with all parameter variations, as well as with the new underlying feedback controller, and to yield similar rates of tracking error reduction in all scenarios.

Besides this, it was assumed above that the controller activation is synchronized with the blood pressure pulses. The human heart rate, however, is known to vary. Therefore, the current heart rate must be identified in realtime and the controller activation must be synchronized to the pulsation automatically. To achieve both goals, the following strategy is employed: While the controller is inactive, falling edges are detected in the ultrasound flow signal. From the duration between these edges, the pulse rate is determined. At the third falling edge, the feedback control loops are activated. After a short period of time, during which a large portion of the initial state dynamics of the feedback control loops decays, the ILC start to apply the input trajectory $\mathbf{u}_j$ as a reference to the underlying flow controller. Another d sample periods later, the ILC starts to record the output trajectory $\mathbf{y}_j$. As soon as the trial has reached a duration of two pulse periods, the controller is deactivated, and the heart rate identification is restarted.

The proposed strategy ensures that the ILC is always activated at the same instant of a pulse, i.e. shortly before the minimum of the flow signal. Furthermore, it ensures that the trial duration is always adjusted to be twice the pulse period. If the heart

rate varies, the ILC trials will exhibit varying reference lengths, a phenomenon that has been discussed in Chapter 4. If these variations are slow, the persistent adaptation of the ILC will compensate them and maintain a small tracking error. However, if the heart rate varies very quickly, then the knowledge gained in previous trials is hardly useful for the next trial. If the blood pressure trajectories exhibit some similarity across very different heart rates, then techniques similar to those proposed by Moore et al. [66] might be employed. At the present state of development, however, this aspect is not yet of interest. The available laboratory model of the cardiovascular system does not allow experiments with variable pulse rate, and it does not model the heart-rate-dependent variations of the blood pressure profile. Therefore, we focus on the case of slowly varying heart rates and, in the following, answer the question whether the designed ILC improves the accuracy of the novel blood pressure measurement technique.

5.3 Experimental Validation of the Measurement Principle

In the previous section, the controller design was discussed in detail. We now investigate whether the achieved regulation of the arterial flow yields a precise measurement of the blood pressure. The artificial cardiovascular system is again used with physiologically pulsating blood pressure. In addition to the previously described setup, the true pressure inside the arterial artery is measured and used as a reference measurement for benchmarking the novel control-based measurement technique.

A series of experiments are performed, in which the learning cascade controller is evaluated in combination with the automatic pulse rate detection. The experiments differ slightly in positioning of the ultrasound sensor, in thickness and consistency of the gelatin layer, in the value of the flow reference and in the concentration of the tracer particles of the liquid flowing through the artificial artery. Each of these variations is found to have an effect on the tracking performance, but the control deviation is always reduced, within few trials, to values clearly below the control deviations of the first trial, in which only the robust feedback control is active. Figure 5.10 shows five trials from an experiment with a blood pressure of 135 mmHg and 80 mmHg (systolic and diastolic, respectively). Within two to three learning steps, the repeating portions of the control deviation are eliminated, and the balloon pressure resembles the reference measurement signal. Hence, precise values for the heart rate and the arterial blood pressure are obtained within three trials.

5.4 Conclusions and Future Research

A novel blood pressure measurement technique was considered, which is based on control of the arterial blood flow. For the inherent control problem, we developed a learning cascade controller. It was demonstrated that the performance of standard feedback controllers is severely limited by the poor signal-to-noise ratio of the ultrasound-based flow measurement and by the large uncertainties in the system dynamics. To overcome these limitations, an iterative learning controller was added, which exploits the periodic nature of the control problem and the controller activation cycles. Controller performance was evaluated in a laboratory model of the cardiovascular system with physiologically pulsating blood pressure. Thereby, it was demonstrated that the improved controller yields precise measurements of the heart rate and blood pressure within less than twenty seconds, without impairing blood circulation.

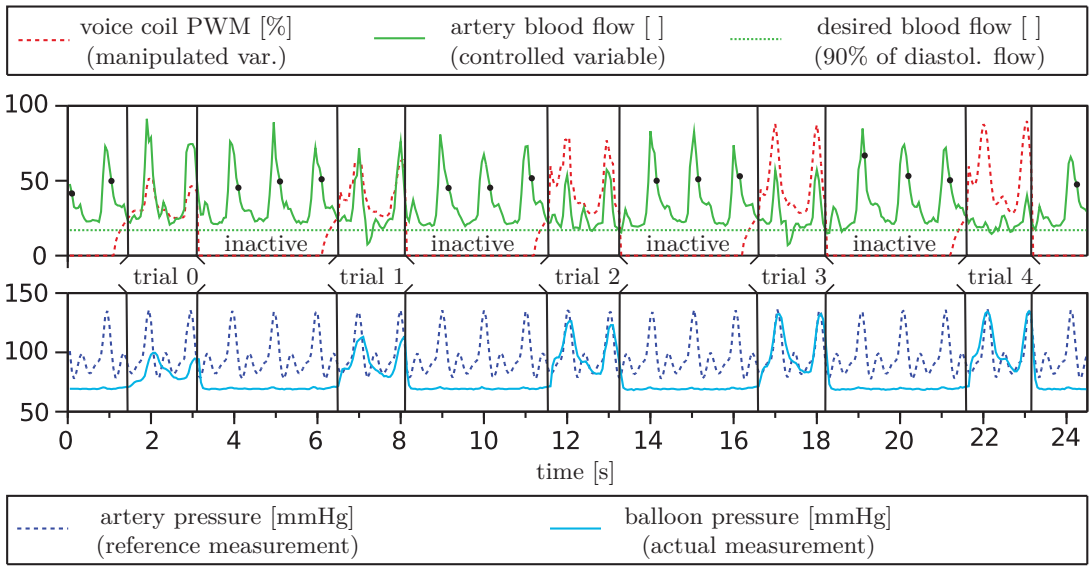

Figure 5.10: Blood pressure measurement by learning cascade control of the arterial blood flow. During the first trial, only the (slow but robust) cascade feedback control is active. From trial to trial, the reference signal of that feedback loop is adjusted by an iterative learning controller in such a way that the residual control deviation is reduced. Simultaneously, and in accordance with the intended measurement principle, the balloon pressure resembles the arterial pressure better and better. For example, the deviation between maximum balloon pressure and systolic arterial pressure decreases from the first to the fifth trial as follows: 36.3; 22.1; 9.3; 3.9; 2.1 mmHg.

The implications of variable heart rates for the present control problem were discussed. With respect to a practical implementation, further investigation of the speed of heart rate and blood pressure changes are advisable. Furthermore, improving the signal quality of the Doppler ultrasound flow measurement is expected to further improve the controller performance and, thus, the accuracy of the novel method.

6 Design of an Adaptive Drop Foot Neuroprosthesis

Many stroke patients suffer from the drop foot syndrome, which is characterized by a limited ability to lift (the lateral and/or medial edge of) the foot and leads to a pathological gait. In this chapter, we consider the treatment of this syndrome via functional electrical stimulation (FES) of the peroneal nerve during the swing phase of the paretic foot.

A novel three-electrodes setup will allow us to manipulate the recruitment of m. tibialis anterior and m. fibularis longus almost independently without violating the zero-net-current requirement of FES. In order to cope with the nonlinearities in patients' stimulation intensity tolerance, we will apply a piecewise linear controller output mapping. The pitch and roll angle of the foot will be estimated by means of an Inertial Measurement Unit (IMU) and controlled via a decentralized Iterative Learning Control (ILC) scheme. Finally, we will evaluate the effectiveness of this approach in experimental trials with drop foot patients walking on a treadmill. Starting from conventional stimulation parameters, the controller automatically achieves physiological foot pitch and roll angle trajectories within only two strides.

6.1 Introduction to the Application

According to the World Health Organization (WHO), more than a million people suffer a stroke in Europe each year [116]. Due to demographic changes and an increasing life expectancy, this number will rise as with the demand for efficient rehabilitation and medical devices. Stroke often leads to impaired motor function. Even after weeks of rehabilitation, many patients suffer from a limited ability to lift the foot by voluntary muscle contraction. This syndrome is known as drop foot (or foot drop), and it also appears in patients with other neurological disorders. Regardless of the cause, foot drop leads to a pathological gait with an increased risk of fall and injuries like ankle sprain.

A common treatment is to fix the foot in the lifted (dorsiflexed) position by a passive orthosis. This approach may improve safety and stability in the patient's gait, but it further promotes muscle atrophy and joint stiffness.

If the lesion affects the central nervous system and the peripheral nerves are still intact, then an alternative treatment can be provided by means of the technology known as

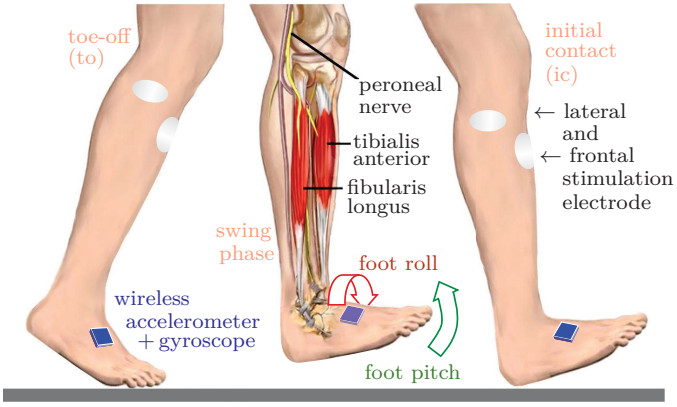

Figure 6.1: The foot is raised by m. tibialis anterior whose tendon is attached to the inner edge of the foot and by m. fibularis longus that lifts the outer edge. By means of FES, physiological foot motions can be achieved (in both pitch and roll direction) even in paretic limbs.

functional electrical stimulation [90]. As explained in Chapter 2, functional electrical stimulation enables the artificial activation of muscle contraction by applying tiny electrical pulses via skin electrodes with an adhesive, conductive gel layer or via implanted electrodes. Due to the risk of complications associated with surgery and implants, we restrict our discussion to the former case. Drop foot neuroprostheses, also known as peroneal stimulators, are FES devices that aim at generating a natural foot lift via activation of the patient's shank muscles. To this end, the electrodes are placed on the skin near the peroneal nerve, whose branches innervate several shank muscles, as depicted in Figure 6.1. When FES with well-chosen pulse dimensions is applied via well-positioned electrodes in a well-synchronized manner during gait, then the physiological motion of the foot can be restored even in paretic limbs.

6.1.1 Challenges in FES-based Drop Foot Treatment

There are several challenges that need to be faced when developing FES-based gait support systems for drop foot patients. One is that the ankle joint has two degrees of freedom that are actuated in a non-trivial way by at least two major shank muscles, cf. Figure 6.1. More precisely, the human ankle includes the talocrural joint and the subtalar[1] joint. The former admits dorsiflexion and plantarflexion, i.e. lift and drop of the foot with respect to the tibia, which corresponds to foot pitch in Euler angle notation.

[1] including the talocalcaneal part of the talocalcaneonavicular joint

In contrast, the subtalar joint allows for supination and pronation, which corresponds to rotation of the foot about a combined pitch, roll and yaw axis that is oriented 16° from the sagittal plane and 42° from the horizontal plane [83]. Since this implies that every yaw motion of the foot[2] is directly affiliated with a roll motion[3], we can disregard the yaw motion and characterize the rotational state of the foot entirely by the pitch and roll angle, cf. Figure 6.1.

The peroneal nerve divides into a superficial and a deep branch, which innervate the m. fibularis longus and m. tibialis anterior, respectively. Both muscles can be activated by FES via skin electrodes placed on the shank as depicted in Figure 6.1. Experiments show that the motion that FES triggers depends on the subject, varies with time, and is sensitive to small ($\sim 1\,\mathrm{cm}$) changes in the electrode positions. In most subjects, however, precise electrode placement leads to the following observations: Electrical pulses applied with the cathode being the frontal electrode mainly recruit m. tibialis anterior. This muscle raises the inner edge of the foot and thereby causes a combined pitch and roll motion. On the contrary, pulses applied with the lateral electrode serving as cathode recruit mainly m. fibularis longus and cause foot roll in the opposite direction by lifting the outer edge of the foot. However, at higher intensities, the lateral stimulation increasingly recruits additional muscles that also lift the inner edge to some (patient-individual) extent. Finally, when bi-phasic pulses with a sufficiently long inter-pulse pause are applied, as explained in Chapter 2, then the effect of the lateral stimulation outweighs the effect of the frontal stimulation for most electrode positions, resulting in an exaggerated lift of the outer foot edge. Therefore, and due to the mentioned sensitivity to electrode placement, it is challenging to find electrode positions and stimulation pulse dimensions that generate a straight foot lift without inwards or outwards roll of the foot.

Another important issue is that FES-activated muscles fatigue rapidly [87]. To delay the early onset of fatigue, it is essential to use the optimal stimulation parameters, i.e. the smallest intensities that achieve a safe and physiological foot lift. This optimum changes due to time-variant effects such as varying muscle tone (spasticity) and residual autonomous muscle activity. When patients cross a street, for example, residual voluntary muscle activity as well as the muscle tone (spasticity) often change within a few seconds or strides. Therefore, once a physiological foot motion has been achieved, it is just as challenging to maintain it.

[2] i.e. rotation about a vertical axis; adduction/abduction in medical terms
[3] i.e. rotation about the longitudinal axis of the foot; eversion/inversion in medical terms

6.2 State of the Art in Research and Industry

For drop foot treatment, a few commercially available solutions make use of FES, some via skin electrodes, others via implanted electrodes. The review articles by Lyons et al. [53] and Melo et al. [61] provide an excellent overview of drop foot stimulators in research and industry and classify them in several ways. Until now, all commercially available devices have been solely based on open-loop architectures, they only use sensors to time the stimulation [61]. Most of them employ heel switches to detect two gait phases: one when the heel of the paretic foot is on the ground and the other when it is not. In each stride, as soon as the heel is lifted, FES is applied with a fixed stimulation intensity profile over time, typically a trapezoidal shape tuned by an experienced clinician. Finding stimulation parameters that yield a physiological foot motion is cumbersome and, due to the described time-variant effects, requires repeated manual adaptations of the intensity profile. An obvious escape strategy that is often pursued is to choose larger stimulation intensities and accept exaggerated foot lift. While this strategy provides a certain amount of safety and functionality, it accelerates muscular fatigue and leads to a salient peculiarity in the patient's gait.

The challenges described in Section 6.1.1 can be faced in a much more effective and elegant way by the use of feedback control. The stimulation parameters can be adjusted automatically to delay the onset of fatigue and to induce the optimal level of foot lift. This requires measurement of the foot motion via, for example, an inertial sensor or a goniometer. When inertial sensors are attached to the shank and foot, the ankle dorsiflexion joint angle can be determined, as describe for example in Chapter 3. If only the foot is equipped with an inertial sensor, the foot orientation with respect to the horizontal plane is assessable (see also Chapter 3). Both quantities properly describe to which extent the applied FES compensates the foot drop.

Despite increasing efforts in the last decades to make closed-loop gait neuroprostheses a reality, it is still a challenging task to control paralyzed limbs with FES [61]. Several control techniques have been proposed, and some respectable results have been obtained at least for the much simpler case of a sitting or lying subject, i.e. without the tight time constraints and the strong disturbances imposed by gait. For example, Kobravi et al. [40] and Valtin et al. [117] proposed a fuzzy controller and an iterative learning controller, respectively, and performed experimental trials with sitting subjects. Hayashibe et al. [35] and Benedict and Ruiz [9] suggested the use of predictive control and PID control, respectively, but tested their controllers in simulation studies only. Artificial neural networks were employed by Chang et al. [13] and Chen et al. [14], who validated the controller in trials with subjects lying on a bed.

Besides those simplified in-vitro studies, intense efforts have also been made to close the loop on FES during walking. Veltink et al. [119] used an inertial sensor on the foot to tune an implantable drop foot stimulator such that a desired foot orientation just prior to initial contact was achieved. Negård [74] proposed run-to-run control of the maximum foot pitch angle occurring during swing phase and tested the controller in trials with a walking drop foot patient. Previously, Mourselas et al. [69] had briefly reported similar results obtained with a bend sensor and a fuzzy logic algorithm.

While these latter results represent important improvements with respect to all commercially available stimulators, one major shortcoming remains: The entire foot motion is reduced to a single scalar measure, for example a minimum foot clearance [59] with respect to ground or a desired foot pitch angle at initial contact. Obviously, this is a strong simplification of the control problem. As we will demonstrate, conventional stimulation intensity profiles may yield (for example) a desired *maximum* foot pitch angle, while causing too weak or too strong foot lift during the first half of the swing phase, or while using larger intensities than necessary.

With respect to overcoming these limitations, it was demonstrated by Nahrstaedt et al. [71] in preliminary experiments with healthy subjects that iterative learning control might be used to control the entire foot pitch angle trajectory of drop foot patients during the swing phase, i.e. from the last to the first ground contact (cf. Figure 6.1). Controlling the entire trajectory is expected to actually yield a stimulation intensity profile over time that induces a foot motion close to those of healthy walkers, while using only as much FES as needed.

In the following, we will consider multivariable feedback control of the entire foot motion during swing phase. Unlike all previous approaches, we will investigate in experimental trials with drop foot patients how two FES intensities can be manipulated almost independently to achieve desired foot pitch and roll angle trajectories by means of iterative learning control.

The remainder of this chapter is organized as follows. First, we briefly introduce the sensor concept in Section 6.3. In Section 6.4, a novel three-electrodes setup is used to modify the charges applied to the frontal and the lateral electrode (cf. Figure 6.1) independently without violating the zero-net-current demand. We then introduce a piecewise linear controller output mapping that exploits the entire range of stimulation intensity combinations tolerated by the patient. With this mapping in place, a decentralized ILC scheme for the pitch and roll angle is designed in Section 6.5, which is then evaluated in chronic drop foot patients walking on a treadmill in Section 6.6.

6.3 The Sensor – Inertial Assessment of Foot Motion

As discussed above, inertial measurement units can be employed to assess ankle joint angles and foot orientation angles. In Chapter 3, a set of methods has been development for realtime assessment of both the ankle joint angles and the foot orientation angles. Both motion parameters capture the main characteristics of the pathological gait, and a closed-loop drop foot neuroprosthesis could very well be designed based on any of both measurements. However, as a result of several discussions with experienced clinicians, foot orientation angles are found to be practically more relevant than ankle joint angles, mainly because the foot orientation is more directly linked to the foot clearance with respect to the ground. Therefore, we only consider the case of foot pitch and roll angle measurement in the following.

The foot motion is assessed by means of a single wireless inertial measurement unit, consisting of a three-dimensional accelerometer and a three-dimensional gyroscope. Both MEMS devices are assumed to be properly calibrated and to provide measurements in the same orthogonal coordinate system, which is not required to be aligned with the housing of the IMU. Although some inertial sensors also incorporate magnetometers, we refrain from using their readings, since they are well known to be unreliable inside buildings and in the presence of magnetic disturbances (see for example De Vries et al. [19]).

The IMU is attached to the shoe (or the foot in case of barefoot walking) using adhesive tape, elastic straps, or by putting it inside the shoe or between the shoe tongue and shoelace. Unlike most previous approaches, we assume the orientation and position of the sensor with respect to the foot or shoe to be unrestricted and unknown. This implies maximum freedom of mounting and adds robustness to the methods introduced in the following. Note that the task of inertial foot motion assessment would become much simpler if we attached the sensor such that the sensor coordinate axes coincide with anatomical axes of the foot. However, as discussed in Chapter 3, even surfaces and right angles are rarely found on the human body. Moreover, since most hemiplegic patients can use only one hand to attach the sensor, it would be particularly restrictive to demand a certain sensor-to-foot/shoe orientation.

Therefore, the methods developed in Chapter 3 prove advantageous for the current application. We employ them to detect the gait events *heel-rise* $t_{\mathrm{hr},j}$, *toe-off* $t_{\mathrm{to},j}$, *initial contact* $t_{\mathrm{ic},j}$ and *full contact* $t_{\mathrm{fc},j}$ for every stride j of the paretic foot in realtime. Furthermore, the sensor-to-foot/shoe orientation is automatically identified, as also described in Chapter 3, and drift-free trajectories of the foot pitch angle $\alpha(t), t \in [t_{\mathrm{hr},j}, t_{\mathrm{fc},j}]$, and

foot roll angle $\beta(t), t \in [t_{\mathrm{hr},j}, t_{\mathrm{fc},j}]$, are obtained at full contact, i.e. at the end of each stride.

Figure 6.2 presents example trajectories of the foot pitch and roll angles from experiments with five healthy subjects and with a drop foot patient who received conventional FES support with different stimulation intensity settings. In the trial labeled *standard FES*, we omitted the commonly used, but tedious procedure of manually optimizing the foot motion by iteratively repositioning the stimulation electrodes and adjusting the stimulation intensity. This results in an outwards foot roll (eversion) that is much stronger than the physiological variability in the gait of healthy subjects. With some adjustments, FES parameters are found that yield physiological foot motion (labeled "optimal FES"). However, as discussed previously, this achievement typically vanishes within minutes, or sometimes even seconds, due to muscular fatigue and time-variant muscle tone. This confirms that automatic foot motion control is required in order to avoid cumbersome manual adjustments and re-adjustments.

6.3.1 Scalar Pitch and Roll Indicators

Although our declared goal is to control the entire foot motion during swing phase, it is sometimes cumbersome to handle or present the complete pitch and roll angle trajectories. This is, for example, the case when investigating the effect of FES intensity parameters on the foot motion in general, as we will do in Section 6.4. Therefore, it is desirable to define a meaningful scalar measure that quantifies the overall amount of pitch or roll that occurred during a stride.

In experiments with stroke patients and in discussions with experienced clinicians, it is found that unphysiological foot motion is most undesirable in the second half of swing phase, i.e. when the foot is closer to the ground and a negative pitch or roll angle would increase the risk of stumbling and falling. We therefore define the following pitch and roll indicators:

$$\begin{aligned} p_j &:= \sqrt[3]{\frac{2}{t_{\mathrm{ic},j} - t_{\mathrm{to},j}} \int_{\frac{t_{\mathrm{to},j}+t_{\mathrm{ic},j}}{2}}^{t_{\mathrm{ic},j}} (\alpha(\tau) - \alpha_b)^3 d\tau} + \alpha_b \,, \\ r_j &:= \sqrt[3]{\frac{2}{t_{\mathrm{ic},j} - t_{\mathrm{to},j}} \int_{\frac{t_{\mathrm{to},j}+t_{\mathrm{ic},j}}{2}}^{t_{\mathrm{ic},j}} (\beta(\tau) - \beta_b)^3 d\tau} + \beta_b, \end{aligned} \tag{6.1}$$

where the base values $\alpha_b = -40°$ and $\beta_b = 0°$ are chosen to approximate typical toe-off angles in paretic gait. Please note that the cubic-average operation maintains the sign and gives more weight to large deviations from the base values α_b and β_b. Since, even

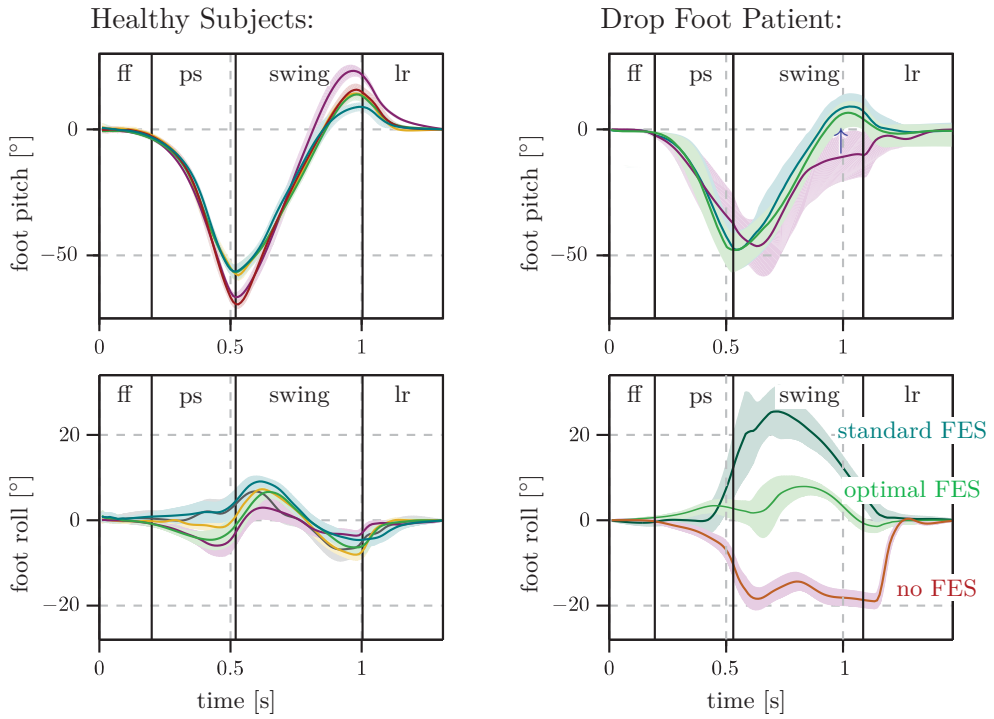

Figure 6.2: Pitch and roll angle trajectories (average lines + standard deviation bands) of healthy subjects (*left*) and of a drop foot patient who received zero, optimal and conventional FES support (*right*). The characteristics of drop foot gait are well captured by foot orientation measurements. Vertical lines indicate average gait phase transition times.

in paretic gait, strong positive and negative deviations from the base values never occur in the same stride, the cubic indicators are usually found to be close to the maximum deviation. But thanks to the averaging approach, they are not only based on one sample, and are therefore less sensitive to measurement errors and noise than the maximum deviation would be.

As demonstrated previously, such indicators correlate well with the foot motion rating of experienced clinicians [107]. Hence, they are considered satisfactory scalar measures of the clinically relevant foot motion in a stride.

6.4 The Actuator – Multi-Channel FES of Shank Muscles

We now investigate how the complex musculature of the frontal and lateral shank can be activated by FES. To this end, we use a three-electrode setup that enables the manipulation of two independent stimulation intensities (pulse charges) via only three surface electrodes and, nevertheless, ensures a zero net current. Subsequently, we solve the problem of interdependent saturation limits in multi-channel FES, and we analyze the multivariable couplings between the stimulation intensities of both channels and the foot motion they trigger during gait.

6.4.1 Novel Three-Electrodes Setup

The force generated by FES increases monotonously with the frequency and the charge (i.e. the product of pulse width and amplitude) of the applied current pulses. Therefore, adjusting the stimulation intensity typically relates to adjusting either (or both) of these quantities (cf. Chapter 2). For the sake of brevity, we assume a fixed pulse frequency of 50 Hz and manipulate only the pulse charge. In order to avoid high and narrow pulses as well as low and wide pulses, we implement all stimulation intensity changes in such a manner that pulse width and amplitude are always increased or decreased by the same factor, i.e. their ratio remains constant.

Most FES devices employ two electrodes per stimulation channel and apply symmetric bi-phasic pulse waveforms, i.e. two current pulses of equal dimensions but opposite sign are applied subsequently, as explained in Chapter 2. Thereby, it is assured that, under each electrode individually, the balance of charge pumped into or out of the body is zero. This is a fundamental requirement, since a non-zero net current through the body is known to cause electrolysis and tissue damage in the long term.

An intuitive approach to the considered application is to apply such bi-phasic pulses via the lateral and frontal electrode, with one of them serving as cathode during the first pulse and the other one serving as cathode during the second pulse (i.e. the counter pulse). This approach would yield only one manipulated variable (the pulse charge of both pulses). However, achieving a straight foot lift with both physiological pitch and balanced roll, in general, requires manipulating the excitation of the nervous tissue below lateral and frontal electrode independently. Therefore, we employ a stimulator with (at least) two independent FES channels and use a novel three-electrode setup.

In this setup, a third electrode is placed below the lateral electrode and next to the frontal electrode, see Figure 6.3. FES pulses applied to this location are found to cause almost no muscle contraction in drop foot patients and only weak recruitment of m. fibularis longus in healthy subjects. Therefore, the third electrode serves as common counter electrode, i.e. as cathode for the balancing pulse of both the frontal and the lateral electrode pulse. Both bi-phasic waveforms are applied subsequently within the 20 ms time window of each stimulation period, as illustrated in Figure 6.3. The product of pulse width and current amplitude of the first channel (the lateral FES channel) shall be denoted by $q_{\mathrm{lat}}(t)$, while the product of pulse width and current amplitude of the second channel (the frontal FES channel) shall be denoted by $q_{\mathrm{fro}}(t)$. Even if these two intensities are chosen independently, the net current is zero for each stimulation period and for each electrode.

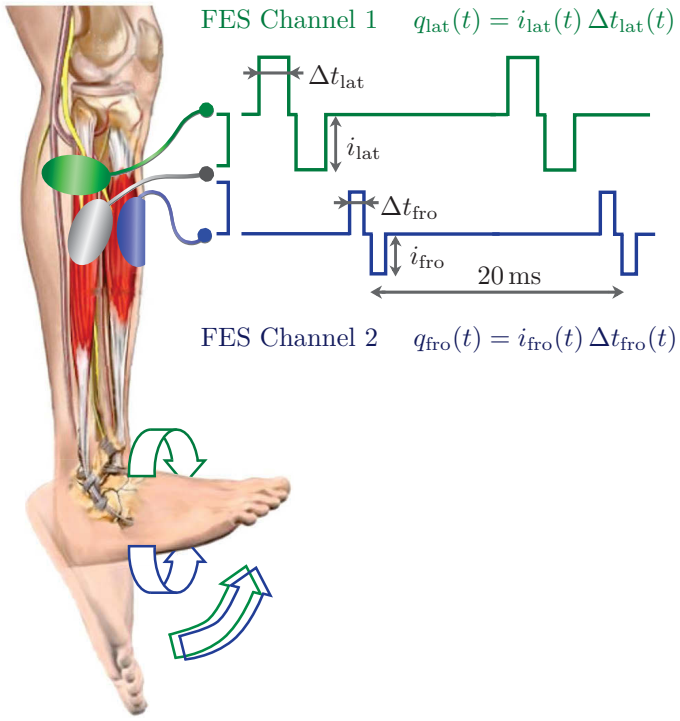

Figure 6.3: Two-channel drop foot stimulation. The third electrode in the middle serves as common counter electrode for both stimulation channels. Each bi-phasic pulse waveform is charge-balanced. The intensity of the second channel can therefore be chosen independently from the intensity of the first channel, without violating the zero-net-current restriction.

6.4.2 Choosing Suitable Stimulation Intensity Parameters

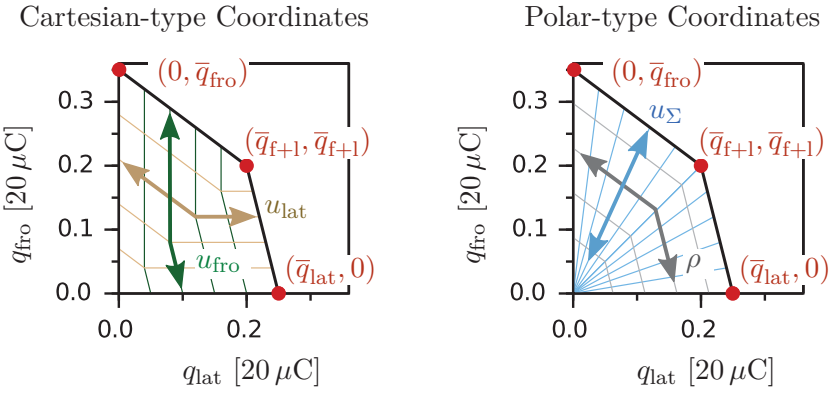

Figure 6.4: The domain $\mathcal{Q}$ of stimulation intensity combinations tolerated by the subject is defined by the initially determined maximum tolerated values $\overline{q}_{\mathrm{lat}}, \overline{q}_{\mathrm{fro}}, \overline{q}_{\mathrm{f+l}}$. It can be parameterized by the Cartesian-type coordinates $u_{\mathrm{lat}}, u_{\mathrm{fro}}$ or by the polar-type coordinates u_Σ, ρ.

Before FES is applied and stimulation intensities are automatically adjusted, it is advisable to identify the maximum intensity tolerated by the subject, i.e. the maximum pulse charges that cause neither discomfort nor pain, and make sure that these values are never exceeded. For the current application, recall that $q_{\mathrm{lat}}(t)$ and $q_{\mathrm{fro}}(t)$ are the stimulation intensities of the first and the second FES pulse, which trigger action potentials in nervous tissue near the lateral and frontal electrode, respectively. Since we can manipulate them independently, we first set $q_{\mathrm{fro}}(t)$ to zero and raise $q_{\mathrm{lat}}(t)$ until the subject reports discomfort, and then vice versa. Denote the obtained maximum tolerated values by $\overline{q}_{\mathrm{lat}}$ and $\overline{q}_{\mathrm{fro}}$, respectively. When both intensities are raised simultaneously, the subject feels the combined sensation of both pulses and typically tolerates only 70–80% of the single-channel maximum intensities. Figure 6.4 shows typical values for $\overline{q}_{\mathrm{lat}}, \overline{q}_{\mathrm{fro}}$ and the maximum tolerated intensity $\overline{q}_{\mathrm{f+l}}$ for simultaneous stimulation via both electrodes ($q_{\mathrm{fro}}(t) = q_{\mathrm{lat}}(t)$). By linear interpolation, we obtain the depicted quadrangle that defines the domain $\mathcal{Q}$ of admissible stimulation intensities.

This gives rise to the question how the intensity should be limited in multivariable control of foot orientation via FES. As discussed above, we aim at employing a decentralized control scheme, i.e. two independent controllers for the foot pitch and roll. If the stimulation intensities $q_{\mathrm{lat}}(t), q_{\mathrm{fro}}(t)$ were used as controller outputs, then the maximum value of each would depend on the current value of the other. This would complicate the implementation of intensity limitations and anti-windup schemes. We avoid this problem by parameterizing the domain $\mathcal{Q}$ in coordinates that are adapted to the geometry of the

quadrangle. For example, we can use the Cartesian-type coordinates $u_{\mathrm{lat}} \in [0,1]$ and $u_{\mathrm{fro}} \in [0,1]$ to section the domain $\mathcal{Q}$ as depicted in the left-hand side of Figure 6.4. Obviously, $u_{\mathrm{lat}} = 0$ implies $q_{\mathrm{lat}} = 0$, and $u_{\mathrm{lat}} = 1$ refers to points on the interpolated line between $\overline{q}_{\mathrm{lat}}$ and $\overline{q}_{\mathrm{f+l}}$, while the same holds for u_{fro}, q_{fro} and $\overline{q}_{\mathrm{fro}}, \overline{q}_{\mathrm{f+l}}$, respectively. For every combination $u_{\mathrm{lat}}(t), u_{\mathrm{fro}}(t)$, the corresponding pulse charges $q_{\mathrm{lat}}(t), q_{\mathrm{fro}}(t)$ are calculated as follows:

$$q_{\mathrm{lat}}(t) = \begin{cases} \overline{q}_{\mathrm{f+l}}\, u_{\mathrm{lat}}(t) & \text{if } u_{\mathrm{lat}}(t) \leq u_{\mathrm{fro}}(t) \\ \overline{q}_{\mathrm{f+l}}\, u_{\mathrm{fro}}(t) + \overline{q}_{\mathrm{lat}}(u_{\mathrm{lat}}(t) - u_{\mathrm{fro}}(t)) & \text{if } u_{\mathrm{lat}}(t) > u_{\mathrm{fro}}(t) \end{cases} \tag{6.2}$$

$$q_{\mathrm{fro}}(t) = \begin{cases} \overline{q}_{\mathrm{f+l}}\, u_{\mathrm{lat}}(t) + \overline{q}_{\mathrm{fro}}(u_{\mathrm{fro}}(t) - u_{\mathrm{lat}}(t)) & \text{if } u_{\mathrm{lat}}(t) \leq u_{\mathrm{fro}}(t) \\ \overline{q}_{\mathrm{f+l}}\, u_{\mathrm{fro}}(t) & \text{if } u_{\mathrm{lat}}(t) > u_{\mathrm{fro}}(t) \end{cases} \tag{6.3}$$

Alternatively, we may describe $\mathcal{Q}$ by the polar-type coordinates $u_{\Sigma} \in [0,1]$ and $\rho \in [-1,1]$. As also illustrated in Figure 6.4, $\rho = -1$ refers to $q_{\mathrm{lat}} = 0$ and $\rho = +1$ refers to $q_{\mathrm{fro}} = 0$, while u_{Σ} scales both q_{lat} and q_{fro} linearly between zero and their ρ-dependent maximum values. These coordinates can therefore be interpreted as an overall (weighted sum) intensity and a distribution of that intensity between both FES channels. For every combination $u_{\Sigma}(t), \rho(t)$, the corresponding pulse charges $q_{\mathrm{lat}}(t), q_{\mathrm{fro}}(t)$ are calculated as follows:

$$q_{\mathrm{lat}}(t) = \begin{cases} u_{\Sigma}(t)(\overline{q}_{\mathrm{f+l}}(1 + \rho(t))) & \text{if } \rho(t) \leq 0 \\ u_{\Sigma}(t)(\overline{q}_{\mathrm{f+l}}(1 - \rho(t)) + \overline{q}_{\mathrm{lat}}\, \rho(t)) & \text{if } \rho(t) > 0 \end{cases} \tag{6.4}$$

$$q_{\mathrm{fro}}(t) = \begin{cases} u_{\Sigma}(t)(\overline{q}_{\mathrm{f+l}}(1 + \rho(t)) - \overline{q}_{\mathrm{fro}}\, \rho(t)) & \text{if } \rho(t) \leq 0 \\ u_{\Sigma}(t)(\overline{q}_{\mathrm{f+l}}(1 - \rho(t))) & \text{if } \rho(t) > 0 \end{cases} \tag{6.5}$$

Each of the proposed parameterizations enables us to implement two independent single-input single-output controllers with properly defined saturation limits, i.e. we can manipulate each of new manipulated variables $u_{\mathrm{lat}}(t), u_{\mathrm{fro}}(t)$ or $u_{\Sigma}(t), \rho(t)$ independently of each other within their defined ranges without causing discomfort. In order to compare the usefulness of both approaches, we investigate the influence of each pair of stimulation intensity coordinates on the foot pitch and roll during swing phase in the following.

6.4.3 Experimental Analysis of Input-Output Couplings

As described above, the influence of FES pulses on the foot motion is not straight forward and depends on the subject, on the electrode position, as well as on the muscle tone and fatigue. Since results in sitting subjects [104] were found to differ from results in walking

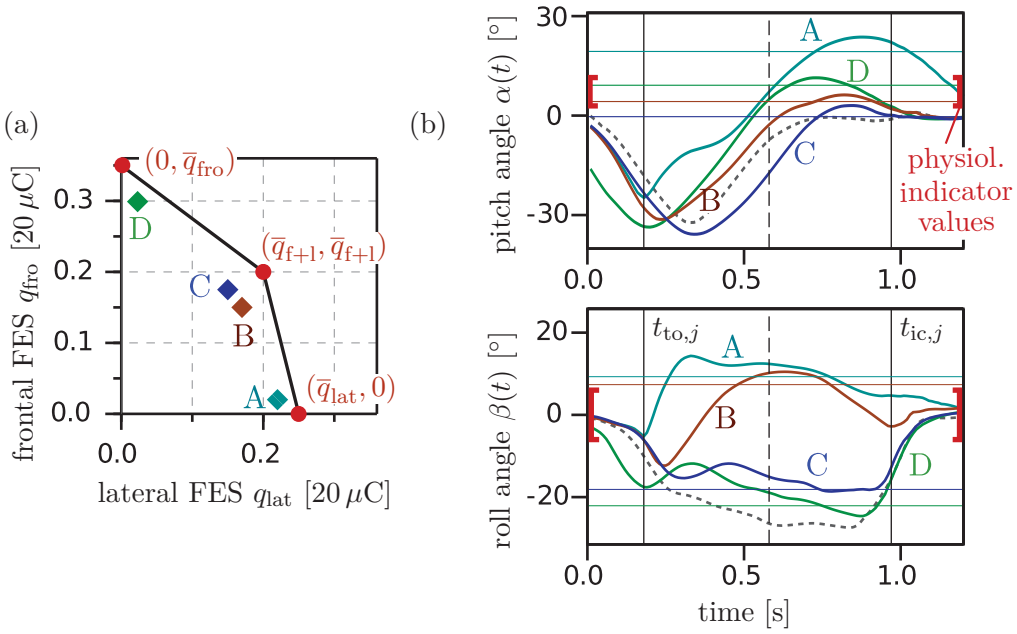

Figure 6.5: *(a)*: Four different stimulation intensity settings A–D. *(b)*: Foot orientation angles of a chronic drop foot patient with settings A–D and witout FES (dotted lines). Horizontal lines mark the respective indicators, as defined in (6.1). Stimulation intensities that yield sufficient pitch and neutral roll (cf. physiological ranges indicated by red brackets) are hard to find.

[107], we investigate this influence in a chronic drop foot patient walking on a treadmill at constant, self-selected speed.

Dual-channel FES is applied with constant intensities q_{lat} and q_{fro} during the entire pre-swing and swing phase of each stride. More precisely, the stimulation starts whenever the heel of the paretic foot leaves the ground, and it stops at initial contact. Figure 6.5 presents foot orientation angle trajectories and pitch/roll indicators for a few example parameterizations of both stimulation channels. It illustrates the aforementioned fact that physiological motions are not easily achieved by manual adjustments.

Preliminary experiments further reveal that certain combinations of q_{fro} and q_{lat} do *not* provide enough support to ensure a safe gait. This is illustrated in Figure 6.6. In order to investigate the influence of the previously defined FES parameters, we perform a large series of walking trials. Therein, we set $u_\Sigma = 0.6$ and collect data from about 60 strides, while gradually raising ρ from -0.3 to 0.3 every five strides. Subsequently, the procedure is repeated for several other values of u_Σ. For each combination of stimulation intensities,

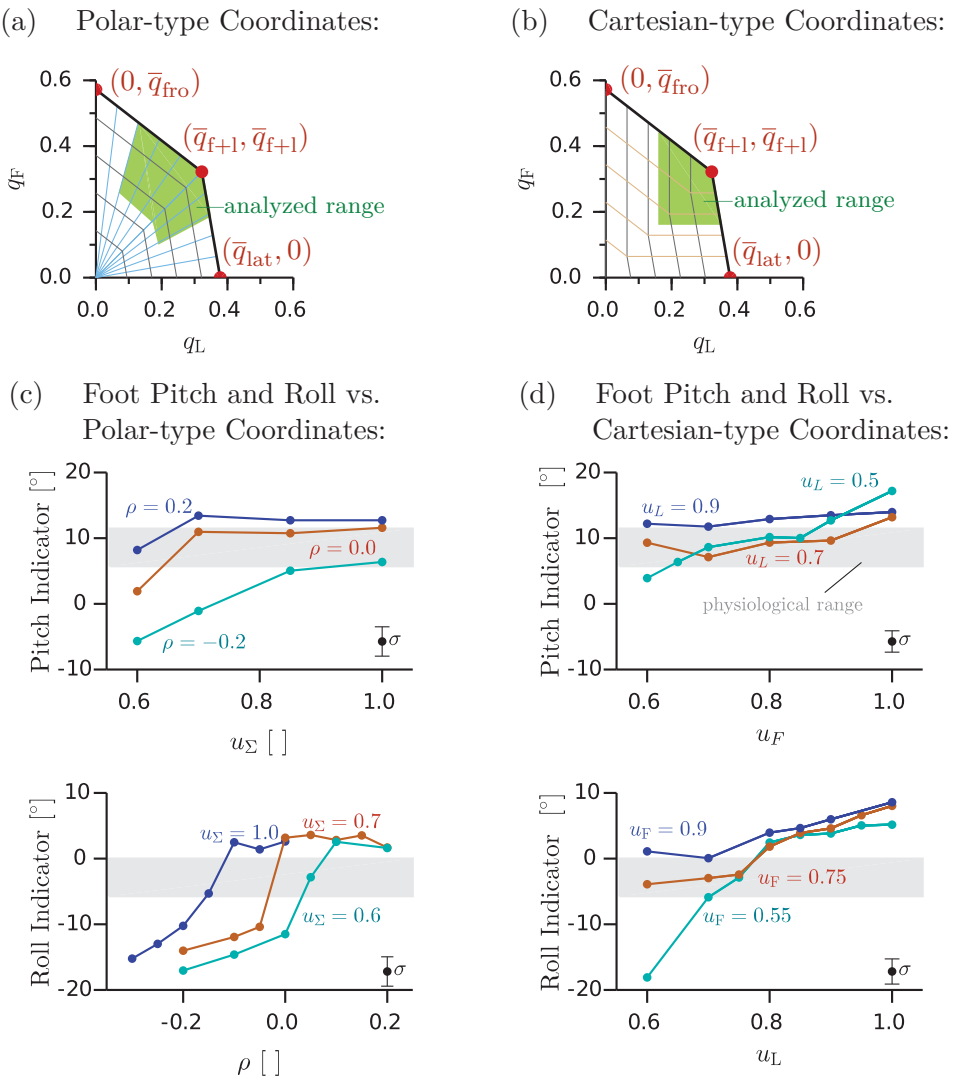

Figure 6.6: *(a,b)* Green polygons mark the subset of $\mathcal{Q}$ in which FES provided sufficient support to enable the patient to walk properly. *(c,d)* Foot pitch and roll during swing phase for various stimulation parameter settings from these ranges. Each dot marker represents the average indicator of about five strides with the respective stimulation settings. Sigma bars in the lower right corner of each subplot indicate the average standard deviation of the presented data points. Gray shades indicate the physiological values found in healthy gait at similar speed.

we calculate the average and standard deviation of the pitch and roll indicators defined in (6.1). Since hysteresis effects are common in FES, we also modify u_Σ between 0.6 and 1.0 while keeping ρ at several constant values.

Subsequently, we repeat the described procedure for the Cartesian-type coordinates: At first we decrease u_{lat} in small steps from 1 to 0.5 while keeping u_{fro} constant. This is done for various values of u_{fro}. We then repeat the process vice versa, i.e. keeping u_{lat} constant while decreasing u_{fro} from 1 to 0.5.

As a major result of these trials, it is found that all FES intensity parameters influence both pitch and roll of the foot to some extend. However, foot pitch is mainly influenced by u_{fro} and u_Σ, while foot roll is primarily influenced by u_{lat} and ρ.

Figure 6.6 shows pitch and roll indicators plotted against the Cartesian-type coordinates $u_{\text{lat}}, u_{\text{fro}}$ as well as against the polar-type coordinates u_Σ, ρ. By repeating the entire procedure on different days and with different patients as well as with small variations of electrode positions we confirm the aforementioned major result. However, apart from that, we obtain different results each time, which is not surprising to those who work with FES and the human neuro-muscular system. Therefore, we refrain from trying to identify detailed models of the observed input-output behavior. Instead, we will employ learning control methods with integral action that adapt the FES parameters repeatedly as long as the foot orientation angles are above or below the desired values.

Figure 6.6 indicates that such methods can be used successfully. By inspecting the slope of the curves, we make the following observations: For any fixed ρ, an increase(/decrease) of u_Σ leads to an increasing(/decreasing) or at least an almost steady foot pitch. Likewise, for any fixed u_Σ, an increase(/decrease) of ρ leads to an increasing(/decreasing) or at least an almost steady foot roll. These monotonicity properties are also found in the results of the Cartesian-type coordinates of most patients. We therefore consider both parameterizations of $\mathcal{Q}$ for decentralized learning control design in the following.

6.5 Iterative Learning Control of Drop Foot Stimulation

In this section, we will design a controller network that manipulates the FES intensity parameters in order to influence the orientation angles of the paretic foot during walking. For the sake of brevity, the procedure is only described for the polar-type parameterization. However, all following statements are analogously true, and the following procedure is analogously carried out, for the Cartesian-type parameterization.

Recall that $\alpha(t)$ and $\beta(t)$ are the measured pitch and roll angle of the foot, respectively, and that the control objective is to manipulate the stimulation intensity parameters $u_\Sigma(t) \in [0, 1]$ and $\rho(t) \in [-1, 1]$ such that the pitch and roll angle trajectories $\alpha(t), \beta(t)$ during swing phase resemble those of healthy subjects.

As discussed in Section 6.4.3, the cross-couplings between these manipulated and controlled variables are considerable but vary from patient to patient and with electrode position as well as with muscular tone and fatigue. In order to design a centralized multivariable controller, one would thus need to gain additional model knowledge from identification procedures (preferably during walking) at the beginning of each trial. While this might be of academic interest, it is far from practical. Therefore, we focus instead on the question whether a decentralized learning control scheme can cope with the cross-couplings and achieve physiological foot motion in walking drop foot patients.

Recall from Section 6.4.3 that $\rho(t)$ usually has a major influence on foot roll, while $u_\Sigma(t)$ influences foot pitch to some extent. Hence, we choose to pair the manipulated variable $u_\Sigma(t)$ with the controlled variable $\alpha(t)$ and to pair the manipulated variable $\rho(t)$ with the controlled variable $\beta(t)$.

6.5.1 Formulating Drop Foot Stimulation as a Repetitive Control Task

While the paretic foot is loaded, FES-induced joint torques hardly influence the motion of the foot or leg. Therefore, drop foot stimulation aims at influencing the foot motion during swing phase, i.e. from toe-off to initial contact. Since the dynamics of FES-induced movements are slow, the stimulation must start sufficiently early, i.e. typically about $\delta t_\mathrm{s} \approx 0.2\,\mathrm{s}$, $\delta \in \mathbb{N}$, before the toe-off. Since drop foot patients usually walk at slow, almost constant speed with pre-swing phase durations $t_{\mathrm{to},j} - t_{\mathrm{hr},j} > \delta t_\mathrm{s}\ \forall j$, we can anticipate the toe-off based on previous pre-swing durations and start to apply FES at

$$t_{0,j} := t_{\mathrm{hr},j} + \sum_{k=\max(1,j-3)}^{j-1} \frac{t_{\mathrm{to},k} - t_{\mathrm{hr},k}}{\min(j-1,3)} - \delta t_{\mathrm{s}} \approx t_{\mathrm{to},j} - \delta t_{\mathrm{s}}. \tag{6.6}$$

In a similar manner, we could anticipate $t_{\mathrm{ic},j} - \delta t_{\mathrm{s}}$ from previous strides and then stop the stimulation at that moment. However, mainly for safety reasons, FES should be applied at least until the initial contact is detected. Therefore, let the trajectories of the stimulation intensity parameters $u_\Sigma(t)$ and $\rho(t)$ applied in stride j be denoted by

$$\begin{aligned} \mathbf{u}_{\alpha,j} &:= [u_\Sigma(t_{0,j}), u_\Sigma(t_{0,j} + t_{\mathrm{s}}), \ldots, u_\Sigma(t_{\mathrm{ic},j})]^T, \\ \mathbf{u}_{\beta,j} &:= [\ \rho(t_{0,j}),\ \ \rho(t_{0,j} + t_{\mathrm{s}}), \ldots,\ \ \rho(t_{\mathrm{ic},j})]^T, \end{aligned} \tag{6.7}$$

where t_{s} is the sampling interval. The resulting pitch and roll angle trajectories are then denoted as follows:

$$\begin{aligned} \boldsymbol{\alpha}_j &:= [\alpha(t_{0,j} + \delta t_{\mathrm{s}}), \alpha(t_{0,j} + \delta t_{\mathrm{s}} + t_{\mathrm{s}}), \ldots, \alpha(t_{\mathrm{ic},j})]^T, \\ \boldsymbol{\beta}_j &:= [\beta(t_{0,j} + \delta t_{\mathrm{s}}), \beta(t_{0,j} + \delta t_{\mathrm{s}} + t_{\mathrm{s}}), \ldots, \beta(t_{\mathrm{ic},j})]^T. \end{aligned} \tag{6.8}$$

Even in subjects walking on a treadmill at constant speed, the time duration $t_{\mathrm{ic},j} - t_{0,j}$ will vary slightly from stride to stride. This natural variance is found to be even larger in hemiplegic patients, as demonstrated for example in Chapter 3. To capture this effect mathematically, we introduce the pass length

$$n_j := \frac{t_{\mathrm{ic},j} - t_{0,j}}{t_{\mathrm{s}}} - \delta + 1 \tag{6.9}$$

of stride j. Then we can write the dimensions of the input and output trajectory of stride j as $\boldsymbol{\alpha}_j, \boldsymbol{\beta}_j \in \mathbb{R}^{n_j \times 1}$ and $\mathbf{u}_{\alpha,j}, \mathbf{u}_{\beta,j} \in \mathbb{R}^{(n_j+\delta)\times 1}$.

Even in paretic gait, the swing phase duration does not become arbitrarily small or large. We can thus easily find a lower bound $\underline{n}$ and a (large) upper bound $\overline{n}$ for n_j such that $n_j \in [\underline{n}, \overline{n} - \delta]$ holds for every stride j.

Finally, we define desired (physiological) pitch and roll angle trajectories $\mathbf{r}_\alpha, \mathbf{r}_\beta \in \mathbb{R}^{\bar{n}\times 1}$ based on data from healthy subjects walking at the same speed, cf. Figure 6.2. From a medical point of view it is most important to ensure a clear *heel-strike*, i.e. positive foot pitch at initial contact. Therefore, we define $\mathbf{r}_\alpha$ such that its last $\overline{n} - \underline{n}$ sample values are larger than $5\,^\circ$. This completes a repetitive trajectory tracking task in which the inputs $\mathbf{u}_{\alpha,j}, \mathbf{u}_{\beta,j}$ must be chosen such that $\boldsymbol{\alpha}_j \approx \langle \mathbf{r}_\alpha \rangle_{n_j}$ and $\boldsymbol{\beta}_j \approx \langle \mathbf{r}_\beta \rangle_{n_j}$ in each stride, where $\langle \cdot \rangle_{n_j}$ is the *remove-last-*$(\overline{n} - n_j)$*-rows* operator defined in Chapter 4.

The large (translational and rotational) acceleration and deceleration of the shank that occur during swing phase impose disturbances on the considered plant dynamics. Due to increased muscle tone (related to spasticity), there is furthermore an additional torque[4] acting on the ankle joint of many drop foot patients. This torque, as well as the patient's residual voluntary muscle activity, also act as disturbances on the previously defined repetitive control task. Finally, please note that the amount of joint torque that can be generated by FES is typically very limited. Therefore, these disturbances represent major challenges.

From the preceding discussion we conclude that peroneal stimulation via surface electrodes during gait requires solving a repetitive, multivariable control task with variable pass length and with large delays and disturbances. As discussed in Section 6.1.1, many of the system parameters and disturbances vary with time – some of them within minutes, others occasionally within less than ten seconds. A control method is required that exploits the repetitiveness of gait and quickly adjusts the FES from stride to stride such that the variability is compensated and the desired pitch and roll angle trajectories are achieved in each stride (up to the natural stride-to-stride variance of healthy gait). This task perfectly fits the framework of iterative learning control for variable pass length systems, which has been introduced in Chapter 4. Therefore, we aim at solving the repetitive trajectory tracking task by a decentralized ILC scheme in the following.

6.5.2 Decentralized Iterative Learning Control Law

As pointed out above, the overall dynamic delay of FES-induced foot motion is approximately 0.2 s, which is longer than a quarter of the typical swing phase duration $t_{\mathrm{ic}} - t_{\mathrm{to}} \approx 0.7\,\mathrm{s}$. Moreover, gaining useful model knowledge requires burdening identification procedures. Therefore, instantaneous feedback (i.e. using current measurement information to adjust stimulation intensities) hardly reaches closed-loop rise times below 0.5 s, and is practically useless for the present application. Instead, the stimulation intensities for each stride must be chosen primarily based on measurement information from previous strides. In terms of ILC theory, this means that we neither employ current-iteration tracking error ILC nor design methods that rely on a (precise) system model.

Since the pass length n_j of stride j is not known before the initial contact of stride j occurs, we must prepare full-length controller output trajectories $\bar{\mathbf{u}}_{\alpha,j}\bar{\mathbf{u}}_{\beta,j} \in \mathbb{R}^{\overline{n}\times 1}$ for

[4] e.g. m. tibialis posterior may cause an inversion-promoting torque

each stride j:

$$\begin{aligned}\bar{\mathbf{u}}_{\alpha,j} &:= [u_\Sigma(t_{0,j}), u_\Sigma(t_{0,j}+t_\mathrm{s}), \ldots, u_\Sigma(t_{0,j}+(\overline{n}-1)t_\mathrm{s})]^T,\\ \bar{\mathbf{u}}_{\beta,j} &:= [\ \rho(t_{0,j}),\ \ \rho(t_{0,j}+t_\mathrm{s}), \ldots,\ \ \rho(t_{0,j}+(\overline{n}-1)t_\mathrm{s})]^T,\end{aligned} \tag{6.10}$$

although only the first $n_j+\delta$ samples of both trajectories (i.e. exactly $\mathbf{u}_{\alpha,j}, \mathbf{u}_{\beta,j}$) will actually be applied to the system.

In the first stride, when no measurement information from previous strides is available, a conservative strategy is advisable: For example, we may set $\mathbf{u}_{\beta,0}$ to constant zero (corresponding to $q_\mathrm{fro} = q_\mathrm{lat}$) and $\mathbf{u}_{\alpha,0}$ to a trapezoidal profile with an amplitude of 0.9 (corresponding to 90 % of the maximum tolerated intensities) and a considerably short rise time. In most patients, this assures a safe swing phase with sufficient but most likely exaggerated foot lift.

At the beginning of each following stride, we determine the element-wise deviation between the measured angle trajectories $\boldsymbol{\alpha}_j, \boldsymbol{\beta}_j$ and the first n_j samples of the respective reference trajectories $\mathbf{r}_\alpha, \mathbf{r}_\beta$ to calculate the following error information vectors:

$$\begin{aligned}\mathbf{e}_{\alpha,j} &:= \langle \mathbf{r}_\alpha \rangle_{n_j} - \boldsymbol{\alpha}_j, \quad \mathbf{e}_{\alpha,j} \in \mathbb{R}^{n_j \times 1},\\ \mathbf{e}_{\beta,j} &:= \langle \mathbf{r}_\beta \rangle_{n_j} - \boldsymbol{\beta}_j, \quad \mathbf{e}_{\beta,j} \in \mathbb{R}^{n_j \times 1}.\end{aligned} \tag{6.11}$$

For the last $(\overline{n}-n_j)$ samples of the reference trajectory there exists no corresponding measurement information, since the trial actually ended after n_j sample periods. The incomplete error information can nevertheless be used to adjust the controller output trajectory $\bar{\mathbf{u}}_j$, by using the following modified version of a standard ILC learning law (cf. Chapter 4):

$$\begin{aligned}\bar{\mathbf{u}}_{\alpha,j+1} &= \mathrm{sat}_0^{+1}\left(\mathbf{Q}\left(\bar{\mathbf{u}}_{\alpha,j} + \lambda_\alpha \mathbf{I}_{\overline{n}\times\overline{n}} \begin{bmatrix}\mathbf{e}_{\alpha,j}\\ \mathbf{0}_{(\overline{n}-n_j)\times 1}\end{bmatrix}\right)\right),\\ \bar{\mathbf{u}}_{\beta,j+1} &= \mathrm{sat}_{-1}^{+1}\left(\mathbf{Q}\left(\bar{\mathbf{u}}_{\beta,j} + \lambda_\beta \mathbf{I}_{\overline{n}\times\overline{n}} \begin{bmatrix}\mathbf{e}_{\beta,j}\\ \mathbf{0}_{(\overline{n}-n_j)\times 1}\end{bmatrix}\right)\right),\end{aligned} \tag{6.12}$$

where $\lambda_\alpha, \lambda_\beta \in \mathbb{R}_{\geq 0}$ are adjustable learning gains, and $\mathrm{sat}_a^b(\cdot)$ denotes element-wise saturation to the interval $[a, b]$. Furthermore, $\mathbf{Q} \in \mathbb{R}^{\overline{n}\times\overline{n}}$ is a symmetric matrix with Toeplitz structure containing the Markov parameters of a lowpass filter (2^nd order, Butterworth) with cutoff frequency denoted by $f_\mathbf{Q}$. As explained in Chapter 2, multiplying a trajectory vector by $\mathbf{Q}$ corresponds to applying a non-causal (zero-phase) lowpass filter to the trajectory [23]. Thereby, we avoid the discomfort that is usually associated with sudden large increases in stimulation intensity. Moreover, this improves the robustness of the

ILC by restricting the learning process to the low frequency range in which at least some model knowledge is available, as discussed in Chapter 4.

The rationale behind this learning approach is as follows: When a certain section of an angle trajectory is lower than it should be, the update law (6.12) increases the corresponding section of the respective controller output trajectory. On the contrary, whenever the foot pitch or roll is stronger than necessary, the respective stimulation intensity parameter is reduced.

Please note that the large delay in the system dynamics is partially compensated by the time shift δ in the trajectory definitions (6.7). If, for example, the roll angle is too low during the first five samples of the swing phase in stride j, then the controller increases the first five entries of $\mathbf{u}_{\beta,j+1}$, which will be applied δ samples before the swing phase of the next stride, i.e. early enough to correct the observed control deviation.

If an adjustment was not sufficient, the deviation remains and will be adjusted again, i.e. the employed learning law has integral action. By integrating the control output saturation directly into the learning law (6.12), we prevent integrator windup effects that would otherwise occur whenever the controller outputs reach the boundary of the domain $\mathcal{Q}$ of admissible stimulation intensities, cf. Figure 6.4.

6.5.3 Choosing Suitable Controller Parameters

Controlling foot motion by functional electrical stimulation during the swing phase of gait represents a classic example of an ILC task with variable pass length. To apply the controller design guidelines derived in Chapter 4, a lifted model of the plant dynamics is needed. We therefore perform experiments with subjects sitting on a table with relaxed shank and foot. The subject's m. tibialis anterior is stimulated with an intensity profile that is typical for walking support of drop foot patients. The dynamics of foot pitch (measured in radians) induced by the electrical stimulation (normalized to tolerated maximum) are identified using least-squares system identification methods (see for example Ljung [52]). The obtained transfer function

$$G_{\text{pitch}}(z) = \frac{1.0494z - 1.0174}{z - 0.9816}\, z^{-10}, \text{ with sample rate } f_{\text{s}} = 50\,\text{Hz}, \tag{6.13}$$

roughly approximates the dynamics from the stimulation intensity $u_\Sigma(t)$ to the foot pitch angle $\alpha(t)$ defined in Section 6.4. The lifted-system matrix $\mathbf{P}$ is calculated from the (nonzero) Markov parameters of $G_{\text{pitch}}(z)$ as described in Chapter 2. In the following, we

use this model to find suitable values for the learning gain λ_α and the Q-filter cutoff frequency $f_\mathbf{Q}$ of the iterative learning control scheme defined above.

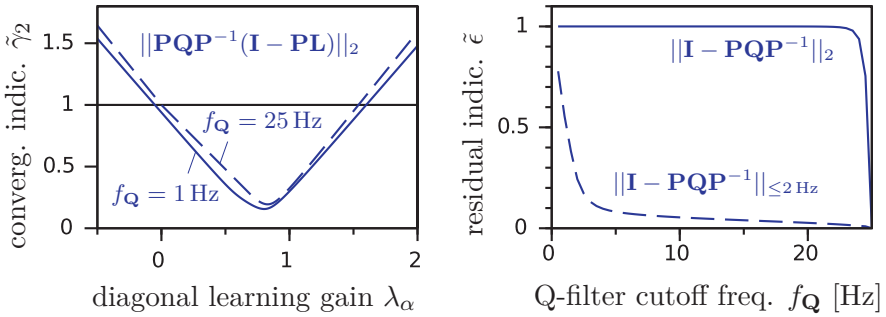

Figure 6.7: Convergence indicator $\tilde{\gamma}_2$ and residual indicator ϵ plotted over controller design parameters.

We choose to analyze error reduction in the Euclidean norm $||\cdot||_2$. Figure 6.7 shows the convergence indicator $\tilde{\gamma}_2$ plotted against the diagonal learning gain λ_α for Q-filter cutoff frequencies $f_\mathbf{Q}$ from the practically relevant interval[5] $f_\mathbf{Q} \in [1, 25]\,\mathrm{Hz}$. Recall from Chapter 4 that positive learning progress and MPL error decrease for large error norms are only assured if $\tilde{\gamma}_2 < 1$. This is given if $\lambda_\alpha \in [0, 1.5]$, while the best convergence is predicted for $\lambda_\alpha \in [0.5, 1]$. Very similar $\tilde{\gamma}_2$-values are obtained for all $f_\mathbf{Q} \in [1, 25]\,\mathrm{Hz}$.

Moreover, we find $||\mathbf{PQP}^{-1}||_2 \approx 1\ \forall f_\mathbf{Q} \in [1, 25]\,\mathrm{Hz}$. To resolve this issue, please recall the concept of the frequency-weighted residual indicator proposed in Chapter 4. From Sections 6.3 and 6.5, we conclude that a trial (i.e. a swing phase) is typically shorter than one second and that both the defined reference and the large disturbance imposed by the shank motion contain only frequencies below 2 Hz. In order to obtain a less conservative result for low-frequency signals $(\mathbf{r} - \mathbf{v})$, we calculate the frequency-weighted residual indicator

$$\tilde{\epsilon}_{\leq 2\,\mathrm{Hz}} := ||(\mathbf{I}_{\overline{n}\times\overline{n}} - \mathbf{PQP}^{-1})||_{\leq 2\,\mathrm{Hz}}\,. \tag{6.14}$$

Figure 6.7 shows that $\tilde{\epsilon}_{\leq 2\,\mathrm{Hz}}$ grows as the cutoff frequency $f_\mathbf{Q}$ of the Q-filter is reduced. However, as discussed before, a small $f_\mathbf{Q}$ improves robustness with respect to model uncertainties. To balance both aspects, we choose $f_\mathbf{Q} = 5\,\mathrm{Hz}$. With $\lambda_\alpha = 0.5$, this implies that the tracking error $\mathbf{e}_j$ on the first n_j samples is reduced in each learning step at least until it falls below $\frac{1}{1-0.4}(||\hat{\mathbf{e}}_j||_2 + 0.08||\mathbf{r} - \mathbf{v}||_2)$. In the following section, we will evaluate experimentally how conservative this statement still is and how small the tracking error gets in practice.

[5] Note that for the given sample frequency $f_\mathrm{s} = 50\,\mathrm{Hz}$, the Nyquist frequency is 25 Hz.

Prior to this, we shall briefly discuss robustness of our previous statements. As the analysis of Section 6.4.3 indicated, it is a strong simplification to describe FES dynamics by a linear model. In fact, the transfer function (6.13) captures the input-output dynamics only for the small region of stimulation intensities that have a strong influence on the foot pitch angle. As Figure 6.6 demonstrates, the gain between $u_\Sigma(t)$ and $\alpha(t)$ varies with $u_\Sigma(t)$ (and $\rho(t)$). If smaller intensities are chosen, the delay and lag time of G_{pitch} might still have similar values, but the gain of the dynamics will certainly be much smaller. Likewise, if the stimulation intensity and the pitch angle are very large, then even a large increase of intensity will only cause a small additional increase of the pitch angle. Therefore, the gain of G_{pitch} used for controller design is only the maximum gain that occurs in that patient between $u_\Sigma(t)$ and $\alpha(t)$. Finally, experimental results of numerous other subjects show that this maximum gain can be up to twice as large in other subjects as in (6.13).

As discussed before, it is hardly feasible and (most of all) not practical to (re-)identify these dynamics in their full complexity for each subject on each usage of the adaptive neuroprosthesis. Instead, we account for these variations by considering the class of linear systems $G = k_G G_{\text{pitch}}$ with $k_G \in \mathbb{R}, k_G > 0$. By calculating the convergence indicator $\tilde{\gamma}_2$ for $\lambda = 0.5$ and for many values of k, we find that $\tilde{\gamma}_2 < 1 \; \forall k \in [0.1, 2.9]$. This means that, with the chosen controller parameters, our previously established convergence properties are still guaranteed, even if the gain of the input-output dynamics is more than twice as large as or ten times smaller than its nominal value[6]. Within this robustness lies a major advantage of using iterative learning control for the present application.

To complete the controller design of the decentralized controller network, a second iterative learning controller needs to be designed that manipulates the stimulation distribution $\rho(t)$ based on measurements of the foot roll angle $\beta(t)$. Likewise, we need to implement two single-input single-output iterative learning controllers when using the Cartesian-type FES parameterization. For all three of these design tasks, the procedures described above can be carried out analogously. Several preliminary experiments, however, reveal that the respective input-output dynamics vary largely from patient to patient and that the gain and lag time are typically close to the values found in (6.13). Therefore, and for the sake of brevity, the same learning gain and Q-filter cutoff frequency are employed for each single iterative learning controller in the following. Since ILC is known to yield strong robustness with respect to model uncertainties, we may nevertheless expect good performance.

[6] Even outside this range, monotonic convergence is typically achieved for a large set of initial input trajectories, and asymptotic stability is achieved for an even larger set.

6.6 Experimental Evaluation in Stroke Patients

In experimental trials with drop foot patients, we now evaluate the previously designed ILC scheme in combination with both FES parameterizations proposed in Section 6.4. The six patients that were recruited for these trials are ambulatory, aged 50–70, BMI 20-27, at least three months post-stroke and suffer from a drop foot syndrome in combination with at most moderately increased muscle tone (hypertonia) of the leg musculature. Some of them use a walking stick or an ankle-foot orthosis in everyday walking. All of them have used FES before (at least three sessions of at least 30 min). Informed consent of the patients was obtained and the trials have been approved by the ethics committee of Charité Universitätsmedizin Berlin.

Initially, we determine the maximum tolerated stimulation intensities $\overline{q}_{\mathrm{lat}}, \overline{q}_{\mathrm{fro}}, \overline{q}_{\mathrm{f+l}}$ of the patient by increasing the intensities of both FES channels (each individually and then both together, respectively) until the patient reports discomfort. These values are then used to implement the two previously defined controller output mappings, along with the decentralized ILC network, on a realtime computer system.

During the subsequent evaluation trials, the patient walks on a treadmill at constant, self-selected speed. A wireless inertial sensor is attached to the paretic foot and three FES electrodes are placed on the shank as depicted in Figure 6.3. The measured accelerations and angular rates are used to calculate the current gait phase as well as the foot pitch angle and roll angle trajectories for each stride in realtime, cf. Section 6.3.

For the first stride $j = 0$, we choose $\mathbf{u}_{\alpha,0}$ and $\mathbf{u}_{\beta,0}$ as trapezoidal input profiles with manually chosen heights and rise times. After each stride $j \geq 0$, during the short period of time for which the heel and toes of the paretic foot are on the ground, the controller uses the measured pitch and roll angle trajectories $\boldsymbol{\alpha}_j, \boldsymbol{\beta}_j$ to adjust the stimulation intensities $\mathbf{u}_{\alpha,j+1}, \mathbf{u}_{\beta,j+1}$ automatically according to the update law (6.12). During the subsequent stride $j+1$, stimulation intensity trajectories $\mathbf{q}_{\mathrm{fro},j+1}, \mathbf{q}_{\mathrm{lat},j+1}$ are applied via the frontal and lateral electrode, according to the chosen controller output mapping, cf. Section 6.4.

We first employ the polar-type parameterization of the domain of admissible stimulation intensities, i.e. the pitch angle controller manipulates the FES parameter $u_\Sigma(t)$, while the roll angle controller manipulates the FES parameter $\rho(t)$. Throughout a large number of trials, both iterative learning controllers simultaneously adjust the stimulation in a way that the foot motion resembles the desired physiological motion.

Results from a representative trial are depicted in Figure 6.8. The desired foot pitch and roll angle trajectories are indicated by large circle markers to improve readability and to emphasize that, in practice, perfect tracking is not required. Instead, any trajectory that is close to $\mathbf{r}_\alpha$ (or $\mathbf{r}_\beta$) is desirable. For each sample instant of a stride, the curves in the upper and lower subplot indicate the foot orientation measurements and FES parameter values, respectively. The solid segments of these curves highlight which sample values belong to the input trajectories $\mathbf{u}_{\mathrm{fro},j}, \mathbf{u}_{\mathrm{lat},j}$ and output trajectories $\boldsymbol{\alpha}_j, \boldsymbol{\beta}_j$, as defined in Section 6.5.

Let us briefly analyze the learning process that is evident in Figure 6.8a. The manually chosen initial stimulation intensity trajectories $\bar{\mathbf{u}}_{\alpha,0}, \bar{\mathbf{u}}_{\beta,0}$ induce a foot motion with too weak foot pitch $\boldsymbol{\alpha}_0$ and strong negative roll $\boldsymbol{\beta}_0$, i.e. the foot drops and exhibits inversion similar to the foot depicted in Figure 3.8 of Chapter 3. Consequently, the controller prepares input profiles $\mathbf{u}_{\alpha,1}, \mathbf{u}_{\beta,1}$ with increased values of $u_\Sigma(t)$ and $\rho(t)$ for the next stride. The resulting output trajectories $\boldsymbol{\alpha}_1, \boldsymbol{\beta}_1$ exhibit clearly better foot lift and less inversion. Therefore, the controllers perform only minor adaptations of the FES parameters between the following strides.

However, we shall note that the FES distribution $\rho(t)$ saturates shortly before the end of the swing phase and that the roll angle at initial contact remains negative despite all parameter adjustments. An explanation for this behavior is found in the fact that the pitch angle controller chooses, at the same time instants, small values for the overall stimulation intensity $u_\Sigma(t)$. Since foot pitch is sufficient, this is the expected behavior of the pitch angle controller. With the polar-type controller output mapping, however, this entails that the manipulated variable of the roll angle controller becomes ineffective. This represents a major drawback of the polar-type parameterization – negative roll cannot be compensated if pitch is (more than) sufficient.

Figure 6.9a shows results from a similar trial, but with the Cartesian-type controller output mapping in place. This time, the initial stimulation intensity trajectories $\mathbf{u}_{\alpha,0}, \mathbf{u}_{\beta,0}$ are chosen conservatively high to assure a safe (but exaggerated) foot lift from the first stride. Since these inputs induce a foot motion with too large foot pitch $\boldsymbol{\alpha}_0$ and roll $\boldsymbol{\beta}_0$, the stimulation intensities $\mathbf{u}_{\alpha,1}, \mathbf{u}_{\beta,1}$ are reduced before the next stride. Since the resulting foot pitch $\boldsymbol{\alpha}_1$ still lies entirely above the desired reference trajectory, the intensity of the frontal stimulation channel is further reduced. The foot roll $\boldsymbol{\beta}_1$, however, is too high during the first half of swing phase and too low during the second half. Therefore, the iterative learning controller slightly reduces the first half of the intensity profile $\mathbf{u}_{\beta,2}$ and slightly increases its second half. In all following strides $j > 1$, the deviations of foot pitch and roll are within the natural range that is observed in healthy subjects' gait, as Figure 6.9b indicates.

Due to the natural fluctuation of many FES parameters and gait parameters, tracking accuracies below the few-degrees level are not achieved by any setup. However, more than fifty further walking trials confirm that, by persistent adaptation, the controller scheme maintains the physiological foot motion, even when the muscles fatigue or when the patient modifies his/her walking style (for example by increasing knee flexion during swing phase and decreasing circumduction).

Similar series of trials with the five other drop foot patients yield similar results and confirm all of the above findings. Since this dissertation only aims at providing a proof of concept rather than a clinical study, these results are not analyzed in detail. It is, however, important to note that the iterative learning process leads to highly individualized FES parameters that may vary largely from one patient to the next (and often from day to day within one patient), even if the same FES parameterization and reference trajectories are used. Figure 6.10 illustrates this fact using the example of the roll angle control results obtained in four different patients. The ρ-trajectories that lead to a physiological foot roll motion differ considerably. For example, some patients require larger intensities on the lateral stimulation channel than on the frontal channel during pre-swing, while others need the opposite during the same gait phase. That such individual requirements are automatically determined and satisfied is a major achievement of the proposed feedback-controlled drop foot neuroprosthesis.

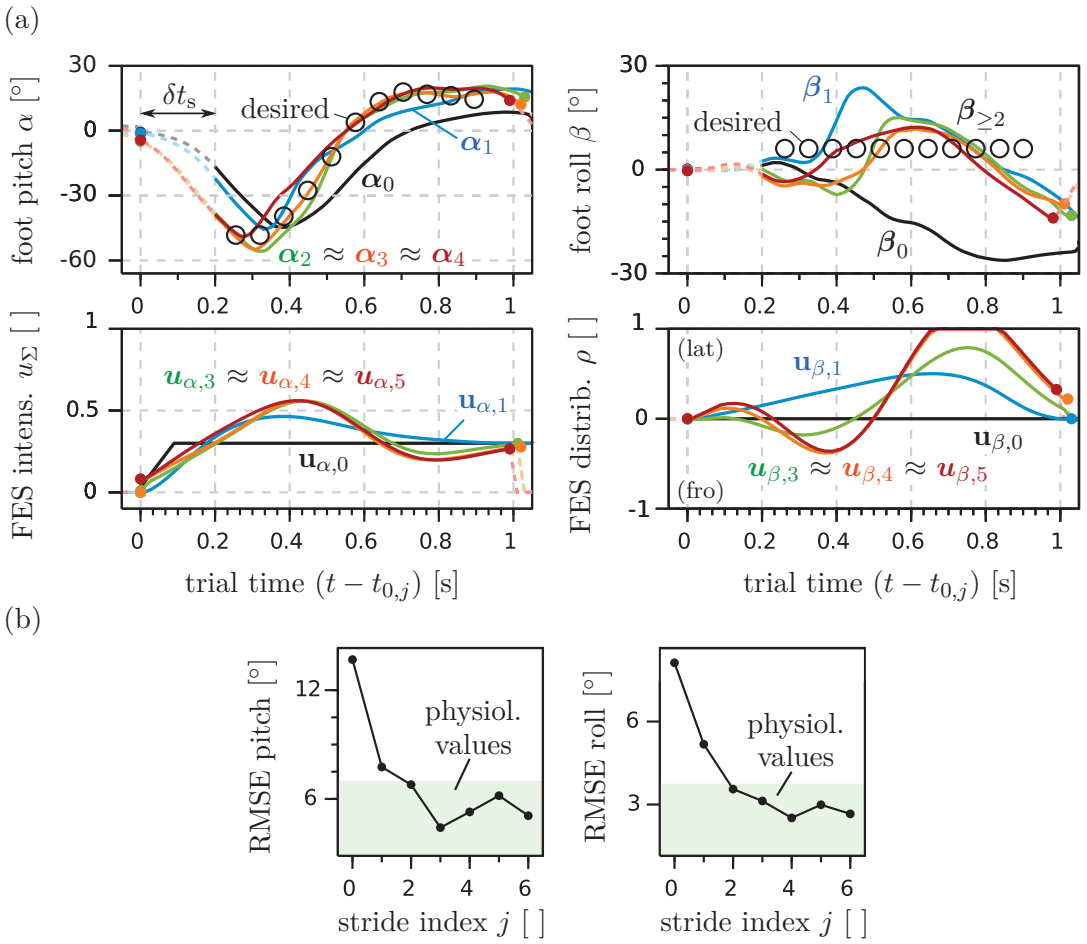

Figure 6.8: Experimental results of ILC with polar-type FES parameters in a chronic drop foot patient. *(a)* Starting from non-individualized values, the controller adjusts the FES parameters from stride to stride and thereby achieves the desired foot motion during swing phase. Dots mark heel-off and initial contact of each stride. *(b)* Root-mean-square errors of the foot pitch and roll are quickly reduced to the ranges found in healthy subject data.

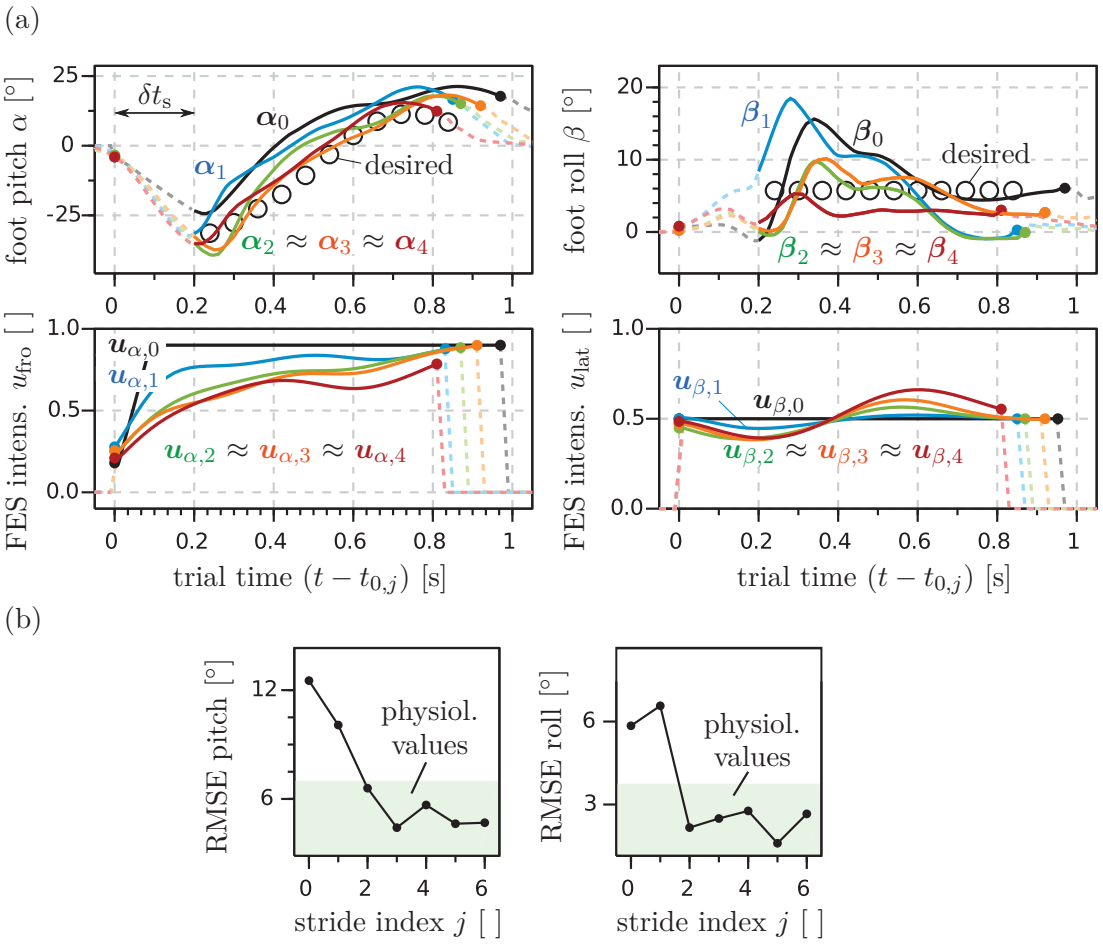

Figure 6.9: Experimental results of ILC with Cartesian-type FES parameters in a chronic drop foot patient. *(a)* Starting from conservatively high values, the controller adjusts the FES parameters from stride to stride and thereby achieves the desired foot motion during swing phase. Dots mark heel-off and initial contact of each stride. *(b)* Root-mean-square errors of the foot pitch and roll are quickly reduced to the ranges found in healthy subject data.

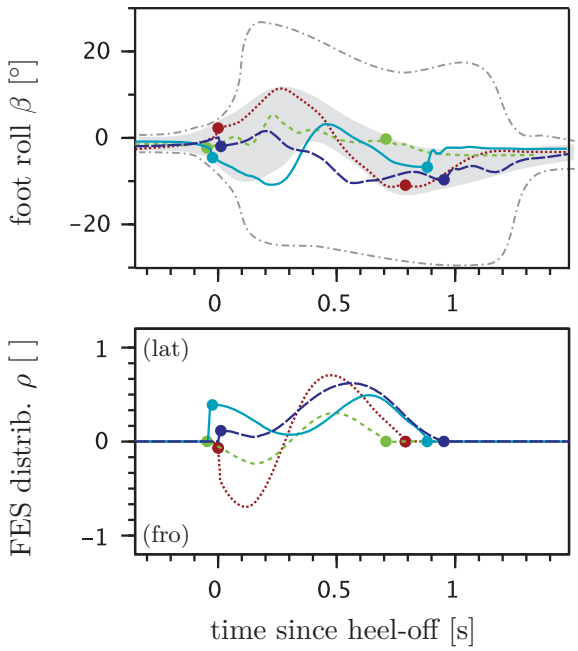

Figure 6.10: Results from ILC of the foot roll angle in four drop foot patients (indicated by different line colors and styles) with equivalent reference trajectories. The achieved roll angle trajectories resemble physiological trajectories (gray band, cf. Section 6.3) and are far from the extreme values observed in the same patients when applying no FES or too much FES (gray dash-dot lines). Dots mark heel-off and initial contact of each stride.

6.7 Conclusions and Further Research

FES-based drop foot treatment via surface electrodes has been considered as an application for inertial foot motion analysis and iterative learning control with variable trial duration. Benefits of a closed-loop approach were highlighted, and the state of the art in research and industry was reviewed. We discussed the challenges arising from the multidimensionality of the control task as well as from large delays and disturbances.

A two-channel stimulator with a three-electrode setup was chosen as the basis for an adaptive drop foot neuroprosthesis. We characterized the domain of admissible stimulation intensities that is defined by the patient's maximum tolerated intensities. Two parameterizations of this domain were proposed, both of which enable decentralized iterative learning control of foot pitch and roll angles with independent input saturation limits and anti-windup. These controller were designed by applying methods for variable-pass-length ILC that had been derived in Chapter 4.

Experimental trials with a chronic drop foot patient revealed that predefined pitch and roll angle trajectories are achieved by the designed controller within only two strides. Unlike existing drop foot stimulators, the proposed system adapts the electrical stimulation to the needs of a specific patient on a specific day with a specific electrode placement and maintains a physiological foot motion even in the presence of disturbances. Regarding the FES parameterization, experimental results suggest that the Cartesian-type coordinates are preferable in patients with weak foot roll and strong foot pitch.

Further research will focus on combining the present achievements with recent results in peroneal stimulation via array electrodes (see e.g. Valtin et al. [117]). Moreover, in subjects with low FES tolerance, we will investigate the effect of input saturation and anti-windup schemes on the controller performance. Finally, variable gait velocity and walking on stairs will be a focus of future research.

7 General Conclusions and Outlook

This dissertation aimed for deriving new methods that facilitate the use of inertial measurement units and learning control techniques in biomedical systems and at demonstrating how improved diagnosis and treatment systems can be designed by incorporating these technologies. To what extent these objectives were achieved is analyzed in the following by recapitulating and assessing the main results of each chapter.

7.1 General Conclusions on the Proposed Methods

In Chapter 3, a modular set of novel methods for inertial realtime gait analysis was developed. On the one hand, this includes methods for the determination of gait phases and foot orientation angles by means of a foot/shoe-mounted inertial sensor. On the other hand, methods were proposed for the measurement of ankle dorsiflexion joint angles and knee flexion/extension joint angles from two inertial sensors, one of which is attached to either side of the respective joint. While the gait phase detection was demonstrated to cope with the irregularity in stroke patients' gait under various circumstances, the foot orientation angles as well as the ankle and knee joint angles were found to be accurate (RMSE$<4^\circ$ in all cases) with respect to reference measurement systems. Unlike the vast majority of previous approaches, the proposed methods use only the measured accelerations and angular rates, while they completely avoid the use of magnetometer readings. Moreover, they neither restrict the sensor-to-segment mounting orientation, nor do they require this orientation to be known. Instead, the algorithms automatically identify these parameters from the measurement data of almost arbitrary motions by exploiting either the kinematic constraints of the joints or the periodic rest of the foot during walking.

Therefore, the proposed methods pave the way for a plug-and-play gait analysis, in which one simply attaches the IMUs arbitrarily, starts walking in any environment and receives gait phases, body segment orientations, as well as joint angles. By superseding precise sensor mounting requirements and restrictive calibration protocols, the new methods largely improve the practical usability of inertial measurement units in ambulatory motion assessment, which is becoming increasingly important for diagnosis of many motion-related diseases and disorders. Since all measurements are provided by the methods in realtime, they can furthermore be used to provide biofeedback during walking as well as to control active leg orthoses or FES-based gait support systems. An increasing number of patients with various motion disorders are treated with such active

gait support systems and might benefit from the advantages of the proposed methods. Regardless of the specific application, the use of inertial measurement technologies in diagnosis and treatment systems has become less restrictive and more practical.

Likewise, in Chapter 4, the theory of iterative learning control was extended to improve its applicability to biomedical systems, in which variable pass length is a frequent phenomenon. To cope with the variable dimension of the measured tracking error, a learning progress measure and the hypothetical maximum-pass-length error were introduced. Necessary and sufficient conditions were derived that guarantee monotonic convergence of that error norm if the standard input-update law without Q-filter is used. For the extended learning law with Q-filter, conditions were deduced that assure a reduction of the tracking error at least until it falls below a potentially very small threshold. In this context, the issue of conservativeness in matrix-norm-based convergence criteria was addressed by proposing a frequency-weighted residual indicator to assess the non-zero residual error that is associated with Q-filter usage. All findings were combined in a set of practical guidelines for the design of iterative learning controllers in the presence of variable pass length.

For many application systems, these extensions of the classic ILC theory open the possibility to design controllers that guarantee practically desirable convergence properties. Since assuring safety and stability is a major concern in the design of treatment and diagnosis systems, this achievement lays the foundation for the enhancement of these systems via incorporation of user- and situation-adaptive learning and control algorithms. Several biomedical applications in which measurement or control tasks repeat periodically might be improved, from artificial pancreas systems to rehabilitation robotics and respiratory support systems. Regardless of the specific application, the employment of learning control methods will lead to less manual calibration effort and parameter-adjustments and to more individualized health care solutions.

7.2 General Conclusions on the Considered Applications

The benefits of using inertial realtime gait analysis or iterative learning control methods in biomedical applications were demonstrated by specific examples in the application-focused Chapters 5 and 6 of this dissertation. In Chapter 5, a novel blood pressure measurement technique was considered, which requires feedback control of the blood flow through a superficial artery. It was demonstrated that the performance of standard feedback controllers is severely limited by the poor signal-to-noise ratio of the ultrasound-based flow measurement and by the large uncertainties in the system dynamics. To

overcome these limitations, an iterative learning controller was added, which exploits the periodic nature of the control problem. By experiments in a laboratory model of the cardiovascular system, it was demonstrated that the improved controller yields precise measurements of the heart rate and blood pressure within less than twenty seconds, while allowing for sufficient blood circulation.

In Chapter 6, an adaptive drop foot neuroprosthesis was developed that controls the entire foot pitch and roll angle trajectories of the swing phase by automatic adjustments of FES parameters. A three-electrode setup as well as two parameterizations of the domain of admissible stimulation intensities were proposed. Experimental trials with a chronic drop foot patient revealed that a predefined foot motion can be achieved within only two strides by decentralized iterative learning control of the foot pitch and roll angle. Unlike existing drop foot neuroprostheses, the proposed system adapts the electrical stimulation to the needs of a specific patient on a specific day with a specific electrode placement and maintains a physiological foot motion even in the presence of disturbances.

Both the novel blood pressure measurement system and the adaptive drop foot neuroprosthesis clearly surpass the state of the art, and in particular all commercially available systems, by adapting quickly to the individual human. Their performance does not only depend on the employed hardware and sensor technologies but also on the methods and algorithms that make the most of these components and adjust them automatically according to the current circumstances. Through the combination of the former and the latter, improved diagnosis and treatment is achieved by both of the developed systems.

7.3 Future Research

Several minor questions of future research have already been mentioned in the conclusion sections of the individual chapters. At this point, these aspects are summarized and discussed in a broader sense as well as with respect to the global topic of the dissertation.

Future efforts will be dedicated to extending and transferring the proposed set of methods for inertial realtime gait analysis to motion analysis of the hip joint as well as of the upper limbs. Another main focus of research will be the compensation or minimization of skin and muscle motion artifacts, which were demonstrated to be a major cause of deviations between inertial and optical motion analysis results. Besides, there is a demand for further extension of ILC theory. In most biomedical applications, the variability of the pass length is only one of the challenges that must be overcome. Model uncertainties,

nonlinearities and time-variance complicate the employment of classic ILC concepts as well as of other learning control methods like repetitive control or run-to-run control. To design and understand closed-loop systems with a human in the loop is a challenge that requires research and progress in many disciplines.

This last statement applies in a remarkable way to both of the considered application systems. Concerning the blood pressure measurement technique, further medical investigation of the speed of heart rate and blood pressure changes are advisable. On the sensory side, improving the signal quality of the Doppler ultrasound flow measurement might largely improve the controller performance and, thus, the accuracy of the novel method. Finally, if the device is used to measure the blood pressure in the radial artery of subjects who are able to raise and lower the arm, then this disturbance must be compensated by the controller. To this end, an inertial sensor might be used that provides realtime information of the arm motion.

The setup of the adaptive drop foot neuroprosthesis might also be improved by employment of additional IMUs. Those would yield realtime information on the shank and thigh motion, which might be influenced via additional FES channels in an adaptive multi-channel gait neuroprosthesis. However, the main potential for improvement of FES-based motion support systems, in general, is the interface between the controller and the muscle. FES will become a far more powerful and versatile technology as soon as neural interfaces reach a state of art at which a muscle can be recruited artificially with the effectiveness and efficiency of the central nervous system.

Acknowledgements

Naturally, my primary and sincere thanks go to my advisors Prof. Jörg Raisch and Dr. Thomas Schauer, who strongly and continuously supported me and my research. I am furthermore indebted to my dissertation evaluators Prof. Dirk Abel and Dr. Juan Moreno and to Prof. Clemens Gühmann for agreeing to chair the doctoral committee. Beyond that, I would like to thank a few colleagues who contributed to the presented results and related publications in one way or another – although I will most certainly fail to mention all of them in the following.

The experimental results on gait phase detection (Section 3.1.3) were obtained with the valuable support of Víctor Cermeño Escobar and Lucian Landgraf who implemented the algorithms and tested them with recorded experimental data. Likewise, Daniel Laidig and David Graurock greatly contributed to implementing and evaluating (respectively) the algorithm for foot orientation estimation (cf. Section 3.2.3). Noelia Chía Bejarano and Simona Ferrante from Politecnico di Milano kindly provided datasets that were analyzed in that study. I am furthermore indebted to Timo von Marcard, Bettina Westebbe and Julius Thiele for their excellence and cooperation before, during and after the gait experiments described in Section 3.4.5. In this regard, Steffen Schäperkötter's and Sebastian Scheel's skillful support in data evaluation is also highly acknowledged.

Sincere thanks go to Mickaël Guth for valuable discussions on variable-pass-length ILC. Charlotte Lamotte, Diana Steinecke and Florian Heptner contributed to the preparation of the experiments on blood pressure measurement. The evaluation results presented in Section 5.3 were obtained with the highly valuable support of Ralph Dorn, who programmed the microcontroller. I am indebted to Sarah Schneider and Peter Scharfschwerdt from the Biofluid Mechanics Lab for the great collaboration. Finally, Thomas Schauer's support of the controller design process and numerous experiments is highly acknowledged.

The research project that Chapter 6 relates to and that lead to the development of the Adaptive Peroneal Stimulator also owes its success to several colleagues. It is due to numerous invaluable contributions of Markus Valtin and due to the support of an ambitious student employee team that the proposed methods were successfully implemented and evaluated in realistic experiments. Steffen Schäperkötter, Daniel Laidig, Boris Henckell, Daniela Friedrich and Mirjana Ruppel sedulously implemented several versions of the proposed algorithms in realtime environments. During the course of the research project, they conducted and evaluated a myriad of experiments with healthy subjects and drop foot patients, the results of which are only in parts presented in the figures of Sections 6.3, 6.4 and 6.6. On the clinical side, we were greatly supported by Cordula Werner and several other members of Stefan Hesse's neurological rehabilitation research team at Charité.

With respect to Chapters 3 and 6, I am furthermore indebted to all subjects who supported this research by participating in experimental trials. It is due to them that the developed solutions are both practical and application-oriented.

In the end, I would like to thank you, my dear reader, for the time and effort spent reading my dissertation and for joining me on this journey through the last years of my research. In case any questions remained unanswered, I truly hope that you will not hesitate to contact me.

Bibliography

[1] H.S. Ahn, Y.Q. Chen, K.L. Moore, "Iterative learning control: brief survey and categorization 1998-2004", *IEEE Transactions on Systems, Man, and Cybernetics, Part C: Applications and Reviews*, 37(6):1099–1121, 2007.

[2] H.-S. Ahn, K.L. Moore, YQ. Chen, "Discrete-time Intermittent Iterative Learning Controller with Independent Data Dropouts", *Proceedings of the 17th IFAC World Congress*, pp. 12442–47, 2008.

[3] A.J. del-Ama, Á. Gil-Agudo, J.L. Pons, J.C. Moreno, "Hybrid FES-robot cooperative control of ambulatory gait rehabilitation exoskeleton", *Journal of NeuroEngineering and Rehabilitation*, 11:27, 2014.

[4] H. Arenbeck, L. Wittschier, D. Kügler, A. Duffe, D. Abel, "Comparison of Two Control Methods for Tracking of Respiratory Motion with an Industrial Robot in Radiotherapy", *Proceedings of the AUTOMED Workshop*, pp. 14–15, 2013.

[5] K. Aminian, B. Najafi, C. Bla, P.F. Lezvraz, P. Robert, "Spatio-temporal parameters of gait measured by an ambulatory system using miniature gyroscopes", *Journal of Biomechanics*, 35:689–99, 2002.

[6] K.J. Åström, B. Wittenmark, "Computer Controlled Systems – Theory and Design", 1984.

[7] E. Bachmann, X. Yun, A. Brumfield, "Limitations of Attitude Estimation Algorithms for Inertial/Magnetic Sensor Modules", *IEEE Robotics & Automation Magazine*, 14:76–87, 2007.

[8] R. Baker, "Gait analysis methods in rehabilitation", *Journal of Neuroengineering and Rehabilitation*, 3:4, 2006.

[9] G.A. Benedict, V.F. Ruiz, "A portable gait analysis and correction system using a simple event detection method", *Proceedings of IEEE International Conference on Systems, Man and Cybernetics*, 2002.

[10] A. Brennan, J. Zhang, K. Deluzio, Q. Li, "Quantification of inertial sensor-based 3D joint angle measurement accuracy using an instrumented gimbal", *Gait & Posture*, 34:320–323, 2011.

[11] D.A. Bristow, M. Tharayil, A.G. Alleyne, "A Survey of Iterative Learning Control", *IEEE Control Systems Magazine*, 26(3):69–114, 2006.

[12] B. Cagneau, N. Zemiti, D. Bellot, G. Morel, "Physiological motion compensation in robotized surgery using force feedback control", *Proceedings of the IEEE International Conference on Robotics and Automation*, pp. 1881–1886, 2007.

[13] M.-H. Chang, Y.-L. Chen, K.-C. Wang, T.-S. Kuo, "Implementation of fuzzy control over FES-assisted locomotion for CVA patients", *Proceedings 20th Annual International Conference of the IEEE Engineering in Medicine and Biology Society*, 5:2721–23, 1998.

[14] Y.-L. Chen, S.-C. Chen, W.-L. Chen, C.-C. Hsiao, T.-S. Kuo, J.-S. Lai, "Neural network and fuzzy control in FES-assisted locomotion for the hemiplegic", *Journal of Medical Engineering and Technology*, 28:32–38, 2004.

[15] P. Cheng, B. Oelmann, "Joint-Angle Measurement Using Accelerometers and Gyroscopes – A Survey", *IEEE Transactions on Instrumentation and Measurement*, 59(2):404–414, 2010.

[16] G. Cooper, I. Sheret, L. McMillian, K. Siliverdis, N. Sha, D. Hodgins, L. Kenney, D. Howard, "Inertial sensor-based knee flexion/extension angle estimation", *Journal of Biomechanics*, 42(16):2678–85, 2009.

[17] A.G. Cutti, A. Ferrari, P. Garofalo, M. Raggi, A. Cappello, A. Ferrari, "Outwalk: A protocol for clinical gait analysis based on inertial and magnetic sensors", *Medical & Biological Engineering & Computing*, 48:17–25, 2010.

[18] R.B. Davis III, S. Ounpuu, D. Tyburski, J.R. Gage, "A gait analysis data collection and reduction technique", *Human Movement Science*, 10(5):575–587, 1991.

[19] W.H. De Vries, H.E. Veeger, C.T. Baten, F.C. van der Helm, "Magnetic distortion in motion labs, implications for validating inertial magnetic sensors", *Gait & Posture*, 29:535–541, 2009.

[20] H. Dejnabadi, B.M. Jolles, K. Aminian, "A new approach to accurate measurement of uni-axial joint angles based on a combination of accelerometers and gyroscopes", *IEEE Transactions on Biomedical Engineering*, 52:1478–84, 2005.

[21] T. Donkers, J. van de Wijdeven, O. Bosgra, "Robustness against model uncertainties of norm optimal iterative learning control", *Proceedings of the American Control Conference*, pp. 4561–4566, 2008.

[22] A. Duschau-Wicke, A. Morger, H. Vallery, R. Riener, "Adaptive Patient Support for Rehabilitation Robots", *at – Automatisierungstechnik*, 58(5):260-268, 2010.

[23] H. Elci, R.W. Longman, M.Q. Phan, J.N. Juang, R. Ugoletti, "Simple Learning Control Made Practical by Zero-Phase Filtering: Applications to Robotics", *IEEE Transactions on Circuits and Systems I: Fundamental Theory and Applications*, 49(6):753–767, 2002.

[24] J. Favre, F. Luthi, B.M. Jolles, O. Siegrist, B. Najafi, K. Aminian, "A new ambulatory system for comparative evaluation of the three-dimensional knee kinematics, applied to anterior cruciate ligament injuries", *Knee Surgery, Sports Traumatology, Arthroscopy*, 14:592–604, 2006.

[25] J. Favre, B.M. Jolles, R. Aissaoui, K. Aminian, "Ambulatory measurement of 3D knee joint angle", *Journal of Biomechanics*, 41(5):1029–35, 2008.

[26] J. Favre, R. Aissaoui, B.M. Jolles, J.A. de Gruise, K. Aminian, "Functional calibration procedure for 3D knee joint angle description using inertial sensors", *Journal of Biomechanics*, 42:2330–2335, 2009.

[27] A. Ferrari, A.G. Cutti, P. Garofalo, M. Raggi, M. Heijboer, A. Cappello, A. Davalli, "First *in vivo* assessment of Outwalk: A novel protocol for clinical gait analysis based on inertial and magnetic sensors", *Medical & Biological Engineering & Computing*, 48:1–15, 2010.

[28] R. Fletcher, "Practical Methods of Optimization", 2nd edition, John Wiley & Sons: New York, USA, 1987.

[29] E. Foxlin, "Handbook of Virtual Environment Technologies", chapter "Motion Tracking Technologies and Requirements", pp. 163–210, *Lawrence Erlbaum Publishers*, 2002.

[30] C.T. Freeman, "Constrained point-to-point iterative learning control with experimental verification", *Control Engineering Practice*, 20(5):489–498, 2012.

[31] C.T. Freeman, A.-M. Hughes, J.H. Burridge, P.H. Chappell, P.L. Lewin, E. Rogers, "Iterative learning control of FES applied to the upper extremity for rehabilitation", *Control Engineering Practice*, 17(3):368-381, 2009.

[32] K. Galkowski, J. Lam, E. Rogers, S. Xu, B. Sulikowski, W. Paszke and D.H. Owens, "LMI based stability analysis and robust controller design for discrete linear repetitive processes", *International Journal of Robust and Nonlinear Control*, 13:1195–1211, 2003.

[33] F. Gustafsson, "Determining the initial states in forward-backward filtering", *IEEE Transactions on Signal Processing*, 44(4):988–992, 1996.

[34] M. Guth, T. Seel, J. Raisch, "Iterative Learning Control with Variable Pass Length Applied to Trajectory Tracking on a Crane with Output Constraints", *Proceedings of the 52nd IEEE Conference on Decision and Control (CDC)*, pp. 6676–6681, 2013.

[35] M. Hayashibe, Q. Zhang, C. Azevedo-Coste, "Dual predictive control of electrically stimulated muscle using biofeedback for drop foot correction", *Proceedings of IEEE/RSJ International Conference on Intelligent Robots and Systems (IROS)*, pp. 1731–1736, 2011.

[36] E. Henneman, "Recruitment of motoneurons: the size principle", *Motor Unit Types, Recruitment and Plasticity in Health and Disease*, Progress in Clinical Neurophysiology, pp. 26–90. Karger, Basel, 9th edition, 1981.

[37] T. Kailath, "Linear Systems", Prentice Hall, 1980.

[38] T.R. Kane, D.A. Levinson, "Dynamics: Theory and Applications", *McGraw-Hill*, 1985.

[39] C. Klauer, T. Schauer, J. Raisch, "High Performance Motion Control by Neuro-Muscular Electrical Stimulation Applied to the Upper-Limb", *Proceedings of the 15th Annual IFESS Conference and 10th Vienna Int. Workshop on FES*, pp. 318–320, 2010.

[40] H.-R. Kobravi, A. Erfanian, "Decentralized adaptive robust control based on sliding mode and nonlinear compensator for the control of ankle movement using functional electrical stimulation of agonist-antagonist muscles", *Journal of Neural Engineering*, 6, 2009.

[41] D. Kotiadis, H.J. Hermens, P.H. Veltink, "Inertial Gait Phase Detection for control of a drop foot stimulator: inertial sensing for gait phase detection", *Medical Engineering & Physics*, 32(4):287–297, 2010.

[42] E. Kurniawan, Z. Cao, Z. Man, "Design of Robust Repetitive Control with Time Varying Sampling Periods", *IEEE Transactions on Industrial Electronics*, 61(6):2834–41, 2013.

[43] H. Lau, K. Tong, "The reliability of using accelerometers and gyroscopes for gait event identification on persons with dropped foot", *Gait & Posture*, 27:248–57, 2008.

[44] W. Lewis, "The evolution of clinical sphygmomanometry", *Bulletin of the New York Academy of Medicine*, 17(11):871–881, 1941.

[45] X.-F. Li, J.-X. Xu, D. Huang, "An Iterative Learning Control Approach for Linear Systems With Randomly Varying Trial Lengths", *IEEE Transactions on Automatic Control*, 59(7):1954–60, 2014.

[46] X.-F. Li, J.-X. Xu, "Lifted system framework for learning control with different trial lengths", *International Journal of Automation and Computing*, 12(3):273-280, 2015.

[47] X.-F. Li, J.-X. Xu, D. Huang, "Iterative learning control for nonlinear dynamic systems with randomly varying trial lengths", *International Journal of Adaptive Control and Signal Processing*, 1099–1115, 2015.

[48] T. Liu, Y. Inoue, K. Shibata, "Development of a wearable sensor system for quantitative gait analysis", *Measurement*, 42:978–988, 2009.

[49] K. Liu, T. Liu, K. Shibata, Y. Inoue, R. Zheng, "Novel approach to ambulatory assessment of human segmental orientation on a wearable sensor system", *Journal of Biomechanics*, 42(16):2747–2752, 2009.

[50] K. Liu, T. Liu, K. Shibata, Y. Inoue, "Ambulatory measurement and analysis of the lower limb 3D posture using wearable sensor system", *Proceedings of the International Conference on Mechatronics and Automation*, pp. 3065–69, 2009.

[51] J. Liu, Y. Wang, H. Tong, R.P.S. Han, "Iterative Learning Control Based on Radial Basis Function Network for Exoskeleton Arm", *Advanced Materials Research*, 415–417:116–22, 2012.

[52] L. Ljung, "System identification: Theory for the User", 2nd edition, Prentice Hall, 1999.

[53] G.M. Lyons, T. Sinkjær, J.H. Burridge, D.J. Wilcox, "A Review of Portable FES-Based Neural Orthoses for the Correction of Drop Foot", *IEEE Transactions on Neural Systems and Rehabilitation Engineering*, vol. 10, no. 4, pp. 260–279, 2002.

[54] T. Liberson, H.J. Holmquest, D. Scot, and M. Dow, "Functional Electrotherapy: Stimulation of the Peroneal Nerve Synchronized with the Swing Phase of the Gait of Hemiplegic Patients", *Archives of Physical Medicine and Rehabilitation*, 21:101–105, 1961.

[55] R.W. Longman, K.D. Mombaur, "Investigating the Use of Iterative Learning Control and Repetitive Control to Implement Periodic Gaits", *Lecture notes in control and information sciences*, 340:189–218, 2006.

[56] H.J. Luinge, P.H. Veltink, "Measuring orientation of human body segments using miniature gyroscopes and accelerometers", *Medical & Biological Engineering & Computing*, 43:273–282, 2005.

[57] H.J. Luinge, D. Roetenberg, P.J. Slycke, "Inertial Sensor Kinematic Coupling", Patent US20110028865 A1, 3 February 2011.

[58] A. Mansfield, G. M. Lyons, "The use of accelerometry to detect heel contact events for use as a sensor in FES assisted walking", *Medical Engineering & Physics*, vol. 25, pp. 879–85, 2003.

[59] B. Mariani, S. Rochat, C. Büla, K. Aminian, "Heel and toe clearance estimation for gait analysis using wireless inertial sensors", *IEEE Transactions on Biomedical Engineering*, vol. 59, pp. 3162–68, 2012.

[60] R.E. Mayagoitia, A.V. Nene, P.H. Veltink, "Accelerometer and rate gyroscope measurement of kinematics: an inexpensive alternative to optical motion analysis systems", *Journal of Biomechanics*, 35(4):537–42, 2002.

[61] P.L. Melo, M.T. Silva, J.M. Martins, D.J. Newman, "Technical developments of functional electrical stimulation to correct drop foot: Sensing, actuation and control strategies", *Clinical Biomechanics*, 30(2):101-113, 2015.

[62] J.-H. Moon, T.-Y. Doh, M.J. Chung, "A Robust Approach to Iterative Learning Control Design for Uncertain Systems", *Automatica*, 34(8):1001–1004, 1998.

[63] K.L. Moore, M. Johnson, M.J. Grimble, "Iterative Learning Control for Deterministic Systems", *Springer (Advaces in Industrial Control)*, 1993.

[64] K.L. Moore, A. Mathews, "Iterative Learning Control with Non-Standard Assumptions Applied to the Control of Gas-Metal ARC Welding (Book Section)", *Iterative Learning Control*, Springer, 1998.

[65] K.L. Moore, "A non-standard iterative learning control approach to tracking periodic signals in discrete-time non-linear systems", *International Journal of Control*, 73(10):955–967, 2000.

[66] K.L. Moore, M. Ghosh, Y.Q. Chen, "Spatial-based iterative learning control for motion control applications", *Meccanica*, 42(2):167–175, 2007.

[67] J.C. Moreno, E.R. de Lima, A.F. Ruíz, F.J. Brunetti, J.L. Pons, "Design and implementation of an inertial measurement unit for control of artificial limbs: Application on leg orthoses", *Sensors and Actuators B: Chemical*, 118:333–337, 2006.

[68] J.C. Moreno, A.J. del-Ama, A. de Los Reyes-Guzmán, Á. Gil-Agudo, R. Ceres, J.L. Pons, "Neurorobotic and hybrid management of lower limb motor disorders: a review", *Medical & Biological Engineering & Computing*, 49(10):1119-30, 2011.

[69] N. Mourselas, M.H. Granat, "Correction of Drop Foot Using a Fuzzy Logic Controlled Miniature Stimulator", *Proceedings of the 5th Annual Conference of the International Functional Electrical Stimulation Society*, pp. 140–141, 2000.

[70] P. Müller, T. Seel, T. Schauer, "Experimental Evaluation of a Novel Inertial Sensor Based Realtime Gait Phase Detection Algorithm", *Proceedings of the Technically Assisted Rehabilitation Conference*, 2015.

[71] H. Nahrstaedt, T. Schauer, R. Shalaby, S. Hesse, J. Raisch, "Automatic Control of a Drop-Foot Stimulator Based on Angle Measurement Using Bioimpedance", *Artificial Organs*, 32(8):649–654, 2008.

[72] H. Nahrstaedt, T. Schauer, S. Hesse, J. Raisch, "Iterative Learning Control of a Gait Neuroprosthesis" (in German), *at – Automatisierungstechnik*, 56(9):494-501, 2008.

[73] N.-O. Negård, R. Kauert, S. Andres, T. Schauer, and J. Raisch, "Gait phase detection and step length estimation of gait by means of inertial sensors", *Proceedings of the 3rd European Medical and Biological Engineering Conference*, 2005.

[74] N.-O. Negård, "Controlled FES-assisted gait training for hemiplegic stroke patients based on inertial sensors", *Doctoral Thesis*, TU Berlin, 2009.

[75] M. Norrlöf, S. Gunnarsson, "Time and frequency domain convergence properties in iterative learning control", *International Journal of Control*, 75(14):1114–1126, 2002.

[76] E. O'Brien, "Blood pressure measuring devices: recommendations of the European Society of Hypertension", *British Medical Journal*, 322(7285):531–536, 2001.

[77] K.J. O'Donovan, R. Kamnik, D.T. O'Keeffe, G.M. Lyons, "An inertial and magnetic sensor based technique for joint angle measurement", *Journal of Biomechanics*, 40(12):2604–11, 2007.

[78] D.H. Owens, J. Hätönen, "Iterative learning control – An optimization paradigm", *Annual Reviews in Control*, 29:57–70, 2005.

[79] I.P. Pappas, M.R. Popovic, T. Keller, V. Dietz, M. Morari, "A reliable gait phase detection system", *IEEE Transactions on Neural Systems and Rehabilitation Engineering*, 9:113–25, 2001.

[80] G.Parati, G. Bilo, G. Mancia, "Blood pressure measurement in research and in clinical practice: recent evidence", *Current Opinion in Nephrology and Hypertension*, 13(3):343–357, 2004.

[81] K.H. Park, Z. Bien, "A generalized iterative learning controller against initial state error", *International Journal of Control*, 73(10):871–881, 2000.

[82] W. Paszke, E. Rogers, K. Galkowski, "On the Design of ILC Schemes for Finite Frequency Range Tracking Specifications", *Proceedings of th IEEE Conference on Decision & Control*, 2010.

[83] C.Payne, S. Munteanu, K. Miller, "Position of the Subtalar Joint Axis and Resistance of the Rearfoot to Supination", *Journal of the American Podiatric Medical Association*, 93(2):131–135, 2003.

[84] P.H. Peckham, J.S. Knutson, "Functional electrical stimulation for neuromuscular applications", *Annual Review of Biomedical Engineering*, 7:327–60, 2005.

[85] J. Penaz, "Method and apparatus for automatic non-invasive blood pressure measurement", European Patent No. EP 0284095, 1993.

[86] J. Perry, J.M. Burnfield, "Gait Analysis: Normal and Pathological Function", *SLACK Incorporated*, 2010.

[87] D. Popovic , T. Sinkjaer, "Control of Movement for the Physically Disabled", *Springer Verlag*, 2000.

[88] F. Rabbia, S. Del Colle, E. Testa, D. Naso, F. Veglio, "Accuracy of the blood pressure measurement", *Minerva cardioangiologica*, 54(4):399–416, 2006.

[89] D.K. Ramsey, P.F. Wretenberg, "Biomechanics of the knee: Methodological considerations in the *in vivo* kinematic analysis of the tibiofemoral and patellofemoral joint", *Journal of Biomechanics*, 14:595–611, 1999.

[90] H. Ring, I. Treger, L. Gruendlinger, J.M. Hausdorff, "Neuroprosthesis for Footdrop Compared with an Ankle-Foot Orthosis: Effects on Postural Control during Walking", *Journal of Stroke and Cerebrovascular Diseases*, 18(1):41–47, 2009.

[91] V. Robertson, A. Ward, J. Low, A. Reed, "Electrotherapy Explained: Principles and Practice", *Butterworth-Heinemann / Elsevier*, 2006.

[92] D. Roetenberg, L. Schipper, P. Garofalo, A.G. Cutti, H.J. Luinge, "Joint angles and segment length estimation using inertial sensors", *Presented at 3DMA-10 Meeting of the Technical Group on 3-D Analysis of Human Movement of the ISB*, 2010.

[93] D. Roetenberg, H. Luinge, P. Slycke, "Xsens MVN: Full 6DOF Human Motion Tracking Using Miniature Inertial Sensors" (version April 2013), available online: http://www.xsens.com/images/stories/PDF/MVN_white_paper.pdf, accessed on October 10, 2015.

[94] E. Rogers, K. Galkowski, D.H. Owens, "Control Systems Theory and Applications for Linear Repetitive Processes", *Springer (Lecture Notes in Control and Information Sciences, 349)*, 2007.

[95] J. Rueterbories, E. G. Spaich, B. Larsen, O. K. Andersen, "Methods for gait event detection and analysis in ambulatory systems",*Medical Engineering & Physics*, 32(6):545–552, 2010.

[96] J. Rueterbories, E. G. Spaich, B. Larsen, O. K. Andersen, "Gait event detection for use in FES rehabilitation by radial and tangential foot accelerations",*Medical Engineering & Physics*, 36(4):545–552, 2010.

[97] D.N. Rushton, "Functional electrical stimulation", *Physiol. Meas.*, 18:241–275, 1997.

[98] A.M. Sabatini, C. Martelloni, S. Scapellato, F. Cavallo, "Assessment of walking features from foot inertial sensing", *Biomedical Engineering*, 52(3): 486–494, 2005.

[99] A.M. Sabatini, "Estimating Three-Dimensional Orientation of Human Body Parts by Inertial/Magnetic Sensing", *Sensors*, 11:1489–1525, 2011.

[100] P.G. Savage, "Strapdown Inertial Navigation Integration Algorithm Design – Part 1: Attitude Algorithms", *Journal of guidance, control, and dynamics*, 21(1):19–28, 1998.

[101] T. Schauer, "Feedback Control of Cycling in Spinal Cord Injury using Functional Electrical Stimulation", PhD thesis, University of Glasgow, 2005.

[102] T. Seel, T. Schauer, J. Raisch, "Iterative Learning Control for Variable Pass Length Systems", *Proceedings of the 18th IFAC World Congress*, pp. 4880–85, 2011.

[103] T. Seel, T. Schauer, J. Raisch, "Joint axis and position estimation from inertial measurement data by exploiting kinematic constraints", *Proceedings of the IEEE International Conference on Control Applications (CCA)*, pp. 45–49, 2012.

[104] T. Seel, T. Schauer, J. Raisch, "Iterative Learning Control with Variable Pass Length applied to FES-based Drop Foot Treatment" (in German), *at- Automatisierungstechnik*, 61(9):630–37, 2013.

[105] T. Seel, S. Schäperkötter, M. Valtin, C. Werner, T. Schauer, "Design and control of an Adaptive Peroneal Stimulator with inertial sensor-based gait phase detection", *Proceedings of the 18th Annual International FES Society Conference*, pp. 177–180, 2013.

[106] T. Seel, S. Weber, K. Affeld, T. Schauer, "Iterative Learning Cascade Control of Continuous Noninvasive Blood Pressure Measurement", *Proceedings of the IEEE International Conference on Systems, Man, and Cybernetics*, pp. 2207–2212, 2013.

[107] T. Seel, D. Laidig, M. Valtin, C. Werner, J. Raisch, T. Schauer, "Feedback Control of Foot Eversion in the Adaptive Peroneal Stimulator", *Proceedings of the 22nd IEEE Mediterranean Conference on Control and Automation*, pp. 1482–1487, 2014.

[108] T. Seel, J. Raisch, T. Schauer, "IMU-based joint angle measurement for gait analysis", *Sensors*, 14(4):6891–909, 2014.

[109] T. Seel, L. Landgraf, T. Schauer, "Online Gait Phase Detection with Automatic Adaption to Gait Velocity Changes Using Accelerometers and Gyroscopes", *Biomedical Engineering / Biomedizinische Techik*, 59(S1):795–798, 2014.

[110] T. Seel, T. Schauer, J. Raisch, "Inertial Sensor-Based Gait Analysis", *website with illustrative computer animations*, available online: http://www.control.tu-berlin.de/IMU-Based_Gait_Analysis, accessed on October 10, 2015.

[111] Y. Shimada, S. Ando, T. Matsunaga, A. Misawa, T. Aizawa, T. Shirahata, E. Itoi, "Clinical application of acceleration sensor to detect the swing phase of stroke gait in functional electrical stimulation", *Tohoku Journal of Experimental Medicine*, vol. 207, pp. 197–202, 2005.

[112] A. Soska, C.T. Freeman, E. Rogers, "ILC for FES-based Stroke Rehabilitation of Hand and Wrist", *Proceedings of the IEEE Multi-Conference on System and Control*, 1267–1272, 2012.

[113] R. Stagni, S. Fantozzi, A. Cappello, A. Leardini, "Quantification of soft tissue artefact in motion analysis by combining 3D fluoroscopy and stereophotogrammetry: A study on two subjects", *Clinical Biomechanics*, 20:320–329, 2005.

[114] R. Takeda, S. Tadano, A. Natorigawa, M. Todoh, S. Yoshinari, "Gait posture estimation using wearable acceleration and gyro sensors", *Journal of Biomechanics*, 42(15):2486–2494, 2009.

[115] D. Titterton, J. Weston, "Strapdown Inertial Navigation Technology", *The American Institute of Aeronautics and Astronautics*, second edition, 2004.

[116] T. Truelsen, B. Piechowski-Jozwiak, R. Bonita, C. Mathers, J. Bogousslavsky, G. Boysen, "Stroke incidence and prevalence in Europe: a review of available data", *European Journal of Neurology*, 13:581–598, 2006.

[117] M. Valtin, T. Seel, J. Raisch, T. Schauer, "Iterative learning control of drop foot stimulation with array electrodes for selective muscle activation", *Proceedings of the 19th IFAC World Congress*, pp. 6587–6592, 2014.

[118] M. Valtin, K. Kociemba, C. Behling, B. Kuberski, M. Weber, T. Schauer, "A Versatile Stimulator for Advanced Transcutaneous FES Applications Enabling User-

Specified Pulse Waveforms", *Biomedical Engineering / Biomedizinische Techik*, 59(S1):S1049–52, 2014.

[119] P.H. Veltink, P. Slycke, J. Hemssems, R. Buschman, G. Bultstra, H. Hermens, "Three dimensional inertial sensing of foot movements for automatic tuning of a two-channel implantable drop-foot stimulator", *Medical engineering & physics*, 25(1):21–28, 2003.

[120] J.C. Van den Noort, A. Ferrari, A.G. Cutti, J.G. Becher, J. Harlaar, "Gait analysis in children with cerebral palsy via inertial and magnetic sensors", *Medical & Biological Engineering & Computing*, 51:377–386, 2013.

[121] Y. Wang, F. Gao, F.J. Doyle III, "Survey on iterative learning control, repetitive control, and run-to-run control", *Journal of Process Control*, 19:1589–1600, 2009.

[122] K.M. Wang T. Schauer, H. Nahrstaedt, J. Raisch, "Iterative Learning Control (ILC) of Cadence for Functional Electrical Stimulation (FES) induced Cycling in Paraplegia", *Proceedings of the 14th Annual Conference of the International Functional Electrical Stimulation Society*, pp. 71–73, 2009.

[123] Y. Wang, E. Dassau, F.J. Doyle III, "Closed-loop control of artificial pancreatic-cell in type 1 diabetes mellitus using model predictive iterative learning control", *IEEE Transactions on Biomedical Engineering*, 57(2):211-219, 2010.

[124] S. Weber, U. Kertzscher, K. Affeld, "Measuring Blood Pressure using Ultrasound-Doppler Signals" (in German), *Biomedizinische Technik*, 55:29–32, 2010.

[125] S. Weber, D. Strommenger, U. Kertzscher, K. Affeld, "Continuous blood pressure measurement with ultrasound", *Biomedizinische Technik*, 57(1):407–410, 2012.

[126] Williamson R, Andrews BJ. Sensor system for lower limb functional electrical stimulation (FES) control", *Medical Engineering and Physics*, 22:313–25, 2000.

[127] R. Williamson, B. J. Andrews, "Gait event detection for FES using accelerometers and supervised machine learning", *IEEE Transactions on Rehabilitation Engineering*, vol. 8, pp. 312–19, 2000.

[128] O.J. Woodman, "An Introduction to Inertial Navigation", *Technical Report 696*, University of Cambridge, 2007.

[129] G. Wu, P.R. Cavanagh, "ISB recommendations for standardization in the reporting of kinematic data", *Journal of Biomechanics*, 28:1257–1261, 1995.

[130] A.D. Young, "Comparison of Orientation Filter Algorithms for Realtime Wireless Inertial Posture Tracking", *Proceedings of the 6th International Workshop on Wearable and Implantable Body Sensor Networks*, pp. 59–64, 2009.

[131] A.D. Young, "Use of Body Model Constraints to Improve Accuracy of Inertial Motion Capture", *International Workshop on Wearable and Implantable Body Sensor Networks*, pp. 180–186, International Conference on Body Sensor Networks, 2010.

[132] J.-T. Zhang, A.C. Novak, B. Brouwer, Q. Li, "Concurrent validation of Xsens MVN measurement of lower limb joint angular kinematics", *Physiological Measurement*, 34:N63–N69, 2013.